

SYNERGY BETWEEN THEORY AND EXPERIMENT AS APPLIED TO H/D EXCHANGE ACTIVITY ASSAYS IN [Fe]H₂ase ACTIVE SITE MODELS

JESSE W. TYE, MICHAEL B. HALL, IRENE P. GEORGAKAKI and
MARCETTA Y. DARENSBOURG

Department of Chemistry, Texas A&M University, College Station, TX 77843, USA

- I. Introduction
- II. Experimental Section
 - A. H/D Exchange in D₂/H₂O Mixture with Fe^IFe^I Complex as Catalyst
 - B. Reactions of $\{(\mu\text{-H})(\mu\text{-pdt})[\text{Fe}(\text{CO})_2(\text{PMe}_3)_2]\}^+ [\text{PF}_6]^-$ with Acetone
 - C. Computational Details
- III. Results and Discussion
 - A. Choice and Validation of the Computational Model
 - B. Creation of the Open Site
 - C. Dihydrogen Complexes
 - D. H/D Exchange Inhibition
 - E. Cleavage of the H–H Bond
 - F. H/D Exchange into the $\mu\text{-H}$ Position
 - G. The Overall Mechanism
 - H. D₂/H₂O Scrambling Catalyzed by $(\mu\text{-pdt})[\text{Fe}(\text{CO})_2(\text{PMe}_3)_2]$
 - I. Reaction of $\{(\mu\text{-H})(\mu\text{-pdt})[\text{Fe}(\text{CO})_2(\text{PMe}_3)_2]\}^+$ with Acetone
 - J. Calculation of NMR Shielding Tensors
- IV. Conclusions
- References

I. Introduction

In view of its application to fuel cell development, research into hydrogen activation remains a forefront area for chemists, physicists, and biologists (*1*). A rekindling of opportunity and excitement in this field of chemistry has come from the delineation of simple catalytic sites of hydrogenase enzymes as displayed by protein crystal structures published within the last decade (*2–10*). These active sites hold out promise of using complexes comprised of base metals such as iron or

a combination of Fe/Ni instead of platinum metal as catalysts for such important technical processes.

The starting point for the chemist is the preparation of synthetic analogues of composition and structure as similar as possible to the natural active site, with the expectation that the electronic properties of the latter might be reproduced in the model complex, ultimately engendering similar function (11). In the case of Fe-only and [NiFe] hydrogenases, the fortunate presence of diatomic ligands, well known to serve as reporters of electron density, has facilitated a comparison between the natural and the synthetic active sites by providing credible reference points for the use of spectroscopy in assigning redox levels for the enzyme at various stages of catalytic activity or deactivation (9). These comparisons have encouraged a unique synergism between computations, spectroscopy and synthetic model development (9,12). The work described herein is an attempt to move such interactions even closer to the goal of predicting properties needed for synthetic catalysts designed for hydrogen activation.

Hydrogenases are biological catalysts responsible for H₂ uptake or production, in which the required H₂ cleavage has been established to occur in a reversible and heterolytic manner (H⁺/H⁻) (13). This activity is typically assayed by H/D exchange reactivity in H₂/D₂O or H₂/D₂/H₂O mixtures (13–17). The active site of iron-only hydrogenase, [Fe]H₂ase (7–10), consists of a 2Fe2S butterfly core in which the sulfur atoms are linked by three light atoms of undetermined identity, but typically modeled by either propane dithiolate (pdt), or ⁻SCH₂N(R)CH₂S⁻. The active site is connected to the first 4Fe4S cluster of the electron-transport chain via a bridging cysteine. Although unusual in nature, the diatomic ligands (CO, CN⁻) that fill the remaining coordination sites of each metal center harken to the genesis of the ancient organisms and the harsh terrestrial conditions under which these enzymes evolved (18).

The [Fe]H₂ase enzyme exists in at least three different redox levels. The oxidized-active form, assigned as Fe^{II}Fe^I, is the state that takes up and activates H₂ (9). In this state both metals are in octahedral coordination geometry by virtue of a μ-CO group, and the distal Fe (the one further removed from the 4Fe4S cluster), is tentatively assigned as Fe^{II}. This iron is coordinated by a labile H₂O molecule in the oxidized form (7), and a CO in the CO-inhibited oxidized form (10) as shown in Fig. 1. Photolytic (CO-loss) conditions allow the CO inhibited form of enzyme to regain activity as assayed by H/D exchange in H₂/D₂O mixtures (19).

The rapid development of [Fe]H₂ase active site model chemistry benefited greatly from early organometallic studies of (μ-S₂)[Fe(CO)₃]₂,

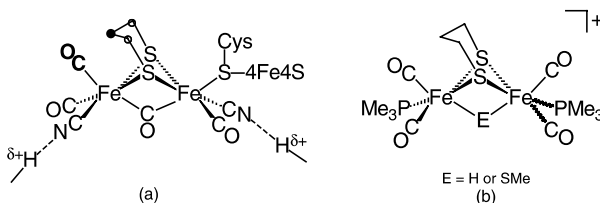


FIG. 1. Stick drawing structures of (a) CO-inhibited oxidized form of $[\text{Fe}]\text{H}_2\text{ase}$ active site; and (b) $\text{Fe}^{\text{II}}\text{Fe}^{\text{II}}$ functional models. The specific orientation of the PMe_3 ligands is E dependent: E = H, transoid; E = SMe, cisoid.

$(\mu\text{-SRS})[\text{Fe}(\text{CO})_3]_2$, and $(\mu\text{-SRS})[\text{Fe}(\text{CO})_2(\text{L})]_2$. Reihlen reported the synthesis of $(\mu\text{-SEt})_2[\text{Fe}(\text{CO})_3]_2$ in 1929 (20). In the 1960s Poilblanc (21) examined the ligand exchange process for a series of complexes of the form $(\mu\text{-SR})_2[\text{Fe}(\text{CO})_3]_2$. Poilblanc (21) and Treichel (22) investigated the attack of electrophiles on the metal-metal bond of $(\mu\text{-SR})_2[\text{Fe}(\text{CO})_2(\text{L})]_2$ complexes to generate $\{(\mu\text{-E})(\mu\text{-SR})_2[\text{Fe}(\text{CO})_2(\text{L})]_2\}^+$. In the 1980s, Seyferth (23) developed the chemistry of the bridged dithiolate complexes of the form $(\mu\text{-S}(\text{CH}_2)_x\text{S})[\text{Fe}(\text{CO})_3]_2$.

Diiron(II) complexes of the type $\{(\mu\text{-E})(\mu\text{-pdt})[\text{Fe}(\text{CO})_2(\text{PMe}_3)]_2\}^+$ (E = H or SMe) as seen in Fig. 1 were examined as potential structural/spectroscopic models of the $[\text{Fe}]\text{H}_2\text{ase}$ active site, using PMe_3 as a substitute for the reactive cyanide ligands (24–26).

With the encouragement of Prof. Dieter Sellmann in 2001, and using his experimental protocol (27) we explored the reactivity of $\text{Fe}^{\text{II}}\text{Fe}^{\text{II}}$ complexes toward D_2 and $\text{D}_2/\text{H}_2\text{O}$ mixtures. In order to establish the factors affecting such reactions, solutions of these complexes under various conditions were pressurized with D_2 in a medium pressure NMR sample tube. The ^2H NMR spectroscopic monitor of the reactions indicated the build-up of D-incorporated species (24–26). Control experiments established that the activation of D_2 in these reactions was facilitated by light and was inhibited by coordinating solvents or the addition of CO (24,25). This last feature is in agreement with the CO-inhibition of $[\text{Fe}]\text{H}_2\text{ase}$ activity and strongly suggests the need for creation of an open site prior to D_2 binding to Fe^{II} .

The relatively simple active site of $[\text{Fe}]\text{H}_2\text{ase}$ and the limited involvement of the protein as ligands in the first coordination sphere has appealed to computational chemists as an appropriate system to explore by Density Functional Theory (12,28–32). The calculations published to date have focused on correlating $\nu(\text{CO})/\nu(\text{CN})$ vibrational frequencies of the different redox levels of the diiron active site with

model complexes, on defining plausible possibilities for the unique three light-atom S to S linker, and on delineating mechanistic possibilities for H₂ activation (12,28–32). Until now, none of the published computational models have attempted to explore how the [Fe]H₂ase active site performs the activity assay, i.e., the H/D exchange reactivity in H₂/D₂O or D₂/H₂O mixtures. Herein, DFT calculations are described that suggest reasonable mechanistic explanations for the experimentally observed H/D exchange reactivity, not of the enzyme active site, but of Fe^{II}Fe^{II} functional model complexes. New experiments have also been carried out in order to test the hypotheses implied by some of the individual steps of the proposed mechanism, which were calculated to be energetically feasible.

II. Experimental Section

Reagents used in the preparation of starting materials, procedures, and instrumentation have been described earlier (24,25).

A. H/D EXCHANGE IN D₂/H₂O MIXTURE WITH Fe^IFe^I COMPLEX AS CATALYST

In a typical experiment 0.8 mL portions of solutions made from 0.029 g (μ-pdt)[Fe(CO)₂(PMe₃)₂] in 1 mL CH₂Cl₂ were placed in medium-pressure NMR sample tubes (Wilmad, 528-PV-7) together with 2 μL H₂O. The tubes were degassed, pressurized with 10 bar D₂ and exposed to sunlight as shown in Fig. 2. ²H NMR spectra were taken at time intervals to follow the formation of HOD.

B. REACTIONS OF {(μ-H)(μ-pdt)[Fe(CO)₂(PMe₃)₂]}⁺[PF₆][−] WITH ACETONE

A solution made from 0.095 g {(μ-H)(μ-pdt)[Fe(CO)₂(PMe₃)₂]}⁺[PF₆][−] in 10 mL acetone was exposed to sunlight for 50 min. The acetone was removed under vacuum and the resulting solid was redissolved in 7–10 mL CH₂Cl₂. The IR spectrum (ν(CO) region only) of this solution showed a mixture of the starting complex (bands at 2031(s) and 1978(s) cm^{−1}) and the presumed acetone complex (bands at 2031(s), 1989(m), 1978(s), and 1945(s) cm^{−1}). After bubbling CO through the solution for 5 min, the IR spectrum showed the disappearance of the ν(CO) bands at 2031, 1989, 1978, and 1945 cm^{−1}, while the ν(CO) bands at 2031 and



FIG. 2. Medium pressure NMR sample tubes containing solutions of the diiron complexes, pressurized with 10 bar D_2 and were exposed to sunlight on the windowsill.

1978 cm^{-1} regained intensity. A similar reaction was carried out in an NMR sample tube using 10 mg of $\{(\mu\text{-H})(\mu\text{-pdt})[\text{Fe}(\text{CO})_2(\text{PMe}_3)_2]\}^+ [\text{PF}_6]^-$ in 0.8 mL acetone- d_6 . After exposure to sunlight for 1 h the ^1H NMR spectrum showed two sets of resonances in the upfield region. A quartet centered at -7.7 ppm with $J_{\text{H-P}}$ coupling constants of 29.7 and 21.3 Hz was assumed to be the acetone complex, $\{(\mu\text{-H})(\mu\text{-pdt})[\text{Fe}(\text{CO})_2(\text{PMe}_3)][\text{Fe}(\text{CO})(\text{PMe}_3)(\text{acetone})]\}^+$; and a triplet centered at -15.0 ppm with $J_{\text{H-P}}$ 22.8 Hz, derived from the parent compound, $\{(\mu\text{-H})(\mu\text{-pdt})[\text{Fe}(\text{CO})_2(\text{PMe}_3)_2]\}^+$. The $^{31}\text{P}\{^1\text{H}\}$ NMR spectrum displayed a doublet centered at 24.3 ppm and another doublet centered at 22.4 ppm, both with $J_{\text{P-P}}$ coupling of 7.4 Hz. Three microliters of CH_3CN were added and the sample was maintained in the dark for 30 min. The ^1H NMR spectrum of this sample showed the disappearance of the hydride resonance at -7.7 ppm and the appearance of a new hydride resonance as a doublet of doublets centered at -10.9 ppm. This hydride signal was identical to that of a bona fide sample of $\{(\mu\text{-H})(\mu\text{-pdt})[\text{Fe}(\text{CO})_2(\text{PMe}_3)][\text{Fe}(\text{CO})(\text{PMe}_3)(\text{CH}_3\text{CN})]\}^+$, whose preparation and full characterization was reported earlier (33).

C. COMPUTATIONAL DETAILS

All DFT calculations were performed using a hybrid functional [the three-parameter exchange functional of Becke (B3) (34) and the correlation functional of Lee, Yang, and Parr (LYP) (35)] (B3LYP) as implemented in Gaussian 98 (36). The iron, sulfur, and phosphorus atoms used the effective core potential and associated basis set of Hay and Wadt (LANL2DZ) (37,38). For iron, the two outermost p functions were replaced by the re-optimized $4p$ functions as suggested by Couty and Hall (39). For phosphorus and sulfur, the basis set was augmented by the d polarization function of Höllwarth *et al.* (40). Dunning's correlation-consistent polarized valence double zeta basis set (cc-pVDZ) (41) was employed for the CO ligands, H_2O , CH_2Cl_2 , the carbonyl group of $\text{CH}_3\text{C}(\text{O})\text{CH}_3$, the nitrile group of CH_3CN , hydridic hydrogens, and dihydrogen. The carbon and hydrogen atoms of the ethane dithiolate bridge, the hydrogen atoms of PH_3 , and the methyl groups of CH_3CN , $\text{CH}_3\text{C}(\text{O})\text{CH}_3$, and $\text{P}(\text{CH}_3)_3$ use Dunning's double zeta basis (D95) (42,43). Unless otherwise noted, all geometries are fully optimized and confirmed as minima or n -order saddle points by analytical frequency calculations at the same level. Transition states were fully optimized beginning from either a scan of the metal–ligand distance or the Quadratic Synchronous Transit (QST3) method as implemented in Gaussian 98.

NMR shielding tensors were calculated using the Gauge-Independent Atomic Orbital (GIAO) method as implemented in Gaussian 98 (44–46). The basis sets and level of theory are the same as used in the geometry optimizations and frequency calculations mentioned above.

III. Results and Discussion

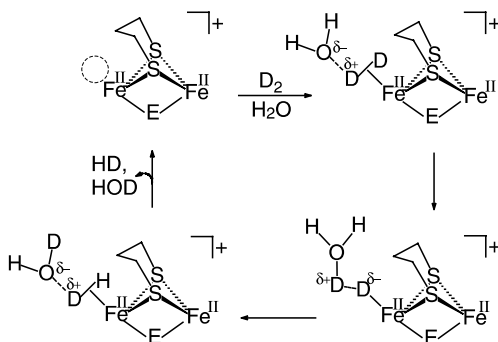
Homovalent $\text{Fe}^{\text{II}}\text{Fe}^{\text{II}}$ complexes may be derived from $\text{Fe}^{\text{I}}\text{Fe}^{\text{I}}$ precursors via binuclear oxidative addition of electrophiles such as H^+ or SMe^+ yielding $\{(\mu\text{-H})(\mu\text{-pdt})[\text{Fe}(\text{CO})_2(\text{PMe}_3)_2]\}^+$ and $\{(\mu\text{-SMe})(\mu\text{-pdt})[\text{Fe}(\text{CO})_2(\text{PMe}_3)_2]\}^+$, respectively, from $(\mu\text{-pdt})[\text{Fe}(\text{CO})_2(\text{PMe}_3)_2]$ (24–26). The role of the PMe_3 ligands in the precursor complex (analogues to cyanide in the enzyme active site) is to increase both the basicity of the $\text{Fe}^{\text{I}}\text{Fe}^{\text{I}}$ bond and to stabilize the $\text{Fe}^{\text{II}}\text{Fe}^{\text{II}}$ oxidation level of the resulting compound. The protonation of $\{(\mu\text{-pdt})[\text{Fe}(\text{CO})_2(\text{CN})_2]\}^{2-}$ to yield $\{(\mu\text{-H})(\mu\text{-pdt})[\text{Fe}(\text{CO})_2(\text{CN})_2]\}^-$ is complicated by the basicity

of the cyanide nitrogen, which leads to decomposition presumably via the loss of HNC (or HCN) (24,47,48). The $\{(\mu\text{-SMe})(\mu\text{-pdt})[\text{Fe}(\text{CO})_2(\text{CN})]_2\}^-$ analogue was prepared by a different route to obviate the electrophilic attack on the cyanide nitrogen (49).

Using ^2H NMR spectroscopy as an *in situ* reaction monitor, the $\text{Fe}^{\text{I}}\text{Fe}^{\text{II}}$ complexes were assayed for hydrogenase-like activity. In the presence of D_2 , the observation of incorporation of deuterium into the bridging hydride position of the diiron complex, indicated activation of D_2 . Consistent with this result, even in the absence of added water, H_2 and D_2 mixtures underwent H/D scrambling with $\{(\mu\text{-H})(\mu\text{-pdt})[\text{Fe}(\text{CO})_2(\text{PMe}_3)]_2\}^+$ as a catalyst, concomitantly with H/D exchange into the $\mu\text{-H}$ position. Experiments under various conditions showed that in all cases the H/D scrambling process was facilitated by light and inhibited by the coordinating solvents, CH_3CN and acetone, or by the addition of CO. These conclusions suggested that an open site is required for H_2 activation and that the required open site is created under photolytic CO-loss conditions (as in the CO inhibited form of the enzyme). As confirmation of this view, ^{13}CO was incorporated into the model complexes under similar photolytic conditions (33). From such test reactions, $\{(\mu\text{-H})(\mu\text{-pdt})[\text{Fe}(\text{CO})_2(\text{PMe}_3)]_2\}^+$ was found to serve as a functional model of $[\text{Fe}]_{\text{H}_2}\text{ase}$ in the catalytic isotopic scrambling of $\text{D}_2/\text{H}_2\text{O}$ mixtures. As in the CO-inhibited oxidized enzyme, our model catalysts require photolytic conditions to affect CO-loss and to achieve activity.

Analogous studies found that $\{(\mu\text{-SMe})(\mu\text{-pdt})[\text{Fe}(\text{CO})_2(\text{PMe}_3)]_2\}^+$ can also catalyze the H/D exchange reaction in $\text{D}_2/\text{H}_2\text{O}$ mixtures under similar conditions as the $\mu\text{-H}$ analogue. The $\mu\text{-SMe}$ derivative, however, does not catalyze the H_2/D_2 scrambling process under standard anhydrous conditions. Neither was there any evidence for formation of MeSD or $\{(\mu\text{-D})(\mu\text{-pdt})[\text{Fe}(\text{CO})_2(\text{PMe}_3)]_2\}^+$ when solutions of the $\mu\text{-SMe}$ complex were pressurized with D_2 . In other words, H/D exchange reactions employing $\{(\mu\text{-SMe})(\mu\text{-pdt})[\text{Fe}(\text{CO})_2(\text{PMe}_3)]_2\}^+$ do not proceed via a $\{(\mu\text{-D})(\mu\text{-pdt})[\text{Fe}(\text{CO})_2(\text{PMe}_3)]_2\}^+$ intermediate. These results taken together suggest that $\text{D}_2/\text{H}_2\text{O}$ scrambling can occur independently of $\mu\text{-H}/\text{D}_2$ scrambling and that the former may proceed via reversible deprotonation of $\{(\mu\text{-E})(\mu\text{-S}(\text{CH}_2)_x\text{S})[\text{Fe}(\text{CO})_2(\text{PMe}_3)]_2[\text{Fe}(\text{L})(\text{L}')(\eta^2\text{-H}_2)]\}^+$.

Based on the above experimental results, and given the lability of the CO ligands under photolytic conditions, the mechanism presented in Scheme 1 was proposed as a reasonable first attempt to accommodate the observations (50). Scheme 1 is not intended to suggest the location of the open site, but is drawn in this way to accent the similarities



SCHEME 1.

between our model and the active site of Fe-only hydrogenase, given in Fig. 1. In fact, products isolated from solvent inhibition studies, *vide infra*, suggested that in the case of $\{(\mu\text{-H})(\mu\text{-pdt})[\text{Fe}(\text{CO})_2(\text{PMe}_3)_2]\}^+$ the open site should be *cis* to the $\mu\text{-H}$ (33).

The computations presented herein use Scheme 1 as a starting point to support and thoroughly explore such mechanistic possibilities in terms of the energetically favorable possibilities for the open site and the detailed steps of the H_2 activation.

A. CHOICE AND VALIDATION OF THE COMPUTATIONAL MODEL

Only minor experimental differences were observed for H/D exchange catalysis using different $\mu\text{-S}(\text{CH}_2)_x\text{S}$ bridges in $\{(\mu\text{-H})(\mu\text{-S}(\text{CH}_2)_x\text{S})[\text{Fe}(\text{CO})_2(\text{PMe}_3)_2]\}^+$, where $x=2$ (ethanedithiolate \equiv edt) or $x=3$ (propanedithiolate \equiv pdt). It seems therefore likely that the reaction proceeds via a similar mechanism for these two dithiolate bridges. The molecular structures, derived from X-ray crystallography for the two- and three-carbon bridged compounds, overlay very well (25). If only the Fe, S, and P atoms and CO ligands are considered, the RMS deviation for the two molecules is 0.098 Å; inclusion of the carbon atoms involved in S–C bonding increases the RMS deviation to 0.227 Å. Because of the structural and experimental similarities we have used the smaller edt bridge in the computations as it is computationally less expensive and the higher symmetry of this molecule limits the number of isomers to be considered at each step in the reaction.

Most of the calculations presented use what we designate as the small model, $\{(\mu\text{-H})(\mu\text{-edt})[\text{Fe}(\text{CO})_2(\text{PH}_3)_2]\}^+$, where the PMe_3 ligand has been replaced by the simple phosphine, PH_3 . In order to test the

TABLE I

COMPARISON OF THE SMALL AND FULL MODELS: COMPUTED BOND ENERGIES^a

M-L	ΔE_0 small model ^b	ΔE_0 full model ^c
Fe-P	+ 34.2	+ 50.0
Fe-CO _{ap} ^d	+ 39.6	+ 39.2
Fe-CO _{bas} ^d	+ 37.3	+ 36.6

^a ΔE_0 as defined by Eqs. (1) and (2) and given in kcal mol⁻¹.^b $\{(\mu\text{-H})(\mu\text{-edt})[\text{Fe}(\text{CO})_2(\text{PH}_3)_2]^+\}$.^c $\{(\mu\text{-H})(\mu\text{-edt})[\text{Fe}(\text{CO})_2(\text{PMe}_3)_2]^+\}$.^dDesignation of apical and basal derived from such positions in the edge-bridged square pyramids present in $(\mu\text{-edt})[\text{Fe}(\text{CO})_2(\text{PR}_3)_2]$.

validity of this model, we have computed the bond dissociation energies as defined in Eqs. (1) and (2).



$$\Delta E_0 = [E_0(\text{Fe}_2) + E_0(\text{L})] - E_0([\text{Fe}_2\text{L}]^+) \quad (2)$$

For this process, the ΔE_0 , is the total energy, including only the zero-point correction, of each independently optimized fragment. Values determined for Fe-P, Fe-CO_{ap}, and Fe-CO_{ba} are listed in Table I. Calculations comparing the full model, given in Table I, $\{(\mu\text{-H})(\mu\text{-edt})[\text{Fe}(\text{CO})_2(\text{PMe}_3)_2]^+\}$, and the small model $\{(\mu\text{-H})(\mu\text{-edt})[\text{Fe}(\text{CO})_2(\text{PH}_3)_2]^+\}$, show that the Fe-P bond of Fe-PH₃ is significantly weaker than that of Fe-PMe₃. However, the energy of a given Fe-CO bond is very similar for the two models. Thus reaction steps that involve PMe₃ ligand-loss directly are poorly modeled by PH₃, while the reactivity of the Fe-CO bond (or other Fe-L bonds) in the small model should generally parallel that of the larger model.

A major supposition of this computational mechanistic study is the separation of the photochemical and thermal reaction events. It has been assumed, Scheme 1, that a photochemical reaction takes place to generate a coordinatively unsaturated intermediate that subsequently reacts thermally with dihydrogen. In other words, we are assuming that the reaction is photochemically initiated but that light plays no role in later steps of the reaction (for at least one cycle).

The iron atoms of the reactant $\{(\mu\text{-H})(\mu\text{-S}(\text{CH}_2)_x\text{S})[\text{Fe}(\text{CO})_2(\text{PMe}_3)_2]^+\}$ are both electronically and coordinatively saturated. Therefore, even a minimal mechanism must call for the first step to be

the creation of an open site on one of the iron centers via either an internal rearrangement or ligand loss. Unfortunately, the need for continuous photolysis makes it difficult to delineate further mechanistic details by experiment alone. As the reaction progress of dark-quenched samples was monitored by ^1H or ^2H -NMR spectroscopy, only the products and reactants were observed. There was no indication of intermediates. The displaced ligands, PMe_3 and CO , were trapped in the closed system of the medium pressure NMR sample tube and, in the absence of photolysis, returned to displace weak ligands such as $\eta^2\text{-H}_2$. In this context, density functional theory was used to examine energetically reasonable intermediates for possible reaction paths.

B. CREATION OF THE OPEN SITE

Figure 3 shows five possible paths, designated a–e, generating $\eta^2\text{-H}_2$ complexes from **1** via open site intermediates. Note that paths a–d, leading from **1** to species **7–10**, are all overall endothermic processes. Paths a–c can be resolved into the endothermic creation of the open site, followed by the exothermic coordination of dihydrogen. Species **2**,

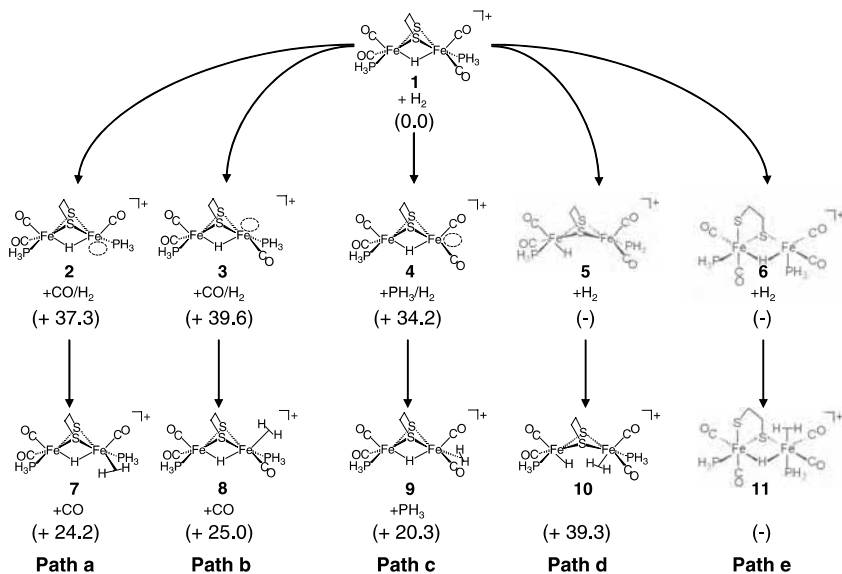


FIG. 3. Creation of the open site and dihydrogen coordination. The energies indicated are relative to $E_0(\text{1}) + E_0(\text{H}_2) = 0$ and are given in kcal mol^{-1} . (Species corresponding to **5**, **6**, and **11** were not located.)

3, and 4 are generated by photo-ejection of either CO or a phosphine ligand via paths a, b, and c. In path d, irradiation initiates the shift of the hydride from fully bridging between the two irons to terminal on one of the iron atoms. The final path calls for photolysis to heterolytically cleave the Fe–S bond in order to convert the face-bridged bioctahedral structure of the reactant into the edge-bridged complex indicated in Fig. 3.

The first three paths in Fig. 3 all involve terminal-ligand dissociation. With either the small or the full model, the calculated Fe–CO bond dissociation energies are in the order: Fe–CO_{apical} > Fe–CO_{basal}. (See Table I for apical/basal definitions. These energies are calculated as the difference in the total energies, ΔE_0 , of the separately optimized products and reactants, *vide supra*.) Noted in Table I is the Fe–P bond energies for Fe–PH₃ and Fe–PMe₃ showing that Fe–PMe₃ is 10 kcal mol^{−1} stronger than Fe–CO. Due to the large amount of energy available from the sunlight (estimated from the cutoff of Pyrex glass at $\lambda = 280$ nm to be about 100 kcal mol^{−1}), the bond energies alone do little to differentiate the three ligand-loss mechanisms. Three experimental facts, however, suggest that CO loss is more likely than phosphine loss (25). First, photolysis of $\{(\mu\text{-H})(\mu\text{-pdt})[\text{Fe}(\text{CO})_2(\text{PMe}_3)]_2\}^+$ under a ¹³CO atmosphere leads to ¹²CO/¹³CO exchange with no displacement of PMe₃. Second, the photolysis of the reactant, in the presence of 1 equivalent of CH₃CN, forms $\{(\mu\text{-H})(\mu\text{-pdt})[\text{Fe}(\text{CO})_2(\text{PMe}_3)][\text{Fe}(\text{CO})(\text{CH}_3\text{CN})(\text{PMe}_3)]\}^+$. (This complex is shown by X-ray crystallography to contain a basal CH₃CN (33).) These processes most likely occur via dissociative mechanisms. Finally, the addition of PMe₃ to a solution of the starting materials results in deprotonation of the bridging hydride. It is likely, therefore, that a mechanism that calls for phosphine loss would lead to decomposition via this route. While the formation of DPMe₃⁺ is observed after prolonged photolysis, it does not occur on the same time scale as that for H/D exchange. Thus, the basal CO loss mechanisms seem the most likely.

The fourth and fifth paths share several similarities. Both call for a ligand which bridges the iron centers in the starting material to shift away from one of the metal centers and bind to a single iron. Minima corresponding to complexes 5 and 6 could not be located. Unrestrained geometry optimization with a variety of ligand starting geometries (both semi-bridging and non-bridging) led back to the fully-bridging $\{(\mu\text{-H})(\mu\text{-edt})[\text{Fe}(\text{CO})_2(\text{PH}_3)]_2\}^+$ complex 1, Fig. 3.

The difficulty in optimizing a structure analogous to 5 did not extend to the $\eta^2\text{-H}_2$ adduct, 10. In fact, a transition state has been found that directly connects species 1 and 10 of Fig. 3. As shown in

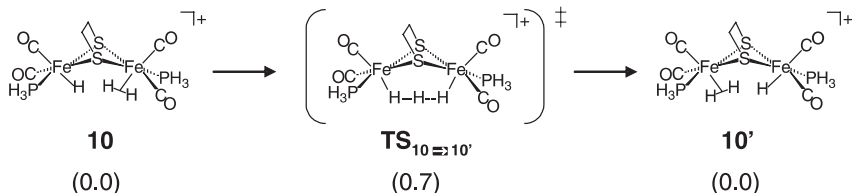


FIG. 4. Hydrogen exchange without ligand loss. Complex **10** proceeds over a low energy C_2 symmetric transition state to the structural isomer **10'**. Relative energies are given in kcal mol⁻¹.

Fig. 4, species **10**, should it be formed, has a very low barrier, +0.7 kcal mol⁻¹, to proton exchange via a trihydride transition state. In addition, the hydride shift mechanism, forming **10** directly from **1** and H₂, can also explain the inhibition of H/D exchange by added CO and coordinating solvents, as well as D₂/H₂O scrambling if complex **10** is formed. In fact, the process of forming CO or acetone analogues of species **10** from complex **1**, is less endothermic than formation of the η^2 -H₂ species, a result that reflects the better binding ability of CO and acetone to the Fe^{II} center. Furthermore, the calculated gas phase proton affinity shows that the acidity of the bound dihydrogen in species **10** is comparable to that of species **7**, **8**, and **9**.

For the reasons described above, species **10**, if accessible, should be competent for H/D exchange of H₂/D₂ and D₂/H₂O mixtures. Species **10**, however, lies 39.3 kcal mol⁻¹ above its separated components, complex **1** and dihydrogen, and the transition state from complex **1** to **10** lies an additional 5 kcal mol⁻¹ higher. For a normal thermal reaction, such a barrier is higher than the energy required to break the M–L bonds and decompose the compound. Thus, for this process to occur, the high-energy excited state molecule would have to bind dihydrogen more rapidly than it decays by ligand loss. In fact, during the short lifetime of an excited state molecule the unimolecular process of ligand loss seems far more likely than the bimolecular process of dihydrogen capture. Furthermore, it should be noted that the computed barrier for dihydrogen loss to reform complex **1** is only 5 kcal mol⁻¹.

No minima resembling species **6** or **11** in Fig. 3 were located. All attempts at optimization of these potential intermediates resulted in previously optimized species **1** and **12**, respectively. Interestingly, the thermodynamics of **1** + H₂ → **12** (+27.8 kcal mol⁻¹) represents the lowest energy cleavage of η^2 -H₂, not involving water (Fig. 5).

Our conclusion is that paths *d* and *e* of Fig. 3 are the least likely and thus these paths will not be considered further.

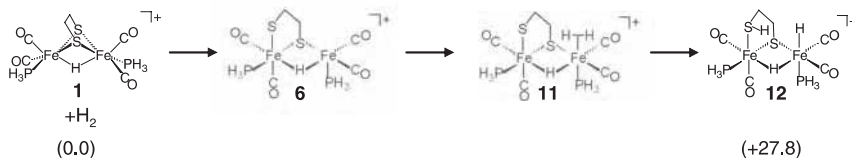


FIG. 5. Insertion of dihydrogen. Complex **12** is formed from the formal insertion of H_2 into the Fe-S bond. The energy of complex **12** is relative to the energy of $1 + \text{H}_2$ and given in kcal mol^{-1} .

C. DIHYDROGEN COMPLEXES

For the first three paths in Fig. 3 the coordination of dihydrogen to the open site forming $\eta^2\text{-H}_2$ species **7**, **8**, and **9**, are comparably, exothermic processes (-13.1 , -14.6 , and $-13.9 \text{ kcal mol}^{-1}$, respectively). The similarity of these values does not permit discrimination between the terminal ligand-loss mechanisms. The binding of dihydrogen to complex **1**, without ligand loss, to give species **10** is a very endothermic process ($+39.3 \text{ kcal mol}^{-1}$), *vide supra*.

D. H/D EXCHANGE INHIBITION

Figure 6 presents results of binding a variety of potential ligands or solvent molecules to the basal open site of **2**. The energies, determined according to Eqs. (3) and (4), include zero-point corrections only.



$$\Delta E_0 = E_0([\text{Fe}_2\text{L}]^+) - [E_0(\text{Fe}_2) + E_0(\text{L})] \quad (4)$$

In all these cases, formation of the iron-ligand bond is calculated to be an exothermic process. Consistent with their roles as inhibitors of H/D exchange catalysis, the coordinating solvents, acetonitrile and acetone, bind some $15\text{--}20 \text{ kcal mol}^{-1}$ more strongly to the iron center than does dihydrogen. Dichloromethane, on the other hand, is similar to dihydrogen. Furthermore, the isolation of a stable acetonitrile complex, *vide supra*, is explained by the fact that the strengths of the Fe-NCMe and Fe-CO bonds are similar ($\Delta E_0 = -36.0$ vs. $-37.3 \text{ kcal mol}^{-1}$). Paradoxically, water, which is known to accelerate the rate of H/D exchange into the $\mu\text{-H}$ position, coordinates to the iron with the same affinity as acetone and much more strongly than H_2 .

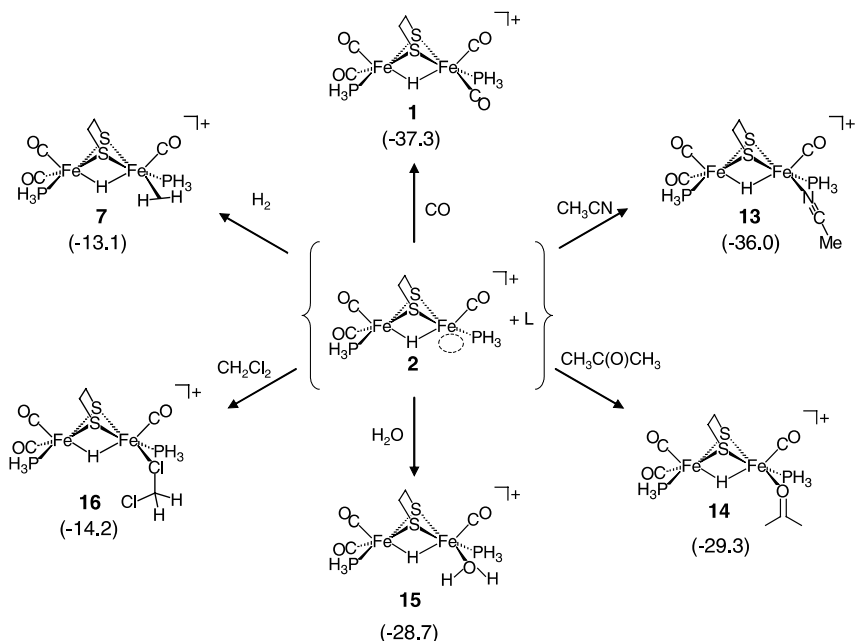


FIG. 6. Trapping the open site. The energy released by coordination of a series of relevant ligands to the open site of **2**. Bond energies are calculated according to Eq. (4) and are given in kcal mol⁻¹.

We have not systematically examined the open site capture process for species **3** and **4**. However, it seems reasonable that the same trend as observed for **2**, and presented in Fig. 6 will be followed for **3** and **4**: (i.e., $\text{Fe-CO} > \text{Fe-NCMe} > \text{Fe-O}=\text{C}(\text{CH}_3)_2 \approx \text{Fe-OH}_2 > \text{Fe-H}_2 \approx \text{Fe}(\text{ClCH}_2\text{Cl})$). In other words, CO, acetonitrile, and acetone (and H_2O) should be inhibitors of H/D exchange regardless of the location of the open site.

E. CLEAVAGE OF THE H-H BOND

We have explored both water-free and water-assisted routes to the cleavage of the H-H bond in certain $\eta^2\text{-H}_2$ species of Fig. 3. For the former route, the bridging thiolate sulfur donor and the bridging hydride were considered as possible internal bases for the heterolytic cleavage of H_2 from each of the dihydrogen species, Fig. 7. In the water-assisted routes, H_2O is used as an external base to deprotonate H_2 , Fig. 8.

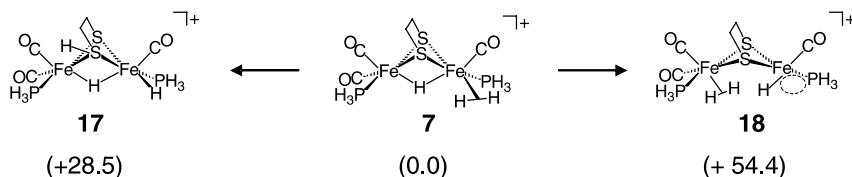


FIG. 7. Water-free activation of dihydrogen via Path a. The anhydrous activation of dihydrogen using the thiolate sulfur (left) or hydride (right). Relative energies in kcal mol⁻¹.

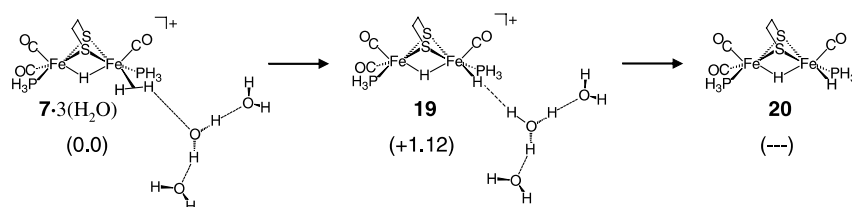
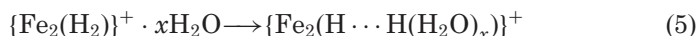


FIG. 8. Water Assisted Activation of dihydrogen via Path a. The water-assisted cleavage of the H–H bond. Differences in charge does not allow the direct comparison of the energies of **19** and **20**. Relative energies given in kcal mol⁻¹.

The water-assisted mechanism of H–H cleavage is a challenge for our gas-phase DFT calculations. An attempt was made to gain a qualitative understanding for the energetics of this step by calculating the species with explicit water molecules and the resulting “deprotonated species” as given by Eqs. (5) and (6).



$$\Delta E_0 = E_0(\{\text{Fe}_2(\text{H} \cdots \text{H}(\text{H}_2\text{O})_x)\}^+) - E_0(\{\text{Fe}_2(\text{H}_2)\}^+ \cdot x(\text{H}_2\text{O})) \quad (6)$$

Complexes of the form $(\mu\text{-H})(\mu\text{-edt})[\text{Fe}(\text{CO})_2(\text{PH}_3)][\text{Fe}(\text{CO})(\text{PH}_3)(\text{H} \cdots \text{H}(\text{H}_2\text{O})_x)]^+$, where $x=1$ or 2 returned to the form $(\mu\text{-H})(\mu\text{-edt})[\text{Fe}(\text{CO})_2(\text{PH}_3)][\text{Fe}(\text{CO})(\text{PH}_3)(\eta^2\text{-H}_2) \cdot x(\text{H}_2\text{O})]^+$ upon relaxed geometry optimization. In other words, either one or two water molecules were insufficient as a gas-phase base for deprotonation of species **7**. Addition of three water molecules led to the optimization of $\{(\mu\text{-H})(\mu\text{-edt})[\text{Fe}(\text{CO})_2(\text{PH}_3)][\text{Fe}(\text{CO})(\text{PH}_3)(\text{H} \cdots \text{H}(\text{H}_2\text{O})_3)]\}^+$; the latter is shown as its optimized structure in Fig. 7. Using this method we calculated the

deprotonation of these $\eta^2\text{-H}_2$ complexes to be essentially thermoneutral. (Our test calculations show that the extremely acidic dihydrogen complex of Morris, $\{(\eta^2\text{-H}_2)\text{Fe}[\text{PEt}_2(\text{CH}_2)_2\text{PEt}_2]_2\text{CO}\}^{2+}$ (51), modeled by us as $\{(\eta^2\text{-H}_2)\text{Fe}[\text{PH}_2(\text{CH}_2)_2\text{PH}_2]_2\text{CO}\}^{2+}$, also requires two water molecules for deprotonation.) While we have not been able to address the exact energetics or the activation energy for this process, the results *suggest* that these complexes are sufficiently acidic to be deprotonated by small water clusters or perhaps by small clusters of water with other polar molecules.

Figure 7 gives two modes of cleavage of the H–H bond starting from the $\eta^2\text{-H}_2$ species, **2** that do not involve water. The first route is the heterolytic cleavage of dihydrogen using the lone pair on the bridging thiolate sulfur to yield **17**. The thermodynamic difference for this path is 28.5 kcal mol^{−1}. The other route, which uses the hydride to effect cleavage of the H–H bond, giving **18**, is even higher in energy, 54.4 kcal mol^{−1}. Although the hydride route is clearly energetically non-viable, the route through S is not impossible. However, the water-assisted route is clearly the more energetically favorable than either of the water-free routes.

In all cases heterolytic cleavage of the bound dihydrogen of the apical $\eta^2\text{-H}_2$ species, **8**, was high in energy relative to those derived from the basal $\eta^2\text{-H}_2$ species, **7**. The deprotonation of **8** by either an external base or the thiolate sulfur leads to a high energy intermediate due to the presence of a *trans* hydride ligand in the resulting intermediate. In addition, experimental data, *vide supra*, suggest that H/D exchange most likely occurs from the basal position.

F. H/D EXCHANGE INTO THE $\mu\text{-H}$ POSITION

Theory and experiment, taken together, suggest that the dihydrogen species **7–10**, Fig. 1 are sufficiently acidic to be deprotonated by small water-containing clusters and re-deuterated to affect D₂/H₂O (or H₂/D₂O) exchange. This process alone, however, does not explain how deuterium gets exchanged into the $\mu\text{-H}$ position. Experimentally, the incorporation of deuterium into the $\mu\text{-H}$ from the reaction of $\{(\mu\text{-H})(\mu\text{-pdt})[\text{Fe}(\text{CO})_2(\text{PMe}_3)_2]\}^+$ with D₂O, with or without light, is exceedingly slow. In other words, while the bridging hydride exchanges readily with deuterium from D₂ or D₂/H₂O, there is a high barrier to exchange with D₂O alone.

The computations have suggested a somewhat unexpected, but energetically reasonable route for H/D exchange into the $\mu\text{-H}$ position,

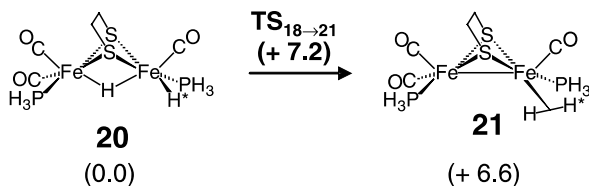


FIG. 9. Binuclear reductive elimination. The dihydride complex, **20**, passes over a low energy transition state to form a dihydrogen complex, **21**. Relative energies given in kcal mol⁻¹.

Fig. 9. As mentioned earlier, the cationic $\eta^2 - H_2^+$ species, **7**, can readily be deprotonated to afford the *neutral* species, **20** that contains both a bridging and a terminal hydride. This dihydride can pass over a low-energy transition state ($\Delta E_{20 \rightarrow \text{TS}} = +6.6$ kcal mol⁻¹) to form the *neutral* Fe^IFe^I η^2 -HH* species, **21**. The formation of $\mu\text{-H}^*$ can then be accomplished in one of two ways. The Fe–Fe bond may be reprotonated by $\{(\text{H}_2\text{O})_x\text{H}^+\}^+$ to form $\mu\text{-H}^*$. Another possibility is a rotation of the $\eta^2\text{-HH}^*$ ($\Delta E_{21 \rightarrow \text{TS}} = +4.4$ kcal mol⁻¹), followed by reformation of the dihydride can also afford $\mu\text{-H}^*$.

G. THE OVERALL MECHANISM

When taken together, the theoretical and experimental data suggest a integrated mechanism for H/D exchange in D₂/H₂O mixtures as catalyzed by $\{(\mu\text{-E})(\mu\text{-S}(\text{CH}_2)_x\text{S})[\text{Fe}(\text{CO})_2\text{PMe}_3]_2\}^+$. Figure 10 presents this mechanism in a way that is equally valid for the $\mu\text{-H}$ and for the $\mu\text{-SMe}$ complex. The most important feature in the main cycle (right side of Fig. 10) is $\eta^2\text{-H}_2$ binding at a single Fe^{II} site that is deprotonated by the external base, D₂O. The left side of Fig. 10 shows a binuclear reductive elimination process that produces a $\eta^2\text{-HD}$ bound to the Fe^IFe^I binuclear complex and holds only for the $\mu\text{-H}$ parent catalyst.

This mechanism thus invokes a species, **2**, whose trapping by exogenous bases or ligands might account for inhibition of H/D exchange. It also suggests the possibility of H/D exchange facilitated by a $\eta^2\text{-H}_2$ complex of Fe^IFe^I. Experiments designed to test such implications are described below.

H. D₂/H₂O SCRAMBLING CATALYZED BY $(\mu\text{-pdt})[\text{Fe}(\text{CO})_2(\text{PMe}_3)]_2$

While most $\eta^2\text{-H}_2$ complexes of iron are in Fe^{II} complexes, the results presented above suggest that the creation of an open site on the Fe^IFe^I

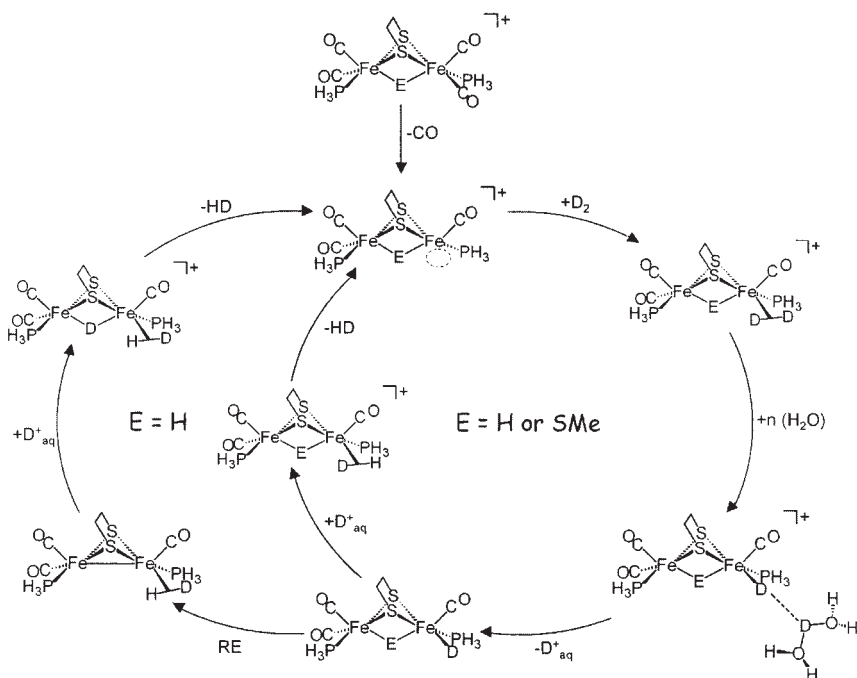


FIG. 10. The general mechanism of H/D exchange. The right cycle for E = H or SMe. The left cycle holds only for E = H. $D_{\text{aq}}^+ = (\text{H}_2\text{O})_n\text{D}^+$ and RE = reductive elimination.

species, $(\mu\text{-pdt})[\text{Fe}(\text{CO})_2(\text{PMe}_3)]_2$, might also bind and activate dihydrogen. Gas-phase calculations show that binding of H_2 to $(\mu\text{-edt})[\text{Fe}(\text{CO})_2(\text{PH}_3)][\text{Fe}(\text{CO})(\text{PH}_3)]$ to form $(\mu\text{-edt})[\text{Fe}(\text{CO})_2(\text{PH}_3)][\text{Fe}(\text{CO})(\eta^2\text{-H}_2)(\text{PH}_3)]$, **21**, is an exothermic process. This complex may rearrange, proceeding over a very small barrier (see Fig. 9; $\Delta E_{21 \rightarrow \text{TS}} = +0.6 \text{ kcal mol}^{-1}$) to form species **20**. The reversible conversion between **20** and **21** would lead to scission of the H–H or D–D bond but no isotope exchange in the absence of water. The deprotonation of a $\eta^2\text{-H}_2$ intermediate, like **21**, however, could lead to the H/D exchange of $\text{D}_2/\text{H}_2\text{O}$ mixtures.

In order to establish the viability of the $\text{Fe}^{\text{I}}\text{Fe}^{\text{I}}$ species for activation of dihydrogen for H/D exchange in $\text{D}_2/\text{H}_2\text{O}$ mixtures, an experiment similar to the one performed for $\{(\mu\text{-E})(\mu\text{-pdt})[\text{Fe}(\text{CO})_2\text{PMe}_3]_2\}^+$ (E = H and SMe) was carried out using the $(\mu\text{-pdt})[\text{Fe}(\text{CO})_2\text{PMe}_3]_2$ complex as a potential H/D exchange catalyst (24–26). Details are given in Section II. The formation of HOD was monitored by ^2H NMR spectroscopy. The ^2H -NMR spectra, presented in Fig. 11, were recorded

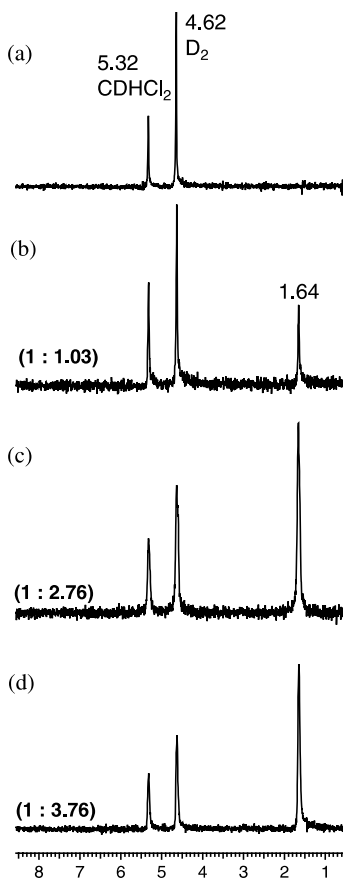


FIG. 11. ^2H NMR spectra showing the formation of HOD ($\delta=1.64$ ppm) in CH_2Cl_2 solution containing $(\mu\text{-pdt})[\text{Fe}(\text{CO})_2\text{PMe}_3]_2$, 10 bar D_2 and 2 μL H_2O : (a) before exposure to sunlight, (b) after 4 h of photolysis, (c) after 10 h of photolysis and (d) after 13 h of photolysis. Relative ratios of the intensity of the resonance of CHDCl_2 (natural abundance) to HOD are given in parentheses.

before exposure of the solutions to light and at intervals during several hours of exposure. For $(\mu\text{-pdt})[\text{Fe}(\text{CO})_2\text{PMe}_3]_2$, the intensity of the resonance at 1.65 ppm corresponding to D-enriched H_2O in the solvent increased from 1.03 (4 h) to 3.76 (13 h). While this isotopic exchange activity is poorer than that emanating from the $\text{Fe}^{\text{II}}\text{Fe}^{\text{II}}$ catalysts, the fact that the $\text{Fe}^{\text{I}}\text{Fe}^{\text{I}}$ catalyst is competent at all is consistent with the computational prediction of an $(\eta^2\text{-H}_2)\text{Fe}^{\text{I}}\text{Fe}^{\text{I}}$ intermediate.

I. REACTION OF $\{(\mu\text{-H})(\mu\text{-pdt})[\text{Fe}(\text{CO})_2(\text{PMe}_3)]_2\}^+$ WITH ACETONE

One of our basic assumptions was that the only role of light in the reaction was the creation of an open site on one of the metal centers. Our computations showed that an $\eta^2\text{-H}_2$ intermediate, if formed, could facilitate $\text{D}_2/\mu\text{-H}$ exchange thermally in the presence of water. In other words, if a basal open site could be generated in the absence of light then $\text{D}_2/\mu\text{-H}$ exchange should proceed via a dark, thermal reaction.

The acetonitrile complex, $\{(\mu\text{-H})(\mu\text{-pdt})[\text{Fe}(\text{CO})_2(\text{PMe}_3)][\text{Fe}(\text{CO})(\text{CH}_3\text{CN})(\text{PMe}_3)]\}^+$, was not active for thermal H/D exchange. Computations suggested that acetone should bind to the iron center somewhat more weakly than acetonitrile. A similar experimental approach to the preparation and isolation of $\{(\mu\text{-H})(\mu\text{-pdt})[\text{Fe}(\text{CO})_2(\text{PMe}_3)][\text{Fe}(\text{CO})(\text{CH}_3\text{CN})(\text{PMe}_3)]\}^+$ was attempted with acetone, albeit with poor results. The prolonged photolysis of mixtures of $\{(\mu\text{-H})(\mu\text{-pdt})[\text{Fe}(\text{CO})_2(\text{PMe}_3)]_2\}^+$ and 1–5 equivalents of acetone in CH_2Cl_2 lead to extensive decomposition. Although attempts to isolate and fully characterize the complex formed in this case were unsuccessful, infrared and NMR spectral data support the formation of an acetone complex *in situ* as described below.

When a solution of $\{(\mu\text{-H})(\mu\text{-pdt})[\text{Fe}(\text{CO})_2(\text{PMe}_3)]_2\}^+$ in acetone was exposed to sunlight for one hour the color gradually changed from orange-red to dark brown-red. The IR spectrum showed the presence of the starting ($\nu(\text{CO}) = 2031, 1991\text{ cm}^{-1}$) complex together with a species with $\nu(\text{CO})$ stretching frequencies displaced by ca. 50 cm^{-1} (Fig. 12). (While few acetone complexes of metal carbonyls have been isolated, available data suggest the electron donating ability of $(\text{CH}_3)_2\text{C}=\text{O}$ is better than that of CO (52), consistent with the lower values of $\nu(\text{CO})$ observed here.) Bubbling CO through this solution led to the disappearance of the new $\nu(\text{CO})$ bands and the reappearance of the $\nu(\text{CO})$ bands of $\{(\mu\text{-H})(\mu\text{-pdt})[\text{Fe}(\text{CO})_2(\text{PMe}_3)]_2\}^+$, indicating the replacement of acetone by CO had reformed the starting complex.

Further support for the formation of the acetone complex was provided by an experiment carried out in an NMR sample tube. When an acetone solution of $\{(\mu\text{-H})(\mu\text{-pdt})[\text{Fe}(\text{CO})_2(\text{PMe}_3)]_2\}^+$ was exposed to sunlight for one hour, two hydride resonances were observed as shown in Fig. 12. The doublet of doublets centered at -7.7 ppm with $J_{\text{H-P}}$ coupling of 21 and 30 Hz corresponded to the coupling of the bridging hydride to two non-equivalent phosphines of the presumed acetone complex, $\{(\mu\text{-H})(\mu\text{-pdt})[\text{Fe}(\text{CO})_2(\text{PMe}_3)][\text{Fe}(\text{CO})(\text{PMe}_3)(\text{acetone})]\}^+$; a triplet at -15.0 ppm with $J_{\text{H-P}}$ of 22 Hz was characteristic of the starting hydride species $\{(\mu\text{-H})(\mu\text{-pdt})[\text{Fe}(\text{CO})_2(\text{PMe}_3)]_2\}^+$. Addition of CH_3CN

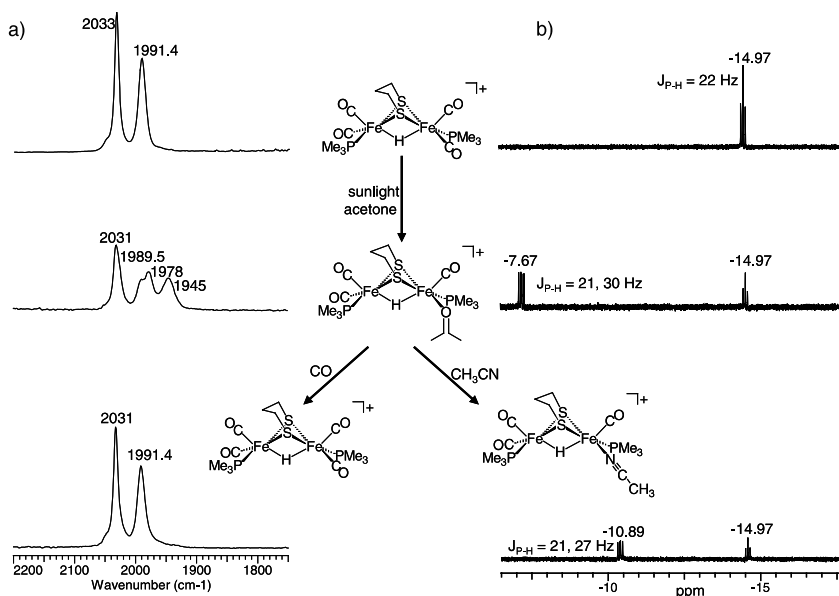


FIG. 12. (a) Infrared spectra (CO region) and (b) ¹H NMR spectra (hydride region) of $\{(\mu\text{-H})(\mu\text{-pdt})[\text{Fe}(\text{CO})_2\text{PMe}_3]_2\}^+$ as it reacts with $\text{Me}_2\text{C}=\text{O}$ to form $\{(\mu\text{-H})(\mu\text{-pdt})[\text{Fe}(\text{CO})\text{PMe}_3(\text{O}=\text{CMe}_2)][\text{Fe}(\text{CO})_2\text{PMe}_3]\}^+$ and acetone displacement upon reaction with CO to reform $\{(\mu\text{-H})(\mu\text{-pdt})[\text{Fe}(\text{CO})_2\text{PMe}_3]_2\}^+$ and CH_3CN to form $\{(\mu\text{-H})(\mu\text{-pdt})[\text{Fe}(\text{CO})\text{PMe}_3(\text{CH}_3\text{CN})][\text{Fe}(\text{CO})_2\text{PMe}_3]\}^+$, respectively.

to this sample in the dark caused the resonance at -7.7 ppm to disappear with the appearance of a new signal centered at -10.9 ppm (doublet of doublets with $J_{\text{H-P}}$ of 21 and 27 Hz) corresponding to the acetonitrile complex, $\{(\mu\text{-H})(\mu\text{-pdt})[\text{Fe}(\text{CO})_2(\text{PMe}_3)][\text{Fe}(\text{CO})(\text{PMe}_3)(\text{CH}_3\text{CN})]\}^+$. An identical sample of $\{(\mu\text{-H})(\mu\text{-pdt})[\text{Fe}(\text{CO})_2(\text{PMe}_3)]_2\}^+$ in d_6 -acetone, maintained in the dark, gave no indication of the *thermal* displacement of CO by acetone; neither did subsequent addition of CH_3CN result in CO/ CH_3CN exchange in the dark. We conclude that the acetone complex, generated by photolytic CO loss followed by solvent molecule capture, can be converted to the acetonitrile complex in a thermal (non-photolytic) ligand exchange process. The acetonitrile complex, here generated in situ from the acetone complex, is known to contain a basally coordinated CH_3CN ligand (33). Since the most likely mechanism for this exchange is a dissociative replacement of an acetone molecule by a CH_3CN molecule, we conclude that the photolysis of $\{(\mu\text{-H})(\mu\text{-pdt})[\text{Fe}(\text{CO})_2(\text{PMe}_3)]_2\}^+$ in acetone results in the formation of $\{(\mu\text{-H})(\mu\text{-pdt})[\text{Fe}(\text{CO})_2(\text{PMe}_3)][\text{Fe}(\text{CO})(\text{acetone})(\text{PMe}_3)]\}^+$.

Unfortunately, the acetone complex did not give clear answers about the validity of a dark, thermal H/D exchange process. Acetone solutions of the complex did not catalyze H_2/D_2 or $\text{D}_2/\mu\text{-H}$ exchange. The complex decomposes in the presence of water and in solutions other than acetone.

J. CALCULATION OF NMR SHIELDING TENSORS

The experimentally observed ^1H -NMR spectrum of the “acetone complex” shows a doublet of doublets centered at -7.7 ppm. To help assign this resonance, a series of structural candidates for the acetone complex, as well as the known parent hydride, **1**, and the CH_3CN complex, **12**, were geometry optimized and their NMR spectra were calculated. (NOTE: The edt/ PH_3 model was used for these calculations while experiments were carried out with the pdt/ PMe_3 complex.) The NMR chemical shift calculation gives absolute shielding values. These values were scaled by setting the value for $\mu\text{-H}$ hydrogen of $\{(\mu\text{-H})(\mu\text{-edt})[\text{Fe}(\text{CO})_2\text{PH}_3]_2\}^+$ equal to the observed chemical shift for the hydride of $\{(\mu\text{-H})(\mu\text{-pdt})[\text{Fe}(\text{CO})_2(\text{PMe}_3)]_2\}^+$ in acetone (-15.0 ppm). Accordingly, the chemical shift of the $\mu\text{-H}$ of the acetonitrile complex, **12**, was computed to be at -10.5 ppm (experimental value = -10.8 ppm). Examples of structural isomers computed for the acetone complex are shown in Fig. 13.

The experimental value of -7.7 ppm is in good agreement with the basal-substituted species, **13** that is computed to have a $\mu\text{-H}$ hydride shift of -7.4 ppm. The next closest match is the μ -acetone-terminal hydride species, **22**, with a calculated hydride chemical shift of -7.2 ppm. This structure is less likely than **13**, both for its higher energy ($+28.7$ kcal mol $^{-1}$ relative to **13**), as well as the expected coupling pattern for this structure (a doublet is expected for **22**, as opposed to

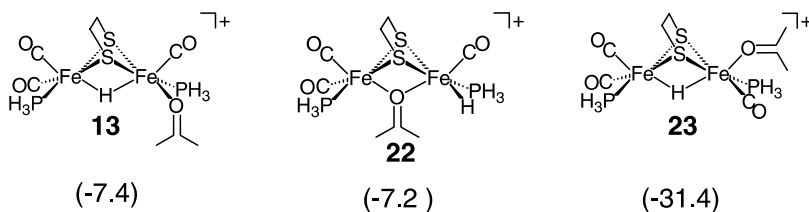


FIG. 13. Possible isomers for the monosubstituted acetone complex. Calculated chemical shifts, given in parentheses, are in ppm and scaled to that of species **2** = -15.0 ppm.

the doublet of doublets observed experimentally.) The apically substituted acetone species, **23**, calculated to have a chemical shift of -31.4 ppm, is much too far upfield to be considered a viable candidate for the structure of the experimentally observed acetone complex.

IV. Conclusions

The growing importance of computational chemistry in mechanistic inorganic chemistry may be ascribed to the broad accessibility and application of Density Functional Theory and related techniques to large molecules, in this case a diiron complex with 10 to 12 coordination sites filled with diatomic or larger ligands. For simple substrates, as in the H/D isotopic scrambling process described here, conclusions from experimental techniques are typically limited to issues involving the rate-determining step of the reaction path. While chemical intuition arising from knowledge of stable ground state structures assists in formulating experimental tests of reasonable scenarios for events prior to and following the highest barrier, experimental proofs of these steps are often difficult; here calculation may be critical to formulating a complete mechanism.

The case in point in our studies of simple isotopic exchange in $\text{H}_2/\text{D}_2\text{O}$ or $\text{D}_2/\text{H}_2\text{O}$ mixtures as facilitated by Fe(II) in dinuclear complexes is a particular mechanistic challenge as the catalysis is light-driven and the experiments thus far have been non-wavelength specific. The critical step of ligand loss preceding a most reasonable step of H_2 binding draws on the experimental verification and chemical precedence of $(\eta^2\text{-H}_2)\text{Fe}^{\text{II}}$ complexes in organometallic-like coordination environments (51). Experimental data suggested CO labilization was the most likely effect of sunlight.

The observation of inhibition of the H/D exchange reaction by CO and CH_3CN implicates coordinatively unsaturated intermediates in the H_2 capture process. As a part of this manuscript we report evidence for the existence of an acetone derivative of the $(\mu\text{-H})(\text{Fe}^{\text{II}})_2$ complex, as suggested by theory. As it has obvious ramifications for technical development of such H_2 -uptake catalysts, the possibility that water might similarly compete for the open site and serve both as a required reagent and a catalyst inhibitor deserves a future detailed study.

The reaction paths explored by theory were closely tied to published experimental results, and provided support for previously suggested mechanisms. The predictive power of theory beyond what the

experimentalist can readily do was displayed in steps likely to follow the highest barrier process. Most notably, theory accounted for the enhanced H/D exchange into the bridging hydride position of $\{(\mu\text{-H})(\mu\text{-pdt})[\text{Fe}(\text{CO})_2]\text{PMe}_3\}_2\}^+$ from $\text{D}_2/\text{H}_2\text{O}$ mixtures over either of the individual components, D_2 or D_2O as D-sources independent of each other. An unexpected path (reductive elimination) from a terminal hydride/bridging hydride intermediate suggested the possibility that the $\text{Fe}^{\text{I}}\text{Fe}^{\text{I}}$ parent complex might facilitate H/D exchange in $\text{H}_2/\text{D}_2\text{O}$ mixtures. This possibility was substantiated by experiment.

Many issues are involved in decisions as to the detail required to “complete” a mechanistic study, i.e., to further test assumptions used to formulate the proposed reaction path that have gained credibility from theory. Prominent in decisions to go further are the effective use of time and resources, and the technical feasibility of more sophisticated experiments. As development of H_2 uptake and activation by base metal catalysts, hopefully linked to electrode surfaces, appear to be exceedingly important for technological progress, further study of this system seems to be mandated.

DEDICATION

This manuscript is dedicated to the memory of Professor Dieter Sellmann, a superb scientist whose depth of knowledge was exceeded only by his generous spirit. It was our joy and blessing to call him “Friend”. Marcetta and Don Darensbourg, and Michael B. Hall.

ACKNOWLEDGMENTS

We acknowledge financial support from the National Science Foundation (CHE-0111629 and CHE-9800184) and R. A. Welch Foundation (A-0648 and A-0924). We also thank the Supercomputing Facility at Texas A&M University for computer time and the Laboratory for Molecular Simulation at Texas A&M University for computer time and software.

REFERENCES

1. Cammack, R.; Frey, M.; Robson, R. “*Hydrogen as a Fuel*”; Taylor and Francis: London, 2001.
2. Volbeda, A.; Charon, M.-H.; Piras, C.; Hatchikian, E. C.; Frey, M.; Fontecilla-Camps, J. C. *Nature* **1995**, 373, 580–586.
3. Volbeda, A.; Garcin, E.; Piras, C.; De Lacey, A. L.; Fernandez, V. M.; Hatchikian, E. C.; Frey, M.; Fontecilla-Camps, J. C. *J. Am. Chem. Soc.* **1996**, 118, 12989–12996.
4. Garcin, E.; Vernede, X.; Hatchikian, E. C.; Volbeda, A.; Frey, M.; Fontecilla-Camps, J. C. *Structure* **1999**, 7, 557–566.

5. Higuchi, Y.; Yagi, T.; Yasuoka, N. *Structure* **1997**, *5*, 1671–1680.
6. Higuchi, Y.; Ogata, H.; Miki, K.; Yasuoka, N.; Yagi, T. *Structure* **1999**, *7*, 549–556.
7. Peters, J. W.; Lanzilotta, W. N.; Lemon, B. J.; Seefeldt, L. C. *Science* **1998**, *282*, 1853–1858.
8. Nicolet, Y.; Piras, C.; Legrand, P.; Hatchikian, C. E.; Fontecilla-Camps, J. C. *Structure* **1999**, *7*, 13–23.
9. Nicolet, Y.; De Lacey, A. L.; Vernéde, X.; Fernandez, V. M.; Hatchikian, E. C.; Fontecilla-Camps, J. C. *J. Am. Chem. Soc.* **2001**, *123*, 1596–1601.
10. Lemon, B. J.; Peters, J. W. *Biochemistry* **1999**, *38*, 12969–12973.
11. Lee, S.; Holm, R. H. *Proc. Nat. Acad. Sci. USA* **2003**, *100*, 3595–3600.
12. Cao, Z.; Hall, M. B. *J. Am. Chem. Soc.* **2001**, *123*, 3734–3742.
13. Yagi, T. *J. Biochem.* **1970**, *68*, 649–657.
14. Krasna, A. I.; Rittenberg, D. *J. Am. Chem. Soc.* **1954**, *76*, 3015–3020.
15. Adams, M. W. W.; Mortenson, L. E.; Chen, J.-S. *Biochim. Biophys. Acta* **1981**, *594*, 105–176.
16. Albracht, S. P. J. *Biochim. Biophys. Acta* **1994**, *1188*, 167–204.
17. Farkas, A.; Farkas, L.; Yudkin, J. *Proc. Roy. Soc. (London)* **1934**, *B115*, 373.
18. Wächtershäuser, G. *Science* **2000**, *289*, 1307–1308.
19. Lemon, B. J.; Peters, J. W. *J. Am. Chem. Soc.* **2000**, *122*, 3793–3794.
20. Hieber, W.; Spacu, P. Z. *Anorg. Allg. Chem.* **1937**, *233*, 852–864.
21. Fauvel, K.; Mathieu, R.; Poilblanc, R. *Inorg. Chem.* **1976**, *15*, 976–978.
22. Treichel, P. M.; Rublein, E. K. *J. Organomet. Chem.* **1989**, *359*, 195–203.
23. Seyferth, D.; Womack, G. B.; Gallagher, M. K.; Cowie, M.; Hames, B. W.; Fackler, J. P. Jr.; Mazany, A. M. *Organometallics* **1987**, *6*, 283–294.
24. Zhao, X.; Georgakaki, I. P.; Miller, M. L.; Yarbrough, J. C.; Darensbourg, M. Y. *J. Am. Chem. Soc.* **2001**, *123*, 9710–9711.
25. Zhao, X.; Georgakaki, I. P.; Miller, M. L.; Mejia-Rodriguez, R.; Chiang, C.-Y.; Darensbourg, M. Y. *Inorg. Chem.* **2002**, *41*, 3917–3928.
26. Georgakaki, I. P.; Miller, M. L.; Darensbourg, M. Y. *Inorg. Chem.* **2003**, *42*, 2489–2494.
27. Sellmann, D.; Geipel, F.; Moll, M. *Angew. Chem. Int. Ed.* **2000**, *39*, 561–563.
28. Dance, I. *Chem. Comm.* **1999**, *17*, 1655–1656.
29. Fan, H.-J.; Hall, M. B. *J. Am. Chem. Soc.* **2001**, *123*, 3828–3829.
30. Liu, Z.-P.; Hu, P. *J. Chem. Phys.* **2002**, *117*, 8177–8180.
31. Bruschi, M.; Fantucci, P.; De Gioia, L. *Inorg. Chem.* **2002**, *41*, 1421–1429.
32. Liu, Z.-P.; Hu, P. *J. Am. Chem. Soc.* **2002**, *124*, 5175–5182.
33. Zhao, X.; Chiang, C.-Y.; Miller, M. L.; Rampersad, M. V.; Darensbourg, M. Y. *J. Am. Chem. Soc.* **2003**, *125*, 518–524.
34. Becke, A. D. *J. Chem. Phys.* **1993**, *98*, 5648–5652.
35. Lee, C.; Yang, W.; Parr, R. G. *Phys. Rev.* **1988**, *37*, 785–789.
36. Frisch, M. J.; Trucks, G. W.; Schlegel, H. B.; Scuseria, G. E.; Robb, M. A.; Cheeseman, J. R.; Zakrzewski, V. G.; Montgomery, J. A.; Stratmann, R. E.; Burant, J. C.; Dapprich, S.; Millam, J. M.; Daniels, A. D.; Kudin, K. N.; Strain, M. C.; Farkas, O.; Tomasi, J.; Barone, V.; Cossi, M.; Cammi, R.; Mennucci, B.; Pomelli, C.; Adamo, C.; Clifford, S.; Ochterski, J.; Petersson, G. A.; Ayala, P. Y.; Cui, Q.; Morokuma, K.; Malick, D. K.; Rabuck, A. D.; Raghavachari, K.; Foresman, J. B.; Cioslowski, J.; Ortiz, J. V.; Stefanov, B. B.; Liu, G.; Liashenko, A.; Piskorz, P.; Komaromi, I.; Gomperts, R.; Martin, R. L.; Fox, D. J.; Keith, T.; Al-Laham, M. A.; Peng, C. Y.; Nanayakkara, A.; Gonzalez, C.; Challacombe, M.; Gill, P. M. W.; Johnson, B.; Chen, W.; Wong, M. W.; Andres, J. L.; Gonzalez, A. C.;

- Head-Gordon, M.; Replogle, E. S.; Pople, J. A. “*Gaussian 98, revision A.11*”; Gaussian Inc.: Pittsburgh, PA, **2002**.
37. Hay, P. J.; Wadt, W. R. *J. Chem. Phys.* **1985**, *82*, 284–298.
38. Hay, P. J.; Wadt, W. R. *J. Chem. Phys.* **1985**, *82*, 270–283.
39. Couty, M.; Hall, M. B. *J. Comp. Chem.* **1996**, *17*, 1359–1370.
40. Höllwarth, A.; Böhme, M.; Dapprich, S.; Ehlers, A. W.; Gobbi, A.; Jonas, V.; Köhler, K. F.; Stegmann, R.; Veldkamp, A.; Frenking, G. *Chem. Phys. Lett.* **1993**, *208*, 237–240.
41. Dunning, T. H. Jr. *J. Chem. Phys.* **1989**, *90*, 1007–1023.
42. Dunning, T. H. Jr. *J. Chem. Phys.* **1970**, *53*, 2823–2833.
43. Dunning, T. H. Jr.; Hay, P. J. “*Methods of Electronic Structure Theory*”, vol. 3, 3rd edn.; Eds. Schaefer, H. F.; Plenum Press: New York, **1977**.
44. A. London, F. *J. Phys. Radium* **1937**, *8*, 397–409.
45. Ditchfield, R. *Mol. Phys.* **1974**, *27*, 789–807.
46. Wolinski, K.; Hinton, J. F.; Pulay, P. *J. Am. Chem. Soc.* **1990**, *112*, 8251–8260.
47. Schmidt, M.; Contakes, S. M.; Rauchfuss, T. B. *J. Am. Chem. Soc.* **1999**, *121*, 9736–9737.
48. Lawrence, J. D.; Li, H.; Rauchfuss, T. B.; Bénard, M.; Rohmer, M.-M. *Angew. Chem., Int. Ed.* **2001**, *40*, 1768–1771.
49. Liaw, W.-F.; Tsai, W.-T.; Gau, H.-B.; Lee, C.-M.; Chou, S.-Y.; Chen, W.-Y.; Lee, G.-H. *Inorg. Chem.* **2003**, *42*, 2783–2788.
50. Darensbourg, M. Y.; Lyon, E. J.; Zhao, X.; Georgakaki, I. P. *Proc. Nat. Acad. Sci. USA* **2003**, *100*, 3683–3688.
51. Landau, S. E.; Morris, R. H.; Lough, A. J. *Inorg. Chem.* **1999**, *38*, 6060–6068.
52. Drew, D.; Darensbourg, D. J.; Darensbourg, M. Y. *Inorg. Chem.* **1975**, *14*, 1579–1584.

ELECTRONIC STRUCTURE AND SPECTROSCOPIC PROPERTIES OF MOLYBDENUM AND TUNGSTEN N_2 , NNH , NNH_2 , AND NNH_3 COMPLEXES WITH DIPHOSPHINE CO-LIGANDS: INSIGHTS INTO THE END-ON TERMINAL REDUCTION PATHWAY OF DINITROGEN

FELIX TUCZEK

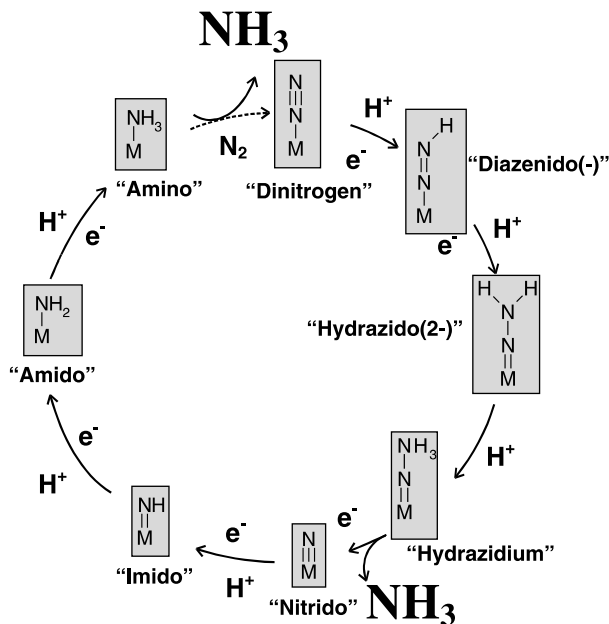
Institut für Anorganische Chemie, Christian Albrechts Universität,
D-24098 Kiel, Germany

- I. Introduction
- II. Vibrational Spectroscopy and QCA-NCA
 - A. Dinitrogen Complexes
 - B. $\text{W-N}_2\text{H}_x$ Complexes; $x = 1, 2, 3$
- III. Electronic Structure and Electronic Absorption Spectroscopy
- IV. Conclusions
- References

I. Introduction

The conversion of dinitrogen to ammonia is one of the important processes of chemistry. Whereas the technical ammonia synthesis requires high temperature and pressure (1), this reaction proceeds at room temperature and ambient pressure in nature, mediated by the enzyme nitrogenase (2). There is evidence that N_2 is bound and reduced at the iron–molybdenum cofactor (FeMoco), a unique Fe/Mo/S cluster present in the MoFe protein of nitrogenase. Although detailed structural information on nitrogenase has been available for some time (3), the mechanism of N_2 reduction by this enzyme is still unclear at the molecular level. Nevertheless, it is possible to bind and reduce dinitrogen at simple mono- and binuclear transition-metal systems which allow to obtain mechanistic information on elemental steps involved

in this process (4). Based on the “classic” Mo and W phosphine systems, all the intermediates of the following reduction pathway have been isolated (5):



SCHEME 1.

Importantly, this end-on terminal reduction pathway of N_2 has been suggested to apply to nitrogenase. In agreement with the Thorneley/Lowe kinetic scheme of nitrogenase (6), it requires a sequence of one-electron reduction and protonation steps. The reduction of bridging N_2 , in contrast, proceeds via diazene and hydrazine and therefore requires a series of two-electron reductions. The conversion of dinitrogen to ammonia described in Scheme 1 has also been performed in a catalytic way, achieving three cycles (7). More recently, a catalytic conversion (six cycles) of N_2 at a sterically protected site provided by a Mo triamidoamine complex has been realized (8). In this reaction sequence, analogous species as shown in Scheme 1 have been evidenced and characterized, respectively (9).

Of central importance in the chemistry of nitrogen fixation is the concept of activation (4f). This involves a transfer of electronic charge from the transition metal to the coordinated N_2 by metal \rightarrow ligand back donation, making this very inert molecule susceptible

to protonation. A theoretical estimate of the charge transmitted to the N_2 ligand is provided by charge analysis in the framework of molecular orbital calculations. In order to achieve a systematic understanding of the degree of N_2 activation and to obtain more insight into the reduction pathway of N_2 , we have been studying N_2 complexes and their protonated intermediates with spectroscopy coupled to DFT calculations (10–16). One of the most sensitive probes for the state of reduction of the N_2 molecule is vibrational spectroscopy. Infrared and Raman spectroscopy therefore have played a prominent role in our investigations. Vibrational data have been evaluated with a Quantum Chemistry Assisted Normal Coordinate Analysis (QCA-NCA) which is based on calculation of the f-matrix by DFT and subsequent fitting of important force constants to match experimentally observed frequencies (12–16). The information obtained from DFT is also employed to calculate electronic transitions by TDDFT (time-dependent DFT) which are compared to experimental UV/Vis data. As a result, a close check of the quality of the quantum chemical calculations is obtained, and these calculations can then be employed to understand and optimize the reactivity of the intermediates of N_2 fixation.

In pursuit of this goal, we have in particular studied the N_2 , N_2H , and N_2H_2 complexes $[W(N_2)_2(dppe)_2]$ (**I**), $[WF(NNH)(dppe)_2]$ (**II**), and $[WF(NNH_2)(dppe)_2]^+$ (**III**); $dppe = 1,2$ -bis(diphenylphosphino)ethane) with the help of infrared and Raman spectroscopy coupled to DFT calculations (12). More recently, these studies were complemented by investigation of the Mo and W hydrazidium complexes $[MF(NNH_3)(depe)_2](BF_4)_2$, $M=Mo$ (**IVa**) and W (**IVb**) (15). The analogous NNH_3 compounds with $dppe$ could not be isolated so far; i.e., protonation of the corresponding N_2 precursors was found to lead to NNH_2 systems (5). We therefore had to switch to $depe$ (1,2-bis(diethylphosphino)ethane) in the latter investigation. The hydrazidium complexes **IV** were prepared from the N_2 complexes $[M(N_2)_2(depe)_2]$, $M=Mo$ and W by protonation with HBF_4 . Protonation of these systems with HCl , on the other hand, was found to lead to the $depe$ - NNH_2 systems $[MCl(NNH_2)(depe)_2]Cl$, $M=Mo$ (**Va**) and W (**Vb**) (15) which are related to the complex $[MoBr(NNH_2)(depe)_2]Br$ originally described by Chatt (17). This allowed us to compare the results of vibrational and optical absorption spectroscopy obtained on Mo/W - N_2 and $-NNH_2$ $dppe$ complexes with data obtained on their $depe$ analogs (18). The vibrational and UV/Vis spectroscopic properties of **I–V** as well as their electronic structures are the subject of the present review.

X-ray structures of Mo and W dinitrogen, hydrazido(2-), and hydrazidium complexes with $dppe$ and $depe$ co-ligands exist. Figure 1 gives

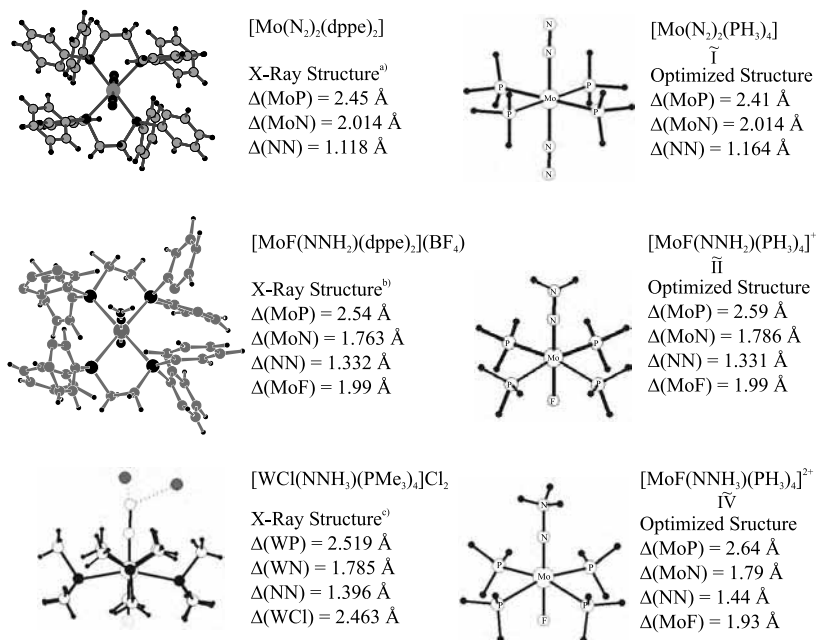


FIG. 1. Structurally characterized examples of Mo and W dinitrogen and hydrazido (2-) complexes and model systems. ^(a)Uchida, T.; Uchida, Y.; Hidai, M.; Kodama T. *Acta Cryst.* **1975**, *B31*, 1197. ^(b)Hidai, M.; Kodama, T.; Sato, M.; Harakawa, M.; Uchida, Y. *Inorg. Chem.* **1976**, *15*, 2694. ^(c)Galindo, A.; Hills, A.; Hughes, D. L.; Richards, R. L. *J. Chem. Soc. Dalton Trans.* **1990**, 283.

a selection of structurally characterized complexes and model systems derived from these structures; important bond lengths are collected in Table I. In order to treat the Mo/W–N₂ and –N₂H_x complexes ($x = 1, 2, 3$) by DFT, they were simplified by approximating the phosphine ligands by PH₃ groups. Input parameters for the corresponding model complexes **I**–**IV** for complexes **I**–**IVa,b** can be found in Refs. (12) and (15).

II. Vibrational Spectroscopy and QCA-NCA

A. DINITROGEN COMPLEXES

Raman and IR spectra of the [W(N₂)₂(dppe)₂] complex **I** are given in Figs. 2 and 3, respectively. Vibrational analysis is based on the model system [M(N₂)₂P₄] (**I'**, symmetry D_{2h} , M=Mo, W) shown in Scheme 2 along with the definition of the coordinate system and the internal

TABLE I

Mo/W-N₂, -NNH, -NNH₂, AND -NNH₃ COMPLEXES AND CORRESPONDING MODELS: BOND LENGTHS FROM X-RAY AND DFT GEOMETRY OPTIMIZATIONS

	Model		M-P	M-N	N-N	M-X	N-H	Ref.
[Mo(N ₂) ₂ (PH ₃) ₄]	I	Opt	2.510	2.014	1.164	—	—	12
[Mo(N ₂) ₂ (dppe) ₂]		X-ray	2.45	2.014	1.118	—	—	^d
[MoF(NNH)(PH ₃) ₄]	II	Opt	2.54	1.826	1.276	2.07 ^a	1.083	12
[MoF(NNH ₂)(PH ₃) ₄] ⁺	III	Opt	2.594	1.786	1.331	1.99 ^a	1.01	12
[MoF(NNH ₂)(dppe) ₂] ⁺		X-ray	2.54	1.763	1.332	1.99 ^a	1.09	^e
[WCl(NNH ₂)(dppe) ₂] ⁺		X-ray	~2.5	1.73	1.37	2.42 ^b	—	^f
[WF(NNH ₂)(depe) ₂] ⁺		X-ray	~2.5	1.771	1.355	2.027 ^c	—	^g
[MoF(NNH ₃)(PH ₃) ₄] ²⁺	IV	Opt	2.64	1.79	1.44	1.93 ^a	1.04	15
[WCl(NNH ₃)(PMe ₃) ₄] ²⁺		X-ray	2.519	1.785	1.396	2.463 ^b	—	^h

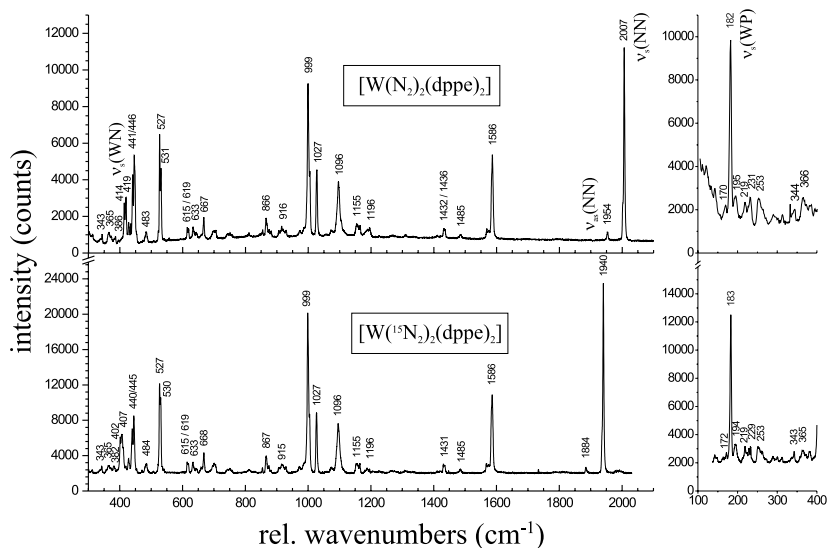
^aMo=F.^bW-Cl.^cW-F.^dUchida, T.; Uchida, Y.; Hidai, M.; Kodama, T. *Acta Cryst.* **1975**, B31, 1197.^eHidai, M.; Kodama, T.; Sato, M.; Harakawa, M.; Uchida, Y. *Inorg. Chem.* **1976**, 15, 2694.^fHeath, G. A.; Mason, R.; Thomas, K. M. *J. Am. Chem. Soc.* **1974**, 96, 259.^gBarclay, J. E.; Hills, A.; Hughes, D. L.; Leigh, G. J.; Macdonald, C. J.; Abu-Bakar, M.; Mohd.-Ali, H. *J. Chem. Soc. Dalton Trans.* **1990**, 2503.^hGalindo, A.; Hills, A.; Hughes, D.L.; Richards, R. L. *J. Chem. Soc. Dalton Trans.* **1990**, 283.

FIG. 2. Raman spectra of [W(N₂)₂(dppe)₂] (¹⁴N-I) and [W(¹⁵N₂)₂(dppe)₂] (¹⁵N-I).

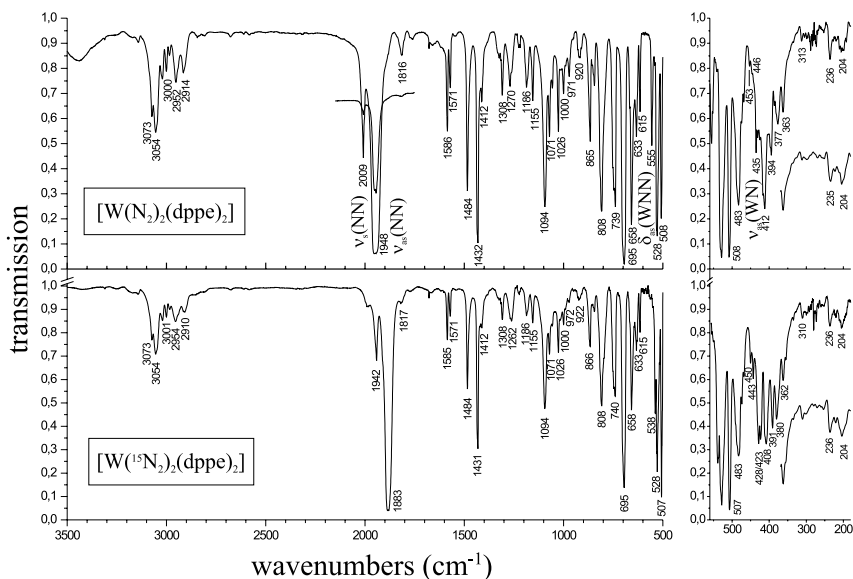
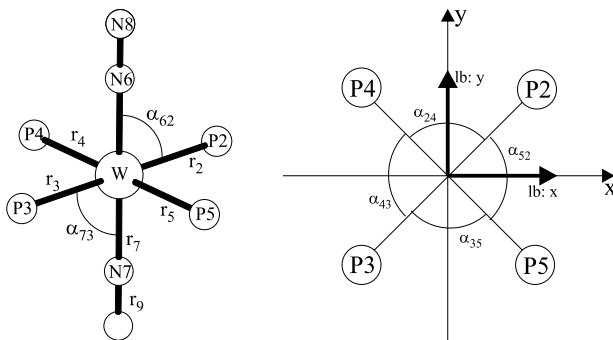


FIG. 3. IR spectra of $[\text{W}(\text{N}_2)_2(\text{dppe})_2]$ (^{14}N -I) and $[\text{W}(^{15}\text{N}_2)_2(\text{dppe})_2]$ (^{15}N -I).



SCHEME 2.

coordinates. \mathbf{I}' is derived from the corresponding, geometry optimized model $\tilde{\mathbf{I}}$ of the DFT calculation by removal of the H-atoms of the PH_3 groups. The eight normal modes of the central N–N–M–N–N unit of \mathbf{I}' are the symmetric and antisymmetric M–N and N–N stretching vibrations $\nu_{\text{s/as}}(\text{WN})$ and $\nu_{\text{s/as}}(\text{NN})$, respectively, and the four linear bends $\delta_{\text{s/as}}(\text{MNN})$ of the M–N–N moieties, two in each orthogonal direction x and y (Scheme 2). The four symmetric modes are Raman and the antisymmetric ones IR active. The vibrational properties of the analo-

gous Mo-dppe complex $[\text{Mo}(\text{N}_2)_2(\text{dppe})_2]$ and of the respective Mo and W dppe counterparts have been described and analyzed as well (12,18).

Figure 2 shows the Raman spectra of $^{14}\text{N-I}$ and $^{15}\text{N-I}$. The features at 2007 and 1954 cm^{-1} that shift by about 70 cm^{-1} down to 1940 and 1884 cm^{-1} , respectively, have been assigned to the N–N stretching vibrations. The symmetric, Raman active mode $\nu_s(\text{NN})$ belongs to the intense peak at 2007 cm^{-1} whereas the Raman-forbidden vibration $\nu_{as}(\text{NN})$ is assigned to the peak at 1954 cm^{-1} . The double-peak feature at 419 and 414 cm^{-1} which shifts by 12 cm^{-1} on ^{15}N substitution is assigned to the W–N stretching vibration $\nu_s(\text{WN})$ which therefore appears split in the spectra of **I**. In agreement with Raman data of related systems, (13b) the linear bends $\delta_s(\text{WNN})$ are not visible in the spectra of **I**. The splitting of $\nu_s(\text{WN})$ as well as the high intensity of the Raman-forbidden $\nu_{as}(\text{NN})$ mode are ascribed to correlation effects in the solid state. Other intense peaks in the Raman spectra of **I** that remain unshifted in the spectrum of the ^{15}N isotopomer are found at 527, 999, 1027, and 1586 cm^{-1} . Comparison with Raman data of $[\text{M}(\text{N}_2)_2(\text{depe})_2]$, $\text{M}=\text{Mo}$ and W (12,18), suggests that these vibrations are associated with the phenyl groups of the dppe ligand. In the low-energy region, a very intense peak is observed at 180 cm^{-1} which is assigned to the symmetric W–P stretch.

Infrared spectra of $^{14}\text{N-I}$ and $^{15}\text{N-I}$ are given in Fig. 3. Besides the N–N stretching vibrations $\nu_s(\text{NN})$ (IR-forbidden) at 2009 cm^{-1} and $\nu_{as}(\text{NN})$ (allowed) at about 1948 cm^{-1} which shift on ^{15}N substitution to 1942 and 1883 cm^{-1} , respectively, two other isotope sensitive peaks are found. The peak at 555 cm^{-1} is assigned to the antisymmetric linear bend $\delta_{as}(\text{WNN})$ which shifts to 538 cm^{-1} in the ^{15}N compound, and the antisymmetric metal–N stretching vibration $\nu_{as}(\text{WN})$ is identified with the medium intense peak at 435 cm^{-1} that disappears in the spectrum of $^{15}\text{N-I}$.

Based on the experimental frequencies and isotope shifts, a Quantum-Chemistry Assisted Normal Coordinate Analysis (QCA-NCA) has been performed. Details of the QCA-NCA procedure of **I**, including the f-matrix and the definition of the symmetry coordinates, have been described previously (12a). The NCA is based on model **I'** (vide supra). Assignments of the experimentally observed vibrations and frequencies obtained with the QCA-NCA procedure are presented in Table II. The symbolic F-matrix for model **I'** is shown in Scheme 3. Table III collects the force constants of the central N–N–M–N–N unit of **I'** resulting from QCA-NCA. As evident from Table II, good agreement between measured and calculated frequencies is achieved, demonstrating the success of this method.

TABLE II

OBSERVED AND CALCULATED FREQUENCIES OF $[\text{W}(\text{N}_2)_2(\text{dppe})_2]$ (I) IN cm^{-1}

	Experimental		QCA-NCA	
	N_2	$^{15}\text{N}_2$	N_2	$^{15}\text{N}_2$
$\nu_s(\text{NN})$	2007(R)/2009(IR)	1940(R)/1942(IR)	2007	1940
$\nu_{as}(\text{NN})$	1954(R)/1948(IR)	1884(R)/1883(IR)	1948	1883
$\delta_{as}(\text{WNN})$	555(IR)	538(IR)	556	538
$\nu_{as}(\text{WN})$	435(IR)		435	424
$\nu_s(\text{WN})$	419/414(R)	407/402(R)	420	406
$\delta_s(\text{WNN})$			462	447
$\nu(\text{WP})$	236/204(IR)	236/204(IR)	~ 295	~ 295
$\nu_s(\text{WP})$	182(R)	183(R)		

$\nu_s(\text{MN})$	$\nu_s(\text{NN})$	$\delta_s^x(\text{MNN})$	$\delta_s^y(\text{MNN})$	$\nu_{as}(\text{MN})$	$\nu_{as}(\text{NN})$	$\delta_{as}^x(\text{MNN})$	$\delta_{as}^y(\text{MNN})$
A_g	A_g	B_{2g}	B_{3g}	B_{1u}	B_{1u}	B_{2u}	B_{3u}
$\text{Y} + \text{N}_t$	$\text{N}_s + \text{N}_s t$	0	0	0	0	0	0
$\text{N}_s + \text{N}_s t$	$\text{Z} + \text{NN}_t$	0	0	0	0	0	0
0	0	$\text{Q} - e$	0	0	0	0	0
0	0	0	$\text{Q} - e$	0	0	0	0
0	0	0	0	$\text{Y} - \text{N}_t$	$\text{N}_s - \text{N}_s t$	0	0
0	0	0	0	$\text{N}_s - \text{N}_s t$	$\text{Z} - \text{NN}_t$	0	0
0	0	0	0	0	0	$\text{Q} + e$	0
0	0	0	0	0	0	0	$\text{Q} + e$

SCHEME 3.

TABLE III

FORCE CONSTANTS FOR $[\text{W}(\text{N}_2)_2(\text{dppe})_2]$ (I; UNITS ARE $\text{mdyn}/\text{\AA}$ FOR STRETCHING AND $\text{mdyn}\cdot\text{\AA}$ FOR BENDING MODES; THE DESIGNATIONS REFER TO SCHEME III)

Force constant	Type	
Y	M-N	2.66
Z	N-N	16.43
N_t	M-N: s/as	0.28
NN_t	N-N: s/as	0.28
N_s	M-N/N-N	0.96
$\text{N}_s t$	M-N/N-N: s/as	-0.13
Q	M-N-N	0.70
e	M-N-N: s/as	0.10

The vibrational spectroscopic properties of Mo/W–N₂ depe complexes are very similar to those of their dppe counterparts. Based on the lower N–N stretching frequency ($\nu_s(\text{NN})=1968\text{ cm}^{-1}$) and higher metal–N stretching frequency ($\nu_s(\text{WN})=434\text{ cm}^{-1}$) of the $\text{W}(\text{N}_2)_2(\text{depe})_2$ complex as compared to $\text{W}(\text{N}_2)_2(\text{dppe})_2$ (**I**; $\nu_s(\text{NN})=2007\text{ cm}^{-1}$, $\nu_s(\text{WN})=419/414\text{ cm}^{-1}$, cf. Table II), metal–N₂ back bonding is stronger in the depe than in the dppe system, activating the bound N₂ ligand to a higher degree. Moreover, tungsten mediates stronger back donation than molybdenum since $\nu_s(\text{NN})$ and $\nu_s(\text{Mo–N})$ in $\text{Mo}(\text{N}_2)_2(\text{depe})_2$ are at 1999 and 414 cm^{-1} , respectively (18).

B. W–N₂H_x COMPLEXES; $x=1, 2, 3$

Protonation of the dinitrogen complex **I** gives the NNH₂ complex $[\text{W}(\text{NNH}_2)(\text{depe})_2]\text{BF}_4$ (**III**). As Raman spectra of **III** were found to be almost featureless, vibrational information on this system has exclusively been obtained from infrared spectroscopy. Figure 4 shows the MIR and FIR spectra of **III** and its ¹⁵N and ²H isotopomers ¹⁵N-**III** and ²H-**III**, respectively. Seven peaks can be recognized to shift upon

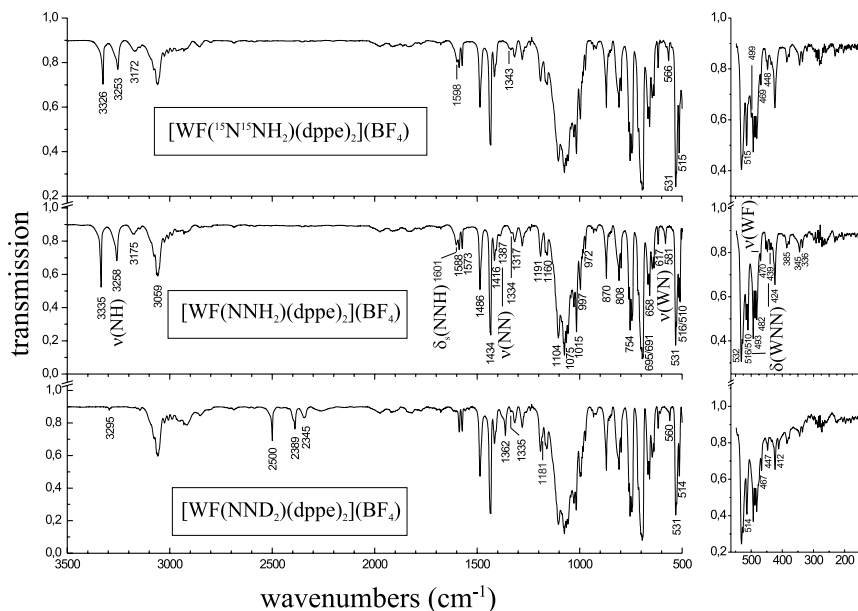


FIG. 4. IR spectra of $[\text{W}(\text{NNH}_2)(\text{dppe})_2](\text{BF}_4)$ (¹⁴N-**III**), $[\text{W}(\text{}^{15}\text{N}^{15}\text{NH}_2)(\text{dppe})_2](\text{BF}_4)$ (¹⁵N-**III**), and $[\text{W}(\text{NND}_2)(\text{dppe})_2](\text{BF}_4)$ (²H-**III**).

isotopic substitution. The two N–H stretching vibrations are clearly identified at 3335 ($\nu_{\text{as}}(\text{NH})$) and 3258 cm^{-1} ($\nu_{\text{s}}(\text{NH})$); both exhibit a strong shift upon deuteration down to 2500 and 2839 cm^{-1} , respectively. A third, much broader peak at 3175 cm^{-1} also appears to shift upon deuteration. It may be due to hydrogen bridges of the two N–H groups with the BF_4^- counterions. The symmetric NNH bending vibration is assigned to the peak at 1601 cm^{-1} . Based on the *ab initio* calculation, it should shift to below 1200 cm^{-1} . This mode is tentatively associated with the shoulder at 1181 cm^{-1} appearing in the deuterated compound.

In the region between 1500 and 500 cm^{-1} two isotope sensitive features are found. Bands at 1387 and 581 cm^{-1} are assigned to the N–N and W–N stretching vibrations, respectively. The 1387 cm^{-1} band shifts to 1343 and 1362 cm^{-1} on ^{15}N and ^2H substitution, respectively. In case of $\nu(\text{WN})$, the isotope shifted bands are clearly identified at 566 (^{15}N) and 560 cm^{-1} (^2H). The low-energy region of the spectra contains two more bands that shift upon isotopic substitution. The feature at 510 cm^{-1} is assigned to the linear bend $\delta_y(\text{WNN})$ which mixes with a more intense vibration at 516 cm^{-1} . At 439 cm^{-1} a band of very low intensity appears which shifts to 412 cm^{-1} upon deuteration and is absent in the ^{15}N compound; this peak is assigned to the $\delta_x(\text{WNN})$ mode. Finally, $\nu(\text{WF})$ is assigned to the peak at 470 cm^{-1} which shifts to 469 and 467 cm^{-1} on ^{15}N and ^2H substitution, respectively. Based on the experimental frequencies and isotope shifts, a QCA-NCA has been performed in analogy to that of the dinitrogen system **I**. Table IV collects the observed frequencies of **III** and those calculated by QCA-NCA.

TABLE IV

OBSERVED AND CALCULATED FREQUENCIES OF $[\text{WF}(\text{NNH}_2)(\text{dppe})_2]\text{BF}_4$ (**III**) IN cm^{-1}

	Experimental			QCA-NCA		
	NNH_2	$^{15}\text{N}^{15}\text{NH}_2$	NND_2	NNH_2	$^{15}\text{N}^{15}\text{NH}_2$	NND_2
$\nu_{\text{as}}(\text{NH})$	3335	3326	2500	3341	3332	2471
$\nu_{\text{s}}(\text{NH})$	3258	3253	2389	3259	3252	2383
$\delta_{\text{s}}(\text{NNH})$	1601	1598	(1181)	1602	1598	1168
$\nu(\text{NN})$	1387	1343	1362	1387	1342	1364
$\delta_{\text{as}}(\text{NNH})$				1245	1233	997
$\nu(\text{WN})$	581	566	560	582	567	558
$\delta^y(\text{WNN})$	(516)/510	499		511	498	484
$\nu(\text{WF})$	470	469	467	470	470	470
$\delta^x(\text{WNN})$	439		412	441	430	407

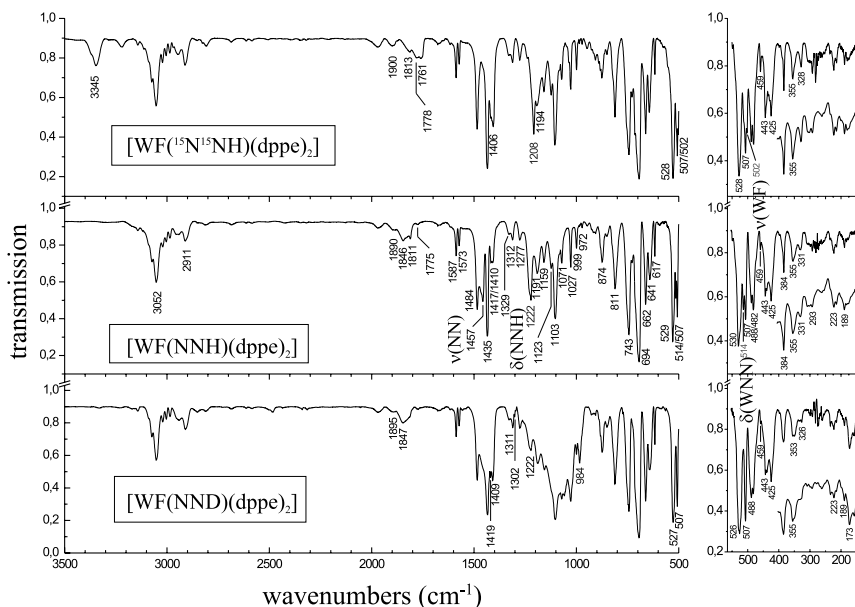


FIG. 5. IR spectra of $[\text{W}(\text{NNH})(\text{dppe})_2](^{14}\text{N-III})$, $[\text{W}(\text{}^{15}\text{N}^{15}\text{NH})(\text{dppe})_2](^{15}\text{N-II})$, and $[\text{W}(\text{NND})(\text{dppe})_2](^2\text{H-II})$.

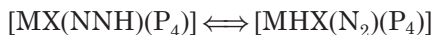
Treatment of the NNH_2 complex **III** with a base allows to isolate the diazenido(−) complex $[\text{WF}(\text{NNH})(\text{dppe})_2]$ (**II**) which corresponds to an intermediate in the formation of **III** upon treatment of **I** with acids. As in the case of **III**, Raman spectra of **II** were found almost featureless, whence vibrational information on **II** is exclusively based on IR spectroscopy. Figure 5 gives the infrared spectra of **II** and its ^{15}N and ^2H substituted isotopomers. In the MIR region two isotope sensitive peaks are observed at 1457 and 1222 cm^{-1} which shift to 1406 and 1208 cm^{-1} on ^{15}N substitution; these features are assigned to $\nu(\text{NN})$ and $\delta(\text{NNH})$, respectively. In the deuterated compound, $\nu(\text{NN})$ is found at 1419 cm^{-1} and the NND bend is identified with the new feature at 984 cm^{-1} . Unfortunately, the N–H stretching vibration could not be assigned from the spectra. The same applies to the W–N stretch which possibly is masked by a strong absorption at 530 cm^{-1} . In the FIR region, only one isotope sensitive feature is observed at 514 cm^{-1} that shows an isotope shift to 502 cm^{-1} on ^{15}N substitution. This peak is identified with the $\delta(\text{WNN})$ bend. As in the case of **III** the assignment of $\nu(\text{WF})$ is difficult because this mode exhibits little isotope shift. One possible candidate is the peak at 459 cm^{-1} which is of

TABLE V

OBSERVED AND CALCULATED FREQUENCIES OF [WF(NNH)(dppe)₂] (**II**) IN cm⁻¹

	Experimental			QCA-NCA		
	NNH	¹⁵ N ¹⁵ NH	NND	NNH	¹⁵ N ¹⁵ NH	NND
ν(NH)				3294	3287	2408
ν(NN)	1457	1406	1419	1452	1411	1419
δ(NNH)	1222	1208	984	1223	1207	984
ν(WN)	(~ 530)			530	515	521
δ(WNN)	514	502		515	501	483
ν(WF)	459	459	459	459	459	459

similar intensity and close in energy to the corresponding feature of **III**. Table V collects the calculated (QCA-NCA) and observed frequencies of **II**. As already observed by Chatt (19), there exists an equilibrium for the mono-protonated dinitrogen complexes between nitrogen and metal protonated species



which depends on the nature of X as well as of the metal and the (P₄) ligation. For [WHF(N₂)(dppe)₂], ν(NN) was found at 1846 cm⁻¹ and ν(WH) at 1811 cm⁻¹, whereas for the corresponding bromo complex the N–N stretch was observed at 1874 cm⁻¹ (ν(W–H) could not be identified in this case) (12a). Infrared spectroscopy can be employed to determine this equilibrium; in case of the bromo complex it is found on the side of the metal hydrido species whereas for the fluoro complex it is on the side of the diazenido(-) species.

The NNH₃ compounds **IV**, finally, are generated from the respective dinitrogen complexes using strong acids in a large excess. As Mo and W–NNH₃ complexes with dppe ligands are not available, the depe complexes [MF(NNH₃)(depe)₂](BF₄)₂, M=Mo (**IVa**) and W (**IVb**), have been employed for this investigation. As in the case of **II** and **III**, Raman spectra of these compounds were found almost featureless. Figure 6 gives the IR spectra of natural abundance-N **IVa** and **IVb**; sections of the spectra showing isotopic shifts are given in Fig. 7. Table VI collects calculated and observed frequencies of **IVa** and **IVb**. Spectral comparison between ¹⁵N-**IVa** and ¹⁴N-**IVa** shows three bands of ¹⁵N-**IVa** which are absent in ¹⁴N-**IVa**. The shoulder at 1347 cm⁻¹ is assigned to the N–N stretch ν(NN) which is of low intensity as in [WF(NNH₂)(dppe)]⁺ (**III**).

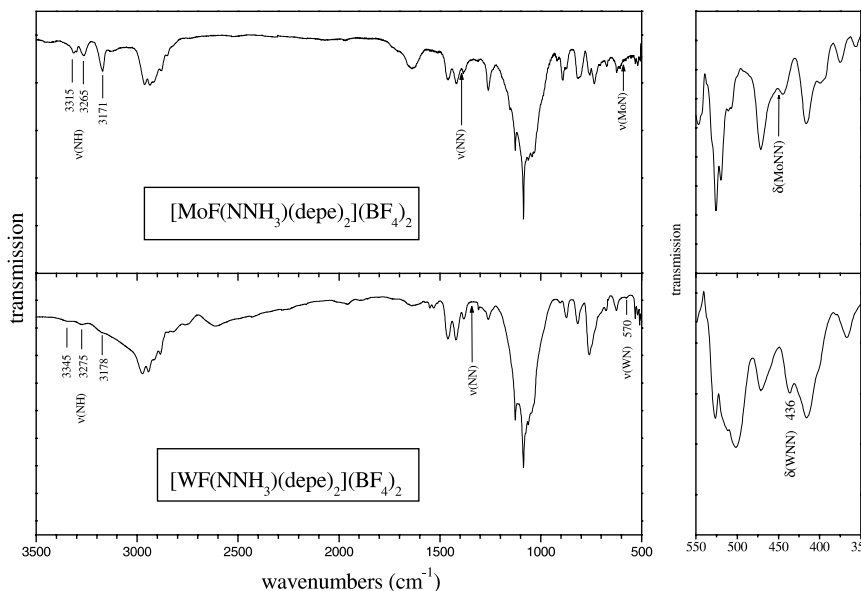


FIG. 6. IR spectra of $\text{MoF}(\text{NNH}_3)(\text{depe})_2(\text{BF}_4)_2$ (^{14}N -IVa), and $[\text{WF}(\text{NNH}_3)(\text{depe})_2](\text{BF}_4)_2$ (^{14}N -IVb).

The Mo–N stretch is assigned to the shoulder at 591 cm^{-1} , in accordance with the W complex showing the metal–N stretch at 570 cm^{-1} (see below). Another feature of low intensity appearing at 434 cm^{-1} in the FIR spectrum of ^{15}N -IVa is assigned to the linear Mo–N–N bend $\delta(\text{MoNN})$. In the region of N–H stretching vibrations bands are found at 3315 , 3265 , and 3171 cm^{-1} which upon isotopic substitution shift to 3305 , 3258 , 3167 cm^{-1} , respectively. Importantly, the appearance of *three* N–H vibrations in the IR spectrum proves the formation of a hydrazidium complex as corresponding NNH_2 systems only show *two* sharp bands in this spectral region (vide supra, Fig. 4). In the IR spectra of the tungsten systems $[\text{WF}(\text{NNH}_3)(\text{depe})_2](\text{BF}_4)_2$ (IVb) no peak belonging to $\nu(\text{NN})$ can be identified (Figs. 7, 8). The three N–H stretching vibrations are now located at 3345 , 3275 , and 3178 cm^{-1} and shift in the ^{15}N experiment to 3334 , 3271 , and 3173 cm^{-1} , respectively. The W–N stretch is found at 570 cm^{-1} and upon ^{15}N substitution shifts to 557 cm^{-1} . The feature at 436 cm^{-1} which in the ^{15}N experiment shifts into a broader band at 415 cm^{-1} is assigned to the linear bend $\delta(\text{WNN})$. Generally, the metal–N and N–N vibrations are more pronounced in the W– NNH_3 spectrum whereas the N–H stretches are

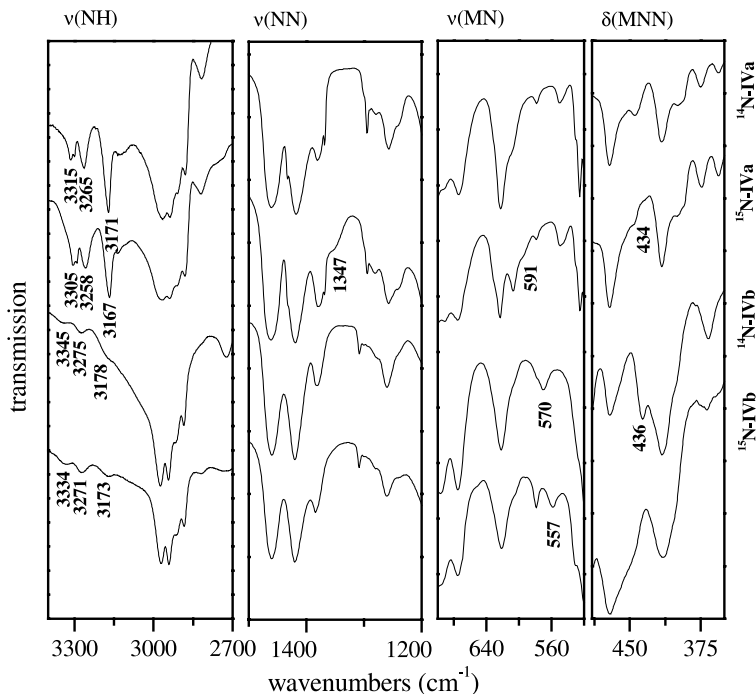


FIG. 7. Relevant sections of IR spectra of $[\text{MoF}(\text{NNH}_3)(\text{depe})_2](\text{BF}_4)_2$ ($^{14}\text{N-IVa}$), $[\text{MoF}(^{15}\text{N}^{15}\text{NH}_3)(\text{depe})_2](\text{BF}_4)_2$ ($^{15}\text{N-IVa}$), $[\text{WF}(\text{NNH}_3)(\text{depe})_2](\text{BF}_4)_2$ ($^{14}\text{N-IVb}$), and $[\text{WF}(^{15}\text{N}^{15}\text{NH}_3)(\text{depe})_2](\text{BF}_4)_2$ ($^{15}\text{N-IVb}$), indicating isotope shifts.

much sharper in the Mo– NNH_3 complex; both systems therefore provide complementary information.

Table VII collects the relevant force constants resulting from QCANCA of the NNH , NNH_2 , and NNH_3 complexes **II**, **III**, and **IV**; a graphical representation of $f(\text{NN})$ and $f(\text{MN})$ for the tungsten systems is given in Fig. 8. The figure shows that upon protonation of $[\text{W}(\text{N}_2)_2(\text{dppe})_2]$ to the NNH complex $[\text{WF}(\text{NNH})(\text{dppe})_2]$ the N–N force constant decreases from about 16 $\text{mdyn}/\text{\AA}$ to a value of 8.27 $\text{mdyn}/\text{\AA}$ and the M–N force constant increases from a value of about 2.5 to 4.5 $\text{mdyn}/\text{\AA}$. This trend continues in the following protonation steps; i.e., for $[\text{WF}(\text{NNH}_2)(\text{dppe})_2]^+$ the N–N force constant is further reduced to a value of 7.2 $\text{mdyn}/\text{\AA}$ and the metal–N force constant further increases to 6.3 $\text{mdyn}/\text{\AA}$. In the NNH_3 complexes $[\text{MF}(\text{NNH}_3)(\text{depe})_2]^{2+}$, $\text{M}=\text{Mo}$ or W , finally, the N–N force constant is found at 6.03 $\text{mdyn}/\text{\AA}$, close to the value of an N–N single bond, while the metal–N force constants

TABLE VI
COMPARISON OF THE OBSERVED AND CALCULATED FREQUENCIES OF $[\text{MF}(\text{NNH}_3)(\text{depe})_2](\text{BF}_4)_2$ AND $[\text{MF}(^{15}\text{N}^{15}\text{NH}_3)(\text{depe})_2](\text{BF}_4)_2$; M=Mo (**IVa**) AND W (**IVb**), IN cm^{-1}

	$[\text{MoF}(\text{NNH}_3)(\text{depe})_2](\text{BF}_4)_2$				$[\text{WF}(\text{NNH}_3)(\text{depe})_2](\text{BF}_4)_2$			
	Experimental		QCA-NCA		Experimental		QCA-NCA	
	NNH_3	$^{15}\text{N}^{15}\text{NH}_3$	NNH_3	$^{15}\text{N}^{15}\text{NH}_3$	NNH_3	$^{15}\text{N}^{15}\text{NH}_3$	NNH_3	$^{15}\text{N}^{15}\text{NH}_3$
$\nu_s(\text{NH})$	3315	3305	3316	3304	3345	3334	3344	3331
$\nu_s(\text{NH})$	3265	3258	3264	3257	3275	3271	3278	3271
$\nu_{as}(\text{NH})$	3171	3167	3170	3168	3178	3173	3176	3174
$\nu(\text{NN})$	n.o	1347	1386	1341	n.o.	n.o.	1341	1305
$\nu(\text{MoN})$	n.o	591	593	587	570	557	569	557
$\nu(\text{MoF})$	n.o	n.o	630	621	n.o.	n.o.	590	588
$\delta(\text{MoNN})$	n.o.	434	445	434	436	n.o.	436	424

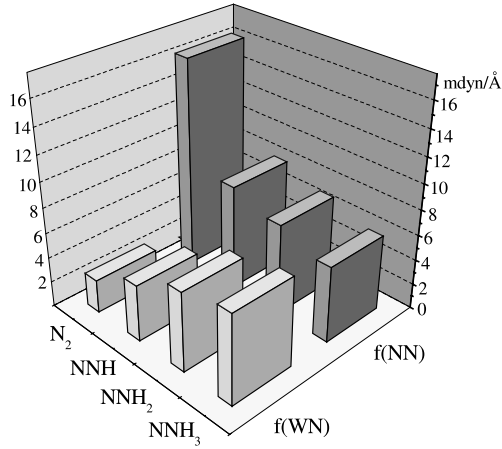


FIG. 8. Evolution of M–N and N–N force constants for the tungsten complexes **I**, **II**, **III**, and **IVb** upon successive protonation.

TABLE VII

FORCE CONSTANTS OF THE W–N₂, –NNH, –NNH₂ AND –NNH₃ COMPLEXES **I–IVb** AND THE Mo–NNH₃ COMPLEX **IVa** (UNITS ARE mdyn/Å FOR STRETCHING AND mdyn · Å FOR BENDING MODES)

	Compound	f(NN)	f(MN)	f(MNN)	Ref.
[W(N ₂) ₂ (dppe) ₂]	I	16.43	2.66	0.70	12a
[WF(NNH)(dppe) ₂]	II	8.27	4.50	0.53	12a
[WF(NNH ₂)(dppe) ₂](BF ₄)	III	7.20	6.31	0.39 / 0.69	12a
[WF(NNH ₃)(depe) ₂](BF ₄) ₂	IVb	6.03	7.31	0.65	15
[MoF(NNH ₃)(depe) ₂](BF ₄) ₂	IVa	6.03	8.01	0.63	15

(8.01 and 7.31 mdyn/Å, respectively) reach values typical for a metal–N triple bond (20). In contrast to the N–N and metal–N force constants, the MNN bending force constants remain approximately constant upon successive protonation (around 0.7 mdyn · Å), with exception of the in-plane bending force constants in the NNH₂ systems which exhibit values of about 0.4 mdyn · Å.

The experimentally determined evolution of N–N force constants upon stepwise protonation thus indicates a successive decrease in N–N bond order initiating bond cleavage, whereas the evolution of metal–N force constants reflects an increase of metal–ligand covalency, indicative of a successive strengthening of the metal–N bond. Besides

providing an energetic driving force for the reduction of the N–N triple bond, this also acts to prevent loss of partly reduced NNH_x substrate, $x=1\text{--}3$, in the course of the transformation of N_2 to ammonia. In the following section, the evolution from an N–N triple bond to an N–N single bond is considered from an electronic structure point of view, and the UV/Vis spectroscopic properties of the corresponding Mo and W complexes are described.

III. Electronic Structure and Electronic Absorption Spectroscopy

The metal–ligand bonding properties of the N_2 and N_2H_x species of the end-on terminal reduction pathway are determined by their respective MO schemes. The highest occupied orbitals of dinitrogen are a σ -bonding orbital p_σ and a doubly degenerate set of π -bonding orbitals π_x/π_y (Fig. 9). The LUMO of N_2 corresponds to a set of π -antibonding orbitals π^*_x/π^*_y . Bonding of three protons and four-electron transfer to N_2 generate the NNH_3^- species (hydrazidum). The vertical (π_x) and horizontal (π_y) π orbitals of N_2 are thereby transformed into two NH

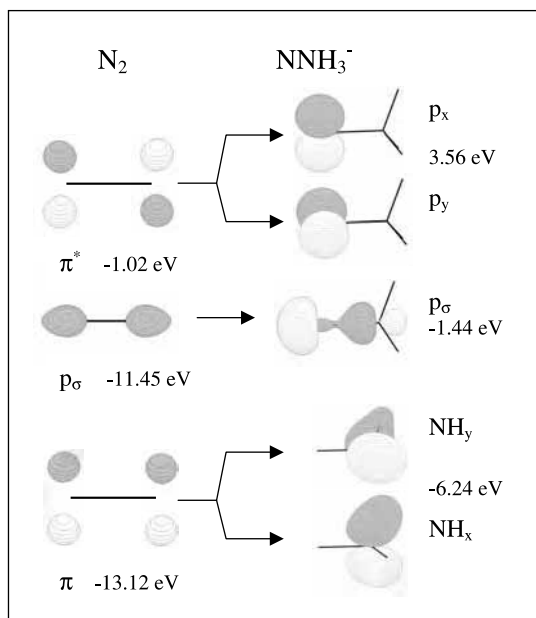


FIG. 9. Evolution of the molecular orbitals of N_2 upon conversion to NNH_3^- .

bonding orbitals on N^β whereas the two degenerate π^* orbitals of dinitrogen have evolved into two orbitals p_x and p_y mostly having p donor character at the coordinating nitrogen atom N^α . Loss of π -bonding interaction between the p orbitals of the coordinating and the terminal nitrogen of N_2 is already beginning in the NNH and NNH_2 intermediates. In the NNH_3 species, N–N bonding is exclusively mediated by the orbital p_σ ; the N–N triple bond of N_2 is therefore reduced to a single σ bond.

A direct probe of the bonding between N_2 and its intermediates and metal centers is provided by UV/Vis absorption spectroscopy, coupled to DFT calculations. In the bis(dinitrogen) complex **I**, the doubly degenerate HOMO's of the dinitrogen ligands form three combinations with the metal: a bonding, a non-bonding, and an antibonding one (Fig. 10, left). The bonding combination primarily has metal character while the non-bonding and antibonding combinations primarily are of ligand character. Based on the occupation of the metal–ligand bonding orbitals d_{xz} and d_{yz} and the non-bonding orbital d_{xy} in **I**, the metal has a d^6 electronic configuration corresponding to $W(0)$. This description is in

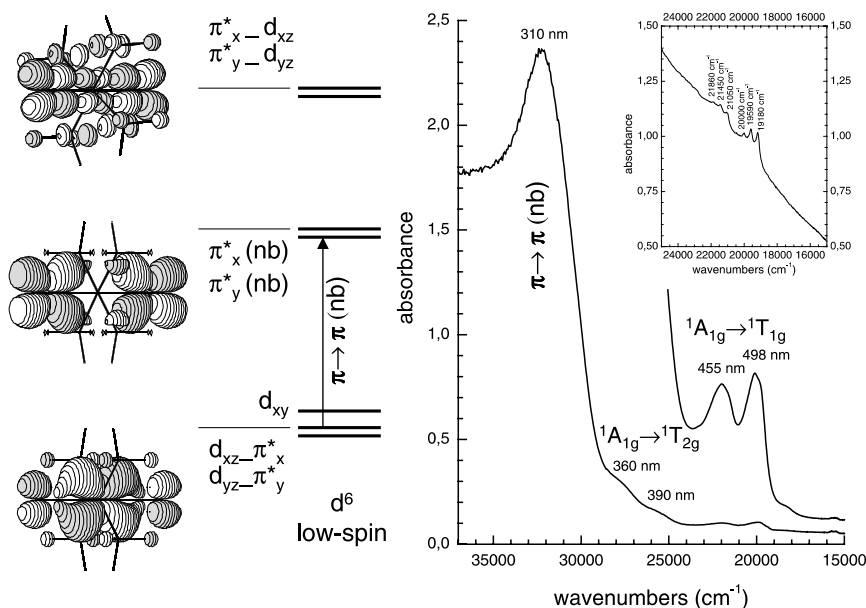


FIG. 10. Section of the MO scheme of the dinitrogen complex **I** and optical absorption spectrum of **I** with assignments. Insert: low-temperature spectrum of a KBr pellet showing vibrational structure of the LF transitions.

full agreement with the optical absorption spectrum showing the LF transitions of a d^6 low-spin system; i.e., $^1A_1 \rightarrow ^1T_1$ and $^1A_1 \rightarrow ^1T_2$ split by the tetragonal symmetry of the complex. $^1A_1 \rightarrow ^1T_1$ is found at 455/498 nm and $^1A_1 \rightarrow ^1T_2$ at 360/390 nm, respectively (Fig. 10, right). These LF transitions are masked by a metal (\rightarrow phosphine CT band at 380 nm in the corresponding dppe complex (see below). The charge-transfer (CT) transition from the bonding combinations between the N_2 π^* and the metal d_{xz} and d_{yz} orbitals into the non-bonding combination of N_2 π^* orbitals is found at 310 nm.

The final stage of N_2 protonation in $[M(\text{diphosphine})_2]$ systems is reached in the hydrazidium complex (in dinitrogen complexes containing monotertiary phosphine ligands, the reaction continues through to ammonia) (5). A section of the MO scheme of the NNH_3 model system \bar{IV} is given in Fig. 11, left. The HOMO of \bar{IV} is the non-bonding orbital d_{xy} . At lower energy are the bonding combinations of d_{xz} and d_{yz} with the NNH_3 p-donor orbitals p_x and p_y , corresponding to two M–N π bonds. These MO's are denoted as p_x-d_{xz} and p_y-d_{yz} and primarily have ligand character. Metal–ligand σ bonding is mediated by $p_\sigma-d_{z^2}$. The LUMO is part of a two-fold degenerate set of the antibonding

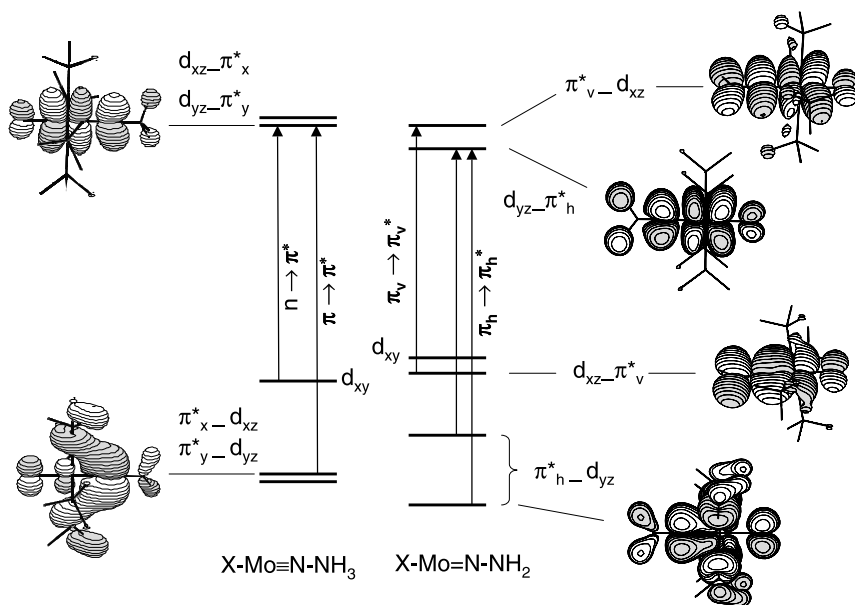


FIG. 11. Sections of the MO schemes of the hydrazidium complex \bar{IV} (left) and the NNH_2 complex \bar{III} (right) along with isodensity surface plots of the corresponding MO's.

TABLE VIII

NPA CHARGES OF $[\text{Mo}(\text{N}_2)_2(\text{PH}_3)_4]$ (**I**), $[\text{MoF}(\text{NNH})(\text{PH}_3)_4]$ (**II**),
 $[\text{MoF}(\text{NNH}_2)(\text{PH}_3)_4]^+$ (**III**), AND $[\text{MoF}(\text{NNH}_3)(\text{PH}_3)_4]^{2+}$ (**IV**)

	M	N ^α	N ^β	H _N	F
$[\text{Mo}(\text{N}_2)_2(\text{PH}_3)_4]$	−1.01	−0.07	−0.06	—	—
$[\text{MoF}(\text{NNH})(\text{PH}_3)_4]$	−0.24	−0.17	−0.56	+ 0.34	−0.64
$[\text{MoF}(\text{NNH}_2)(\text{PH}_3)_4]^+$	+ 0.04	−0.21	−0.68	+ 0.43	−0.55
$[\text{MoF}(\text{NNH}_3)(\text{PH}_3)_4]^{2+}$	+ 0.19	−0.36	−0.60	+ 0.48	−0.44

combinations $d_{xz}-p_x$ and $d_{yz}-p_y$ which predominantly are of metal character (55%). To even higher energy the antibonding combinations of d_{z^2} with p_{σ^*} are found (not shown in Fig. 11). Based on this electronic structure, the NNH_3 ligand has a single N–N σ bond and is coordinated to the metal center by a metal–N triple bond. The metal now has a d^2 electronic configuration with two electrons being in the non-bonding d_{xy} orbital and therefore is assigned a formal +IV oxidation number. Consequently, four electrons from the W(0) center have been transferred to the N_2 ligand, thus forming (along with three protons) a coordinated NNH_3^- species. As evident from NPA (Natural bond Population Analysis; Table VIII), the electronic charge on the complex bound NNH_3 is reduced from (formally) -1 to $+0.48$; i.e., this ligand donates about 1.5 charge units to the metal(IV) center.

The MO scheme of NNH_2 complex **III** is given in Fig. 11, right. Due to the planar geometry of the NNH_2 ligand, the π and π^* orbitals each split into an in-plane (“horizontal”, h) and an out-of-plane component (“vertical”, v). The π^*_h orbital now has the properties of a lone pair (like p_x/p_y in the case of NNH_3) and is responsible for the p donor capability of NNH_2 . The metal–ligand bonding combination $\pi^*_h-d_{yz}$ is split into two orbitals due to interaction with the phosphine ligands. The corresponding antibonding combination $d_{yz}-\pi^*_h$ which is metal-dominated is the LUMO of model **III**. The out-of-plane orbital π^*_v , on the other hand, still has N_2 π^* character and is involved in a π -backbonding interaction with the metal d_{xz} orbital. However, due to the elongation of the N–N bond with respect to N_2 , it is lowered in energy and has a higher contribution to the bonding combination $d_{xz}-\pi^*_v$ than present in the dinitrogen complex **I**, thus forming a highly covalent out-of-plane π bond. Via its p-donor capacity, NNH_2 loses charge to the metal but, on the other hand, receives electron density from the metal by strong back-donation into π^*_v . These two contributions effectively

cancel, leaving the ligand with a slightly negative charge (-0.03 from NPA, Table VIII). Therefore, NNH_2 is coordinated as covalently bound isodiazene in **III**, and the usual “hydrazido(2-)” formulation for these systems overestimates the negative charge on this ligand. The NNH compound **II** has an intermediate position between the N_2 complex and the NNH_2 species **III**. With respect to the parent N_2 complex, the in-plane back bonding interaction of the N_2 ligand is replaced by one strong and covalent π -bond and out-of-plane back donation from the metal into π^*_v is enhanced. On the basis of NPA the NNH species has a charge of -0.4 ; the calculated N–N force constant is 948. From the experimentally determined force constant (8.27, Table VIII), however, the negative charge on this species must be higher, i.e., more toward -1 , corresponding to the usual “diazenido(-)” formulation. Consequently, the major part of charge transfer during the first two protonation steps occurs at the NNH stage, and the second proton transfer more or less corresponds to a Brønsted acid–base reaction at the NNH^- ligand.

Optical absorption spectra of protonated derivatives of Mo and W bis(dinitrogen) complexes are preferably taken from depe systems (15). Solid-state UV/Vis spectra of the Mo– NNH_3 complex **IVa** are shown in Fig. 12, top left. Four bands at 536, 430, 352, and 251 nm can be identified. In the spectrum of the tungsten analog **IVb** only three absorption bands at 446, 310, and 237 nm are found. Table IX collects the observed band positions as well as those obtained from TDDFT on model **IV**. The (metal–ligand) $\pi \rightarrow \pi^*$ optical transition is calculated by TDDFT to 240 nm which shows good agreement with an absorption band at 251 nm (**IVa**) and 237 nm (**IVb**), respectively. The two d-electrons of the metal are located in the non-bonding (n) d_{xy} orbital; the $n \rightarrow \pi^*$ optical transition is calculated by TDDFT at 561 nm which compares well with an absorption band at 536 nm (**IVa**). Higher-energy LF bands in the optical absorption spectra of **IVa** and **IVb** are assigned to $d_{xy} \rightarrow d_{x^2-y^2}$ (430 nm) for **IVa** (446 nm for **IVb**) and $d_{xy} \rightarrow d_{z^2}$ (352 nm for **IVa**, 310 nm for **IVb**), respectively. This sequence of LF transitions is in agreement with that found for analogous Mo(IV) oxo compounds with phosphine coligands (21). The high intensity of the transition to d_{z^2} is attributed to d_{z^2}/p_z mixing in the approximate C_{4v} symmetry of the complex, in agreement with similar observations on $[\text{FeHCl}(\text{depe})_2]^+$ (13a).

For comparison, optical absorption spectra of the Mo- and WCl(NNH_2)(depe) $_2$ complexes **Va** and **Vb**, respectively, have been recorded and interpreted by TDDFT as well (Fig. 12, bottom and Table X) (15). Both LF and $\pi \rightarrow \pi^*$ transition regions of these spectra are markedly different to those of analogous NNH_3 systems. In particular, the $\pi \rightarrow \pi^*$

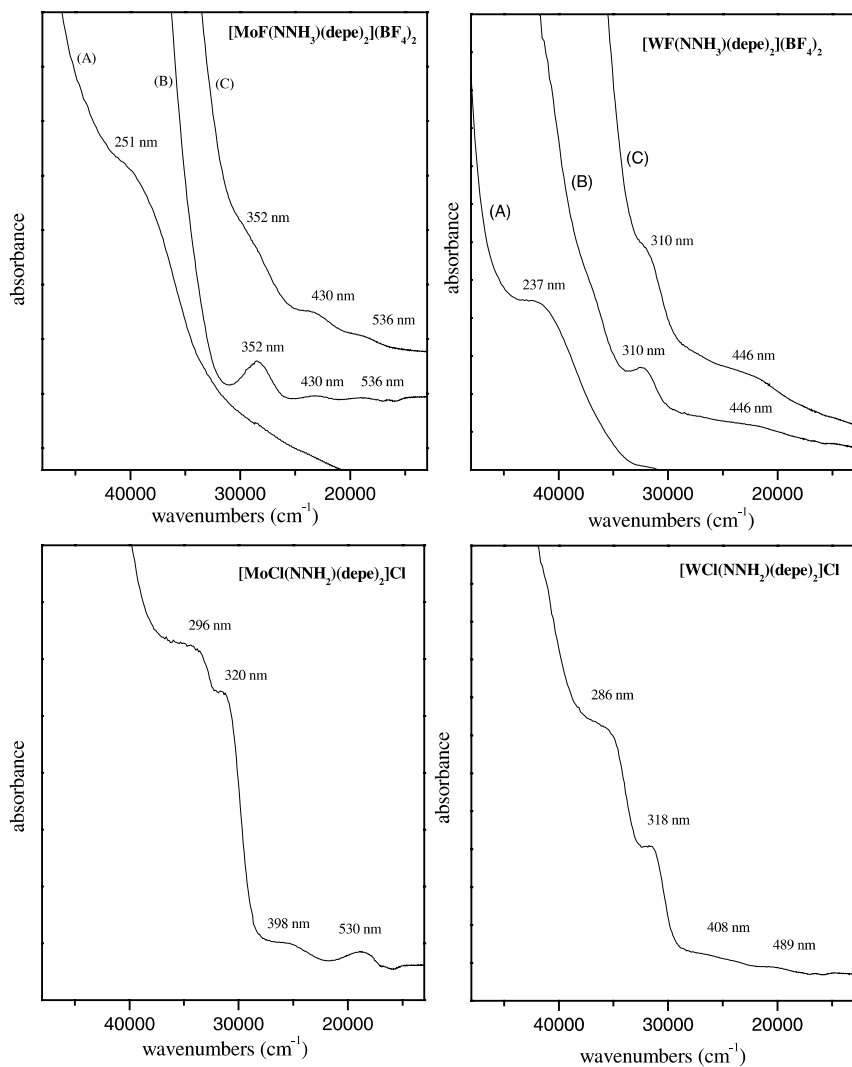


FIG. 12. Solid-state UV/Vis absorption spectra of $[\text{MoF}(\text{NNH}_3)(\text{depe})_2](\text{BF}_4)_2$ (**IVa**), $[\text{WF}(\text{NNH}_3)(\text{depe})_2](\text{BF}_4)_2$ (**IVb**), $[\text{MoCl}(\text{NNH}_2)(\text{depe})_2](\text{BF}_4)_2$ (**Va**), and $[\text{WCl}(\text{NNH}_2)(\text{depe})_2](\text{BF}_4)_2$ (**Vb**). (A) KBr pellet at room temperature, (B) neat complex pressed between sapphire windows at 10 K, (C) concentrated KBr pellet at 10 K.

TABLE IX
EXPERIMENTAL AND CALCULATED TRANSITION ENERGIES FOR
[MF(NNH₃)(depe)₂](BF₄)₂, M = Mo, W

Experimental (nm)		Calculated* (nm)	Assignments
M=W (IVb)	M=Mo (IVa)		
—	536	561	$d_{xy} \rightarrow d_{yz}-\pi^*_y / d_{xy} \rightarrow d_{xz}-\pi^*_x$
446	430	417	$d_{xy} \rightarrow d_{x^2-y^2}$
310	352	341	$d_{xy} \rightarrow d_{z^2}$
237	251	240	$\pi^*_y-d_{yz} \rightarrow d_{yz}-\pi^*_y /$ $\pi^*_{x-}-d_{xz} \rightarrow d_{xz}-\pi^*_x$

* Calculated for model **III**.

TABLE X
EXPERIMENTAL AND CALCULATED TRANSITION ENERGIES FOR
[MCl(NNH₂)(depe)₂]Cl, M = Mo, W

Experimental (nm)		Calculated* (nm)	Assignments
M = W (Vb)	M = Mo (Va)		
489	530	507	$d_{xy} \rightarrow d_{yz}-\pi^*_h / d_{xz} \rightarrow d_{x^2-y^2}$
408	398	370	$d_{xy} \rightarrow \pi^*_{v-}d_{xz}$
318	320	300	$d_{xz}-\pi^*_v \rightarrow \pi^*_{v-}d_{xz} /$
286	296	274	$\pi^*_h-d_{yz} \rightarrow d_{yz}-\pi^*_h$
		237	$\pi^*_h-d_{yz} \rightarrow d_{yz}-\pi^*_h$

* Calculated for model **II**.

transitions are shifted to lower energy and split into two bands at 296/320 nm (**Va**) and 286/318 nm (**Vb**). In agreement with the TDDFT prediction, this is attributed to the splitting of these transitions into one transition within and one transition perpendicular to the NNH₂ plane. The lower energy of the $\pi \rightarrow \pi^*$ transitions in the Mo–NNH₂ complex **Va** as compared to the Mo–NNH₃ complex **IVa** is also reproduced by TDDFT, reflecting the lower degree of metal–ligand covalency in the NNH₂ compared to the NNH₃ system (there is one in-plane $\pi \rightarrow \pi^*$ transition at 237 nm which, however, derives from interaction of π^*_h with the phosphine ligands). The LF region of the NNH₂ complexes exhibit bands at 398 and 530 nm (**Va**; 408 and 498 nm in **Vb**) which are assigned to the transitions $d_{xy} \rightarrow \pi^*_{v-}d_{xz}$ and $d_{xy} \rightarrow d_{yz}-\pi^*_h$, respectively (Table X). These features are masked in the

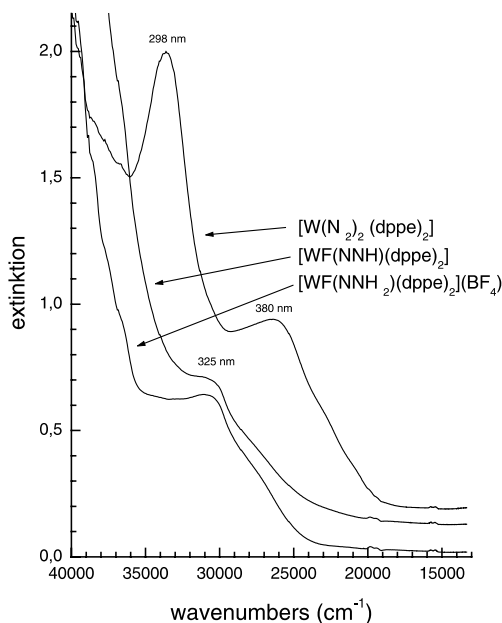


FIG. 13. Solution spectra of **I**, **II**, and **III** in thf at room temperature.

corresponding dppe complex by a metal \rightarrow phosphine CT band (Fig. 13) which in the dinitrogen system **I** appears at 380 nm (12a). This feature is probably due to an electronic transition from metal d to phosphine d orbitals. In the protonated species **II** and **III**, the broad dppe absorption band is shifted to 325 nm.

IV. Conclusions

The investigations presented in the preceding sections have led to a spectroscopic and electronic-structural characterization of molybdenum and tungsten N_2 and N_2H_x complexes ($x=1-3$) with diphosphine ligands. Consideration of the N–N and metal–N force constants of the N_2 complexes and their protonated intermediates provides insight into the ligand activating properties of the various metal–(diphos) $_2$ combinations and allows to monitor the state of the N_2H_x ligand upon successive protonation. As evident from NN and metal–N frequencies and force constants, back donation is stronger in tungsten than molybdenum complexes and for a given metal stronger in depe

than dppe complexes. The stronger activation of N_2 by depe as compared to dppe is caused by a stronger σ donor and/or weaker π -acceptor capability of the former as compared to the latter ligand. This obviously also affects the stability of hydrazidium complexes accounting for the fact that these systems so far only have been isolated with depe co-ligands.

After protonation of one of the N_2 ligands of the bis(dinitrogen) complex, the NNH complex is formed. The in-plane back bonding interaction of the N_2 ligand is replaced by one strong and covalent π -bond and out-of-plane back donation from the metal into π^*_v is increased. In the NNH_2 complex the out-of-plane interaction is enhanced once more, but the in-plane (p donor) interaction is reduced. In total, however, an increase of metal–ligand bond strength and a decrease of NN bond strength is observed (f_{WN} : $4.50 \rightarrow 6.31$, f_{NN} : $8.27 \rightarrow 7.20$, Table VII). The $N-N$ force constant of the coordinated NNH_2 now corresponds to a double bond, i.e., one π bond of dinitrogen has been removed and two electrons have been transferred to the N_2 moiety. This description is in agreement with the NPA analysis which indicates an almost neutral charge state on the NNH_2 ligand, more in agreement with an isodiazene formulation than the usual “hydrazido(2-)” description of this ligand. Although the whole NNH_2 ligand is almost neutral, its terminal N -atom carries a negative partial charge, and a third protonation can occur. In the resulting hydrazidium complex, a metal– N triple bond and an $N-N$ single bond are present. This is supported by the MO scheme and vibrational analysis which indicate a metal– N force constant of 7–8 and an $N-N$ force constant of 6.03 (all values in $\text{mdyn}/\text{\AA}$).

As indicated at the beginning, formation of hydrazidium complexes requires strongly electron-donating equatorial phosphine ligands with terminal alkyl groups. Whereas up to now only $W-NNH_3$ complexes have been isolated and characterized, we found that an analogous molybdenum complex exhibits a comparable stability in the solid state. Generally, crystallization of these species is favored by strong H -bonds stabilizing the NNH_3 groups. Thermal stability of the Mo and W hydrazidium complexes **IVa** and **IVb** in solution, on the other hand, is limited by the phosphine ligands becoming labile at this stage of N_2 reduction. In order to increase thermodynamic stability of the Mo/W complex at the NNH_3 stage of protonation bidentate phosphine co-ligands are therefore required. Thermal stability of the NNH_3 complexes is further limited by their strong Brønsted acidity; i.e., these complexes only exist in solution in the presence of a large excess of acid.

Provided the equatorial phosphine ligands stay bound to the metal center under these conditions, the NNH_3 species is stable with respect to further reduction to NH_3 (15). Mo- and W-hydrazidium complexes therefore mark the ultimate stage of N_2 reduction and protonation at d^6 metal centers in the absence of external reductants. Two-electron transfer to the six-coordinate NNH_3 complexes to mediate N–N splitting, on the other hand, eventually leads to splitting of the metal–N bond and loss of the NNH_3 ligand as the LUMO of the NNH_3 complex is contained in the doubly degenerate set of d_{xz} and d_{yz} metal–N π -antibonding orbitals. In practice, two-electron reduction is performed at the NNH_2 stage, leading to elimination of the *trans* ligand (22). Subsequent protonation of the resulting five-coordinate, two-electron reduced NNH_2 species then leads to N–N cleavage and generation of the imido complex (23). This process continuing the end-on terminal reduction pathway of dinitrogen is currently investigated by our group using the same methodology as applied to the Mo/W– N_2 and – N_2H_x systems (24).

ACKNOWLEDGMENTS

The author thanks Dr. Nicolai Lehnert and Dipl. Chem. Kay Horn who have conducted the research described in this review. Support by the Deutsche Forschungsgemeinschaft and Fonds der Chemischen Industrie is gratefully acknowledged.

REFERENCES

1. (a) “*Catalytic Ammonia Synthesis: Fundamentals and Practice (Fundamental and Applied Catalysis)*”; Ed. Jennings, J. R.; Plenum, 1991; (b) Appl, M. “*Ammonia: Principles and Industrial Practice*”; Wiley-VCH, Weinheim, Germany, 1999.
2. “*Prokaryotic Nitrogen Fixation: A Model System for the Analysis of a Biological Process*”; Ed. Triplett, E. W.; Horizon Scientific Press, Wymondham, England, 2000.
3. Einsle, O.; Tezcan, A. F.; Andrade, S. L. A.; Schmid, B.; Yoshida, M.; Howard, J. B.; Rees, D. C *Science* **2002**, 297, 1696–1700, and refs cited therein.
4. (a) Fryzuk, M.; Johnson, S. A. *Coord. Chem. Rev.* **2000**, 200, 379; (b) Sellmann, D.; Utz, J.; Blum, N.; Heinemann, F. W *Coord. Chem. Rev.* **1999**, 190–192, 607; (c) Rawls, R. L. *Chem. Eng. News* **1998**, 76, 29; (d) Richards, R. L *Coord. Chem. Rev.* **1996**, 154, 83; (e) Hidai, M.; Mizobe, Y. *Chem. Rev.* **1995**, 95, 1115; (f) Tuzcek, F.; Lehnert, N. *Angew. Chemie Int. Ed.* **1998**, 37, 2636–2638.
5. (a) Leigh, G. J. *Accts. Chem. Res.* **1992**, 25, 177; (b) Henderson, R. A.; Leigh, G. J.; Pickett, C. *Adv. Inorg. Chem. Radiochem.* **1983**, 27, 197–292.
6. Thorneley, R. N. F.; Lowe, D. J. “*Molybdenum Enzymes*”; Ed. Spiro, T. G.; John Wiley: New York, 1985.
7. Pickett, C. J.; Talarmin, J. *Nature* **1985**, 317, 652.
8. Yandulov, D. V.; Schrock, R. R. *Science* **2003**, 301, 76.

9. (a) Yandulov, D. V.; Schrock, R. R. *J. Am. Chem. Soc.* **2002**, *124*, 6252; (b) Yandulov, D. V.; Schrock, R. R.; Rheingold, A. L.; Ceccarelli, C.; Davis, W. M. *Inorg. Chem.* **2003**, *42*, 796.
10. (a) Lehnert, N.; Wiesler, B.; Tuzcek, F.; Hennige, A.; Sellmann, D. *J. Am. Chem. Soc.* **1997**, *119*, 8869; (b) Lehnert, N.; Wiesler, B.; Tuzcek, F.; Hennige, A.; Sellmann, D. *J. Am. Chem. Soc.* **1997**, *119*, 8879.
11. Wiesler, E. B.; Lehnert, N.; Tuzcek, F.; Neuhausen, J.; Tremel, W. *Angew. Chem. Int. Ed.* **1998**, *37*, 815.
12. (a) Lehnert, N.; Tuzcek, F. *Inorg. Chem.* **1999**, *38*, 1659; (b) Lehnert, N.; Tuzcek, F. *Inorg. Chem.* **1999**, *38*, 1671.
13. (a) Franke, O.; Wiesler, B. E.; Lehnert, N.; Näther, C.; Neuhausen, J.; Ksenofontov, V.; Tuzcek, F. *Inorg. Chem.* **2002**, *41*, 3491–3499; (b) Franke, O.; Wiesler, B. E.; Lehnert, N.; Tuzcek, F. *Z. Anorg. Allg. Chem.* **2002**, *628*, 2395–2402.
14. Habeck, C. M.; Lehnert, N.; Näther, C.; Tuzcek, F. *Inorg. Chim. Acta* **2002**, *337C*, 11–31.
15. Horn, K. H.; Lehnert, N.; Tuzcek, F. *Inorg. Chem.* **2003**, *42*, 1076.
16. (a) Studt, F.; Morello, L.; Lehnert, N.; Fryzuk, M. D.; Tuzcek, F. *Chem. Eur. J.* **2003**, *9*, 520–530; (b) Studt, F.; MacKay, B. A.; Fryzuk, M. D.; Tuzcek, F. *J. Am. Chem. Soc.* **2004**, *126*, 280–290.
17. (a) Chatt, J.; Heath, G. A.; Richard, R. L. *JCS Dalton* **1974**, 2074; (b) Henderson, R. A. *JCS Dalton* **1984**, 2259.
18. Horn, K.; Tuzcek, F. *Coord. Chem. Rev.* **2003**, *245*, 107–120.
19. Chatt, J.; Kan, C. T.; Leigh, G. J.; Pickett, C. J.; Stanley, D. R. *JCS Dalton* **1980**, 2032.
20. Mersmann, K.; Tuzcek, F. *Manuscript in preparation*.
21. (a) Cowman, C. D.; Trogler, W. C.; Mann, K. R.; Poon, C. K.; Gray, H. B. *Inorg. Chem.* **1976**, *15*, 1747; (b) Bendix, J.; Bøgevig, A. *Inorg. Chem.* **1998**, *37*, 5992–6001.
22. (a) Hussain, W.; Leigh, G. J.; Pickett, C. J. *J. Chem. Soc. Chem. Commun.* **1982**, 747; (b) Pickett, C. J.; Leigh, G. J. *J. Chem. Soc. Chem. Commun.* **1981**, 1033.
23. Henderson, R. A.; Leigh, G. J.; Pickett, C. J. *J. Chem. Soc. Dalton* **1989**, 425.
24. Horn, K.; Böres, N.; Lehnert, N.; Näther, C.; Tuzcek, F. *Manuscript in preparation*.

QUANTUM CHEMICAL INVESTIGATIONS INTO THE PROBLEM OF BIOLOGICAL NITROGEN FIXATION: SELLMANN-TYPE METAL–SULFUR MODEL COMPLEXES

MARKUS REIHER* and BERND A. HESS

Institute for Physical and Theoretical Chemistry, University of Bonn,
Wegelerstrasse 12, D-53115 Bonn, Germany

*Correspondence to Markus Reiher: reiher@thch.uni-bonn.de

- I. Introduction
- II. The Active Site of Nitrogenase: FeMo-Cofactor
 - A. Present Status of Theoretical Studies
- III. Biomimetic Sellmann-Type Metal Complexes
- IV. The First 2-Electron–2-Proton Transfer
 - A. First Step: Hydrogen Bonds in Mononuclear Fe(II) Complexes
 - B. Different Stabilization Effects in Coordinated *cis*- and *trans*-Diazene
 - C. Hydrogen Bonding in Dinuclear Complexes
- V. Reaction Energetics of the Reduction at Mononuclear Fe(II) Centers
 - A. Multiplicities of the Ground States
 - B. End-on Versus Side-on Binding of N₂
 - C. Diazene Isomers
 - D. Ligand Binding Energies
 - E. Analysis of the Catalytic Potential
 - F. Coordinating N₂ to Mononuclear Fe(II) Complexes: The Role of Spin Barriers
- VI. Photoisomerization of Coordinated Diazene
 - A. Secondary Effects Through Chelate Ligand Modification
- VII. Study of the First Dinuclear N₂ Complex with Biologically Compatible Ligand Sphere
 - A. Outlook: A Possible Photo-Chemical Reduction Mechanism
- VIII. Conclusion
- IX. Appendix: Quantum Chemical Methodology
- References

I. Introduction

Biological N_2 fixation (1), i.e., the reduction of N_2 to NH_3 catalyzed by FeMo, FeV, or FeFe nitrogenases, is one of the fundamental synthetic processes of nature (2–4). In spite of intense efforts over the last decades, its molecular mechanism is poorly understood, in particular because the pivotal chemical question has remained unanswered: how do nitrogenases achieve to activate and convert the inert N_2 molecule to ammonia under ambient conditions and mild redox potentials.

A giant step forward to solving the nitrogen fixation problem was the X-ray structural characterization of FeMo nitrogenase and its active sites, the FeMo-cofactor (4). In 2002, a new high-resolution X-ray structure analysis by Rees and collaborators revealed a previously unrecognized central nitrogen atom of FeMoco (5). This new result demonstrated that all theoretical studies conducted until the end of 2002, which did not consider this central atom, were based on an incomplete structural model. Conclusions drawn from these studies are most likely of little value for understanding the mechanism of nitrogenase. Moreover, the turn-over state of the enzyme and all key steps of the reduction process remain unclear. Thus, all chemical mechanisms which were suggested for the nitrogenase-catalyzed N_2 reduction so far remain largely speculative [cf. (6–12) and especially Ref. (13) for reviews].

All *abiological* N_2 -reducing systems proposed so far either need drastic reaction conditions (e.g., the Haber–Bosch process) or abiologically strong reductants such as, for example, alkaline metals (14,15). In addition, most strong-reductant-type N_2 -reducing systems, which include a few metal dinitrogen complexes, do not operate catalytically (16,17). The first catalytic dinitrogen reducing complex, which works under ambient conditions, was presented very recently by Yandulov and Schrock (18,19), who used a molybdenum triamidoamine complex. This complex might be understood as a functional but not as a structural model for nitrogenase activity.

All mechanistic proposals for biological N_2 fixation are left with the problem to explain how nitrogenases enable the catalytic N_2 reduction at mild biological reduction potentials (6,8). These reduction potentials probably represent the biggest challenge in the search for synthetic competitive catalysts that exhibit nitrogenase-like activity.

The X-ray structure of the nitrogenase active site is obviously a good starting point for investigations on mechanistic aspects of the

formidable problem. X-ray structure analyses and methods from molecular biology (sequencing, cloning, mutagenesis) revealed that functional properties of nitrogenases are very similar though they occur in phylogenetically different bacteria. The Mo-based nitrogenase consists of two protein complexes, the Fe and the MoFe protein. While the Fe protein is the highly specific electron donor for the MoFe protein, nitrogen reduction takes place at the FeMo-cofactors (FeMoco) within the MoFe protein. The MoFe protein complex is a tetrameric protein cluster containing two groups of metal clusters, i.e., the FeMoco and the so-called P cluster, which most likely plays a role in electron transfer to FeMoco.

II. The Active Site of Nitrogenase: FeMo-Cofactor

The X-ray structure of the resting state of FeMoco exhibits a central iron prism with three μ -S atoms on top of the three vertical edges of the prism. On top of the two triangular faces of the Fe_6 prism we find another Fe and a Mo atom so that two tetrahedral structures arise. The triangular faces of these tetrahedra are each capped with three additional sulfur atoms (Fig. 1).

The FeMoco can be extracted intact (20) from the acid-denatured MoFe protein, which has the important consequence that modeling of its function may start with studies on the structure of the isolated cluster. The protein environment (and also solvent molecules) may be neglected in the *first* modeling step though they are essential for the reduction mechanism. This simplification appears to be mandatory since the electronic structure of the *isolated* cluster is extremely complicated.

A. PRESENT STATUS OF THEORETICAL STUDIES

To arrive at significant insight for the biological reduction process, all theoretical studies should be taken into account since none of them is free of model-inherent approximations. We emphasize that none of the recent studies, which utilized DFT methods, discussed the theoretical complications with standard density functionals arising from different spin states, which are discussed in the [Appendix](#). The authors thus have assumed that the dependence of the results on the chosen density functional is of little importance in

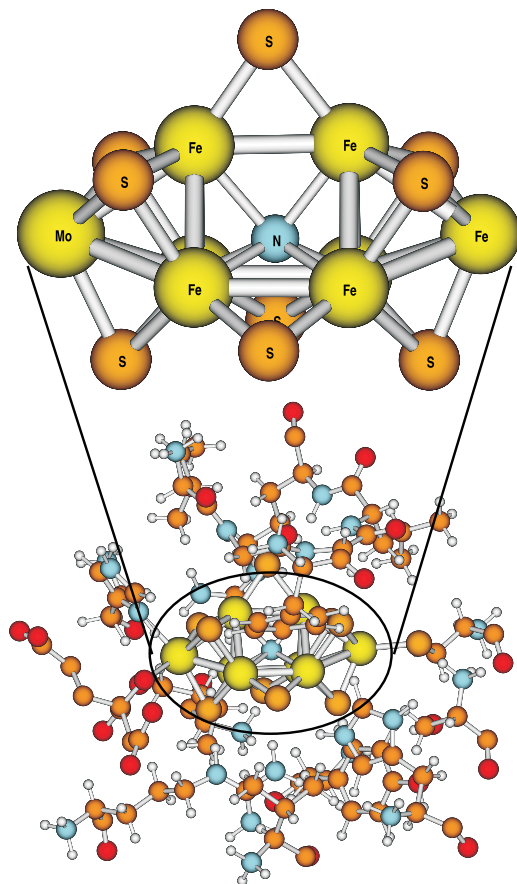


FIG. 1. New structure of the FeMo-cofactor found by Rees and collaborators in 2002 (5). (Top: structure of the cluster; Bottom: FeMoco and surrounding ligands and amino acids in the protein pocket.)

the case of FeMoco although no substantiation is provided for such an assumption.

Pioneering studies with semi-empirical methods were carried out shortly after the discovery of the FeMoco structure via X-ray diffraction experiments (21,22). These extended-Hückel calculations have been carried out for structurally fixed models of FeMoco (23,24) and of FeMoco, FeVco, and FeFeco (25), in which the three amino acid ligands have been replaced by hydride ligands. The main results of these studies are deduced based on the assumption that the character of the frontier orbitals, i.e., their composition in terms of atomic orbitals,

determines the binding of dinitrogen. It was found that the iron atoms in the central prismatic structure of FeMoco are good candidates for the binding site, while the Mo atom is not involved and has therefore probably only a structure-determining function. However, the Mo atom as the potential N₂ coordination site has also been considered in the framework of extended-Hückel theory (26).

Stavrev and Zerner (27,28) studied a more complicated FeMoco model, in which the three amino acid ligands from the protein environment were not replaced by hydride ligands but their essential parts have explicitly been taken into account. In one of their studies (27), N₂ was allowed to move freely in the framework of the semi-empirical INDO method. The preferred position of N₂ on FeMoco was inside the Fe₆ prism of FeMoco. However, the FeMoco was kept fixed in the calculations and the authors admit that this can only be regarded as the very first binding step before the reduction process starts. In subsequent work (29) on the same model, Stavrev and Zerner suggest a mechanism to proceed via hydrazido intermediates on the surface of four Fe centers of FeMoco. Zhong and Liu (30) used the CNDO method to study an extended model for FeMoco in great detail. Some of their mechanistic suggestions also involve opening of FeMoco and binding of N₂ to two iron centers.

In view of the many approximations in these semi-empirical calculations their results can only be regarded as first hints for more elaborate methods. Such are DFT calculations on FeMoco-type clusters and model complexes. As it is discussed, for instance, in Ref. (31), N₂ usually binds very weakly to transition metal complexes. It is thus not certain whether end-on coordination to one or two iron centers can lead to sufficiently strong coordination of dinitrogen.

The possibility of N₂ coordination to up to four (six) iron atoms has been proposed by Dance on the basis of restricted frozen-core Kohn-Sham calculations on a FeMoco model (32,33). It was found that a binding mode intermediate between μ^4, η^1 and μ^4, η^2 coordination to be most stable. However, these propositions are not necessarily the final answer since open-shell states are most likely to become important and exact exchange was not present in the density functional chosen to cure the singlet preference of the pure density functional (cf. discussion in the Appendix).

For largely simplified models, Machado and Davidson used ab initio methods (MP2 and CI) and found that a dimeric Fe(III) site with low coordination number could be useful for N₂ binding, while they did not find stable four-iron N₂ clusters (34). Siegbahn *et al.* obtained the important result from B3LYP calculations on polynuclear Fe-sulfur

complexes that a hydrogen atom attached to a bridging sulfur atom can dramatically change the affinity of the cluster for N_2 (35). From the work of Frenking and co-workers (36), we can conclude that the coordination energy of N_2 can be increased up to 96 kJ/mol in strong ligand fields at the expense of increased binding energies for NH_3 . Modifications of the chelate ligand to stronger ligand fields, protonation of sulfur atoms, and/or reduced coordination numbers are thus a promising way for solving the weak coordination problem for N_2 .

Exhaustive periodic DFT studies have been undertaken by Rod, Nørskov, and collaborators (31,37,38), who investigated FeMoco models from the point of view of heterogeneous catalysis. Two of their most important results are that FeMoco does not dissociate N_2 (N–N bond breaking occurs in the final reduction step) and the reduction takes place at the Fe atoms. It is interesting to note that end-on binding to a single Fe center was found rather than bonding to a Fe_4 face of the cluster.

Much work has been devoted by Noodleman and collaborators to attribute oxidation states extracted from broken-symmetry calculations to the FeMoco resting states, which is frequently denoted M^N with $S=3/2$, in order to meet results from Mössbauer, ENDOR, and EPR experiments. However, these calculations suffer from the general problems like the notion of “oxidation states” and of “broken symmetry” and the determination of the molecular structure from the broken-symmetry and high-spin electronic structure calculations. Not only the artificial broken-symmetry state but also the high-spin wavefunction for FeMoco give a somewhat uneasy feeling, since the high-spin state for FeMoco possesses values as large as $S=31/2$ for $Mo^{4+}4Fe^{2+}3Fe^{3+}$ and $S=29/2$ for $Mo^{4+}6Fe^{2+}1Fe^{3+}$. These high-spin and the artificial construction of such “ensembles” of oxidation states do not favor the broken-symmetry approach. It should not be forgotten that also the experimental reconstruction of single-center spin states is mainly based on phenomenological observations for complexes, which are divided into oxidation state classes as a matter of convenience. Within their broken-symmetry model, the authors have proceeded and proposed binding modes for protons to FeMoco (39).

The studies discussed so far deal – for good reasons – with the isolated FeMoco. However, qualitative molecular modeling has also been used to identify possible proton transfer routes from the surface of the nitrogenase protein to the FeMoco (40) and mechanistic aspects of biological nitrogen fixation are discussed in the light of such data (10–12).

In autumn 2002, Rees and collaborators (5) reported the *new* X-ray structure for the FeMo-cofactor, which differed from the 1992 structure in that it possesses an interstitial atom (see Fig. 1), which is most likely a nitrogen atom (41). All quantum chemical calculations reported until the end of 2002 were thus based on the wrong geometrical structure of the active site with considerable implications for the electronic structure and, thus, for the chemical behavior. Not surprisingly, new (standard) DFT calculations for the new structure were published by Dance (42), by Hinnemann and Nørskov (43), by Lovell *et al.* (44) and by Blöchl and collaborators (45) shortly after the publication of the work of Rees *et al.*

Substantial uncertainties remain with all these calculations in view of the inherent problems of DFT to describe complicated electronic structures with dense-lying states as they occur in the FeMoco and in view of the overwhelming number of structural and electronic degrees of freedom of the FeMoco during reduction of N₂. Such objections lead straight to the study of smaller well-defined model systems for which many more experimental details are known. We believe that such a bottom-up strategy towards an understanding of biological nitrogen fixation is inevitable when using present-day quantum chemical methods. For this reason the focus of this review is on Sellmann-type model complexes, which feature single iron or ruthenium metal centers surrounded by sulfur atoms in the first ligand sphere.

III. Biomimetic Sellmann-Type Metal Complexes

The preceding introduction dealt with a few basic aspects of the highly complicated mechanism of biological nitrogen fixation. In view of the complicated electronic structure of the FeMoco, it is highly desirable to base a theoretical approach on simplified models, whose complexity can be extended step by step. Such a route to the understanding of the biological nitrogen fixation problem allows us to consider the many different complicated questions of the mechanism of nitrogenase subsequently and under well-defined conditions.

Although the biological mechanism is still unsolved, the chemically essential parts can already be identified. From the structural viewpoint, the active site, i.e., the FeMoco in the MoFe protein, is highly complex and so chemically very different complex types can be

designed and utilized to model certain aspects of the biological nitrogen reduction process. All these different types of model complexes are important in order to arrive at a better understanding of the whole system (46). For instance, the occurrence of one molybdenum atom in the active center led to the development of molybdenum model complexes [cf. the extensive experimental work, also supplemented by theoretical investigations, on iron–sulfur-based Mo clusters of high nuclearity by Coucouvanis and collaborators (47–54); see also Refs. (55–59) and the recent discussion by Lee and Holm (60)]. In view of the iron and vanadium nitrogenases it appears to be evident that Mo-based model complexes are not sufficient to understand the whole active center.

Here, we review theoretical studies on mononuclear and dinuclear iron and ruthenium complexes with sulfur ligands synthesized by Sellmann and collaborators [see Refs. (9,61,62) for reviews of the experimental facts]; details on the quantum chemical methods, which were used in the original papers are given in the Appendix. The basic hypotheses discussed in connection with the Sellmann-type complexes are that (i) iron atoms of the FeMoco are involved in binding the N_xH_y species, (ii) the reduction occurs in two-proton–two-electron reduction steps as suggested by experiments (see the references given above), and (iii) the FeMoco opens in order to allow for pseudo-octahedral coordination of N_2 to two iron atoms (Coucouvanis and collaborators recently also argued in favor of a comparable opening mechanism with particular emphasis on the breaking of the Fe–Fe contact upon two-electron reduction (63)). However, we should note that a potential opening mechanism and in particular its justification by coordinationally unsaturated Fe centers is more involved (in view of the recently found interstitial nitrogen atom) than was initially thought. But we should also stress that opening of FeMoco was observed in recent DFT calculations (45) on the new FeMoco structure, which incorporated the central N ligand.

The ambient conditions of biological nitrogen fixation can potentially be met by systems which operate according to Sellmann’s “open-side” model for the cofactor function of FeMo, FeV, or FeFe nitrogenases (9,64,65). The “open-side” model assumes that the FeMoco exhibits different structures in the resting state and in the turn-over state. It proposes that one Fe–S–Fe bridge is cleaved in the turn-over state and vicinal water molecules and donor atoms of the two amino acids Gln α 191 and His α 195, which are essential for the activity of nitrogenase, are added to give two unique five-coordinate Fe(II) centers with Broensted-basic sulfur donors.

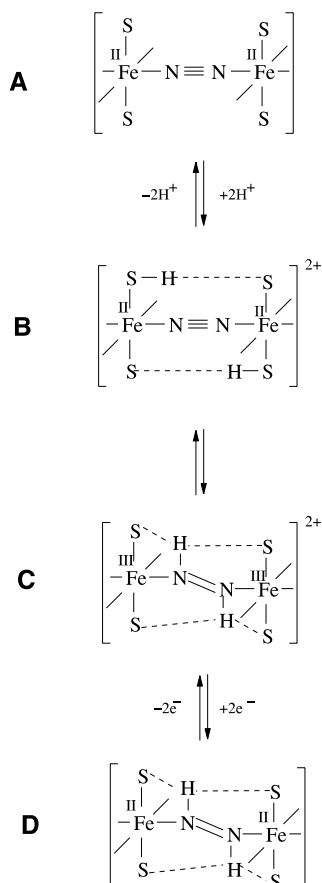


FIG. 2. The first, most important protonation reduction step.

These Fe centers shall bind N_2 which is converted by three consecutive $2\text{H}^+/2\text{e}^-$ transfer steps into N_2H_2 , N_2H_4 and finally to two NH_3 . Figure 2 schematically shows the first $2\text{H}^+/2\text{e}^-$ reduction step, which is the most difficult step for thermodynamic and kinetic reasons. The “open-side” model and the scheme of Fig. 2 take a large number of biological, biochemical, and chemical results into account: (i) all nitrogenase substrates are reduced by multiples of $2\text{H}^+/2\text{e}^-$ transfer steps (66); (ii) N_2H_2 , which is extremely unstable in the free state, is highly stabilized by coordination to iron-sulfur complex fragments (67–71); (iii) primary protonation of Brønsted-basic sulfur donors anodically shifts the redox potentials of iron-sulfur-ligand complexes in such

a way that they become reducible at potentials of about -500 mV (72); (iv) only iron oxidation states accessible in the aqueous phase are involved; (v) N_2H_2 complexes modeling the nitrogenase catalyzed “ N_2 -dependent HD formation from D_2/H^+ exchange” support diazene as the key intermediate of N_2 fixation (62,65,73–75).

IV. The First 2-Electron–2-Proton Transfer

The scheme of Fig. 2 stresses a close coupling of proton and electron transfer steps. This has also been pointed out by Collman *et al.* for the redox reactions of dinuclear porphyrinato ruthenium complexes that bind N_2 , N_2H_2 , N_2H_4 , and NH_3 (76). The scheme further emphasizes the importance of hydrogen bridges for the $N_2 \rightarrow N_2H_2$ conversion. $N-H \cdots S$ hydrogen bridges in species **B** favor the primary protonation of the neutral $[\mu-N_2\{FeS_2\}_x]$ species **A**, and bifurcated $N-H \cdots (S)_2$ bridges in **D** the stabilization of N_2H_2 resulting after the $2e^-$ transfer [see also Refs. (77) and (78,79) for a potential role of $S-H \cdots S$ hydrogen bridges in Sellmann-type complexes]. On the basis of experimental data, it has been estimated that the bifurcated $N-H \cdots (S)_2$ bridges may contribute up to 70 kJ/mol to the total stabilization energy of coordinated N_2H_2 (64,67,68). While the steps $A \rightarrow B \rightarrow C$ of Fig. 2 remain hypothetical as yet, the reversible step $C \rightarrow D$ has been established experimentally for a number of iron and analogous ruthenium complexes exhibiting $[\mu-N_2H_2\{M(S)_2\}_2]$ core structures with sulfur thiolate donors (67–71,80). Fe complexes with the structural features of species **A** or **B** are unknown. Thus, a complete characterization of all four species **A** to **D** by theoretical methods was carried out (81).

A cornerstone in such investigations is the elucidation of the hydrogen bond energies in species **B** to **D**. For example, it can be hypothesized that strong hydrogen bonds destabilize **B** and simultaneously stabilize **C** or **D**, respectively. The whole process $A \rightarrow D$ might further be driven by the structural change when the linear $[\mu-N_2\{M\}_2]$ entity in **A** or **B** transforms into the bent $[\mu-N_2H_2\{M\}_2]$ entity in **C** or **D**.

In view of the protonation and reduction process it is instructive to compare results for Fe(II) compounds with the corresponding data for the positively charged Fe(III) analogues. Iron and ruthenium complexes with two metal centers should be investigated. While the iron complexes model particular features of the FeMo-cofactor in nitrogenase, the ruthenium analogues are analyzed because of their

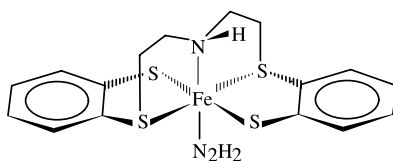
synthetic importance: usually they are more stable than their iron analogues and represent useful compounds for testing synthetic strategies to be later transferred onto their less stable Fe(II) homologues.

A. FIRST STEP: HYDROGEN BONDS IN MONONUCLEAR Fe(II) COMPLEXES

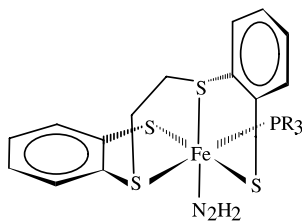
We investigated (82) two iron-sulfur complexes with diazene (diazene) as the sixth ligand, $[\text{Fe}(\text{N}_\text{H}\text{S}_4)(\text{N}_2\text{H}_2)] = \mathbf{1} (\text{N}_2\text{H}_2)$ and $[\text{Fe}(\text{S}_4)\text{PR}_3(\text{N}_2\text{H}_2)] = \mathbf{2} (\text{N}_2\text{H}_2)$ (Fig. 3).

Among these diazene complexes, the dinuclear analogue of $\mathbf{1}(\text{N}_2\text{H}_2)$, $[\mu\text{-N}_2\text{H}_2\{\text{Fe}(\text{N}_\text{H}\text{S}_4)\}_2]$, is the first example in which diazene binds to low-spin Fe(II) centers carrying only biological compatible donor atoms (see also Section IV.C).

We chose two model compounds which differ considerably in their coordination spheres (82) and, therefore, are supposed to react in qualitatively different ways. The ligand sphere of $\mathbf{1}(\text{N}_2\text{H}_2)$ consists of one chelate ligand with four in-plane sulfur atoms. Thus, two different sulfur functionalities are involved in the coordination of the Fe(II)



$[\text{Fe}(\text{N}_\text{H}\text{S}_4)(\text{N}_2\text{H}_2)]$
 $\mathbf{1}(\text{N}_2\text{H}_2)$



$[\text{Fe}(\text{S}_4)\text{PR}_3(\text{N}_2\text{H}_2)]$
 $\mathbf{2}(\text{N}_2\text{H}_2)$

FIG. 3. Two diazene model compounds, $\mathbf{1}(\text{N}_2\text{H}_2)$ and $\mathbf{2}(\text{N}_2\text{H}_2)$, which are expected to emulate a key intermediate in the biological nitrogen fixation problem.

center: two thiolate sulfurs and two thioether sulfurs. By contrast, in compound **2**(N₂H₂) the four sulfur atoms are in an orthogonal configuration, where one sulfur atom is on top of the plane spanned by the three other sulfur atoms, and the fifth ligand is a phosphine. But again, two sulfur atoms are connected via a bridge so that two thiolate sulfur atoms and two thioether sulfur atoms can be identified in the ligand sphere of the Fe(II) center. The phosphine ligands which yield stable *trans*-diazene compounds in the experiment are, e.g., PPr₃ and PBu₃. Assuming that these ligands can be replaced by PMe₃ without crucially changing the electronic structure of the complex, we adopted a simplified model for the sake of computational efficiency. For detailed structural data of these two complexes we refer to the original work (82).

In case of compound **1**(N₂H₂) we find the coordinated *trans*-diazene almost parallel to the axis containing the thiolate sulfurs, whereas the *cis*-diazene is aligned almost parallel to the axis connecting the thioether sulfurs, where the lone-pair repulsion between diazene-N and thioether-S is expected to be slightly weaker than the repulsion of diazene-N and thiolate-S lone pairs. We find similar alignment of the diazenes in compound **2**(N₂H₂), although in **2**(N₂H₂) the *cis*-diazene is rotated out of the alignment due to a repulsive interaction with the PMe₃ moiety. Two close sulfur–hydrogen distances give structural evidence for the existence of hydrogen bonds: For *trans*-**1**(N₂H₂) these are about 265 pm and 245 pm, and for *trans*-**2**(N₂H₂) they are about 253 pm and 260 pm.

For the *cis*-**1**(N₂H₂) structure we do not find hydrogen bonds on the basis of a distance criterion: The shortest sulfur–hydrogen distance is larger than 278 pm. We therefore do not expect to find quantitative evidence for hydrogen bonding in *cis*-**1**(N₂H₂). By contrast, *cis*-**2**(N₂H₂) contains a 258–268 pm hydrogen–sulfur distance (depending strongly on the quantum chemical method used) suggesting the existence of a hydrogen bond.

Table I shows hydrogen bond energies $E_{\text{HS}}^{\text{SEN}}$ as estimated from the shared-electron number (SEN) method (82) (see Appendix). We only attributed (82) a bond energy to those hydrogen–sulfur distances, for which the shared-electron number is larger than 0.005. We found that both *trans*-diazene compounds, *trans*-**1**(N₂H₂) and *trans*-**2**(N₂H₂), contain two hydrogen bonds. The energy of the long hydrogen bond is about 8–9 kJ/mol for *trans*-**1**(N₂H₂) and about 12 kJ/mol for *trans*-**2**(N₂H₂). Note that the dependence of these hydrogen bond energies on the density functional and on the basis set is surprisingly small. The dependence on the functional is slightly larger for the short

TABLE I

HYDROGEN BOND ENERGIES $E_{\text{HS}}^{\text{SEN}}$ FROM REF. (82) IN kJ/mol FOR GLOBAL MINIMA OF MODEL COMPOUNDS **1**(N₂H₂) AND **2**(N₂H₂) ESTIMATED FROM SHARED-ELECTRON NUMBERS (SEE APPENDIX)

Method	BP86/RI/TZVP		B3LYP/TZVP	
	σ_{HS}	$E_{\text{HS}}^{\text{SEN}}$	σ_{HS}	$E_{\text{HS}}^{\text{SEN}}$
<i>trans</i> - 1 (N ₂ H ₂)	0.0391	15	0.0385	20
	0.0200	7.6	0.0175	9.0
<i>trans</i> - 2 (N ₂ H ₂)	0.0203	7.7	0.0166	8.5
	0.0303	12	0.0204	11
<i>cis</i> - 2 (N ₂ H ₂)	0.0118	4.5	0.0092	4.7

hydrogen bond in *trans*-**1**(N₂H₂), for which we obtained 15–20 kJ/mol. For the short hydrogen bond in case of *trans*-**2**(N₂H₂) we got 8–10 kJ/mol. However, the distances between hydrogen and sulfur atoms are approximately the same for both hydrogen bridges in complex *trans*-**2**(N₂H₂) and, therefore, we find almost equal bond energies, whose small difference cannot be resolved by the SEN method.

For *cis*-**1**(N₂H₂) we did not find a hydrogen bond. By contrast, *cis*-**2**(N₂H₂) exhibits a weak one, whose energy is about 5 kJ/mol, as we would have expected in view of its relatively short H...S distance when compared with *cis*-**1**(N₂H₂).

Since in **1**(N₂H₂) and **2**(N₂H₂) the hydrogen bridges are essentially intramolecular, a supermolecular calculation of the hydrogen bond energy E_{HS} is not possible. We therefore determined an additional descriptor for the strength of the hydrogen bond by considering a rotation of *trans*-diazene, which breaks the hydrogen bridges present in the minimum structure. The corresponding energy curve is given in Fig. 4 for the rotation of *trans*-diazene in compound **1**(N₂H₂). Because of the different sulfur functionalities (thiolate and thioether), we find two minima where the *trans*-diazene is aligned along the thiolate axis and two maxima where it is found along the thioether axis. Since the interaction of the diazene with the sulfur atoms is attractive throughout, we take the difference of the maxima and minima of the rotation curve as a lower bound for the energy of the two hydrogen bridges present at the minimum structure.

We did not find shared-electron numbers larger than 0.005 in the 90° rotamer (82), where it is parallel to the thioether sulfurs, so we concluded that the residual attraction is below 5 kJ/mol. Indeed,

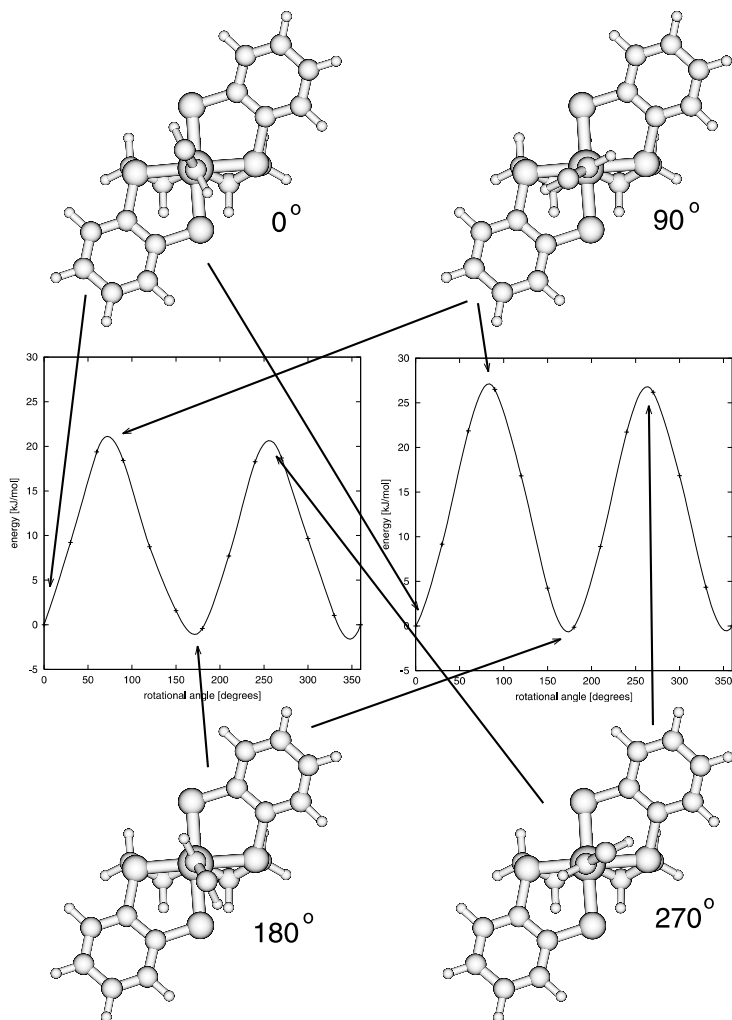


FIG. 4. Curve of rotation of *trans*-diazenide coordinated in complex 1(N₂H₂) using the BP86/RI (left) and B3LYP (right) methods (TZVP basis set). The zero point of rotational energy is fixed arbitrarily. Note that the hydrogen atoms are not aligned with the S–Fe–S axes since they always point into the direction of the sulfurs' lone pairs.

we found (82) a value for E_{HS} of 26 kJ/mol in the case of the B3LYP functional, and 20 kJ/mol for the BP86/RI functional, in very good agreement with the corresponding $E_{\text{HS}}^{\text{SEN}}$ values of 29 kJ/mol and 23 kJ/mol, respectively.

For a discussion of the complicated rotational energy curve of *trans*-diazene in complex **2**(N₂H₂), the reader is referred to the original publication (82).

B. DIFFERENT STABILIZATION EFFECTS IN COORDINATED *cis*- AND *trans*-diazene

We find that *cis*-diazene is more strongly bound in both model complexes than *trans*-diazene. This is apparent in view of the Fe–N bond distances: For **1**(N₂H₂) we find a about 4 pm shorter Fe–N distance for the *cis*-isomer when compared with the *trans*-form, while this distance is 2–3 pm shorter in *cis*-**2**(N₂H₂) than in *trans*-**2**(N₂H₂).

Focusing on the B3LYP/TZVP results, we found that the N₂H₂ isomerization energy is increased by 10 kJ/mol in complex **1**(N₂H₂) and does not change appreciably in the case of complex **2**(N₂H₂) as compared to the uncoordinated diazene isomers (82).

The 10 kJ/mol difference in complex **1**(N₂H₂) is due to two effects: First, *trans*-diazene forms hydrogen bonds, which tend to increase the isomerization energy by $E_{\text{HS}}^{\text{SEN}} = 30$ kJ/mol. Second, *cis*-diazene does not form hydrogen bonds, but is bound more strongly to the [Fe(N_HS₄)] fragment. To yield consistent energetics for the coordination process of the diazene isomers, we can attribute 20 kJ/mol to this additional stabilization of *cis*-diazene.

Figure 5 depicts the different stabilization effects when the diazene isomers bind to the complex fragment **1** (a similar scheme for **2**(N₂H₂) can be found in Ref. (82)). The 20 kJ/mol increase in coordination energy of *cis*- as compared to *trans*-diazene is also consistent with an essentially unchanged isomerization energy for **2**(N₂H₂), where we take into account a contribution of $E_{\text{HS}}^{\text{SEN}} = 20$ kJ/mol for the hydrogen bonds in the *trans*-diazene complex, which is therefore stabilized by the same amount of energy like the *cis*-diazene yielding in total an unchanged isomerization energy.

To conclude from the results, which are in detail given in Ref. (82), we have determined values based on shared-electron numbers for the two hydrogen bridges in *trans*-**1**(N₂H₂) and *trans*-**2**(N₂H₂). Depending on the functional, we obtained for *trans*-**1**(N₂H₂) 8–9 kJ/mol for the long and 15–20 kJ/mol for the short hydrogen bond (thus, about 25–30 kJ/mol for both bridges). For *trans*-**2**(N₂H₂) we got 8–9 kJ/mol for the short and 11–12 kJ/mol for the long hydrogen bond (i.e., about 20 kJ/mol for both bridges). By an independent supermolecular method, namely a rotation curve of *trans*-diazene in **1**(N₂H₂), we obtained a

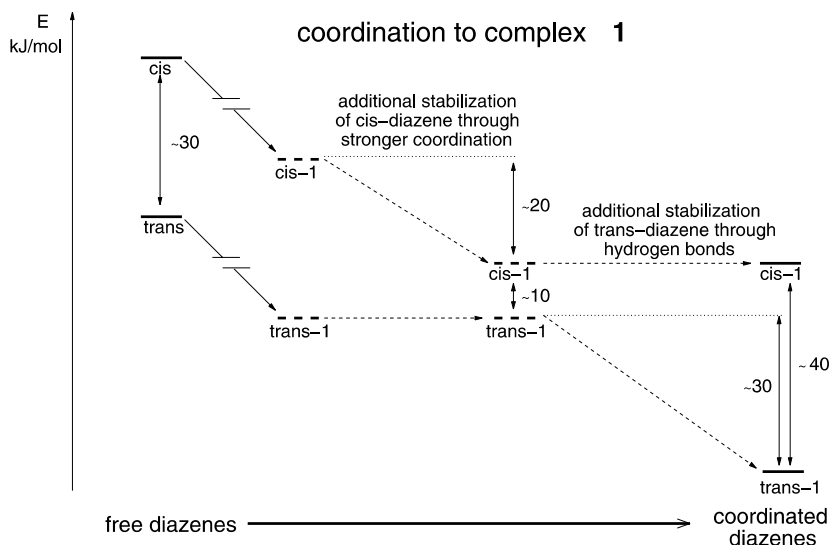


FIG. 5. Relative energetics of the coordination process of *cis*- and *trans*-diazene to complex fragment 1(N_2H_2) starting with the uncoordinated isomers (left). We shift the center of energy due to coordination by the pure *trans*-diazene-Fe binding energy in step one. The next step shows the additional stabilization of *cis*-diazene by about 20 kJ/mol followed by the increase in stabilization energy of the *trans*-isomer due to hydrogen bond interaction yielding, on the right hand side, the final situation in complexes 1(N_2H_2).

lower bond energy of 20–26 kJ/mol, in very good agreement with the SEN result.

For the two model compounds we found that both *trans*-complexes possess two relatively strong hydrogen-sulfur bonds. They are of different strength in 1(N_2H_2), but of similar strength in 2(N_2H_2). The hydrogen bond strength can be modulated through the hydrogen-sulfur distance, which itself is determined through the ligand sphere, provided that the hydrogen atom points in the direction of a sulfur's lone pair. In particular, for H-S distances which are larger than 270 pm we did not find significant hydrogen bonding in complexes 1(N_2H_2) and 2(N_2H_2).

C. HYDROGEN BONDING IN DINUCLEAR COMPLEXES

Coming back to the strength of hydrogen bonding in the more complicated dinuclear complexes, we note that our dinuclear Sellmann-type metal diazene complexes were chosen closely following the lines

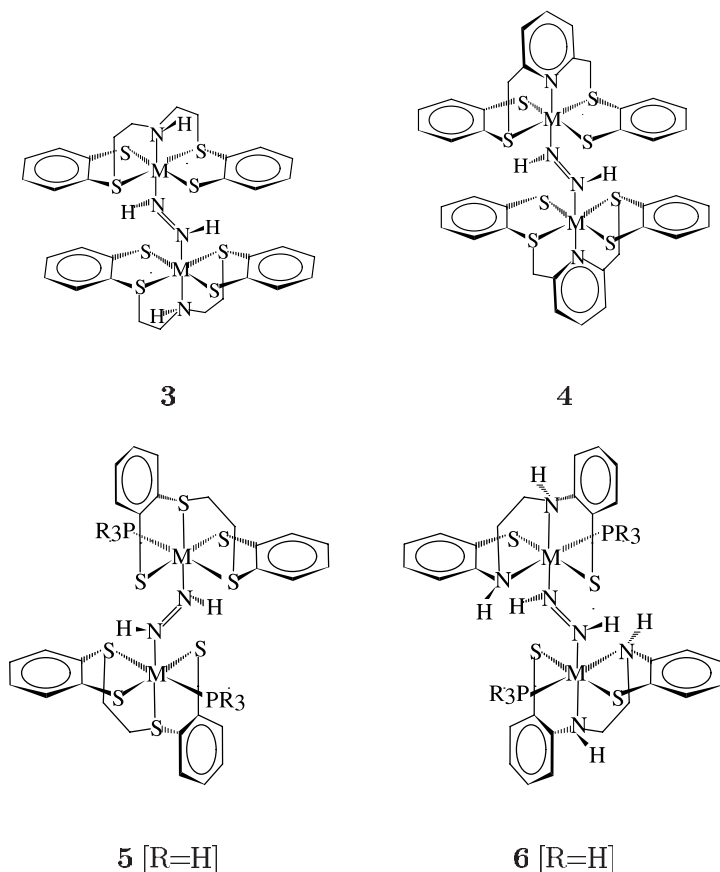


FIG. 6. Lewis structures of dinuclear diazene compounds with M=Fe(II), Fe(III), Ru(II).

of synthetic work on these compounds (64,67–71,83). Their Lewis structures are shown in Fig. 6.

It should be mentioned that such diazene complexes can form different diastereomers; we studied (81) the representatives depicted in Fig. 6. All dinuclear complexes contain a *trans*-diazene bridging two enantiomeric mononuclear fragments arranged to give C_i symmetry for the dinuclear compound. The optimized structures of all complexes are shown and compared with experiment (where applicable) in Fig. 7. Since the metal centers are well separated by the comparatively large [N₂]-bridge, we can expect that a possible spin coupling between the two metal centers is quenched to a large extent.

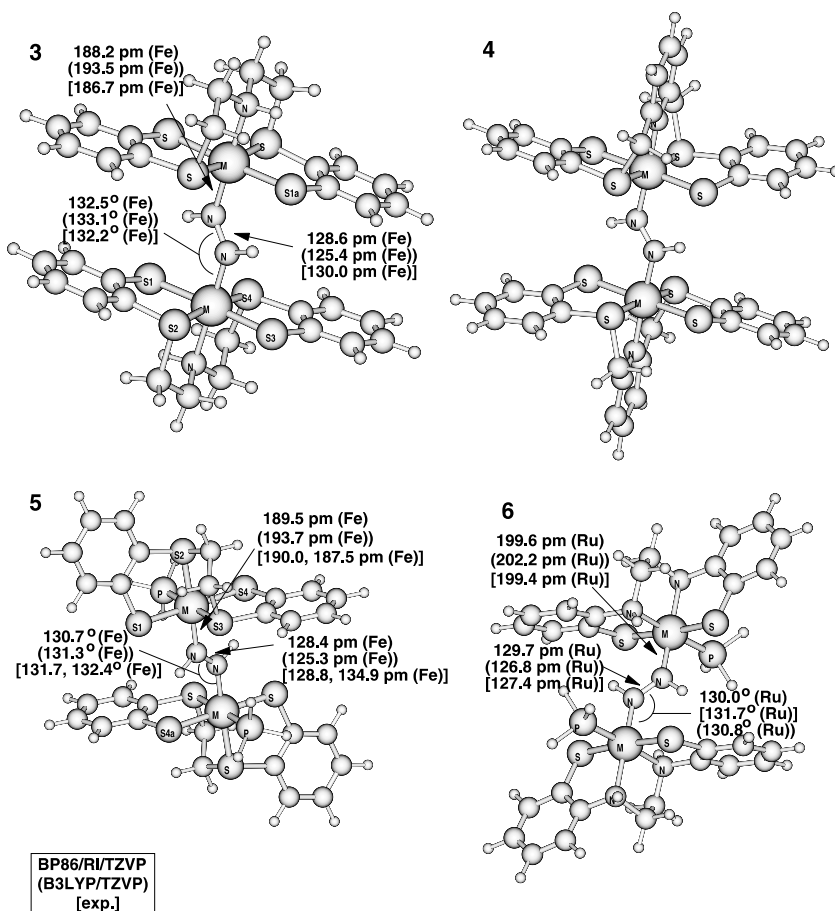


FIG. 7. Optimized structures of complexes **3–6** [C_i point group symmetry, $M=\text{Fe,Ru}$]. Structural data are given for two Fe(II) complexes for which experimental data are available for comparison, i.e., for Fe(II)—**3** ([67,68](#)), Fe(II)—**5** (with PPr_3 [1st exp. value] and PEt_3 [2nd exp. value] phosphines) ([70](#)) and for Ru(II)—**6** (with Me instead of H at the chelate-ammine group) ([112](#)).

In our study of the dinuclear systems ([81](#)), we found in most cases that bond angles calculated with BP86/RI and B3LYP are almost identical and differ by less than 2° from one another. Apart from the α_{FeNH} and α_{NNH} angles in Fe(II)—**3**, all angles are in very good agreement with the angles found experimentally. As far as bond lengths are concerned, the BP86/RI/TZVP distances are closer to experiment

than those obtained with the B3LYP functional. The BP86/RI bond distances differ by about 2–3 pm from the experimental values, while the B3LYP lengths are always up to 7 pm larger than the experimental ones. The differences of the calculated and measured S–H and N–H distances deviate from these general results, which is due to the fact that they are neither by experiment nor in a quantum chemical way easy to determine since the potential energy well of the hydrogen bond is rather shallow.

The *trans*-diazene moiety is always oriented parallel to the thiolate sulfur atoms of the chelate ligands. Complexes **3** and **4** as well as **5** and **6** are similar with respect to the arrangement of benzene rings. The arrangement of two benzene rings within one mononuclear half of these complexes determines the sterical direction of the sulfur lone pairs (as discussed above for the mononuclear analogues) and is consequently a means for controlling hydrogen bonding.

Because of the rigid chelate ligands, the structures of complexes **3** to **6** in their dicationic form are very similar to their uncharged form. Therefore, reducing the Fe(III) to Fe(II) complexes does not lead to large changes in the overall structures. However, large changes can be found for the H···S distances, which is important for the corresponding change in hydrogen bond energies.

The total hydrogen bond energies $E_{\text{HS}}^{\text{SEN}}$ range from 22 to 53 kJ/mol (B3LYP/TZVP). The Fe(II) complexes exhibit the largest total hydrogen bond energies.

Since every hydrogen atom of *trans*-diazene can belong to a short and a long hydrogen bridge simultaneously, in such a way that a bifurcated structure develops, the question arises whether the total energy of this bifurcated structure can be calculated by adding the energies of a short and a long hydrogen bond. To answer this question we compare the B3LYP/TZVP data for the dinuclear Fe(II) complex **3** with data obtained for its mononuclear analogue **1** (see [Section IV.A](#)), which is 29 kJ/mol for one short plus one long hydrogen bond. We find that for **3** the total hydrogen bond energy (46 kJ/mol) is 12 kJ/mol smaller than the doubled value found for the mononuclear analogue (2×29 kJ/mol) indicating that the strength of the individual hydrogen bonds is considerably decreased in the bifurcated hydrogen bridges. Bifurcated hydrogen bonds are only found in dinuclear complexes **3** and **4** with Fe(II) centers. All other complexes contain only two non-bifurcated hydrogen–sulfur bonds. For **3** with Fe(II) a total hydrogen bond energy of 70 kJ/mol has been estimated on empirical grounds ([67,68](#)). The result is in fair agreement with the

SEN value $E_{\text{HS}}^{\text{SEN}}$ of 46 kJ/mol for the total hydrogen bond energy in Fe(II)—**3**.

The complexes with Fe(II) centers exhibit stronger hydrogen bonds than their Fe(III) analogues. This is an important observation with respect to the mechanism proposed in Fig. 2. The protonation of the thiolate donors in **A** of Fig. 2 yields the dicationic species **B**. A consecutive intramolecular proton and electron transfer onto molecular nitrogen bridging the two metal centers yields intermediate **C**. The reduction of structure **C** to **D** would then stabilize the created diazene through an increase in hydrogen bond strength.

While the hydrogen bonds could stabilize dinuclear Fe(II) complexes by more than 20%, this effect is strongly reduced in Ru(II) compounds, where the binding energy of diazene to Ru(II) itself is comparatively large.

Fine tuning of the hydrogen bond energy can be achieved by changing the hydrogen–sulfur distances. The $\text{H}\cdots\text{S}$ distances vary when different chelate ligands (penta- vs. tetra-dentate) coordinate the metals, when iron is replaced by ruthenium or when the formal oxidation state and/or the spin states of the metal centers change. In the light of such large contributions of hydrogen bonding to the stabilization of N_2H_x species the role of hydrogen bonding can hardly be overestimated during a reduction from molecular nitrogen to ammonia.

V. Reaction Energetics of the Reduction at Mononuclear Fe(II) Centers

For the investigation of the reaction energetics of Sellmann-type complexes we chose the mononuclear complexes **2(L)** depicted in Fig. 3 (84), which were experimentally investigated with various metal centers such as Fe, Ni, Mo (85–87), and mainly with Ru (78,79,87–89). While ammonia and hydrazine complexes are comparatively easy to obtain, the most unstable complexes to be considered are the diazene and particularly the dinitrogen complexes. For this reason, the **2(N₂)** complex is not known and the diazene complex is a *dinuclear* species $[\text{2}]_2\text{N}_2\text{H}_2$ (70–71). We investigated mononuclear complexes in order to analyze the binding modes and energetics of the nitrogen species to a single iron center (84). This can be understood as the first step towards an understanding of the binding energetics in the corresponding dinuclear complexes.

A. MULTIPLICITIES OF THE GROUNDS STATES

For reasonable reaction energetics of any kind of mechanism involving first-row transition metal atoms it is mandatory to find the correct multiplicity of the ground state. Neither the standard pure density functional BP86/RI nor the standard hybrid density functional B3LYP are able to reliably predict the ground state multiplicity of the dinuclear Sellmann-type iron-sulfur complexes so that accurate coordination energies could not be calculated (81). These problems can be overcome by using the B3LYP* functional (90). This reparametrized B3LYP functional was especially developed for the accurate description of Sellmann-type Fe(II) complexes, but it turned out to be an improvement of general applicability (see notes in the [Appendix](#)).

B. END-ON VERSUS SIDE-ON BINDING OF N₂

The first step in any nitrogen reduction process is the binding and activation of dinitrogen by metal centers. Apart from the two idealized coordination modes, end-on and side-on binding, others in between have also been observed (92). If “strong activation” occurs, side-on binding becomes important. But even in the case of the so-called “weak activation” of dinitrogen, where the N–N bond distance is very similar to the bond length in the free diatomic molecule, side-on binding also needs to be considered as a possible coordination mode (91,92).

For the *monometallic* complex 2(N₂) we found (84) that the dinitrogen molecule binds end-on, while N₂ dissociates from the complex fragment when forced to bind side-on. The N–N bond distance of 112.8 pm and the harmonic vibrational wavenumber 2134 cm^{−1} indicate only very weak activation by the metal complex fragment (BP86/RI/TZVP; compared with 110.4 pm and 2361 cm^{−1} for free N₂). For the Sellmann-type complexes 1(N₂) we found a large energetical stabilization of end-on over side-on binding; the stabilization energy (0 K without zero-point vibrational energy (ZPE) correction) was estimated to be more than 100 kJ/mol (BP86) though the B3LYP functional shows dissociation of the side-on structure (independent of the basis set chosen). We have concluded that the side-on binding mode is not likely to occur in the corresponding *dinuclear* Sellmann-type complexes because the end-on coordination mode is

energetically much more favorable for the mononuclear complexes investigated (84).

C. DIAZENE ISOMERS

We analyzed (84) how different isomers of N_2H_2 are stabilized by the five-coordinate metal fragment **2**. For mononuclear molybdenum and tungsten complexes, an important role has been attributed to asymmetric reduction products of which the NNH_2 species is an example (16,93,94). This view is based on earlier suggestions (95), where the generation of a single NH_3 molecule has been considered as an important intermediate step in the reduction process. A nitrido complex remains and releases the second NH_3 upon protonation and reduction. These nitrido complexes are well known for molybdenum as the coordinating metal (96,97).

The three diazene isomers are all stabilized significantly upon coordination to Fe by the direct coordination energy as well as by hydrogen bonding. They should all be taken into account as possible stable intermediates in the FeMoco mechanism. Different open FeMoco structures could favor different isomers; while *trans*-diazene needs a larger Fe–Fe distance than *cis*-diazene, *cis*-diazene, and especially NNH_2 will become important if FeMoco opens only little.

Isomerization mechanisms of isolated *trans*- to *cis*-diazene were studied and transition states for two possible interconversion routes were found to be more than 200 kJ/mol unstable than *trans*-diazene (98). The relative stability of *trans*- to *cis*-diazene was calculated to be 21 to 29 kJ/mol using different quantum chemical methods and basis sets [see Ref. (98) and references cited therein]. The NNH_2 isomer is about 87 kJ/mol (almost independent of the density functional) higher in energy than *trans*-diazene.

The energy difference of coordinated *cis*-diazene and *trans*-diazene is almost the same as for the free molecules. This has already been discussed above as a cancellation of stronger coordination of *cis*-diazene versus lone-pair–lone-pair repulsion. The picture changes for NNH_2 upon coordination to metal fragment **2**. **2**(NNH_2) is 43.4 kJ/mol (B3LYP*) higher in energy than *trans*-**2**(N_2H_2) and thus by more than 40 kJ/mol more stabilized than *trans*-diazene upon coordination.

While *cis*-diazene and NNH_2 need not be considered for symmetry reasons in dinuclear Sellmann-type complexes, they both can become important intermediates for open structures of FeMoco.

D. LIGAND BINDING ENERGIES

The ligand binding energies, which were given for all ligands in Ref. (84), and which refer to the following reaction,



allowed us to draw conclusions on the role of the single iron center during ligand reduction (84). Our discussion was based on $\Delta D_0 = \Delta E_{\text{CP, B3LYP}^*} + \Delta \text{ZPE}$ values with counter-poise corrected electronic energies from B3LYP* calculations and ZPEs from BP86/RI vibrational analyses. The corresponding ΔH values turned out to hardly differ from these data but contain additional assumptions for the inclusion of temperature effects (84). Furthermore, the accuracy of ΔG values from standard quantum chemical calculations is rather low for reactions, which involve different numbers of reactant and product molecules because they suffer from the rough estimation of vibrational, translational, and rotational entropies; for all reactions studied here, one would have to add a value of about +50 kJ/mol to the ΔH values stemming from the entropic contribution as estimated in the standard quantum chemical procedure [see the discussion in Ref. (84)].

N_2 is stabilized by only 11.9 kJ/mol upon coordination to the metal fragment. This electronic stabilization effect is quenched by the zero-point vibrational level differences of 10.8 kJ/mol and becomes unfavorable in view of the reverse entropic effect. *trans*-Diazene experiences the largest stabilization by -60.3 kJ/mol, while the σ -donating ligands are weakly bound.

Complex **2** thus fulfills two important criteria of a nitrogenase model complex: (i) the unstable diazene ligand is significantly stabilized electronically by -73.1 kJ/mol (which reduces to -60.3 kJ/mol upon inclusion of the ZPE) and (ii) the ammonia ligand may easily dissociate in order to recover the "catalyst". However, even if the first two-proton-two-electron reduction step is assumed to be very fast, the binding of N_2 is too weak. Thus, strategies need to be developed to increase the absolute value of the N_2 coordination energy by variation of the chelate ligand.

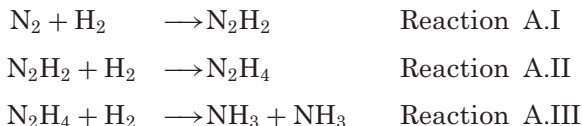
The total *electronic* coordination energy of *trans*-diazene is -73.1 kJ/mol including the estimated total hydrogen bond energy of (-)20 kJ/mol for the mononuclear complex *trans*-**2**(N_2H_2) (see above). Thus, the stabilization of the unstable diazene ligand by hydrogen

bonds is 27% of the total coordination energy in the case of *trans*-**2**(N₂H₂).

E. ANALYSIS OF THE CATALYTIC POTENTIAL

Following these exploratory investigations, we were then able to analyze the hypothetical catalytic cycle of the mononuclear Sellmann-type complex **2** (84). We should emphasize that all energies discussed here are $\Delta D_0 = \Delta E_{\text{CP, B3LYP}^*} + \Delta \text{ZPE}$ energies for reasons explicated in the previous section. Moreover, we compare energies of minimum structures on the potential energy hypersurface. The discussion thus reflects the thermodynamic situation rather than the kinetic details of each reaction step, which would require an analysis of barrier heights.

Since we were aiming at an energy scheme that shows whether the monometallic model compound is able to function as a catalyst we compared the energetics of the uncoordinated ligands with the same reactions at the iron center of the metal fragment **2**. For the metal-free reaction it is straightforward to define the following three reduction steps where one hydrogen molecule is added at a time to model the two-proton–two-electron reductions:



The energetics of these three reactions have been studied very recently in great detail by Sekusak and Frenking (99). The overall reduction energy $\Delta D_{0,\text{tot}} = \sum_i \Delta D_{0,i}$ is -79.5 kJ/mol at 0 K ($i \in \{\text{A.I} - \text{A.III}\}$). It is instructive to give all energies with respect to a common energy reference level. This is done in Fig. 8, where the energy of one dinitrogen and three hydrogen molecules is taken as the reference point of energy. Figure 8 shows that the first reduction step is thermodynamically the most difficult one, while it is likely that the following reductions to hydrazine and ammonia can be more easily achieved once diazene is produced.

In the case of the metal fragment we have to consider two additional reactions, namely the coordination of N₂ and the abstraction

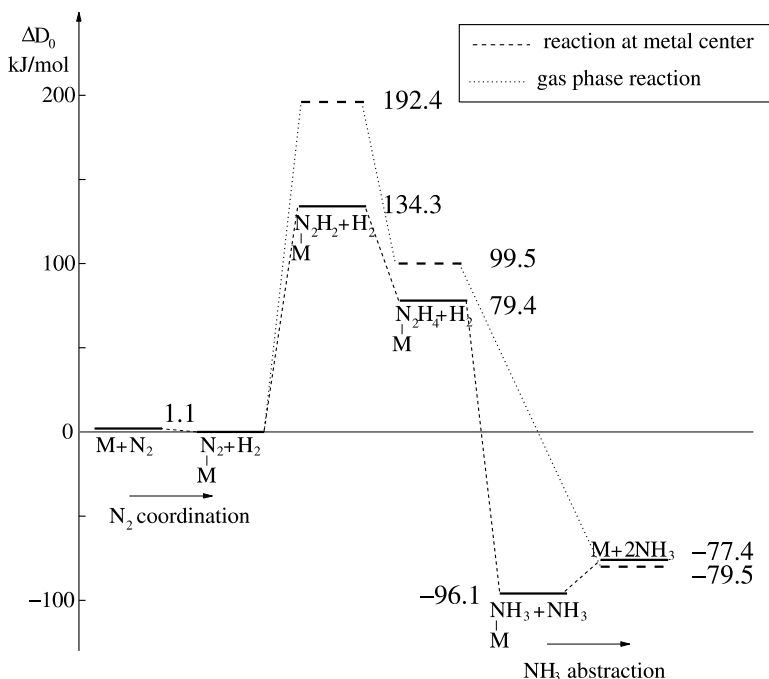
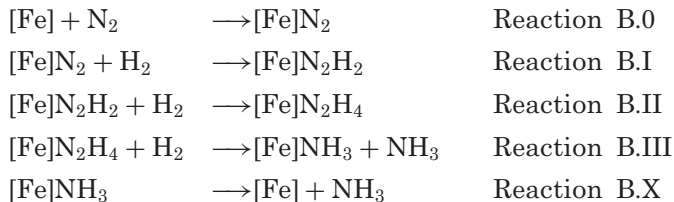


FIG. 8. Energetics of dinitrogen reduction with the mononuclear catalyst **2** (solid lines). The energy D_0 of N_2 bound to **2** and three unbound H_2 molecules has been chosen as the zero-energy reference point $\Delta D_0 = \Delta E_{CP, B3LYP^*} + \Delta ZPE$. Note that the non-reacting H_2 molecules (e.g., two H_2 molecules at the $N_2 + H_2$ step) are not mentioned explicitly. The energetics of dinitrogen reduction without the catalyst are depicted for comparison (dotted lines). Here, the D_0 energy of N_2 and three H_2 has been chosen as the energy reference point.

of NH_3 , which are denoted as B.0 and B.X in the following sequence of reactions:



Apart from the weak coordination of N_2 , which we have discussed already in the preceding section, we find a remarkable energy reduction of the most important first endothermic reduction step from 192.4 kJ/mol to 134.3 kJ/mol. If N_2 can be bound and transformed to N_2H_2 , which is considerably stabilized by the mononuclear complex **2**, the reduction process is straightforward. The production of hydrazine and ammonia is exothermic by -54.9 kJ/mol and -175.5 kJ/mol, respectively. Note that the reduction step **B.II** is less favored by 38 kJ/mol if the iron center is present, which has its origin in the better stabilization of diazene when compared with hydrazine, while reactions **A.III** and **B.III** are equal in energy. This energetical equivalence of these third reduction steps, which involves the formation of two N–H bonds and breaking of the H–H and N–N bonds, indicates that the Fe center, whose primary role is the fixation of the hydrazine reactant, does not affect the thermodynamics of the N–N bond breaking. Frenking and co-workers found similar energetics for the same reduction process mediated by $[(\text{CO})_4\text{Fe}]$ metal fragments (36). For our discussion here, it is important to note that reaction energies are similar while the ligands are bound much more strongly. The overall energy change $\Delta D_{0,\text{tot}} = \sum_i \Delta D_{0,i}$ is -77.4 kJ/mol ($i \in \{\text{B.0, B.I – III, B.X}\}$), which is, of course, equal to the metal-free reduction process (the small difference of 2.1 kJ/mol comes mainly from errors in the numerical vibrational analyses).

We gave the reaction energetics of the complex reaction from the viewpoint of a single energy as the center of reference. In order to obtain the corresponding plot to the metal-free reaction we chose the energy of the five-coordinate metal fragment with bound dinitrogen and three hydrogen molecules as the reference energy level, see Fig. 8.

Figure 8 shows that the (thermodynamic) “barriers” of the stable intermediates are quenched to a certain degree, while at the same time the ammonia coordination is not too strong. An optimum catalyst would quench all transition state barriers, which are not taken into account here, and all energies of high-energy intermediates to give a flat potential energy surface. At the same time, the product (ammonia) must not be bound too strongly in order to be able to recover the catalyst. Note that complex fragment **2** also possesses features which are important for low transition-state barriers, namely, the possibility to protonate sulfur atoms, which brings protons close to the N_2 species.

F. COORDINATING N_2 TO MONONUCLEAR $Fe(II)$ COMPLEXES: THE ROLE OF SPIN BARRIERS

We have seen in [Section V.D.](#) that N_2 is only weakly coordinated by complex **2**. A closer look reveals that dinitrogen is strongly bound (by up to 100 kJ/mol) to singlet states of Sellmann-type metal fragments ([100](#)). The ground state of the metal fragment is, however, often high-spin and the energy gain upon spin flip is of the order of the N_2 binding energy; a detailed investigation is currently under way ([100](#)).

Binding N_2 to high-spin $Fe(II)$ -S metal fragments thus involves a kinetic activation barrier, which must be overcome in order to bind N_2 . This is illustrated in [Fig. 9](#), which shows preliminary B3LYP*/TZVP

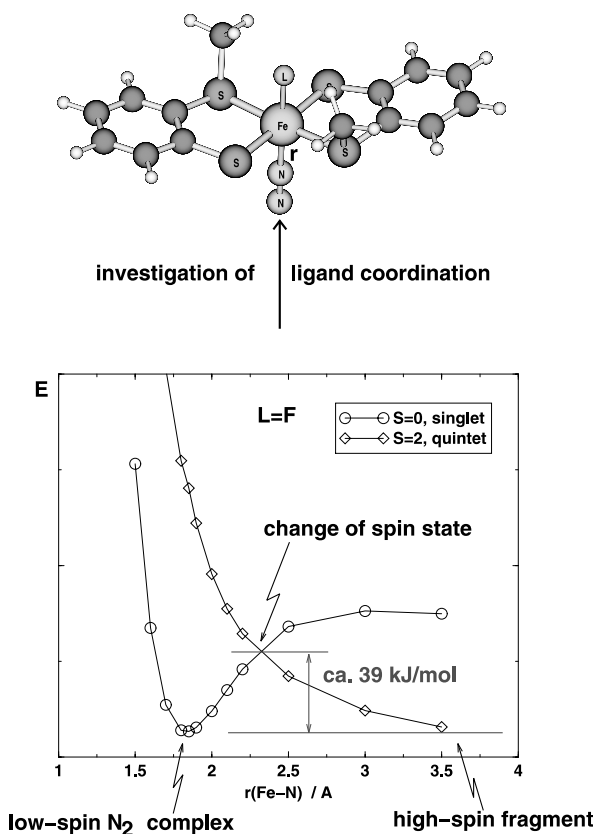


FIG. 9. Coordination of N_2 to a $Fe(II)$ -S model system with a fluorine ligand in *trans*-position requires overcoming a spin barrier.

results for a model system with fluorine as the sixth ligand in the *trans*-position (various other ligands in the *trans*-position were also investigated). Note that the high-spin potential energy surface is repulsive and does not bind N_2 . A barrier height of about 39 kJ/mol for this model complex might tempt one to estimate a rate constant, which facilitates dissociation though it must also be taken into account that switching from one potential energy surface to another one with different spin will depend on the strength of spin-orbit coupling.

Coordination of N_2 to a complex with similar electronic features as the one in Fig. 9 is kinetically not favored because of the spin barrier. However, a single N_2 complex would be metastable since it would be protected by the same barrier.

VI. Photoisomerization of Coordinated Diazene

The dinuclear diazene-coordinating complex $[\{\text{Fe}'\text{S}'_4(\text{PR}_3)_2(\text{N}_2\text{H}_2)\}]$ **5** (70) in Fig. 6 with $[\text{S}'_4]^{2-} = 1,2\text{-bis}(2\text{-mercaptophenylthio})\text{ethane}(2-)$ and $\text{R}=\text{Pr}$ is an example from the very small number of diazene complexes with biologically compatible ligands containing sulfur atoms in the first ligand sphere of the iron center (cf. Section IV.C). The electronic and vibrational properties of this complex have been studied experimentally by resonance Raman methods. A splitting of lines, which occurred only in the resonance Raman spectrum but not in the infrared spectrum, has been observed which was attributed to a suggested photoisomerization process depicted in Fig. 10 (101, 102).

The potential photoisomerization process can be of significant importance to the nitrogen fixation problem as a possible rearrangement mechanism for the conversion of **5(A)** to **5(B)** might involve abstraction of the “H” atoms. These “H” atoms can be accepted by the sulfur atoms in the ligand sphere acting as Lewis bases, in such a way that a linear “ N_2 ” species could be generated within the complex. This “symmetric” transition state, which would represent an intermediate for the reduction of dinitrogen to diazene by a dinuclear complex like **5**, could switch back to the reactant as well as to the product **5(B)**. An alternative pathway by rotation of the metal fragments coordinating to the diazene moiety would require that large rotational barriers need to be overcome. These barriers are generated by strong hydrogen bonds, which must be broken in order to allow free rotation of the metal fragments. However, the photoisomerization

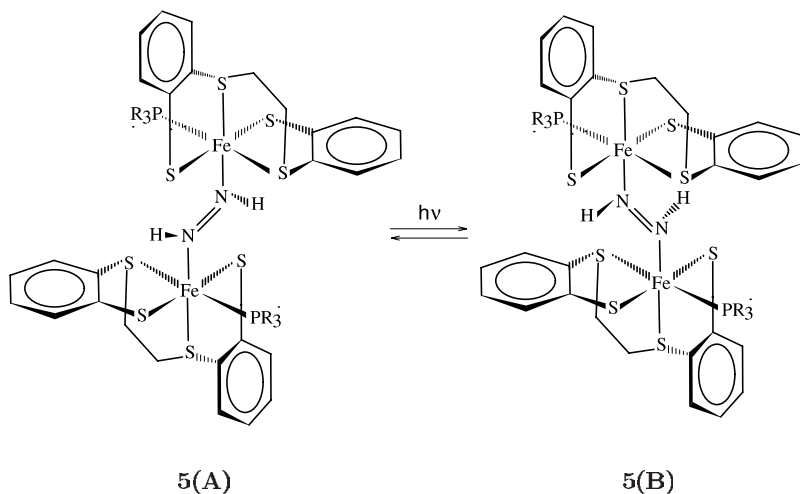


FIG. 10. Lewis structures of two possible isomers, **5(A)** and **5(B)**, which are involved in a postulated photoisomerization reaction of $[\{\text{Fe}^{\text{S}_4'}(\text{PR}_3)_2(\text{N}_2\text{H}_2)\}(\text{S}_4'^{2-} = 1,2\text{-bis}(2\text{-mercaptophenylthio})\text{ethane}(2-); \text{R} = \text{Pr})]$.

occurs in the solid state at low temperatures, which does not favor extended spatial rearrangement of the dinuclear complex.

We demonstrated how the photoisomerization hypothesis can be supported by accurate quantum chemical calculations (103). The experimental infrared and resonance Raman study of complex **5** led to the first determination of normal modes and force constants of diazene coordinated to a metal fragment. Isotope substitution yielding ^{15}N - and ^2H -isotopomers permitted the assignment of diazene normal modes in the experimental spectrum. Moreover, the spectra of these three isotopomers indicated that a laser-induced photoisomerization occurred in the Raman sample. However, a detailed assignment of the split bands was not possible in the experiment.

In order to investigate the photoisomerization hypothesis we started with the two possible candidates, whose Lewis structures are given in Fig. 10. Structure optimization yielded the structures depicted in Fig. 11.

The accuracy of the harmonic BP86/RI/TZVP force field (104) permitted that all bands, which split upon photoisomerization, could be assigned to the two possible isomers **5(A)** and **5(B)**. The accuracy of the harmonic wavenumbers is, in general, better than 6 cm^{-1} for these bands (with the exception of 12 cm^{-1} for the mode at 1270 cm^{-1}).

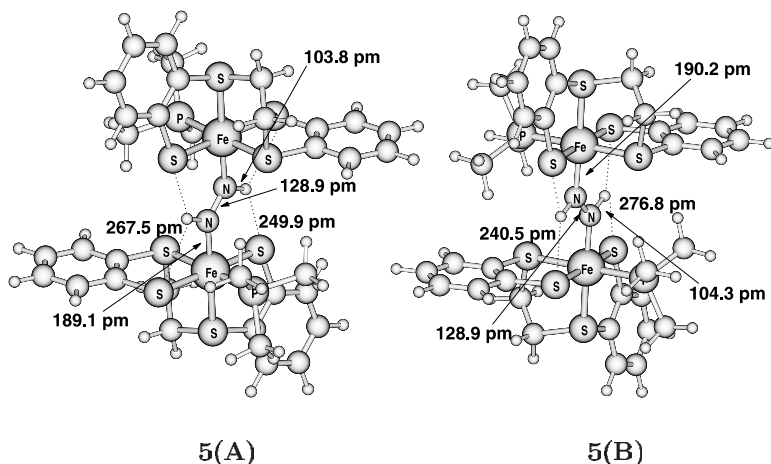


FIG. 11. BP86/RI/TZVP optimized structures of the two isomers **5(A)** and **5(B)** with R=Me. S...N-H, N-N, and Fe-N bond distances.

The calculated modes at 1282, 1296, and 1306 cm^{-1} represent motions of the diazene moiety. The assignment of these vibrations in (101) as overtones of the modes at about 650 cm^{-1} , which was confirmed by the experimental spectra of the isotopomers, was well reproduced by the calculations (103), in which we used the harmonic oscillator model as a zeroth-order approximation for the estimation of the overtone wavenumbers.

The peaks at 663 cm^{-1} and 1455 cm^{-1} belong to isomer **5(A)**, while the peaks at 637 cm^{-1} and 1509 cm^{-1} belong to isomer **5(B)**. The N-N stretch vibration splits only by a very small amount so that two peaks cannot be resolved by the experimental spectrum and only a single band appears at 1365 cm^{-1} .

The calculated isotope shifts were in very good agreement with the experimental ones (103). Only for modes at wavenumbers 1455 cm^{-1} and 1509 cm^{-1} we found (103) larger deviations from the experimental assignment. If, however, we assume that the assignment in (102) for these two modes is exchanged, we get -318 cm^{-1} and -331 cm^{-1} for the experimental spectrum, which compare well with the calculated wavenumbers of -330 cm^{-1} and -346 cm^{-1} . The calculated D isotope shift $\delta\tilde{\nu}(D)$ for peaks above 3100 cm^{-1} could not be identified unambiguously as the corresponding bands are largely shifted and the N-H stretching modes couple with C-H vibrations in the chelate and phosphine ligands.

The different vibrational properties of the coordinated diazene moiety in both isomeric complexes may be explained in terms of different hydrogen bond strengths in **5(A)** and **5(B)**. Again, the SEN method can be used for the estimation of the hydrogen bond energies in both isomers (103). The effect of hydrogen bonding is most prominent for those modes where N–H motions are involved. The modes at 663 cm^{-1} and 637 cm^{-1} also involve the motion of the N–N unit so that the change in electronic energy is not only governed by the change in hydrogen bonding. The other modes at 1455 cm^{-1} and 1509 cm^{-1} involve mainly the motion of the hydrogen atoms of the diazene moiety. Consequently, the hydrogen bonds corresponding to the larger wavenumber 1509 cm^{-1} are the strongest with a SEN energy of 19.3 kJ/mol each for the short $\text{H}\cdots\text{S}$ contacts.

We thus found additional evidence for the potential photoisomerization process, which converts **5(A)** to **5(B)**, since the line splitting observed in experiments can be well understood in terms of the calculated vibrational spectra of the two isomers. The mechanism of the photoisomerization reaction remains, however, unsolved and needs to be investigated in further quantum chemical studies as it could shed light on the reduction of dinitrogen to diazene. The mechanism will be of importance to the protonation of inert molecular nitrogen in the biological nitrogen fixation process if the H abstraction from the diazene moiety generating a linear “ N_2 ” subunit is in favor of a large structural rearrangement of the whole complex by rotation.

A. SECONDARY EFFECTS THROUGH CHELATE LIGAND MODIFICATION

In order to investigate the effect of substituents in the second ligand sphere, we optimized (105) the structures of the two isomers of complex $[\{\text{Fe}'\text{S}_4'(\text{PMe}_3)\}_2(\text{N}_2\text{H}_2)]$ (**7**) in Fig. 12 with ‘ S_4' ’ = 1,2-bis(2-mercaptophenylthio)phenylene(2–), which has also been synthesized (with PPr_3 as the phosphine ligands (106, 107). In **7** the two ethylene bridges of **5** are replaced by two phenylene bridges (indicated by two ovals in **7(A)**).

In contrast with complex **5**, the two isomers **7(A)** and **7(B)** have been isolated and their structure could be characterized by X-ray analyses (106,107). A comparison of the experimental structures and our BP86/RI/TZVP optimized structures, which are in very good agreement, was given in Ref. (105). Since vibrational spectra are not yet available for complex **7**, a photoisomerization process as

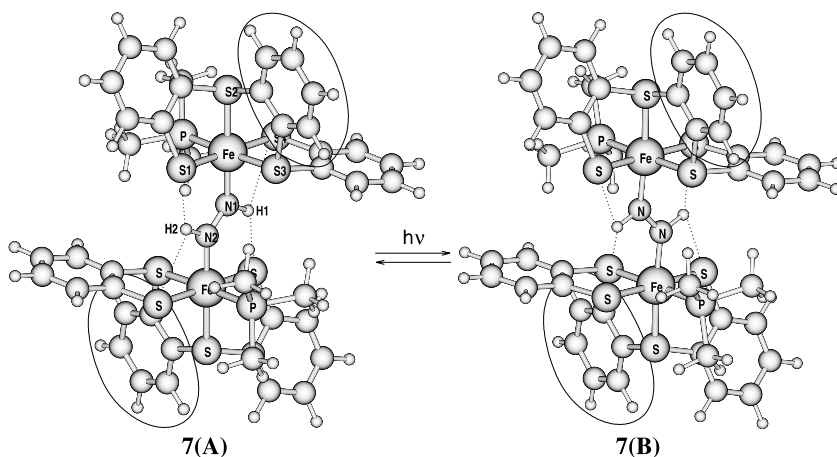


FIG. 12. BP86/RI/TZVP optimized structures of two isomers **7(A)** and **7(B)** with $R=Me$, which may be involved in a similar photoisomerization reaction like complex **5**. The two ovals indicate the structural differences of **7** when compared with **5**.

observed in the resonance Raman spectrum of **5** has not yet been detected. We carried out calculations of the Raman and infrared vibrational spectra of **7** (105).

While the ethylene bridge is in a staggered conformation, the rigid benzene ring forces the two sulfur atoms bound to this ring into the plane of the benzene carbon atoms.

As one would expect, the introduction of the two phenylene bridges has almost no (primary) effect on the bond lengths of the diazene ligand: the N–H bond lengths are 103.8 pm in **5(A)**, 104.3 in **5(B)**, 104.0 pm in **7(A)**, and 104.2 pm in **7(B)**; the Fe–N bond lengths are 189.1 pm in **5(A)**, 190.2 in **5(B)**, 189.5 pm in **7(A)**, and 190.5 pm in **7(B)**; the N–N bond lengths are 128.9 pm in **5(A)** and in **5(B)** and 128.8 pm in **7(A)** and in **7(B)**.

However, there are pronounced secondary effects due to the induced structural changes of the chelate ligand: one of the original equatorial benzene rings in **5**, which is almost in plane with the $\{FeS_3P\}$ fragment in **5** is subject to a deformation upon introduction of the rigid phenylene bridges towards the diazene moiety in **7**. This increases the differences in length and energy of the $S\cdots H$ hydrogen bonds for isomer **(A)**: 267.5 pm and 6.0 kJ/mol for the longer hydrogen bond in **5(A)**, 249.9 pm and 8.3 kJ/mol for the shorter hydrogen bond in **5(A)**, while we have 269.9 pm and 5.7 kJ/mol for **7(A)**

TABLE II

COMPARISON OF CALCULATED SPECTRA FOR COMPLEXES **5** AND **7**

sym	$\tilde{\nu}_{\text{exp}}$	Complex 5 (<i>103</i>)		I_{rel}	Complex 7 (<i>105</i>)		I_{rel}
		isomer	$\tilde{\nu}_{\text{calc}}$		isomer	$\tilde{\nu}_{\text{calc}}$	
a_g	637	5(B)	639	50.4	7(B)	626	165.5
a_g	663	5(A)	666	143.0	7(A)	664	16.3
a_g	1365	5(B)	1352	1434.4	7(B)	1358	1799.0
a_g	1365	5(A)	1363	1308.7	7(A)	1363	1530.5
a_g	1455	5(A)	1449	22.6	7(A)	1455	30.4
a_g	1509	5(B)	1512	100.0	7(B)	1501	142.0
a_g		5(B)	3111	54.0	7(B)	3126	84.3
a_g		5(B)	3112	22.5	7(B)	3127	37.8
a_g		5(A)	3191	< 0.1	7(A)	3167	8.3

Experimental Wavenumbers $\tilde{\nu}_{\text{exp}}$ are given for comparison for **5** with R=Pr (*102*). Note that the two bands at 1363 cm^{-1} and 1352 cm^{-1} are not resolved by experiment which yielded only a single band at 1365 cm^{-1} . All wavenumbers are given in cm^{-1} .

(longer bond) and 246.0 pm with 10.9 kJ/mol in **7(A)** (shorter bond). At the same time the differences in the hydrogen bonds for isomer **B** are decreased: 276.8 pm and 2.4 kJ/mol in **5(B)** (longer bond), 240.5 pm and 19.3 kJ/mol in **5(B)** (shorter bond); 272.2 pm and 3.2 kJ/mol in **7(B)** (longer bond), 244.9 pm and 17.4 kJ/mol in **7(B)** (shorter bond).

Raman vibrational frequencies and intensities for both complexes **5** and **7** are compared in Table II. The relative Raman scattering intensities were calculated from the differential cross sections. For their evaluation we used the wavelength of 613.33 nm (*105*). Polarizabilities were calculated in the limit of a static perturbation.

It has been mentioned above that the frequencies of the N–H bending mode at about 1500 cm^{-1} are influenced by the $\text{S}\cdots\text{H}$ contacts for complex **5**. Although the change in the hydrogen bond energies is only a few kJ/mol for complex **7** in comparison to **5**, we were able to verify this correlation between the hydrogen bond energies and the vibrational frequencies for this pair of isomers: The wavenumbers for the corresponding modes are 1501 cm^{-1} for **7(B)**, which exhibits the stronger $\text{S}\cdots\text{H}$ hydrogen bond (17.4 kJ/mol), and 1455 cm^{-1} for **7(A)**. This bond energy for **7(B)** is slightly smaller than that of **5(B)**, and consequently, the wavenumber is smaller by 11 cm^{-1} . Considering the complexes **5(A)** and **7(A)** we find that the strongest hydrogen bond of 10.9 kJ/mol also corresponds to the

larger wavenumber of 1455 cm^{-1} for **7(A)**, although the difference is only 6 cm^{-1} in this case.

This example shows that small modifications in the second ligand sphere can be applied for a fine-tuning of the bonding between the substrate (here modeled by the diazene moiety) and the complex via hydrogen bridges.

VII. Study of the First Dinuclear N_2 Complex with Biologically Compatible Ligand Sphere

A cornerstone for our model complex studies was the synthesis (108) of a $\mu\text{-N}_2$ dinuclear species $\{[\text{Ru}(\text{P}^i\text{Pr}_3)(\text{N}_2\text{Me}_2\text{S}_2)]_2\text{N}_2\}$ **8**, which is a complex of type **6** and which represents the first dinuclear dinitrogen complex with sulfur ligands (see Fig. 13 for the (S,S) stereoisomer), from the mononuclear $\text{Ru}[(\text{N}_2\text{Me}_2\text{S}_2)']\text{N}_2$ complex (109,110). As has been discussed earlier, binding of inert N_2 to Fe(II) is hard to achieve. Moreover, it is also well known that vacant metal coordination sites in sulfur complexes are easily blocked after formation of M–S–M sulfur bridges (2,14,92,111). With the dinuclear N_2 complex at hand, Sellmann *et al.* have examined the potential reduction process (112) as discussed in principle in Section V for a different Sellmann-type Fe complex. Though all N_2H_2 intermediates of this process were synthesized (112), the first reduction step to diazene has not yet been accomplished.

Most important is that complex **8** is formed under ambient conditions (standard pressure and temperature). The N–N distance in **8** is about 3 pm larger than in free dinitrogen. We discuss a possible activation mechanism, which would yield diazene, in the following section.

In order to determine the relative energy of various stereoisomers, in particular of the (S,S) and (R,S) species, we calculated the rotational energy curve of a rotation of one of the chelate ligands about the Ru–N–N–Ru axis shown in Fig. 14. The rotation produces two stable conformers with the two phosphines in orthogonal positions. These conformers are separated by barriers of more than 30 kJ/mol, which result from a steric hindrance of the phosphines and the methyl groups of the amine-nitrogen atoms in the chelate ligand. The steric hindrance is small if two phosphine-methyl-group repulsions occur when compared with the phosphine-phosphine and methyl-methyl repulsions in the maximum-rotation-energy structure.

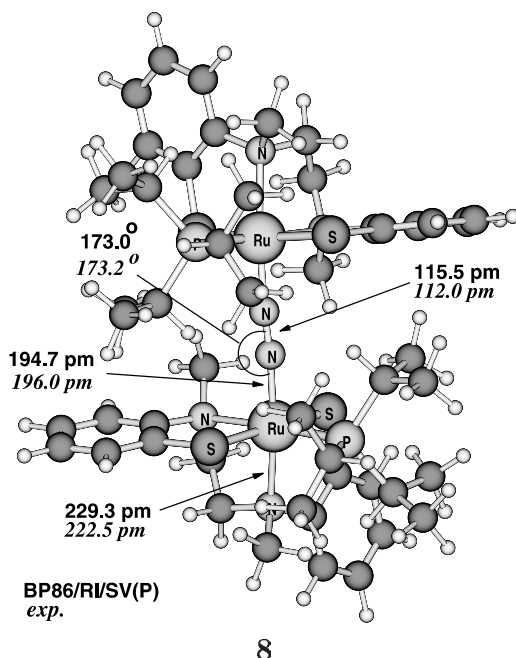


FIG. 13. BP86/RI/SV(P)-optimized structure of the (S,S)-stereoisomer of $\{[\text{Ru}(\text{P}^i\text{Pr}_3)(\text{N}_2\text{Me}_2\text{S}_2)]\text{N}_2\}$ **8** compared with corresponding X-ray structure (*108*).

Particularly for this maximum-energy structure we find a finer rotational structure around the maximum, which can induce local maxima and minima owing to the hindered rotation of the phosphine's methyl groups.

A. OUTLOOK: A POSSIBLE PHOTO-CHEMICAL REDUCTION MECHANISM

The (R,S) stereoisomer of a model complex of **8** possesses C_i symmetry and allows us to classify the molecular orbitals in terms of the irreducible representations a_g and a_u . It turned out that HOMO and LUMO belong to different irreducible representations. Exchange of occupation of these orbitals thus leads to different electronic configurations. While only one of the two electronic configurations corresponds to the ground state and then has a valid description in the framework of DFT, both electronic configurations can be subjected to a geometry optimization in C_i symmetry and yield two different structures; the results of the optimizations are depicted in Fig. 15. We took the

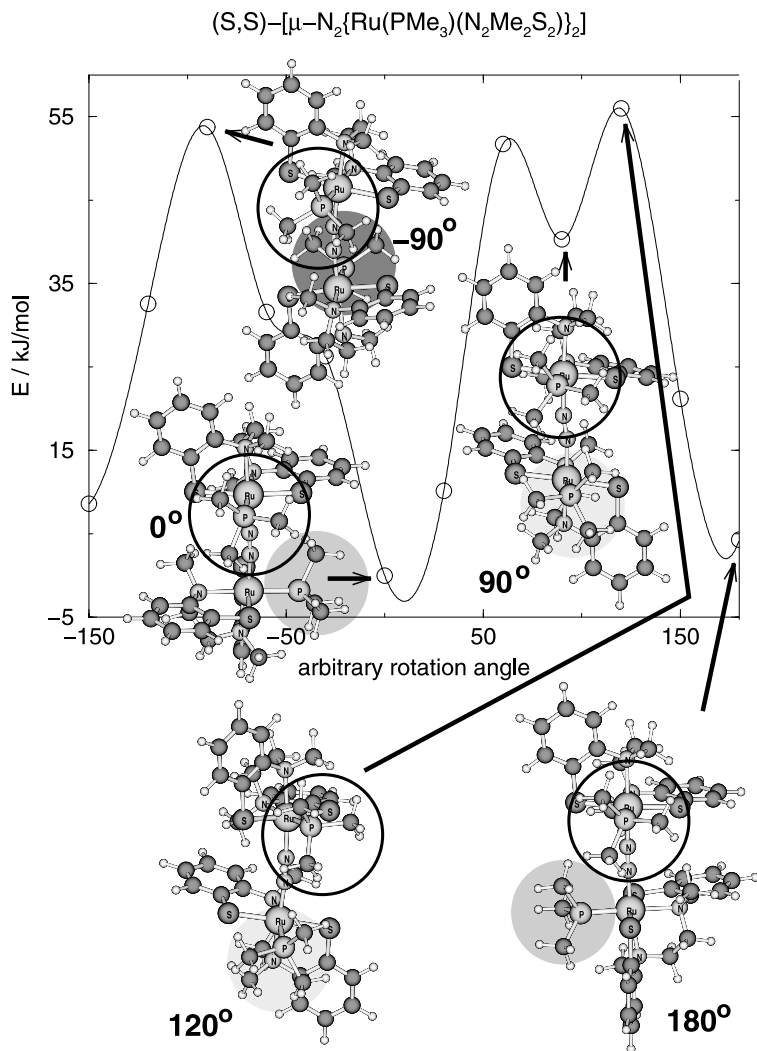


FIG. 14. Curve of rotation about the Ru–N–N–Ru axis of C_1 -symmetric (S,S)-8, which produces two stable conformers in which the two phosphines are in orthogonal positions (the phosphine has been modeled by PMe_3 , the upper PMe_3 is marked by an open circle and the position of the lower PMe_3 by a closed circle). The curve was calculated with BP86/RI/SV(P) under partially relaxation of the structure at each point (*139*) (some structural parameters were kept frozen in order to map the rotation coordinate on a dihedral angle).

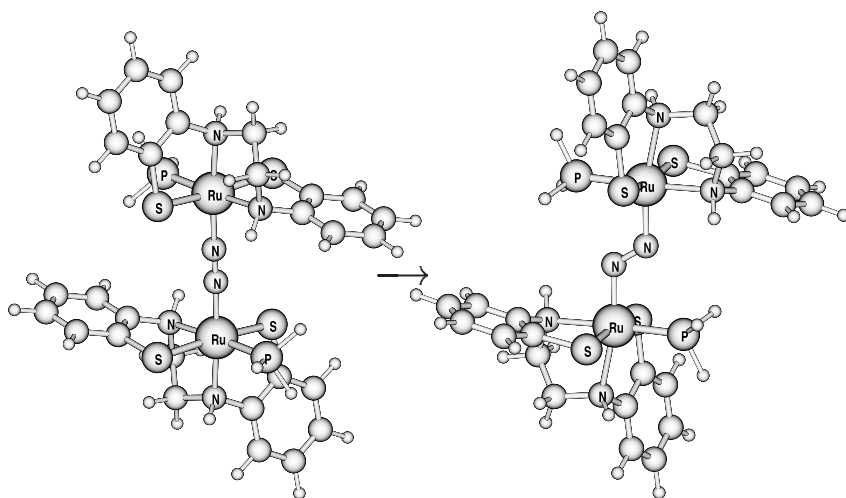


FIG. 15. Two optimized C_2 -symmetric structures of $(R,S)\text{-}\{[\text{Ru}(\text{PMe}_3)(\text{N}_2\text{H}_2\text{S}_2)]\text{N}_2\}$, which may be interconverted by electronic excitation (or by reduction).

“double-excited” configuration as a rough model for double excitation, which gave us a first hint on a drastically changed equilibrium geometry upon excitation leading to a diazenoid geometric arrangement of the N_2 moiety. We should note that the diazene-like configuration is observed in “doubly excited” RKS as well as in “singly excited” UKS calculations, which indicates that already a single excitation to the LUMO can induce the diazene-like structure. All results presented in the following are based on RKS calculations.

As it becomes clear from Fig. 15, a diazene-like conformation can be induced through energy transfer of about 300 kJ/mol. It should thus be possible to induce this conformational change photochemically. The diazene-like conformation corresponds to a double-bonded N_2 moiety with two lone pairs, which can play an important role as hydrogen atom acceptors in the reduction process. This appears to be most important for a *kinetic* activation of the first endothermic reduction step.

It is noteworthy that the energy-induced conformational change of N_2 in a diazene-like position is also observed for the diprotonated complex. This implies that **8** may be first protonated, then transformed through energy transfer (e.g., through irradiation of visible light) into a diazene-like conformation and finally reduced to

give diazene, which is exothermic by about 150 kJ/mol per formed N–H bond.

To summarize, the *photochemical* mechanism is, of course, not a feasible mechanism for dinitrogen reduction in the case of nitrogenase, though the general structural motif, i.e., the transformation to a diazene-like conformation, has most likely also to be achieved by nitrogenase (a “mechanical” movement of, say, two metal centers to which the N₂ moiety is bound could accomplish this). This formation of a pre-diazene conformation appears to be a very important step even if the reduction would not occur in 2H⁺/2e[−] steps but only in 1H⁺/1e[−] steps. We should note that the formation of ammonia from dinitrogen at room temperature has very recently been detected by a mesoporous titanium oxide molecular sieve (113), though a detailed mechanism could not be established. However, the dinitrogen Ru complex described above offers the possibility to study in detail proton transfer reactions on dinitrogen. The electronic-chemical coupling mechanism, which is proposed here, parallels recent conceptual developments on mechano-chemical coupling in cytochrome *c*₃ (114).

An extensive quantum chemical investigation into the proposed photochemical activation process is currently under way. First results show that this activation pathway also shows up in a consistent quantum mechanical treatment of electronic excitations in the framework of time-dependent DFT (115), which allowed us to optimize the structure in the first excited singlet state.

VIII. Conclusion

In this work, we have reviewed theoretical studies on Sellmann-type Fe(II)- and Ru(II)-sulfur complexes for the modeling of functional aspects of the enzyme nitrogenase. While the mechanism of N₂ reduction by nitrogenase has not yet been resolved, we followed the work by Dieter Sellmann and his group and adopted reasonable assumptions, which are likely to be generally valid for biomimetic model complexes, in order to study specific features of nitrogen reduction processes under well-defined conditions. Such features are the role of hydrogen bonds or states of different spin multiplicity. We have demonstrated that the reliable calculation of such chemical concepts is not straightforward but requires new ideas and approaches.

We believe that these studies are important for the design of non-molybdenum based catalytic complexes for nitrogen reduction.

Establishing a catalytic N_2 reduction cycle is a formidable experimental task, but the theoretical aspects are by no means less complicated. Therefore, the extensive work on Fe-sulfur complexes by Sellmann provided well-defined systems and a large body of experimental reference data, which are of great value for theoretical investigations. From the theoretical point of view, the active site of nitrogenase appears to be electronically much too complicated to be treated with current standard quantum chemical methods (the failure for the energetical order of different spin states is only one example). But relying on the well-defined experimental systems guarantees a close connection of quantum-chemical results and experiment.

A Fe-S-based catalytic transition metal complex has not yet been found, but the present status of quantum chemical calculations encourages further work into this direction. Finally, the complexity of this task assures that results are obtained, which can be generalized for transition-metal-mediated catalysis in general. These results are of methodological and chemical nature since they provide improved quantum chemical methods and approaches for the calculation of structural motifs, which do also occur in many other catalytic systems.

IX. Appendix: Quantum Chemical Methodology

For all DFT calculations reported in this review the highly efficient density functional programs provided by the TURBOMOLE 5.1 and 5.4 suites (116) were used. We employed the Becke-Perdew functional dubbed BP86 (117,118) and the hybrid functional B3LYP (119,120) as implemented in TURBOMOLE. We always used for the BP86 functional the resolution-of-the-identity (RI) technique (121,122), which speeds up the calculations considerably. Note that the implementation of the B3LYP function in TURBOMOLE differs in the choice of the particular form of the E_c^{VWN} functional from the one employed in the GAUSSIAN program (123): GAUSSIAN98 uses the VWN(III) correlation functional (124) for B3LYP while the VWN(V) correlation functional is employed in TURBOMOLE 5.1 and 5.4.

It turned out that using these well-established standard functionals for the reaction energies we obtained highly unreliable energetics for complexes of the type under study (the spin state energies were wide off the experimental results and consequently the ground state reaction energies came out wrong) (81). A systematic study showed

that these iron complexes represent critical cases where high-spin-low-spin energy splittings are small and can differ largely when calculated with pure and hybrid density functionals (90). In order to avoid these uncertainties we use in addition to BP86 and B3LYP our reparametrized B3LYP*, which was tailored particularly for these Sellmann-type complexes (90) but which has shown to be of general applicability (125). For the discussion of reaction energetics we rely on the B3LYP* data.

Results for first-row transition metal compounds were obtained from *all-electron* restricted and unrestricted Kohn-Sham calculations. Only for atoms of fifth or higher periods of the periodic table of the elements we have applied those effective core potentials (ECPs) of the Stuttgart group, which are the standard ECPs in TURBOMOLE for the core electrons. These ECPs account very well for the scalar relativistic effect in heavy-element atoms (126,127).

Closed-shell systems tempt one to use the fast converging restricted Kohn-Sham method to obtain all-singlet energetics for a catalytic process. However, states of different multiplicities need to be considered particularly for weak ligand fields. Consequently, we probed, whether spin polarization of the singlet states occurs by comparison of the unrestricted Kohn-Sham calculations on the open-shell singlets with the corresponding results from closed-shell singlet restricted Kohn-Sham calculations. Moreover, the singlet structures were checked for singlet and triplet stability (128,129) by a stability test implemented in TURBOMOLE.

Three different basis sets were employed: the first one, dubbed SV(P), is Ahlrichs' split-valence basis set (130) with polarization functions on heavy atoms, but not on hydrogen. Moreover, the TZVP basis set featuring a valence triple-zeta basis set with polarization functions on all atoms was used (131). This TZVP basis set is our recommended basis set, which yields accurate structural parameters and (spin, conformational, and reaction) energies in combination with the counter poise correction technique (132,133). For comparison, a larger basis set with additional polarization functions, denoted TZVPP, was used as implemented in TURBOMOLE. For most atoms this is a valence-triple-zeta basis with additional polarization functions taken from the cc-pVTZ basis by Dunning and Woon (134–136). The TZVPP calculations took considerably more computer time than the TZVP calculations. For a sufficiently large number of test calculations the TZVP and TZVPP reaction energies differed by only about 5 kJ/mol without correcting for the basis-set superposition error (BSSE). If a counter poise correction is added, our test

calculations on coordination energies have shown that results obtained with the TZVP and TZVPP basis sets differ by less than 1 kJ/mol. We were thus led to the conclusion that the TZVP basis set in combination with the counter poise correction is sufficiently accurate for our purposes. For the SV(P) basis set the combination with the counter poise correction is mandatory in order to get results which might be competitive with TZVP results.

The shared-electron number (SEN) method was used for the evaluation of hydrogen bond energies. This method was developed for the evaluation of hydrogen bonds in compounds which cannot be decomposed into two parts such that the decomposition energy can be solely attributed to the broken hydrogen bond. Details of the SEN method are described in Ref. (82).

For the vibrational analyses in a harmonic force field we calculated the second derivatives of the total electronic energy computed as numerical first derivatives (137) of analytic energy gradients obtained from TURBOMOLE. We do not employ empirical scaling factors for the comparison of calculated harmonic frequencies and experimental fundamentals, since it is known that scaling factors for the BP86 functional are very close to unity (104). The good agreement between harmonic frequencies from BP86 calculations and experimentally observed fundamentals is clearly caused by an error cancellation effect; see the analysis given in Ref. (104).

Raman intensities were calculated by differentiation of the molecular polarizability with respect to nuclear coordinates. It is often sufficient or desirable to calculate only Raman intensities for selected modes instead of for all $3N - 6$ vibrational modes of a large molecule, which can be achieved if the normal modes of the molecule are already known. Therefore, a frequency analysis was performed using numerical differentiation of analytical gradients with respect to Cartesian nuclear coordinates in the first step. This yields vibrational frequencies and normal modes. Then, we used displacements along selected mass-weighted normal coordinates Q_k , for which (static and/or dynamic) polarizabilities are calculated. With a step size s_{Q_k} ,

$$s_{Q_k} = s_R / |\Delta \mathbf{R}_k| = s_R \left[\sum_{i=1}^{3N} \left(Q_{k,i}^{\text{norm}} \right)^2 / m_i \right]^{-1/2} \left[\frac{[\text{unit of length}]}{[\text{unit of mass}]^{1/2}} \right], \quad (1)$$

for the generation of the displacement structures. The numerical derivatives of the components of the polarizability tensor are then

obtained as

$$\left(\bar{\alpha}'_{ij}\right)_k = \frac{\partial \alpha_{ij}}{\partial \mathbf{Q}_k} = \frac{\alpha_{ij}(\mathbf{R}_{\text{eq}} + s_R \Delta \mathbf{R}_k^{\text{norm}}) - \alpha_{ij}(\mathbf{R}_{\text{eq}} + s_R \Delta \mathbf{R}_k^{\text{norm}})}{2s_{Q_K} |\Delta \mathbf{Q}_k^{\text{norm}}|}, \quad (2)$$

if a three-point central differences formula is used; $\alpha_{ij}(\mathbf{R}_{\text{eq}} \pm s_R \Delta \mathbf{R}_k^{\text{norm}})$ are the components of the polarizability tensor of the displaced structures.

Theoretically determined Raman intensities are given in terms of Raman scattering factors S_k for mode k ,

$$S_k = 45a_k'^2 + 7\gamma_k'^2, \quad (3)$$

where a'_k and γ'_k contain the derivatives $(\bar{\alpha}'_{ij})_k$ [cf. (137–138)],

$$a'_k = \frac{1}{3} \left\{ (\bar{\alpha}'_{xx})_k + (\bar{\alpha}'_{yy})_k + (\bar{\alpha}'_{zz})_k \right\}, \quad (4)$$

$$\gamma_k'^2 = \frac{1}{2} \left\{ \begin{aligned} & [(\bar{\alpha}'_{xx})_k - (\bar{\alpha}'_{yy})_k]^2 + [(\bar{\alpha}'_{yy})_k - (\bar{\alpha}'_{zz})_k]^2 \\ & + [(\bar{\alpha}'_{zz})_k - (\bar{\alpha}'_{xx})_k]^2 + 6 \left[(\bar{\alpha}'_{xy})_k^2 + (\bar{\alpha}'_{yz})_k^2 + (\bar{\alpha}'_{zx})_k^2 \right] \end{aligned} \right\}. \quad (5)$$

For comparison with experimental data it is more suitable to state relative intensities in terms of differential cross sections, since these are proportional to the relative intensities obtained in the experiment. The Q-branch differential cross section for a scattering angle of 90° and an incident light beam which is plane polarized perpendicular to the scattering plane is

$$\frac{d\sigma}{d\Omega} = \frac{\pi^2}{\epsilon_0^2} (\tilde{v}_{in} - \tilde{v}_k)^4 \frac{h}{8\pi^2 c \tilde{v}_k} \left(\frac{45a_k'^2 + 7\gamma_k'^2}{45} \right) \frac{1}{1 - \exp[-hc\tilde{v}_k/k_B T]}. \quad (6)$$

ACKNOWLEDGMENTS

We are indebted to Prof. Dr. Dieter Sellmann for numerous stimulating and fruitful discussions on the complexes, which were synthesized in his group. All work reviewed here was funded by the collaborative research project SFB 583 at the Friedrich-Alexander-University Erlangen-Nuremberg.

REFERENCES

1. Ferguson, S. H. *Curr. Opin. Chem. Biol.* **1998**, *2*, 182–183.
2. Burgess, B. K.; Lowe, D. J. *Chem. Rev.* **1996**, *96*, 2983–3012.
3. Eady, R. R. *Chem. Rev.* **1996**, *96*, 3013–3030.
4. Howard, J. B.; Rees, D. C. *Chem. Rev.* **1996**, *96*, 2965–2982.
5. Einsle, O.; Tezcan, F. A.; Andrade, S. L. A.; Schmid, B.; Yoshida, M.; Howard, J. B.; Rees, D. C. *Science* **2002**, *297*, 1696–1700.
6. Leigh, G. J. *Eur. J. Biochem.* **1995**, *229*, 14–20.
7. Coucouvanis, D. J. *Biolog. Inorg. Chem.* **1996**, *1*, 594–600.
8. Pickett, C. J. *J. Biolog. Inorg. Chem.* **1996**, *1*, 601–606.
9. Sellmann, D.; Sutter, J. *J. Biolog. Inorg. Chem.* **1996**, *1*, 587–593.
10. Durrant, M. C. *Biochemistry* **2002**, *41*, 13934–13945.
11. Durrant, M. C. *Biochemistry* **2002**, *41*, 13946–13955.
12. Barriere, F. *Coord. Chem. Rev.* **2003**, *236*, 71–89.
13. Noodleman, L.; Lovell, T.; Liu, T.; Himo, F.; Torres, R. A. *Curr. Opin. Chem. Biol.* **2002**, *6*, 259–273.
14. Hidai, M.; Mizobe, Y. *Chem. Rev.* **1995**, *95*, 1115–1133.
15. Henderson, R. A.; Leigh, G. J.; Pickett, C. J. *Adv. Inorg. Chem. Radiochem.* **1983**, *27*, 198–292.
16. Nishibayashi, Y.; Wakiji, I.; Hirata, K.; Rakowski Du Bois, M.; Hidai, M. *Inorg. Chem.* **2001**, *40*, 578–580.
17. Nishibayashi, Y.; Iwai, S.; Hidai, M. *Science* **1998**, *279*, 540–542.
18. Yandulov, D. V.; Schrock, R. R. *J. Am. Chem. Soc.* **2002**, *124*, 6252–6253.
19. Yandulov, D. V.; Schrock, R. R. *Science* **2003**, *301*, 76–78.
20. Shah, V. K.; Britt, W. *Proc. Natl. Acad. Sci. USA* **1977**, *74*, 3248.
21. Kim, J.; Rees, D. C. *Science* **1992**, *257*, 1677.
22. Kim, J.; Rees, D. C. *Nature* **1992**, *360*, 553.
23. Deng, H.; Hoffmann, R. *Angew. Chem. Int. Ed. Engl.* **1993**, *32*, 1062.
24. Deng, H.; Hoffmann, R. *Angew. Chem.* **1993**, *105*, 1125–1128.
25. Plass, W. *J. Molec. Struct. (THEOCHEM)* **1994**, *315*, 53–62.
26. Barriere, F.; Pickett, C. J.; Talarmin, J. *Polyhedron* **2001**, *20*, 27–36.
27. Stavrev, K. K.; Zerner, M. C. *Chem. Eur. J.* **1996**, *2*, 83–87.
28. Stavrev, K. K.; Zerner, M. C. *Int. J. Quantum Chem.* **1997**, *96*, 141–145.
29. Stavrev, K. K.; Zerner, M. C. *Int. J. Quantum Chem.* **1998**, *70*, 1159–1168.
30. Zhong, S.-J.; Liu, C.-W. *Polyhedron* **1997**, *16*, 653–661.
31. Rod, T. H.; Nørskov, J. K. *J. Am. Chem. Soc.* **2000**, *122*, 12751–12763.
32. Dance, I. G. *Aust. J. Chem.* **1994**, *47*, 979–990.
33. Dance, I. *Chem. Commun.* **1997**, 165–166.
34. Machado, F. B. C.; Davidson, E. R. *Theor. Chem. Acc.* **1995**, *92*, 315–326.
35. Siegbahn, P. E. M.; Westerberg, J.; Svensson, J.; Crabtree, R. H. *J. Phys. Chem.* **1998**, *102*, 1615–1623.
36. Chen, Y.; Hartmann, M.; Frenking, G. *Eur. J. Inorg. Chem.* **2001**, 1441–1448.
37. Rod, T. H.; Hammer, B.; Nørskov, J. K. *Phys. Rev. Lett.* **1999**, *82*, 4054–4057.
38. Rod, T. H.; Logadottir, A.; Nørskov, J. K. *J. Chem. Phys.* **2000**, *112*, 5343–5347.
39. Lovell, T.; Li, J.; Case, D. A.; Noodleman, L. *J. Am. Chem. Soc.* **2001**, *124*, 4546–4547.
40. Durrant, M. C. *Biochem. J.* **2001**, *355*, 569–576.
41. Lee, H.-I.; Benton, P. M. C.; Laryukhin, M.; Igarashi, R. Y.; Dean, D. R.; Seefeldt, L. C.; Hoffman, B. M. *J. Am. Chem. Soc.* **2003**, *125*, 5604–5605.
42. Dance, I. *Chem. Comm.* **2003**, 324–325.

43. Hinnemann, B.; Nørskov, J. K. *J. Am. Chem. Soc.* **2003**, *125*, 1466–1467.
44. Lovell, T.; Liu, T.; Case, D. A.; Noodleman, L. *J. Am. Chem. Soc.* **2003**, *125*, 8377–8383.
45. Schimpl, J.; Petrilli, H. M.; Blöchl, P. E. *J. Am. Chem. Soc.* **2003**, *125*, 15772–15778.
46. Dance, I. *Chem. Commun.* **1998**, 523–530.
47. Demadis, K. D.; Malinak, S. M.; Coucouvanis, D. *Inorg. Chem.* **1996**, *35*, 4038–4046.
48. Tyson, M. A.; Coucouvanis, D. *Inorg. Chem.* **1997**, *36*, 3808–3809.
49. Malinak, S. M.; Simeonov, A. M.; Mosier, P. E.; McKenna, C. E.; Coucouvanis, D. *J. Am. Chem. Soc.* **1997**, *119*, 1662–1667.
50. Han, J.; Beck, K.; Ockwig, N.; Coucouvanis, D. *J. Am. Chem. Soc.* **1999**, *121*, 10448–10449.
51. Han, J.; Coucouvanis, D. *J. Am. Chem. Soc.* **2001**, *123*, 11304–11305.
52. Han, J.; Koutmos, M.; Ahmad, S. A.; Coucouvanis, D. *Inorg. Chem.* **2001**, *40*, 5985–5999.
53. Stavrev, K. K.; Urahata, S.; Herz, T.; Han, J.; Coucouvanis, D. *Int. J. Quantum Chem.* **2001**, *85*, 469–474.
54. Han, J.; Coucouvanis, D. *Inorg. Chem.* **2002**, *41*, 2738–2746.
55. Schrauzer, G. N.; Doemeny, P. A.; Palmer, J. G. *Z. Naturforsch.* **1993**, *48b*, 1295–1298.
56. Zhou, H.-C.; Su, W.; Achim, C.; Rao, P. V.; Holm, R. H. *Inorg. Chem.* **2002**, *41*, 3191–3201.
57. Grand, N. L.; Muir, K. W.; Pétillon, F. Y.; Pickett, C. J.; Schollhammer, P.; Talarmin, J. *Chem. Eur. J.* **2002**, *8*, 3115–2127.
58. Szilagyi, R. K.; Musaev, D. G.; Morokuma, K. *Inorg. Chem.* **2001**, *40*, 766–775.
59. Bell, J.; Dunford, A. J.; Hollis, E.; Henderson, R. A. *Angew. Chem. Int. Ed.* **2003**, *42*, 1149–1152.
60. Lee, S. C.; Holm, R. H. *Proc. Natl. Acad. Sci.* **2003**, *100*, 3595–3600.
61. Sellmann, D.; Sutter, J. Biological N₂ fixation: Molecular mechanism of the nitrogenase catalyzed N₂ dependent HD-formation, the N₂ fixation inhibition and the open-side FeMoco model, “*Perspectives in Coordination Chemistry*”; Vol. 5; Eds. Trzeciak, A. M.; Sobota, D.; Ziolkowski, J.; University of Wrocław: Poland, **2000**.
62. Sellmann, D.; Utz, J.; Blum, N.; Heinemann, F. W. *Coord. Chem. Rev.* **1999**, *190–192*, 607–627.
63. Coucouvanis, D.; Han, J.; Moon, N. *J. Am. Chem. Soc.* **2002**, *124*, 216–224.
64. Sellmann, D.; Sutter, J. *Acc. Chem. Res.* **1997**, *30*, 460–469.
65. Sellmann, D.; Fürsattel, A. *Angew. Chem. Int. Ed.* **1999**, *38*, 2023–2026.
66. Hardy, R. W. F. Reducible Substrates of Nitrogenase, “*A Treatise on Dinitrogen Fixation*”; Eds. Hardy, R. W. F.; Bottomley, F.; Burns, R. C.; J. Wiley & Sons: New York, **1979**.
67. Sellmann, D.; Soglowek, W.; Knoch, F.; Moll, M. *Angew. Chem.* **1989**, *101*, 1244–1245.
68. Sellmann, D.; Soglowek, W.; Knoch, F.; Moll, M. *Angew. Chem. Int. Ed.* **1989**, *28*, 1271–1272.
69. Sellmann, D.; Soglowek, W.; Knoch, F.; Ritter, G.; Dengler, J. *Inorg. Chem.* **1992**, *31*, 3711–3717.
70. Sellmann, D.; Friedrich, H.; Knoch, F.; Moll, M. *Z. Naturforsch.* **1993**, *48b*, 76–88.
71. Sellmann, D.; Hennige, A.; Heinemann, F. W. *Inorg. Chim. Acta* **1998**, *280*, 39–49.
72. Sellmann, D.; Becker, T.; Knoch, F. *Chem. Eur. J.* **1996**, *2*, 1092–1098.
73. Hoch, G. E.; Schneider, K. C.; Burris, R. H. *Biochim. Biophys. Acta* **1960**, *37*, 273–279.
74. Burgess, B. K.; Wherland, S.; Newton, W. E.; Stiefel, E. I. *Biochemistry* **1981**, *20*, 5140–5146.
75. Sellmann, D.; Fürsattel, A.; Sutter, J. *Coord. Chem. Rev.* **2000**, *200–202*, 541–561.

76. Collman, J. P.; Hutchison, J. E.; Ennis, M. S.; Lopez, M. A.; Guillard, R. *J. Am. Chem. Soc.* **1992**, *114*, 8074–8080.
77. Aullón, G.; Capdevila, M.; Clegg, W.; González-Duarte, P.; Lledós, A.; Mas-Ballesté, R. *Angew. Chem. Int. Ed.* **2002**, *41*, 2776–2778.
78. Sellman, D.; Lechner, P.; Knoch, F.; Moll, M. *Angew. Chem. Int. Ed. Engl.* **1991**, *30*, 552–553.
79. Sellman, D.; Lechner, P.; Knoch, F.; Moll, M. *Angew. Chem.* **1991**, *103*, 599–601.
80. Gottschalk-Gaudig, T. *Aktivierung und Stabilisierung kleiner Moleküle durch Ruthenium-Komplexe mit vierzähligen Thioether-Thiolat-Liganden*, Thesis, University of Erlangen-Nuremberg, **1997**.
81. Reiher, M.; Salomon, O.; Sellmann, D.; Hess, B. A. *Chem. Eur. J.* **2001**, *7*, 5195–5202.
82. Reiher, M.; Sellmann, D.; Hess, B. A. *Theor. Chem. Acc.* **2001**, *106*, 379–392.
83. Sellmann, D.; Emig, S.; Heinemann, F. W.; Knoch, F. *Z. Naturforsch.* **1998**, *53b*, 1461–1474.
84. Reiher, M.; Hess, B. A. *Chem. Eur. J.* **2002**, *8*, 5332–5339.
85. Sellmann, D.; Friedrich, H.; Knoch, F. *Z. Naturforsch.* **1993**, *48b*, 1675–1680.
86. Sellmann, D.; Mahr, G.; Knoch, F.; Moll, M. *Inorg. Chim. Acta* **1994**, *224*, 45–59.
87. Sellmann, D.; Bail, P.; Knoch, F.; Moll, M. *Chem. Ber.* **1995**, *128*, 653–663.
88. Sellmann, D.; Lechner, P.; Knoch, F.; Moll, M. *J. Am. Chem. Soc.* **1992**, *114*, 922–930.
89. Sellmann, D.; Käppler, J.; Moll, M.; Knoch, F. *Inorg. Chem.* **1993**, *32*, 960–964.
90. Reiher, M.; Salomon, O.; Hess, B. A. *Theor. Chem. Acc.* **2001**, *107*, 48–55.
91. Tuzek, F.; Lehnert, N. *Angew. Chem. Int. Ed.* **1998**, *37*, 2636–2638.
92. Fryzuk, M. D.; Johnson, S. A. *Coord. Chem. Rev.* **2000**, *200–202*, 379–409.
93. Lehnert, N.; Tuzek, F. *Inorg. Chem.* **1999**, *38*, 1659–1670.
94. Lehnert, N.; Tuzek, F. *Inorg. Chem.* **1999**, *38*, 1671–1682.
95. Thorneley, R. N. F.; Lowe, D. J. “*Molybdenum Enzymes*”, Vol. 4; Ed. Spiro, T. G.; John Wiley & Sons: New York, **1985**.
96. Dehnicke, K.; Strähle, J. *Angew. Chem.* **1981**, *93*, 451–464.
97. Dehnicke, K.; Strähle, J. *Angew. Chem.* **1992**, *104*, 978–1000.
98. Angeli, D.; Cimraglia, R.; Hofmann, H.-J. *Chem. Phys. Lett.* **1996**, *259*, 276–282.
99. Sekusak, S.; Frenking, G. *J. Molec. Struct. (THEOCHEM)* **2001**, *541*, 17–29.
100. Reiher, M.; Moritz, G.; Hess, B. A. **2004**, to be submitted.
101. Lehnert, N.; Wiesler, B. E.; Tuzek, F.; Hennige, A.; Sellmann, D. *J. Am. Chem. Soc.* **1997**, *119*, 8869–8878.
102. Lehnert, N.; Wiesler, B. E.; Tuzek, F.; Hennige, A.; Sellmann, D. *J. Am. Chem. Soc.* **1997**, *119*, 8879–8888.
103. Reiher, M.; Neugebauer, J.; Hess, B. A. *Z. Physik. Chem.* **2003**, *217*, 91–103.
104. Neugebauer, J.; Hess, B. A. *J. Chem. Phys.* **2003**, *118*, 7215–7225.
105. Neugebauer, J.; Reiher, M.; Hess, B. A. Structure, Energetics, and Spectroscopy of Models for Enzyme Cofactors, “*High-Performance Computing in Science and Engineering 2000–2002 – Transactions of the First Joint HLRB and KONWIHR Status and Result Workshop*”; Eds. Wagner, S.; Hanke, W.; Bode, A.; Durst, F.; Springer-Verlag: Berlin, **2003**, pp. 157–169.
106. Blum, D. C. F. *Synthese, Struktur und Reaktivität neuer Eisen-Komplexe mit S_4 -, N_2S_2 - und N_3S_2 -Donoratomsätzen und biologisch relevanten Koliganden*, Thesis, Universität Erlangen-Nürnberg, **1998**.
107. Sellmann, D.; Blum, D. C. F.; Heinemann, F. W. *Inorg. Chim. Acta* **2002**, *337*, 1–10.
108. Sellmann, D.; Hille, A.; Heinemann, F. W.; Moll, M.; Brehm, G.; Reiher, M.; Hess, B. A.; Schneider, S. *Inorg. Chim. Acta.* **2003**, *348*, 194–198.

109. Sellmann, D.; Hautsch, B.; Rösler, A.; Heinemann, F. W. *Angew. Chem.* **2001**, *113*, 1553–1558.
110. Sellmann, D.; Hautsch, B.; Rösler, A.; Heinemann, F. W. *Angew. Chem. Int. Ed.* **2001**, *40*, 1505–1507.
111. Eady, R. R.; Leigh, G. J. *J. Chem. Soc. Dalton Trans.* **1994**, 2739–2748.
112. Sellmann, D.; Hille, A.; Rösler, A.; Heinemann, F. W.; Moll, M.; Brehm, G.; Schneider, S.; Reiher, M.; Hess, B. A.; Bauer, W. *Chem. Eur. J.* **2004**, *10*, 819–830.
113. Vettraino, M.; Trudeau, M.; Lo, A. Y. H.; Schurko, R. W.; Antonelli, D. *J. Am. Chem. Soc.* **2002**, *124*, 9567–9573.
114. Louro, R. O.; Catarino, T.; LeGall, J.; Turner, D. L.; Xavier, A. V. *ChemBioChem.* **2001**, *2*, 831–837.
115. Reiher, M.; Kirchner, B.; Hutter, J. Sellmann, D.; Hess, B. A. *Chem. Eur. J.* **2004**, in press.
116. Ahlrichs, R.; Bär, M.; Häser, M.; Horn, H.; Kölmel, C. *Chem. Phys. Lett.* **1989**, *162*, 165–169.
117. Becke, A. D. *Phys. Rev. A.* **1988**, *38*, 3098–3100.
118. Perdew, J. P. *Phys. Rev. B.* **1986**, *33*, 8822–8824.
119. Becke, A. D. *J. Chem. Phys.* **1993**, *98*, 5648–5652.
120. Stephens, P. J.; Devlin, F. J.; Chabalowski, C. F.; Frisch, M. J. *J. Phys. Chem.* **1994**, *98*, 11623–11627.
121. Eichkorn, K.; Treutler, O.; Öhm, H.; Häser, M.; Ahlrichs, R. *Chem. Phys. Lett.* **1995**, *240*, 283–390.
122. Eichkorn, K.; Weigend, F.; Treutler, O.; Ahlrichs, R. *Theor. Chem. Acc.* **1997**, *97*, 119–124.
123. Frisch, M. J., *et al.* “*Gaussian 98 (Revision A.7)*”; Gaussian, Inc.: Pittsburgh PA, **1998**.
124. Vosko, S. H.; Wilk, L.; Nusair, M. *Can. J. Phys.* **1980**, *58*, 1200–1211.
125. Salomon, O.; Reiher, M.; Hess, B. A. *J. Chem. Phys.* **2002**, *117*, 4729–4737.
126. Dolg, M. Relativistic Effective Core Potentials, “*Relativistic Electronic Structure Theory – Part 1. Fundamentals*”; Ed. Schwerdtfeger, P.; Elsevier: Amsterdam, **2002**, pp. 793–862.
127. Hess, B. A.; Dolg, M. Relativistic Quantum Chemistry with Pseudopotentials and Transformed Hamiltonians, “*Relativistic Effects in Heavy-Element Chemistry and Physics*”; Ed. Hess, B. A.; Wiley: Chichester, **2002**, pp. 89–122.
128. Chambaud, G.; Levy, B.; Millie, P. *Theoret. Chim. Acta (Berl.)* **1978**, *48*, 103–118.
129. Bauernschmitt, R.; Ahlrichs, R. *J. Chem. Phys.* **1996**, *104*, 9047–9052.
130. Schäfer, A.; Horn, H.; Ahlrichs, R. *J. Chem. Phys.* **1992**, *97*, 2571–2577.
131. Schäfer, A.; Huber, C.; Ahlrichs, R. *J. Chem. Phys.* **1994**, *100*, 5829–5835.
132. Boys, S. F.; Bernardi, F. *Mol. Phys.* **1970**, *19*, 553–566.
133. van Duijneveldt, F. B.; van Duijneveldt-van de Rijdt, J. G. C. M.; van Lenthe, J. H. *Chem. Rev.* **1994**, *94*, 1873–1885.
134. Dunning, Thom H. Jr. *J. Chem. Phys.* **1989**, *90*, 1007–1023.
135. Woon, D. E.; Dunning, Thom H. Jr. *J. Chem. Phys.* **1993**, *98*, 1358–1371.
136. Woon, D. E.; Dunning, Thom H. Jr. *J. Chem. Phys.* **1994**, *100*, 2975–2988.
137. Neugebauer, J.; Reiher, M.; Kind, C.; Hess, B. A. *J. Comput. Chem.* **2002**, *23*, 895–910.
138. Long, D. A. “*Raman Spectroscopy*”; McGraw-Hill: New York, **1977**.
139. Reiher, M. Unpublished results, **2002**.

PROTON AND ELECTRON TRANSFERS IN [NiFe] HYDROGENASE

PER E. M. SIEGBAHN

Department of Physics, Stockholm Centre for Physics, Astronomy and Biotechnology
(SCFAB), Stockholm University, S-106 91 Stockholm, Sweden

- I. Introduction
- II. Computational Details
- III. Results and Discussion
 - A. The Model with an Uncharged His77
 - B. The Model with a Charged His77
 - C. The Effect of the Selenium Substitution
- IV. Conclusions
- References

I. Introduction

The hydrogenase enzymes (1) catalyse the heterolytic cleavage of dihydrogen into protons and electrons,



For the forward reaction k_{cat} of 10^3 s^{-1} (2) indicates a rate-limiting free energy barrier of around 13 kcal/mol. In one physiological role (3), H_2 crosses the bacterial membrane and undergoes the oxidation reaction of Eq. (1). The resulting pH gradient across the membrane drives ATP formation via ATPase, which allows the use of H_2 as an energy source. A typical fate for the electrons, formed in Eq. (1), is in acetylCoA synthesis. Hydrogenases also recapture the reducing power lost in nitrogen fixation by the unavoidable formation of H_2 as a by-product in N_2 reduction by nitrogenase. Alternatively, hydrogenases can drive the reverse reaction and dispose excess electrons in the form of H_2 . Four main classes of hydrogenases have been identified.

The [NiFe] hydrogenases, contain both metals and are the most numerous, followed by the [NiFeSe] enzymes which also contain one selenocysteine residue as a ligand for Ni. There are also Fe-only (4) and metal-free hydrogenases (5). Depending on the source, [NiFe] hydrogenases contain different numbers of metal clusters, but there is always one Ni-Containing cluster and at least one Fe-S cluster. The former is the site of H₂ binding and the latter is being involved in electron transfer. Many hydrogenases also contain additional Fe-S clusters or a more complex subunit structure; some are soluble and others are membrane-bound (6).

The first crystal structure of a [NiFe] hydrogenase was obtained for the oxidized form of *D. gigas* at a resolution of 2.54 Å (7). Subsequently, X-ray structures from three other organisms have also been obtained, for the oxidized form of *D. fructosovorans* (8,9), for the oxidized and reduced forms of *D. vulgaris* (Miyazaki) (10) and for the reduced form of *Dm. baculatum* (11), where the last one is the first [NiFeSe] hydrogenase structure. This structure, see Fig. 1, is the one used as a starting point for the present structural optimizations. The most surprising feature of the Ni-Fe dimer is the ligand structure around iron with three diatomic ligands. The identity of these ligands as two CN and one CO ligand, which is unique for a biochemical system, was demonstrated by infrared spectroscopy for *C. vinosum* and *D. gigas* (12). For *D. vulgaris* one of these ligands was instead suggested to be an SO, based on an analysis of the high resolution X-ray structure (10). There are also four cysteine derived ligands, where two are bridging between the metals and two are terminal nickel ligands. In the [NiFeSe] enzyme, selenium is substituted for sulfur in one of these terminal ligands. Also shown in the figure is the most nearby Fe-S cluster, to which the electrons are transferred from the Ni-Fe dimer, and two possible proton transfer pathways. One of these pathways leads from the bridging Cys495 ligand straight out to the surface via hydrogen bonds over His77, His430, and Tyr442. This pathway is reminiscent of the one in Ni-CO dehydrogenase (13,14). The other proton transfer pathway starts at CysSe492 and goes over Glu23 and several conserved water molecules, of which two are shown in the figure, out to a Mg-complex (not shown) near the surface (2).

Extensive EPR spectroscopic studies indicate the accessibility of a number of several different enzyme states. Under aerobic conditions, an inactive form is isolated which can show two types of EPR signal, known as Ni-A (unready form) and Ni-B (ready form), as well as containing an EPR-silent form. The ready form can be rapidly activated by H₂ in the presence of certain electron carriers, to give the active form

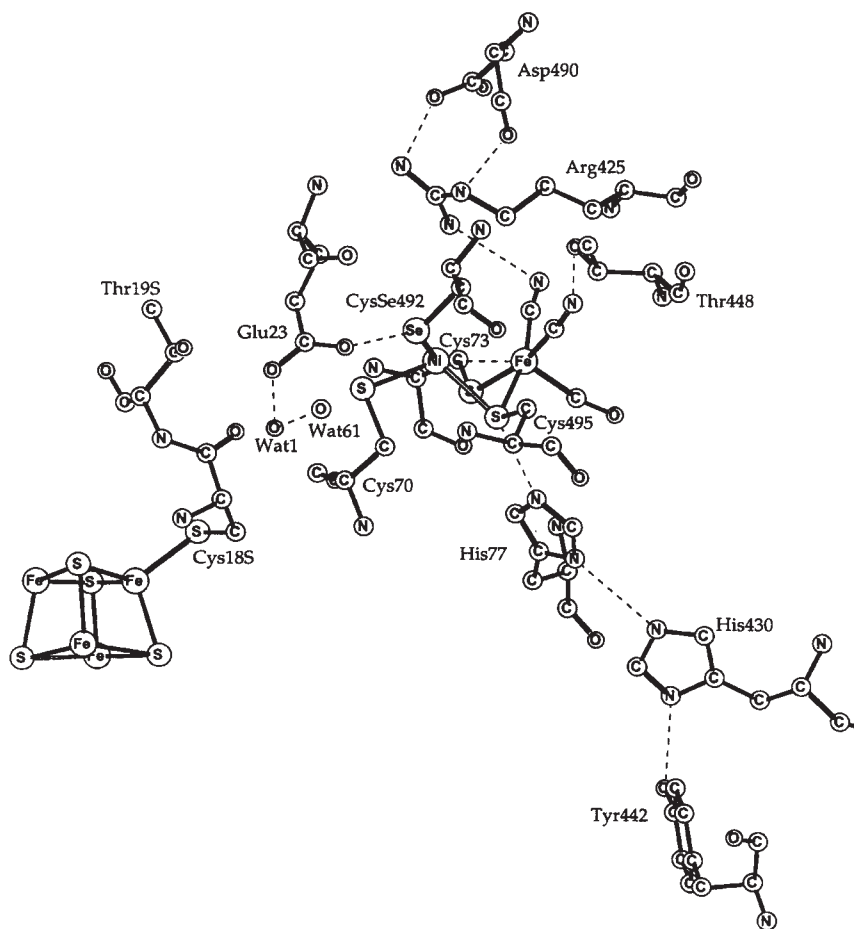


FIG. 1. The X-ray structure for the reduced form of the NiFe dimer in hydrogenase from *Desulfomicrobium baculatum*.

that shows the Ni-C EPR signal; reduction of this form yields two further EPR-silent forms. The Ni-A form is only activated by H_2 over several hours. The Ni-C form is sensitive to visible light and below 100 K a change in the EPR signal to Ni-C' is seen on irradiation. CO is a competitive inhibitor with H_2 and photolysis of the CO-inhibited form also gives the Ni-C' signal. The X-ray structure in Fig. 1 has been identified as a mixture of the Ni-SI (silent), Ni-C, and Ni-R (reduced) states. The Ni-Fe distance is quite short with 2.5 Å and may suggest a bridging hydride ligand. The Ni-Fe distance for the X-ray structure

of *D. gigas* obtained under aerobic conditions, mainly containing the Ni–A state, is longer with 2.9 Å and is believed to have an oxygen derived bridging ligand. In contrast, for the oxidized form of *D. vulgaris* (Miyazaki), mainly containing the Ni–B state, a distance of only 2.55 Å was found and the bridging ligand was suggested to be sulfur derived. Another interesting feature of the X-ray structure in Fig. 1 is that one of the Ni–S distances is unusually long, the one to Cys495 of 2.6 Å. A possible reason for this will be suggested below.

Several theoretical studies have been made in attempts to clarify the mechanism of [NiFe] hydrogenase (15–19). The main focus has been on the activation of dihydrogen but other questions concerning the mechanism have also been addressed. Even though substantial progress has been made, several important questions have not yet been resolved (20). Uncertainties in the modeling of the Ni–Fe active site concerns, for example, the total charge state and the influence of residues outside the first coordination shell. For these reasons, the oxidation state of the active species that cleaves dihydrogen is not yet clear. The structures from which electrons and protons are transferred from the Ni–Fe complex are not clear either. In order to address these questions, another hybrid density functional theory (DFT) study has been undertaken. The model adopted is more advanced than the ones previously used to investigate the dihydrogen cleavage mechanism. Important, possibly charged, residues in the second coordination shell have been included and their positions have been partly fixed from the X-ray structures in order to avoid artificial, large rearrangements. Transition states have been fully optimized. Two different proton transfer pathways have been investigated, the ones shown in Fig. 1.

II. Computational Details

The calculations were performed in three steps. For each structure considered, a geometry optimization was performed using the hybrid density functional B3LYP method (21). For open shell systems unrestricted DFT was used. In this first step, a standard valence double zeta basis set (the *lacvp* basis set) was used. Since models including also second shell amino acid residues were used, a full geometry optimization is not possible. The second shell residues would then move in unrealistic ways. For this reason, one atom of each amino acid residue was frozen from the X-ray structure. This procedure has been found to work very well in previous studies (22,23). It might be thought that this

procedure could lock the structure too much, but this is not the experience so far. On the contrary, in the present study it was actually found that two atoms, rather than one, had to be frozen in one residue, the arginine, in order to avoid artificial structures. When relative energies are calculated it is obviously necessary to use structures where identical schemes for freezing the atoms have been used. The same basis set was used also for the calculations of the Hessians. These Hessians were used to determine the structures of the transition states and to obtain zero-point vibrational effects. The entropy effects calculated could not be used since some coordinates were fixed during the optimizations.

In the second step, the B3LYP energy was evaluated at the optimized geometries using a larger basis set, the *lacv3p*** basis set, which is of triple zeta quality and uses a single set of polarization functions on all atoms.

In the third step, the surrounding protein was treated with a self-consistent reaction field method, using a Poisson–Boltzmann solver. The dielectric constant of the homogeneous dielectric medium was set equal to 4.0 in line with previous modelling of enzymes (24). The probe radius was initially set to 1.40 Å corresponding to the water molecule. However, a few cases of unrealistic effects were encountered and the radius was therefore increased to 2.50 Å. No geometry optimizations including the dielectric continuum were made since the calculated dielectric effects were found to be quite small. The calculations can thus in short-hand notation be written as B3LYP/*lacv3p*** energies including zero-point and solvent contributions based on B3LYP/*lacvp* geometries. All the calculations were carried out using the Jaguar program (25). Recent experience using the present models and methods can be found in recent reviews (23,26,27).

III. Results and Discussion

The mechanism for dihydrogen activation, including proton and electron transfers, was studied for [NiFe] hydrogenase with several different models. The results for two of these models will be described below. Both these models obviously contain the first shell ligands. Standard charges of the ligands lead to a charge of the core of the Ni–Fe complex of -2 for the NiFe(II,II) oxidation state. Apart from the first shell ligands, those ligands in the active site region that might be charged are also included. This means that Arg425, which hydrogen-binds to one of the cyanides, is included as a positively charged formamidinium group.

Since previous studies, using smaller models of enzyme active sites (23,26,27), have found that including a charged residue without its charge-balancing counter ion can lead to artifacts, Asp490 is also included in the model as a formate anion. A large number of calculations were initially performed without the aspartate and the results were indeed found to be unstable in several cases. For example, in one case for the NiFe(III,II) state a proton became transferred from the arginine to the cyanide leading to large distortions of the geometry. This did not happen for the model including Asp490. An obvious residue to also include in the model is Glu23 which is hydrogen bonded to CysSe492, and which is also a likely member of a proton transfer pathway (2). Since there is a hydrogen bond between Glu23 and CysSe492, one of these residues should be protonated. The calculations show that Glu23 is the one that is most likely protonated and is therefore modeled as a neutral formic acid. Apart from Arg425, Thr448 also hydrogen bonds to the cyanide ligands of iron. However, since Thr448 is neutral the effect of this ligand is expected to be small. This was tested in a number of calculations which confirmed this expectation and Thr448 was therefore left out of the model. Another possibly charged residue is His77 which is also included in the model. The charge state of this residue is very uncertain and will in fact define the two leading models discussed here. In a recent study by Stadler *et al.* (17), the charge state of this histidine was carefully investigated using calculated magnetic resonance parameters and it was concluded that for the Ni-A state this histidine (His72 in *D. gigas*) should be uncharged. A neutral His77 was therefore chosen initially also in the present study. However, as the results were summarized, it became of interest to investigate also the protonated form of His77. The results for both these models, which differ at significant places, will be described in two different subsections below. The unprotonated His77 model is shown in Fig. 2. In the third subsection the effect of the selenium substitution will be discussed.

A. THE MODEL WITH AN UNCHARGED His77

The first question investigated is the oxidation state of the reactant for dihydrogen cleavage. Several different models were used and the conclusion from the most realistic models is that it is the NiFe(II,II) state that activates dihydrogen. This is different from the conclusions drawn from some previous studies using smaller models (15,16) where the NiFe(III,II) state was suggested as the active state. The origin of this difference is the choice of charge state of the NiFe-core. In the

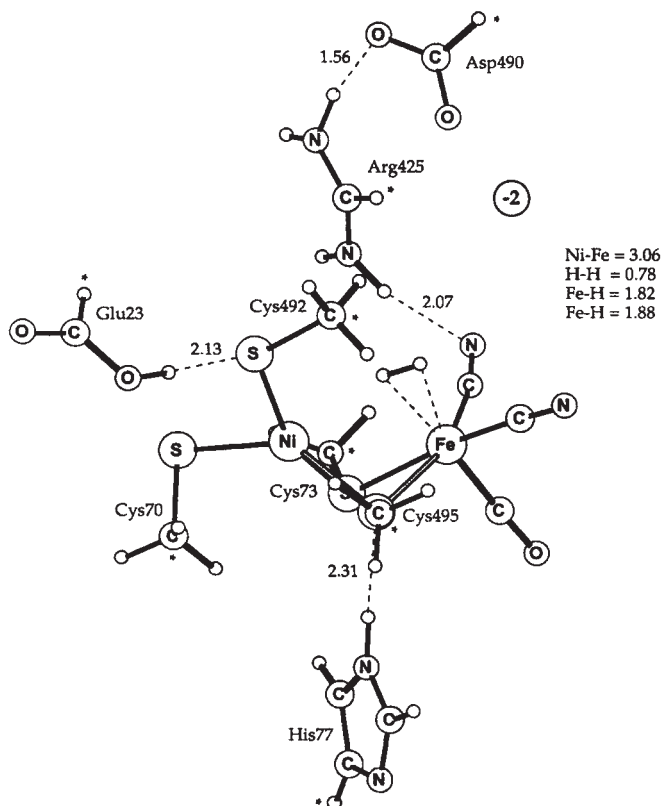


FIG. 2. Molecular hydrogen complex (structure 2) in [NiFe] hydrogenase. The oxidation states are Ni(II) and Fe(II). Distances are given in Å. Atoms marked with * were kept frozen from the X-ray structure during the optimization.

present study the charge of the core is -2 (see above), while in the previous studies it was neutral. This difference has a surprisingly large effect on the potential curve for dihydrogen cleavage. With the neutral model the H_2 cleavage is strongly endergonic for the NiFe(II,II) oxidation state but becomes quite exergonic with a charge of -2 . This shift of the appearance of the potential surface also leads to a realistic barrier for the NiFe(II,II) bond cleavage with a charge of -2 . In contrast, the H_2 cleavage for the NiFe(III,II) state becomes unreasonably exergonic with the charge of -2 . It should be added that the NiFe(II,II) state as the active state has been suggested experimentally (1) and was for that reason chosen in two other previous theoretical studies of the hydrogenase mechanism (17,18).

The next question investigated is where H_2 binds on the NiFe-dimer. The result of the optimization for the closed shell singlet NiFe(II,II) state is shown in Fig. 2. As seen in the figure, dihydrogen prefers to bind on iron. This is the same result as obtained in previous studies (15,16) but different from what has been suggested from experiments on the enzyme. Xenon binding experiments have located a likely path for dihydrogen transport to the active site which ends at nickel (8,17), which was therefore suggested as the site for dihydrogen binding. Also, X-ray crystal structures show that a CO-inhibitor binds at nickel, not at iron (10). The nickel binding site was therefore carefully investigated using the model in Fig. 2 but no local minimum was found. The main reason for this is undoubtedly the higher repulsion from the larger number of d-electrons on nickel than on iron. For iron there is an empty d-orbital pointing towards dihydrogen, but this is not possible for nickel. From the experience of organometallic dihydrogen model complexes, the iron site is the expected site for dihydrogen binding. This site for binding and activation would also give a natural explanation for the unusual choice of iron ligands. These ligands force a low-spin coupling on iron which is ideal for activating dihydrogen.

In order to shed further light on the question of dihydrogen binding, CO binding was also investigated. The calculations indeed gave the most stable state for CO bound on nickel in agreement with experiments (10). Two states were investigated, the closed shell singlet and the open shell triplet states. The triplet state was actually found to be most stable with a binding energy of 13.9 kcal/mol (without entropy contributions, see Section II). The singlet binding energy is 5.5 kcal/mol. Since B3LYP is known to sometimes artificially favor high-spin states (28), the calculations were redone with only 15% exact exchange (instead of 20%) but the triplet remained the lowest state by 4 kcal/mol. An interesting feature of the optimized structure is that NiCO is bent, which was also observed in the experimental structure. The Ni-C-O bond angle is 155° for the singlet and 165° for the triplet. The experimental angle is 160° . The reason for the bending is the close steric interaction with Arg425. The presence of this residue is also the reason CO prefers to bind at an external nickel site rather than on iron or in between nickel and iron. The steric interaction to Arg425 is much smaller for H_2 than for CO and therefore allows dihydrogen to preferably bind to iron. However, it should be added that the first interacting site (of van der Waals type) for dihydrogen cannot be predicted from the present type of calculations. What is indicated by the present results is that the *activation* of dihydrogen should start at the Fe site.

Even though H_2 prefers to bind to iron, see Fig. 2, it is only a local minimum. In fact, the binding is calculated to be endothermic by 6.3 kcal/mol. A surprising effect of +3.3 kcal/mol comes from zero-point vibrational effects. Entropy effects, which are not included, are expected to increase this energy difference further. However, other enzyme effects like van der Waals interactions, are expected to lower the energy difference (29). A repulsive binding energy between H_2 and the NiFe-complex might at first sight appear as unreasonable for a system particularly designed to activate H_2 , but the final energetics for the entire catalytic cycle of hydrogenase, see further below, does in fact make an endergonic binding of H_2 quite logical. On the other hand, it is still significant that there is a local minimum for binding H_2 on iron. This minimum implies a favorable electronic interaction between H_2 and the metals which will allow an effective cleavage of H_2 with a low barrier.

With dihydrogen positioned as in Fig. 2 there are essentially only two possible mechanisms for cleaving H_2 heterolytically. Both these mechanisms leave the resulting hydride bound in between iron and nickel. In the first mechanism the proton goes to the bridging Cys495 while in the other one the proton goes to the terminal CysSe492. In previous studies the bridge cleavage has been favored in actual transition state optimizations, but the terminal cleavage has also been suggested from structural considerations (16). For the present model, with an uncharged His77, the bridging mechanism is found slightly favored. The fully optimized TS structure is shown in Fig. 3. The barrier counted from the dihydrogen minimum in Fig. 2 is only 4.6 kcal/mol, but with the additional energy of 6.3 kcal/mol to reach the molecular minimum, the total barrier becomes 10.9 kcal/mol. In the process of cleaving H_2 , the Ni–SCys495 distance increases significantly since the Ni–S bond is replaced by a Ni–H bond. The Ni–Fe bond distance remains essentially the same from the molecular minimum to the TS, but then shortens due to the formation of the bridging hydride. The hydrogens remain close both to iron and nickel during the reaction.

The fully optimized transition state for the alternative terminal pathway is shown in Fig. 4. Notable structural effects are that the hydrogen bond from Glu23 shifts from Cys492 to Cys70, and that the hydrogens in this mechanism stay very close to nickel. The Ni–Fe distance shortens significantly by 0.32 Å from the molecular minimum to the TS. The barrier for this pathway is only slightly higher than for the bridging pathway by 1.1 kcal/mol. Replacing sulfur by selenium on Cys492 actually increases this energy difference slightly, see further below. The preference for the bridging pathway is thus very small and

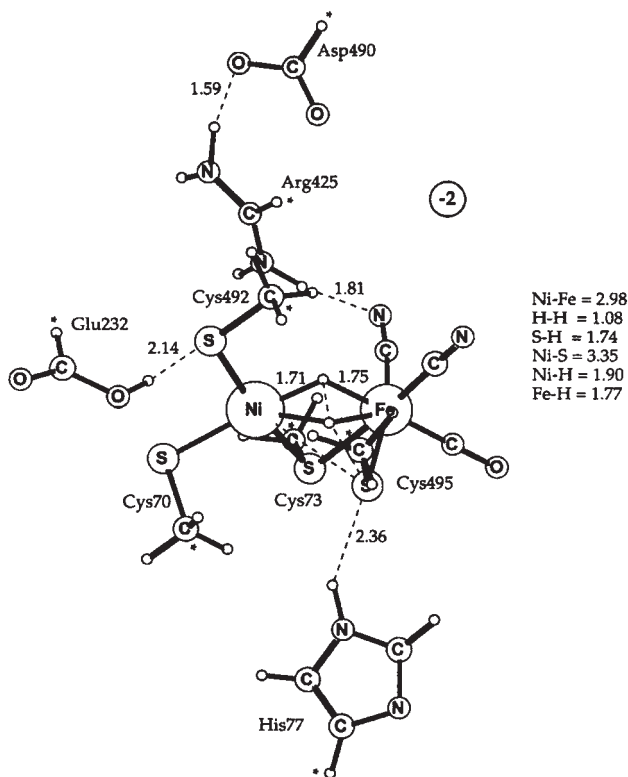


FIG. 3. Fully optimized transition state (structure 2-3 TS) for H-H bond cleavage in [NiFe] hydrogenase. The oxidation states are Ni(II) and Fe(II). Distances are given in Å.

cannot be safely predicted by the present methods and models. However, it can be argued that the structural changes for the two pathways are so similar that the calculated relative effect should be taken with some significance. It can be noted that the bridging reaction pathway is the same as the one obtained in some previous studies (15) but that the oxidation states are different.

The products of the heterolytic H-H bond cleavage show some minor differences for the two pathways. The Ni-Fe distance is 2.76 Å for the bridging pathway, while it is as short as 2.66 Å for the terminal pathway. The reason is that Cys492 remains bridging for the terminal pathway. The reaction energies are still quite similar. The product of the bridging pathway is 12.8 kcal/mol below the molecular minimum, and 11.4 kcal/mol below this minimum for the terminal pathway.

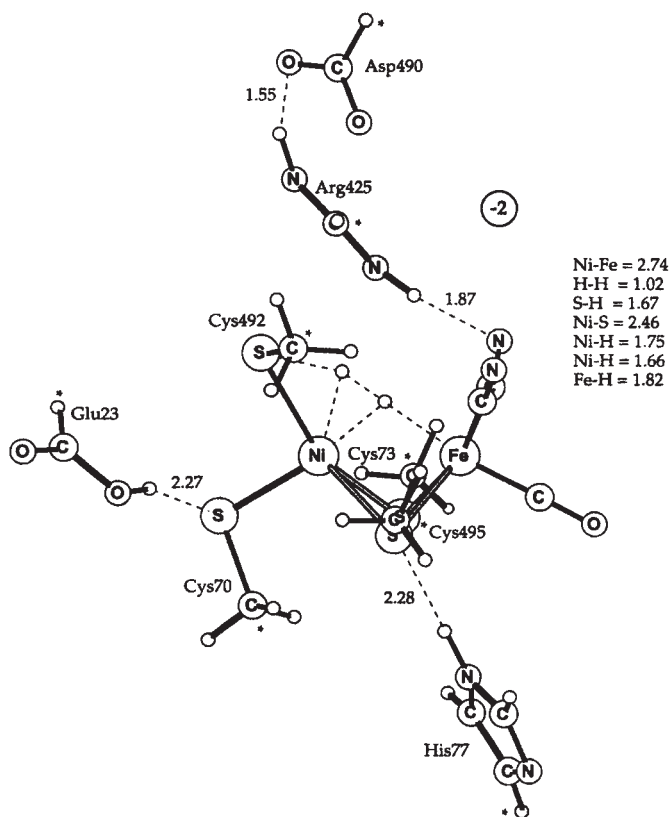


FIG. 4. Alternative transition state for H-H bond cleavage in [NiFe] hydrogenase. The oxidation states are Ni(II) and Fe(II). Distances are given in Å.

The consequence of these rather large exergonicities will be discussed further below.

Since the barrier is slightly lower for the bridging pathway, it is here assumed that the reaction takes this pathway (when His77 is unprotonated). The next step is then to get rid of one proton and one electron. The electron transfer should occur at a point where the electron transfer energy has a minimum and where the initial NiFe(II,II) and final NiFe(III,II) states have very similar geometries. A point wise search led to an approximate transition state for the electron transfer, shown in Fig. 5. The electron transfer is strongly coupled to proton transfer from Cys495 to His77 as seen from the proton distances to sulfur of 1.61 Å and to nitrogen of 1.40 Å. This structure is obviously not a minimum for any of the potential surfaces involved. On the reactant NiFe(II,II)

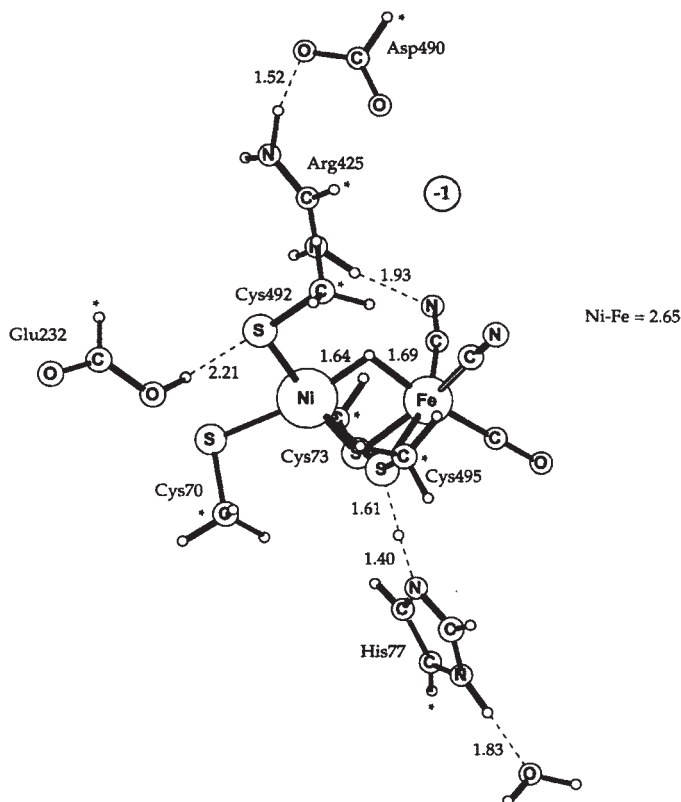


FIG. 5. Approximate transition state (structure 4) for the first electron transfer in [NiFe] hydrogenase. The oxidation states are Ni(II-III) and Fe(II). Distances in Å and spins larger than 0.1 are marked.

surface an energy of 8.0 kcal/mol is required to reach this point and on the product NiFe(III,II) state the energy decreases by 8.9 kcal/mol when the system reaches its next minimum with the proton on His77. The first of these energies will be part of the barrier for the electron transfer, which will also have contributions from reorganisation effects on the accepting Fe-S cluster, see Fig. 1. The calculated electron affinity of the reactant at the transition state structure is 73.3 kcal/mol and proton affinity of His77 is 299.2 kcal/mol for the product. Another energy of relevance for the energetics of the catalytic cycle of hydrogenase is the energy difference between the reactant and the product, considering that all together one entire hydrogen atom has left the system. The binding energy of this hydrogen atom is 56.4 kcal/mol.

This is a reasonable energy, fairly close to half of the binding energy of H_2 (103.5 kcal/mol) as expected for a hydrogenase enzyme. Further implications of these energies will be discussed at the end of this section where an energy diagram is constructed.

With the proton on His77 the question is how this proton should reach the surface. As already mentioned in the introduction, there is indeed a straight proton transfer pathway from His77 to the surface going via His430 and Tyr442. This pathway is very similar to the one identified in nickel-containing CO dehydrogenase (14). Whether this proton transfer pathway is actually used will be discussed further below.

The product of the previous electron and proton transfer step is thus a NiFe(III,II) state with a bridging hydride. The assignment of the oxidation states is unproblematic in this case since the spin-population on iron is 0.00 and the one on nickel 0.95. The Ni(I) oxidation state can be ruled out on electrostatic grounds since nickel is surrounded by five negative groups. The distance between nickel and iron is quite short with 2.63 Å. The reason for this is the presence of the bridging hydride. The question whether a bridging hydride is needed or not to obtain such a short distance, has been debated (20). During the course of this study a few complexes with short Ni–Fe distances without a bridging hydride have in fact been encountered, but these systems turned out to be poor models for any state of the hydrogenase catalytic cycle. An interesting case of this type appeared for one of the models where Asp490 was left out, which led to a substantial shortening of the Ni–Fe bond to 2.60 Å for the NiFe(III,II) state. At the same time a very strong hydrogen bond between Arg425 and one of the cyanides could be noted. To investigate this effect further Arg425 was simply replaced by a proton on the cyanide, which led to a short Ni–Fe bond of 2.61 Å even for the closed shell singlet state (corresponding to NiFe(II,II)). It should be noted that no constraints from the X-ray structure were present for that model. The reason for the shortening of the bond is thus of purely electronic origin. A likely interpretation of this effect is that the added proton removes part of an electron from iron to form the CN–H bond, and induced some Fe(III) character. An additional bonding possibility thus appeared for iron and the bond formed was to nickel leading to the short bond. For the more realistic models described here no such effect was found, and the only short Ni–Fe bonds were therefore found with a bridging hydride.

An interesting aspect of the bridging hydride structure concerns the direction of the Jahn-Teller axis on nickel. With the hydride, there are five ligands around nickel and one of these are therefore forced to

be axial. Since the other four ligands should be in one plane, there is essentially only one possible axial ligand and this is Cys495, which thus forms a longer Ni–S distance than the other ones, 2.55 Å compared to 2.30–2.35 Å. The hydrogen bond to His77 stabilizes this structure further. It is interesting to note that the Ni–S distances of the X-ray structure of the reduced enzyme (11) actually shows exactly the same distortion of the cysteine ligands, see Fig. 1. This has led to the suggestion of a possible involvement of the nickel triplet state (30,31). From the present calculations it is instead suggested that the distortion is due to the presence of a bridging hydride, which is too small to be seen in the X-ray structure. With the presence of the hydride the structure is quite normal with a plane with four ligands with short distances, and with one axial ligand with a longer distance.

The next step of the catalytic cycle is the only one where a redox reaction is involved (apart from the obvious electron transfers). The bridging hydride should move to one of the cysteines. There are a few possibilities. One of them is to move the hydride to Cys495 with the idea to use the same proton transfer pathway over His77 as for the previous step. However, the barrier was found to be prohibitively high with 25.1 kcal/mol. In this case the transfer to Cys492 is much easier with a barrier of only 6.5 kcal/mol. The optimized transition state is shown in Fig. 6. The reason for this difference is that with a transfer to Cys492, the coordination around nickel can stay essentially the same along the entire transfer, since both the hydride and Cys492 are in the stable coordination plane. In contrast, for the transfer to Cys495, the hydride is forced out of this plane to the less weakly coordinated position for the axial Cys495.

The product of the hydride transfer is thus in a NiFe(I,II) oxidation state and with a proton on Cys492. In order to use the same proton transfer pathway as in the step following dihydrogen cleavage, the proton needs to move from Cys492 to Cys495. Several pathways were investigated, a direct one and one over Cys70, for example, but they all had prohibitively high barriers. Instead, a proton transfer pathway suggested by experiments may be used (2). This pathway goes over Glu23, then over a few conserved water molecules (Wat1 and Wat2 are shown in Fig. 1), and finally to a Mg-complex near the surface. Moving the proton along this pathway, and proceeding as in the previous search for an electron transfer transition state, the approximate transition state shown in Fig. 7 was found. This transition state differs from the immediate product of the hydride transfer in that both Cys492 and Glu23 have swung around, with their protons pointing out toward the proton channel. The positions of the protons do not

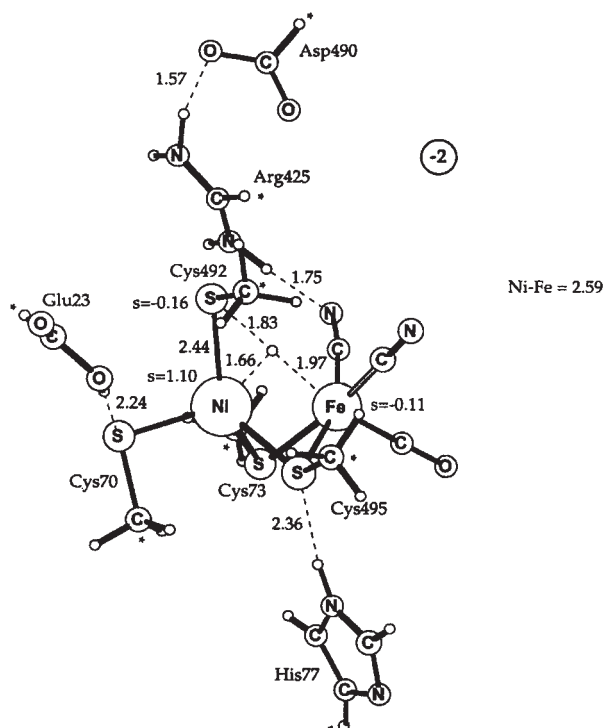


FIG. 6. Fully optimized transition state (structure 6-7) for hydride transfer to Cys492 in [NiFe] hydrogenase. The oxidation states are Ni(I-III) and Fe(II). Distances in Å and spins larger than 0.1 are marked.

indicate a significant proton-coupling of the electron transfer as in the transition state in Fig. 5, where the proton is in between two groups, Cys495 and His77. The calculated electron affinity of the structure in Fig. 7 is 75.4 kcal/mol and the proton affinity (after the electron has left) is 299.5 kcal/mol. Together, the transfer of an electron and a proton leads to a transfer of a hydrogen atom with a binding energy of 59.9 kcal/mol. All these values are very close to those of the previous electron and proton transfers in Fig. 5 of 73.3 kcal/mol, 299.2 kcal/mol, and 56.4 kcal/mol, respectively. This kind of similarity is necessary if energy should not be wasted in the process. A much smaller electron affinity in one case would lead to an exergonic, wasteful electron transfer in one of the electron transfers since the electron acceptor is the same in both cases.

The above electron and proton transfers complete one cycle of the hydrogenase enzyme. The entire mechanism as suggested above is

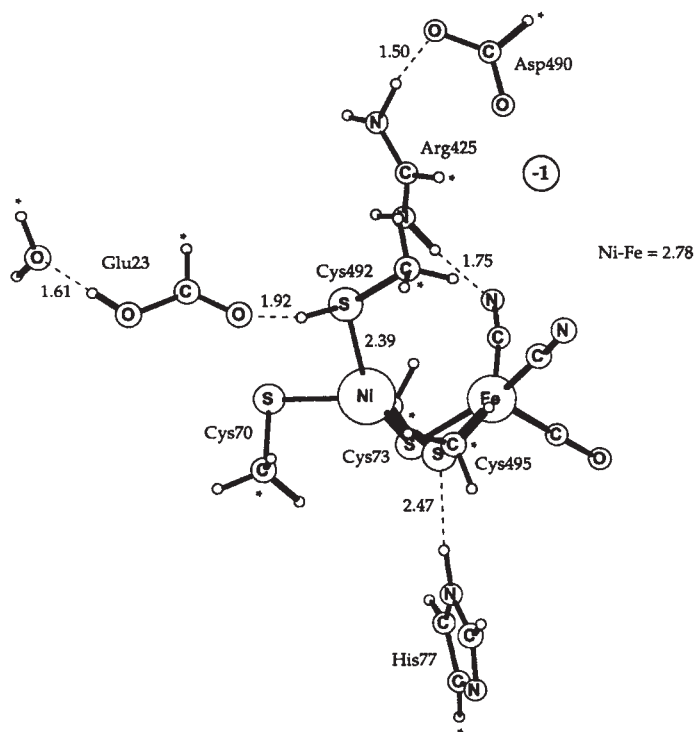


FIG. 7. Approximate transition state (structure 8) for the second electron transfer in [NiFe] hydrogenase. The oxidation states are Ni(I-II) and Fe(II). Distances are given in Å.

shown in Fig. 8. When the energetics for this scheme was constructed a few possible problems could be noted. First, the calculated electron transfer energies (electron affinities) of 73.3 and 75.4 kcal/mol can be translated to redox potentials. If this is done using the standard calomel electrode of 4.19 V (32-34), redox potentials of -1.0 V and -0.9 V, respectively, are obtained. The redox potentials of the 4Fe-4S clusters of [NiFe] hydrogenase should be around -0.3 V (2). The difference in these redox potentials of 0.7 V appears quite large. A few comments can be made in this context. First, redox potentials are known to be rather difficult to calculate and depend, for example, on the size of the model. A second comment is that the redox potentials of the [NiFe] and 4Fe-4S clusters need not be exactly the same. Another problem with the above results concerns the calculated energetics for the reverse process of dihydrogen formation, considering that some enzymes catalyze

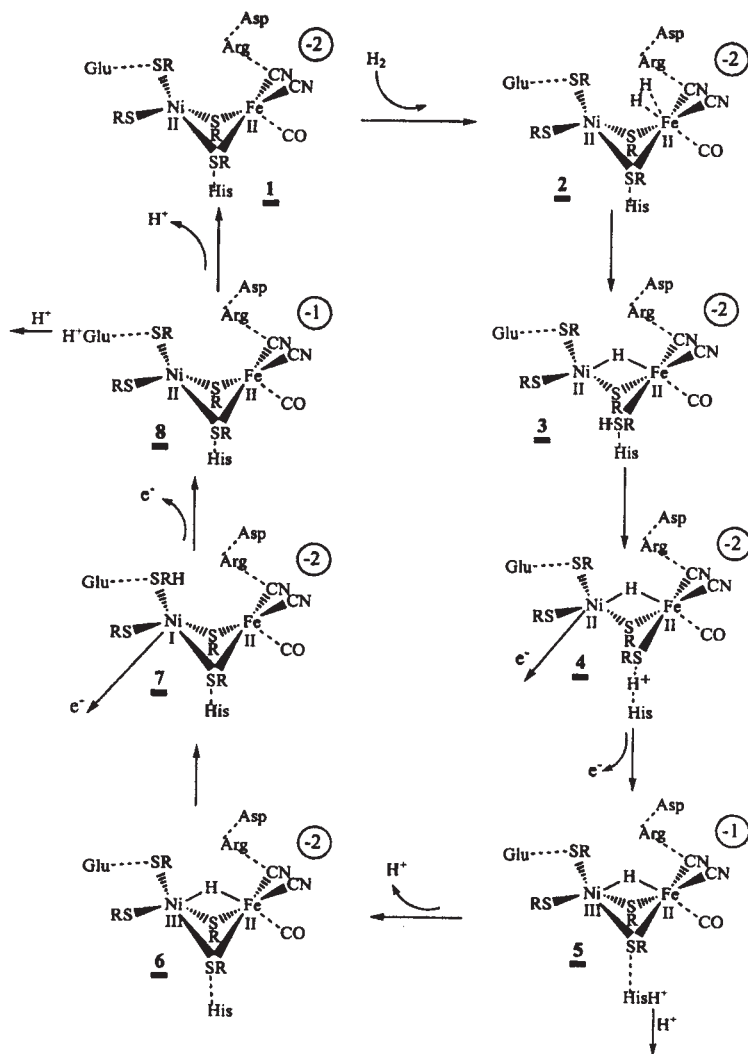


FIG. 8. Suggested catalytic cycle for [NiFe] hydrogenase with an uncharged His77.

that process. Since the barrier for dihydrogen cleavage is 10.9 kcal/mol and this process is exergonic by 6.5 kcal/mol (starting from a system with dihydrogen at a long distance from the complex), the reverse process will have a barrier of 17.4 kcal/mol, which appears somewhat high since this would correspond to a rate of about 1.0 s^{-1} .

The experimental barrier for the forward reaction is only around 13 kcal/mol (2). While this discrepancy is not alarming (it is in fact rather normal for the present method) it might still indicate a problem in the model. A third possible problem of the reaction scheme in Fig. 8 is that two different proton transfer pathways are being used rather than one. This is not necessarily a problem either but it is rather unusual. For these reasons an alternative model was also investigated, and this is described below.

B. THE MODEL WITH A CHARGED His77

The alternative model discussed here uses a protonated His77. There were three reasons for this choice. First, it is expected that increasing the charge of the complex would increase the calculated redox potentials to become closer to those measured for the 4Fe–4S cluster. Second, a proton on His77 is likely to block the proton transfer pathway over the Cys495 residue after the dihydrogen bond cleavage, which might then lead to the same proton transfer pathway for both steps in the catalytic cycle. Finally, a proton on His77 might decrease the exergonicity of the dihydrogen bond cleavage step, since it blocks the most favorable pathway, and may then make the reverse reaction more feasible. The recent theoretical investigation by Stadler *et al.* (17), where it was found that His77 is most likely unprotonated in the Ni–A state, might argue against using a model where it is protonated. However, the dihydrogen bond cleavage does not occur for the Ni–A state and a different protonation for another state is certainly still possible.

The general appearance of the binding of molecular dihydrogen is the same for the protonated His77 model as for the unprotonated one. The binding is preferred on iron and the binding is endothermic by 4.4 kcal/mol as compared to 6.3 kcal/mol in the unprotonated case. The barrier for dihydrogen cleavage following the bridging mechanism to Cys495 is now 12.0 kcal/mol compared to the previous 10.9 kcal/mol. As expected, the proton on His77 has made this pathway less likely. The terminal pathway going over Cys492 actually has a somewhat lower barrier than before, 7.8 kcal/mol compared to 12.0 kcal/mol previously. This means that if His77 is protonated the favored pathway is now the non-bridging one, leaving the proton on Cys492 rather than on Cys495.

The next step of electron and proton transfer occurs for a structure similar to the one in Fig. 7. The calculated electron affinity for this structure is 91.4 kcal/mol and the proton affinity of the product is 284.4 kcal/mol. The electron affinity can be translated to a redox

potential of -0.23 V, which is much closer than before to the experimental one of -0.3 V for the 4Fe-4S cluster. The calculated proton affinity goes, as expected, in the opposite direction and is now substantially smaller than the previous value of 299.2 kcal/mol. The effects of protonating His77 on the electron and proton affinities, are both about 15 kcal/mol, but in opposite directions.

The next step is the hydride transfer which occurs in the same way as before. The calculated barrier is only 3.0 kcal/mol. After the minor proton motion as described in Section III.A, there is again an electron and proton release. The calculated electron affinity is now 90.7 kcal/mol corresponding to a redox potential of -0.26 V. The proton affinity of the product is 289.9 kcal/mol. The entire catalytic cycle for the case with the protonated His77 is shown in Fig. 9.

From the calculated values described above, energy diagrams can be constructed for the catalytic cycles using the two different models. These diagrams are shown in Fig. 10. In order to make the diagrams for the two models comparable they were both calibrated to lead to an exergonicity for the entire cycle of 1.0 kcal/mol. This value was selected as a reasonable value which drives catalysis forward but still does not waste too much energy. This calibration leads to endergonic proton and electron releases, where the differences between the different steps and models are taken directly from the calculated values. An alternative procedure would have been to actually use the calculated (and experimental for 4Fe-4S) redox potentials and the calculated proton affinities (pK_a values). However, considering the inherent difficulty to accurately predict these values by calculations, it was considered more informative to construct energy diagrams based on a reasonable calibration. This will undoubtedly lead to more accurate energy diagrams.

With the relatively large difference of 15 kcal/mol for the calculated redox potentials and pK_a values for the two models, the most interesting aspect of the energy diagrams in Fig. 10 is that they are remarkably similar, in particular considering the inherent uncertainty of the B3LYP energies of 3–5 kcal/mol. The largest difference appears for the barrier for hydride transfer which is 4.4 kcal/mol lower when His77 is protonated (counted from the resting state **3**). With these small differences it is not clear which model corresponds best to experiments. Since both barriers are lower for the case with a protonated His77, and the redox potentials are more reasonable, it can be argued that this is the best model. This model also uses only one proton transfer pathway, which is a more attractive solution. However, this argument is not very strong.

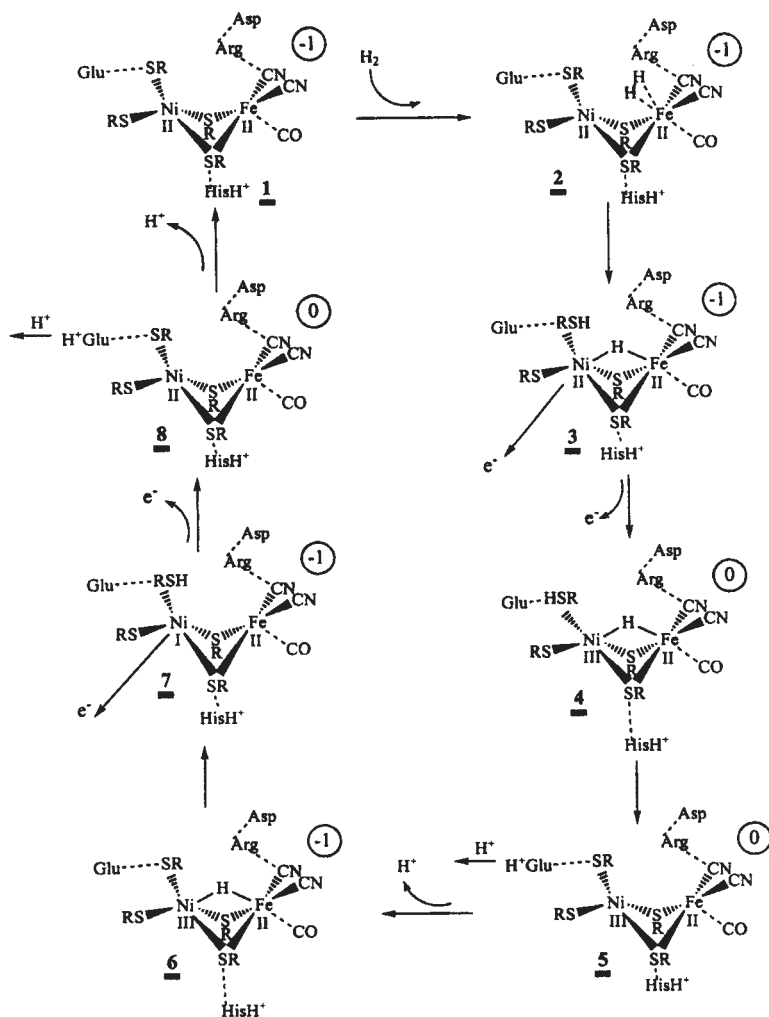


FIG. 9. Suggested catalytic cycle for [NiFe] hydrogenase with a charged His77.

An important point to note in the energy diagrams is that the resting state for H-H bond cleavage is not structure 1 but 3 of the previous cycle. This means that the rate-limiting step of H-H bond cleavage has a barrier of 17.4 kcal/mol for the unprotonated His77 case and 17.5 kcal/mol in the protonated case. These barriers are somewhat higher than the barrier of 13 kcal/mol indicated by experiments but still within the normal uncertainty of 3-5 kcal/mol. From the experience

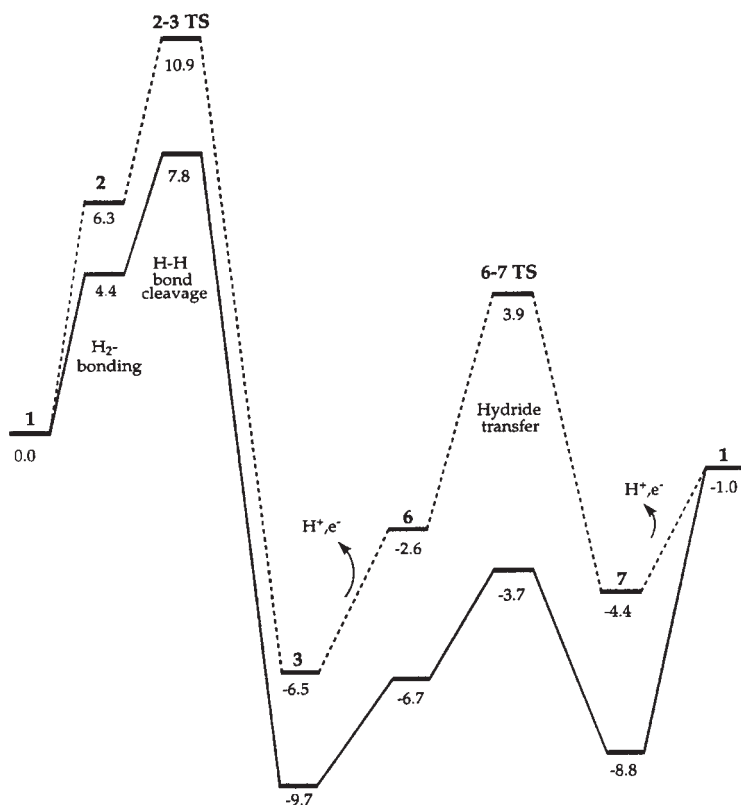


FIG. 10. Energetics for the suggested catalytic cycle for [NiFe] hydrogenase. The numbers for the structures are those from Fig. 9. The full line corresponds to a charged His77, while the dashed line is for an uncharged His77.

obtained so far (23,26,27), barriers using B3LYP for the present types of processes appear to always be somewhat high.

C. THE EFFECT OF THE SELENIUM SUBSTITUTION

In the final part of the present study the effect of substituting sulfur by selenium for Cys492 was investigated. As mentioned in the introduction, the [NiFeSe] enzymes represent one of the major classes of hydrogenases found in nature. Six different processes were investigated and the results are collected in Table I.

The most interesting aspect of the selenium substitution is how it affects the heterolytic H–H bond cleavage. For the H–H cleavage over

TABLE I

ENERGETIC EFFECTS (kcal/mol) OF SUBSTITUTING SULFUR BY SELENIUM IN Cys492

Process	Sulfur	Selenium
H–H cleavage ^a	5.3	5.6
H–H cleavage ^b	6.8	8.9
Hydride transfer	8.1	6.6
2nd e [−] -transfer	75.4	74.1
2nd H ⁺ -transfer	299.5	295.4
H ⁺ , e [−] -transfer	59.9	55.6

The model with an unprotonated His77 was used. Zero-point effects are not included.

^aCleavage over the Ni–Fe bridge. Proton goes to Cys495.

^bNon-bridging cleavage. Proton goes to Cys492.

the Ni–Fe bridge with the proton going to Cys495, the effect of the substitution is rather small. This is expected since Cys492 is not directly involved. The difference in the barrier heights of 0.3 kcal/mol is within the convergence threshold of the calculations. The effect is larger for the alternative cleavage where the proton ends up at Cys492. Still, the difference is only 1.5 kcal/mol. The fact that the barrier is lower for the sulfur case is not unexpected since selenium is more acidic than sulfur. It appears clear that selenium is not being substituted to make the heterolytic H–H bond cleavage more efficient.

For the hydride transfer the effect of the selenium substitution goes in the opposite direction compared to the H–H bond cleavage, with a 1.5 kcal/mol lower barrier for the selenium case. This effect can be explained by a larger mobility and acidity of selenium. The mobility is indicated by the bond distance to nickel which is 2.30 Å for the hydride in the sulfur case and 2.40 Å for the selenium case. At the transition states the Ni–S and Ni–Se distances increase to 2.44 Å and 2.61 Å, respectively. It is also interesting to note that the Se–H distance of 1.71 Å at the transition state is shorter than the S–H distance of 1.83 Å. Since selenium is more acidic this indicates a dominating hydride character of the hydrogen at the transition state.

For the first proton and electron transfers, the substitution is not expected to have any significant effects and these processes were therefore not studied. For the second electron transfer there is a small effect of 1.3 kcal/mol, with the lower redox potential in the selenium case. The effect on the second proton transfer is larger with 4.1 kcal/mol, which is the most significant effect that can be noted in the table. It is thus much easier to remove the proton from selenium than from sulfur, which is expected since selenium is more acidic.

IV. Conclusions

The entire catalytic cycle of [NiFe] hydrogenase has been studied using hybrid DFT with larger models than used previously. Several different models were used, the two leading ones with a charged and uncharged His77. Normalized to give the same exothermicity, these models give quite similar shapes of the energy curves. There are two main transition states to be passed, for H–H cleavage and for hydride transfer. The model with the charged His77 gives somewhat lower barriers for these steps. The charged model also gives more reasonable redox potentials. An interesting difference between the two models is that the uncharged model has to make use of two different proton channels, while the charged model uses only one, the one suggested by experiments. Both models agree that it is the NiFe(II,II) state that activates the H–H bond in agreement with experiments, but in disagreement with previous B3LYP results using smaller models. The reason for this is that inclusion of charged second shell residues stabilizes the -2 charge of the NiFe(II,II)-core substantially. The origin of the peculiar X-ray structure for the reduced enzyme with a short Ni–Fe bond and one long Ni–S bond was analyzed. The origin of the short Ni–Fe bond is suggested to be the presence of a bridging hydride, in agreement with most previous suggestions, but in disagreement with some. The presence of the hydride is also suggested to be the reason for the long Ni–S bond, since the hydride takes a position in the stable equatorial plane, where all ligands have short distances. This pushes one of the sulfur ligands out along the the less stable axial coordination.

The effects of substituting sulfur by selenium in Cys492 was also investigated. The largest effect was found for the proton affinity (pK_a -value) which is 4.1 kcal/mol lower for selenium, in line with its expected higher acidity. The barrier for hydride transfer is somewhat lower for selenium, while the H–H cleavage barrier is actually higher. The selenium substitution is therefore suggested to simplify hydride and proton transfers, but not to make H–H bond cleavage easier.

REFERENCES

1. Albracht, S. P. J. *Biochim. Biophys. Acta* **1994**, *1188*, 167–204.
2. Frey, M.; Fontecilla-Camps, J. C.; Volbeda, A. “*Handbook of Metalloproteins*”, Eds. Messerschmidt, A.; Huber, R.; Poulos, T.; Wieghardt, K.; Wiley: Chichester, **2001**, pp. 880–896.
3. Collman, J. P. *Nat. Struct. Biol.* **1996**, *3*, 213.

4. Peters, J. W.; Lanzilotta, W. N.; Lemon, B. J.; Seefeldt, L. C. *Science* **1998**, *282*, 1853–1858.
5. Thauer, R. K.; Klein, A. R.; Hartmann, G. C. *Chem. Rev.* **1996**, *96*, 3031–3042.
6. “*The Bioinorganic Chemistry of Nickel*”; Ed. Lancaster, J. R.; VCH: Weinheim, **1988**.
7. (a) Volbeda, A.; Charon, M. H.; Piras, C.; Hatchikian, E. C.; Frey, M.; Fontecilla-Camps, J. C. *Nature* **1995**, *373*, 580–587; (b) Volbeda, A.; Garcin, E.; Piras, C.; de Lacey, A. L.; Fernandez, V. M.; Hatchikian, E. C.; Frey, M.; Fontecilla-Camps, J. C. *J. Amer. Chem. Soc.* **1996**, *118*, 12989–12996.
8. Montet, Y.; Amara, P.; Volbeda, A.; Vernede, X.; Hatchikian, E. C.; Field, M. J.; Frey, M.; Fontecilla-Camps, J. C. *Nat. Struct. Biol.* **1997**, *4*, 523–526.
9. Rousset, M.; Montet, Y.; Guigliarelli, B.; Forget, N.; Asso, M.; Bertrand, P.; Fontecilla-Camps, J. C.; Hatchikian, E. C. *Proc. Natl. Acad. Sci. USA* **1998**, *95*, 11625–11630.
10. (a) Higuchi, Y.; Yagi, T.; Yasuoka, N. *Structure* **1997**, *5*, 1671–1680; (b) Higuchi, Y.; Ogata, H.; Miki, K.; Yasuoka, N.; Yagi, T. *Structure* **1999**, *7*, 549–566; (c) Ogata, H.; Mizoguchi, Y.; Mizuno, N.; Miki, K.; Adachi, S.-I.; Yasuoka, N.; Yagi, T.; Yamauchi, O.; Hirota, S.; Higuchi, Y. *J. Am. Chem. Soc.* **2002**, *124*, 11628–11635.
11. Garcin, E.; Vernede, X.; Hatchikian, E. C.; Volbeda, A.; Frey, M.; Fontecilla-Camps, J. C. *Structure* **1999**, *7*, 557–566.
12. Happe, R. P.; Roseboom, W.; Pierik, A. J.; Albracht, S. P. J.; Bagley, K. A. *Nature* **1997**, *385*, 126.
13. Dobbek, H.; Svetlitchnyi, V.; Gremer, L.; Huber, R.; Meyer, O. *Science* **2001**, *293*, 1281–1285.
14. Drennan, C. L.; Heo, J.; Sintchak, M. D.; Schreiter, E.; Ludden, P. W. *Proc. Natl. Acad. Sci. USA* **2001**, *98*, 11973–11978.
15. Pavlov, M.; Siegbahn, P. E. M.; Blomberg, M. R. A.; Crabtree, R. H. *J. Am. Chem. Soc.* **1998**, *120*, 548–555; Pavlov, M.; Blomberg, M. R. A.; Siegbahn, P. E. M. *Int. J. Quantum Chem.* **1999**, *73*, 197–207; Siegbahn, P. E. M.; Blomberg, M. R. A.; Wirstam, M.; Crabtree, R. H. *J. Biol. Inorg. Chem.* **2001**, *6*, 460–466.
16. Niu, S. Q.; Thomson, L. M.; Hall, M. B. *J. Am. Chem. Soc.* **1999**, *121*, 4000–4007; Fan, H.-J.; Hall, M. B. *J. Biol. Inorg. Chem.* **2001**, *6*, 467–473; Li, S.; Hall, M. B. *Inorg. Chem.* **2001**, *40*, 18–24; Niu, S.; Hall, M. B. *Inorg. Chem.* **2001**, *40*, 6201–6203.
17. Amara, P.; Volbeda, A.; Fontecilla-Camps, J. C.; Field, M. J. *J. Am. Chem. Soc.* **1999**, *121*, 4468–4477; Stadler, C.; de Lacey, A. L.; Montet, Y.; Volbeda, A.; Fontecilla-Camps, J. C.; Conesa, J. C.; Fernandez, V. M. *Inorg. Chem.* **2002**, *41*, 4424–4434.
18. De Gioia, L.; Fantucci, P.; Guigliarelli, B.; Bertrand, P. *Inorg. Chem.* **1999**, *38*, 2658–2662; De Gioia, L.; Fantucci, P.; Guigliarelli, B.; Bertrand, P. *Int. J. Quantum Chem.* **1999**, *73*, 187–195.
19. Stein, M.; van Lenthe, E.; Baerends, E. J.; Lubitz, W. *J. Am. Chem. Soc.* **2001**, *123*, 5839–5840; Stein, M.; Lubitz, W. *Phys. Chem. Chem. Phys.* **2001**, *3*, 2668–2675.
20. Maroney, M. J.; Bryngelson, P. A. *J. Biol. Inorg. Chem.* **2001**, *6*, 453–459.
21. Becke, A. D. *Phys. Rev.* **1988**, *A38*, 3098; Becke, A. D. *J. Chem. Phys.* **1993**, *98*, 1372; Becke, A. D. *J. Chem. Phys.* **1993**, *98*, 5648.
22. Pelmeshnikov, V.; Blomberg, M. R. A.; Siegbahn, P. E. M. *J. Biol. Inorg. Chem.* **2002**, *7*, 284–298.
23. Siegbahn, P. E. M. *Quart. Rev. Biophys.* **2003**, *36*, 91–145.
24. Blomberg, M. R. A.; Siegbahn, P. E. M.; Babcock, G. T. *J. Am. Chem. Soc.* **1998**, *120*, 8812–8824.
25. Jaguar 4.0, Schrödinger, Inc., Portland, OR, **1991–2000**.
26. Siegbahn, P. E. M.; Blomberg, M. R. A. *Chem. Rev.* **2000**, *100*, 421–437.

27. Siegbahn, P. E. M.; Blomberg, M. R. A. *J. Phys. Chem. B* **2001**, *105*, 9375–9386.
28. Reiher, M.; Salomon, O.; Hess, B. A. *Theor. Chem. Acc.* **2001**, *107*, 48–55.
29. Wirstam, M.; Lippard, S. J.; Friesner, R. A. *J. Am. Chem. Soc.* **2003**, *125*, 3980–3987.
30. Wang, H.; Ralston, C. Y.; Patil, D. S.; Jones, R. M.; Gu, W.; Verhagen, M.; Adams, M.; Ge, P.; Riordan, C.; Marganian, C. A.; Mascharak, P.; Kovacs, J.; Miller, C. G.; Collins, T. J.; Brooker, S.; Croucher, P. D.; Wang, K.; Stiefel, E. I.; Cramer, S. P. *J. Am. Chem. Soc.* **2000**, *122*, 10544–10552.
31. Fan, H.-J.; Hall, M. B. *J. Am. Chem. Soc.* **2002**, *124*, 394–395.
32. Baik, M.-H.; Friesner, R. A. *J. Phys. Chem. A* **2002**, *106*, 7407–7412.
33. Reiss, H.; Heller, A. *J. Phys. Chem.* **1985**, *89*, 4207.
34. Bard, A. J.; Faulkner, L. R. “*Electrochemical Methods*”; John Wiley & Sons: New York, **1980**.

HETEROLYTIC SPLITTING OF H–H, Si–H, AND OTHER σ BONDS ON ELECTROPHILIC METAL CENTERS

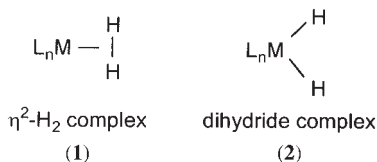
GREGORY J. KUBAS

Chemistry Division, Los Alamos National Laboratory, MS-J514,
Los Alamos, NM 87545, USA

- I. Introduction
- II. Heterolytic Cleavage and Acidity of Coordinated H_2
 - A. Background
 - B. Intermolecular Heterolytic Cleavage of Coordinated H_2
 - C. Intramolecular Heterolytic Cleavage of H_2
- III. Heterolytic Cleavage of Si–H Bonds
 - A. Background
 - B. Heterolytic Cleavage of Silanes on Electrophilic Cationic Centers
 - C. Silane Alcoholysis
- IV. Heterolytic Cleavage of B–H and C–H Bonds
- V. Concluding Remarks
- References

I. Introduction

The coordination of a dihydrogen molecule (H_2) to a transition metal complex in $W(CO)_3(P^iPr_3)_2(H_2)$ (Fig. 1), was discovered about 20 years ago (1,2) and was the first well-established σ -complex. In this complex the H_2 ligand is nearly intact with a stretched H–H bond (H–H distance is 0.89 vs. 0.75 Å in free H_2) while dihydrides have H–H > 1.6 Å.



Since then nearly 600 metal– H_2 complexes, representing every transition metal from vanadium to platinum, have been isolated or observed

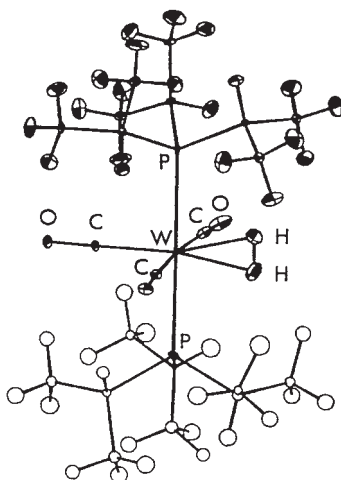
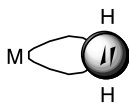


FIG. 1. ORTEP drawing of the structure of $\text{W(CO)}_3(\text{P}^i\text{Pr}_3)_2(\text{H}_2)$, showing intact H-H bond elongated to 0.82(1) Å. Lower phosphine is disordered. The actual H-H distance is longer (0.89 Å from solid-state NMR) because rapid rotation of the H_2 results in foreshortening of the neutron distance.

spectroscopically, and over 1000 papers have been published relating to this field (3-8). Extensive computational analyses of the structure, bonding, and reactions of coordinated dihydrogen have been carried out because of the innate "simplicity" of the H_2 ligand (9-12). However, this is quite deceptive because M-H_2 systems have proven to exhibit astonishingly complex structure, bonding, and dynamics, including quantum mechanical behavior. The H_2 complexes are the most prominent members of a rapidly growing class of compounds referred to as σ complexes which contain a 3-center interaction of the *bonding* electron pair in H-H or other X-Y bonds with M (7, 8). These complexes complement classical Werner-type compounds (4) where a ligand donates electron density through its *non-bonding* electron pair(s) and π -complexes (5).



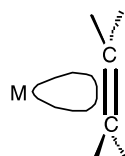
σ -complex

(3)



Werner complex

(4)



π -complex

(5)

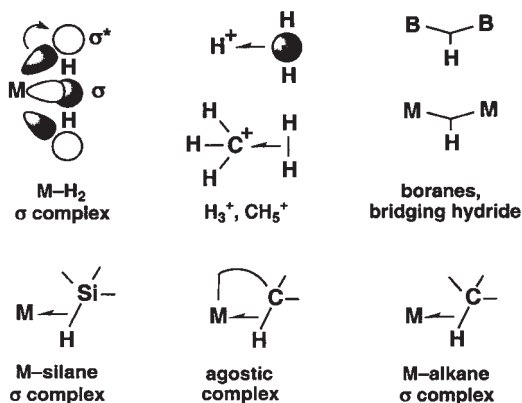
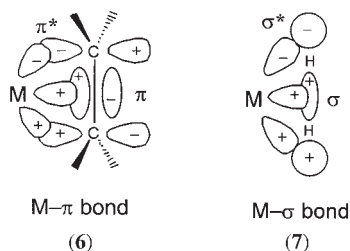


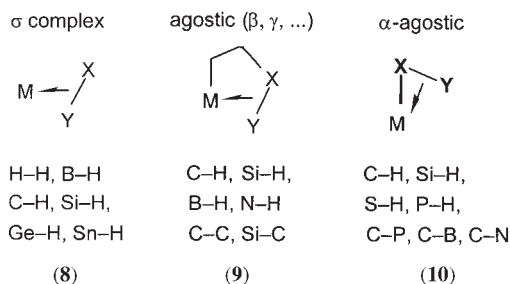
FIG. 2. Examples of non-classical 3-center, 2-electron (3c-2e) bonding.

The side-on (η^2) bonding in $M-\eta^2-H_2$ and other σ -complexes has been termed *non-classical*, on analogy to the 3-center, 2-electron bonding in non-classical carbocations and boranes (Fig. 2). One of the first questions raised when H_2 complexes were discovered is whether they would be important in catalytic reactions. As will be shown below the answer is an emphatic yes, as exemplified by the elegant asymmetric catalytic hydrogenation systems of Nobel-laureate Ryoji Noyori. Also, the mechanism of catalytic silane alcoholysis directly involves two different σ complexes: $M(\eta^2-Si-H)$ and $M(\eta^2-H_2)$. In both of these systems, the crucial step is heterolytic cleavage of the H-H and/or Si-H bond, the primary subject of this review.

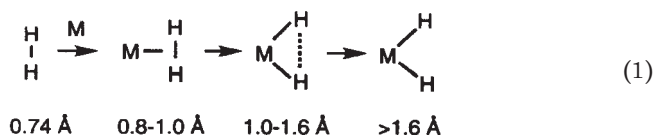
Positively-charged fragments such as $[ML_n]^+$, CH_3^+ , and H^+ are all strong electrophiles (“superelectrophiles” in the extreme sense (13)) towards the Lewis basic H_2 , but transition metals can uniquely stabilize H_2 and other σ -bond coordination by *back donation* from d-orbitals that main group analogues cannot do. This bonding is then remarkably analogous (14) to the Dewar-Chart-Duncanson model (15) for π -complexes (6).



Thus, H_2 is a good π -acceptor ligand like CO and ethylene. In principle *any* $X-Y$ σ bond can coordinate to a metal center providing that steric and electronic factors are favorable, e.g., substituents at X and Y do not block the metal's access. A large number and variety of σ bonds have been found to interact intermolecularly (8) or intramolecularly (9, 10) with metal centers.

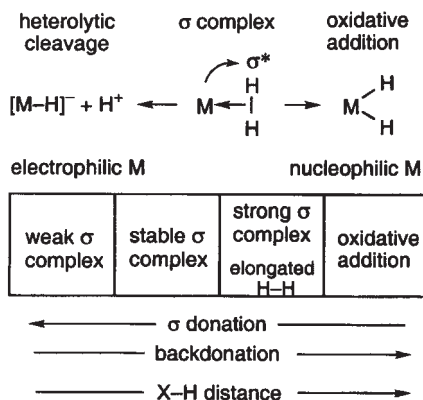


A coordinated σ bond $X-Y$ can be cleaved as exemplified in Eq. (1) for $X = H$ and $Y = H$, a process termed oxidative addition (OA).



A large variety of dihydrogen complexes have been isolated and found to display a near *continuum* of H-H distances ranging from 0.82 Å to nearly 1.6 Å, at which point the complex is best viewed as a “compressed dihydride” (6b). The OA process can thus be arrested at various points along the reaction coordinate merely by varying the M-L sets, thus changing the electronics at M. When $M \rightarrow H_2$ back bonding becomes too strong, e.g., if more electron-donating co-ligands are put on M, the σ bond breaks to form a dihydride because of overpopulation of its antibonding orbital. Depending on electronic and steric factors, Eq. (1) can (and often does) rapidly proceed to completion without any sign of the intermediate structures. Oxidative addition and the reverse reaction, reductive elimination, are fundamentally important to catalytic processes such as hydrogenation.

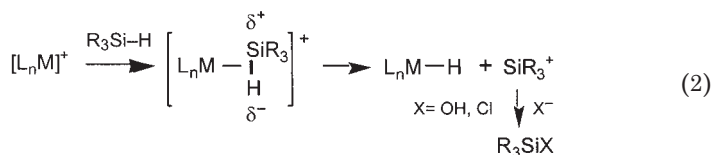
Importantly, H_2 can bind in stable fashion to very electron-deficient metal centers, which are weak back bonders, nearly as well as to more electron-rich M that promote OA. Calculations show that for highly electrophilic M *the reduction in back donation is almost completely*



SCHEME 1.

offset by increased electron donation from H_2 to the electron-poor M . Thus there are two completely different pathways for cleavage of H-H and X-H bonds: homolytic cleavage (OA) and heterolytic cleavage on electrophilic metal centers (Scheme 1).

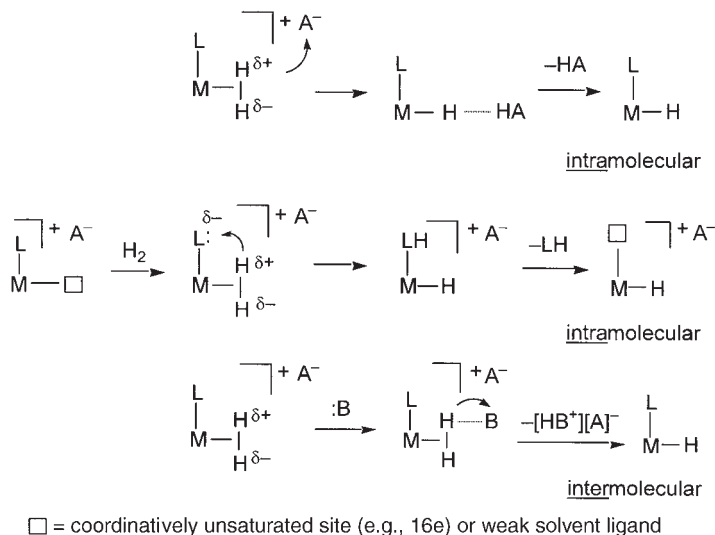
In the latter case, which will be the primary focus of this chapter, the η^2-H_2 ligand becomes acidic, i.e., polarized towards $H^{\delta-}-H^{\delta+}$ where the highly mobile H^+ is ready to transfer. Both pathways have been identified in catalytic hydrogenation and may also be available for other σ bond activations such as C-H cleavage. Heterolytic splitting of X-H bonds via proton transfer to a basic site on a cis ligand or to an external base is a crucial step in both industrial and biological processes. For Si-H bonds coordinated to electrophilic cationic metal centers, the X-H bond becomes polarized in the opposite sense: $Si(\delta^+)-H(\delta^-)$, i.e., silicon becomes positively charged because it is more electropositive than H.



In Eq. (2), very reactive silylium ions are effectively eliminated or, more likely as will be discussed in Section III, the bound silicon is attacked by nucleophiles such as adventitious water or chloride from solvents such as dichloromethane. Similarly, a coordinated B-H bond in a $BH_3 \cdot PMe_3$ ligand in $[Mn(CO)_4(PR_3)(BH_3 \cdot PMe_3)]^+$ has recently

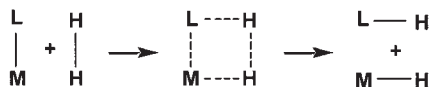
after this). Although heterolytic splitting of H_2 can occur via several mechanisms that may or may not involve dihydrogen complexes as intermediates, emphasis will be placed on the latter here.

There are two ways this can take place on H_2 complexes generated either by addition of H_2 gas to unsaturated precursors (as shown in Scheme 2) or, alternately, by protonation of a $M-H$ bond (4,5,8).



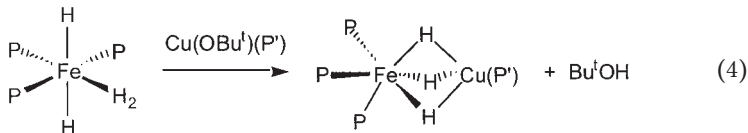
SCHEME 2.

The η^2-H_2 ligand becomes acidic, i.e., polarized towards $H^{\delta-}-H^{\delta+}$ where the highly mobile H^+ is ready to transfer. *Intramolecular* heterolytic cleavage involves proton transfer to a cis ligand L (e.g., H or Cl) or to the counteranion of a cationic complex (for salts such as copper acetate used by Calvin, the acetate anion is protonated to form acetic acid). *Intermolecular* heterolytic cleavage involves protonation of an external base B to give a metal hydride (H^- fragment) and the conjugate acid of the base, HB^+ . This is essentially the reverse of the protonation reaction commonly used to synthesize H_2 complexes (all the reactions in Scheme 2 can be reversible), and the $[HB]^+$ formed can relay the proton to internal or external sites. Such base-assisted heterolytic cleavage of H_2 as well as the acidity of H_2 complexes and hydrogen transfer reactions in general have been studied theoretically (9-12). Intramolecular splitting is closely related to σ -bond metathesis processes that generally occur on less electrophilic centers (8).



Although the heterolytic process here is formally a concerted “ionic” splitting of H_2 as often illustrated by a four-center intermediate with partial charges, the mechanism does not have to involve such charge localization. In other words, the two electrons originally present in the $\text{H}-\text{H}$ bond do not necessarily both go into the newly-formed $\text{M}-\text{H}$ bond while a bare proton transfers onto L or, at the opposite extreme, an external base. The term σ -bond metathesis is thus actually a better description and may comprise more transition states than the simple four-center intermediate shown above, e.g., initial transient coordination of H_2 to the metal cis to L and dissociation of transiently bound $\text{H}-\text{L}$ as the final step. Examples of this type of activation will be given in this Section.

Importantly, H_2 gas can be turned into a strong acid on binding to electrophilic cationic complexes. Free H_2 is an extremely weak acid with a $\text{p}K_{\text{a}}$ near 35 in THF (23), and heterolytic splitting of $\eta^2\text{-H}_2$ in relatively electron-rich neutral complexes is usually achieved only by strong bases. For example, we have shown Eq. (4) that copper alkoxides deprotonate $\text{W}(\text{CO})_3(\text{PR}_3)_2(\text{H}_2)$ and $\text{FeH}_2(\text{H}_2)(\text{PR}_3)_2$ to give heterobimetallic species with bridging hydrides (24).



However, when H_2 is bound to a highly electrophilic cationic metal center, the acidity of H_2 gas can be increased spectacularly, up to 40 orders of magnitude. The $\text{p}K_{\text{a}}$ of H_2 can become as low as -6 and thus the acidity of $\eta^2\text{-H}_2$ becomes as strong as that in sulfuric or triflic acid. As discussed in reviews by Morris (4,5) and Jia (25) and further work by Morris (26,27), such $\text{p}K_{\text{a}}$ values are usually determined by NMR measurement of the concentrations of $\text{M}-\text{H}_2$ complexes in equilibrium with an external base such as a phosphine or amine. Electron deficient cationic and dicationic H_2 complexes with strong short $\text{H}-\text{H}$ bonds (<0.9 Å) and weakly bound H_2 such as $[\text{Cp}^*\text{Re}(\text{H}_2)(\text{CO})(\text{NO})]^+$ and $[\text{Re}(\text{H}_2)(\text{CO})_4(\text{PR}_3)]^+$ are among the most acidic complexes (Table I). These acidic complexes typically have relatively high values of J_{HD} for their $\eta^2\text{-HD}$ isotopomers, although $\text{p}K_{\text{a}}$ values do not correlate

TABLE I

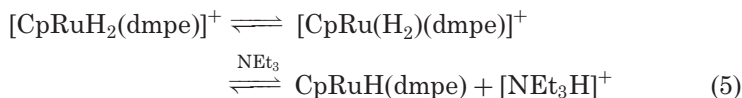
REPORTED pK_a VALUES (PSEUDO AQUEOUS SCALE) AND CORRESPONDING J_{HD} OF SELECTED H_2 COMPLEXES, EMPHASIZING HIGHLY ACIDIC SPECIES

Complex	pK_a	J_{HD} , Hz	Reference
$[Cp^*Re(H_2)(CO)(NO)]^+$	-2	27	32a
$[Re(H_2)(CO)_4(PPh_3)]^+$	-2 to 1	33.9	32b
$[FeH(H_2)(depe)_2]^+$	~ 16	28	136
$[FeH(H_2)(dppe)_2]^+$	12.1	30	136
$[FeH(H_2)(dtfpe)_2]^+$	7.8	32	136
$RuH_2(H_2)(PPh_3)_3$	17		137
$[CpRu(H_2)(dmpe)]^+$	10.1	22.1	30
$[CpRu(H)_2(dppe)]^+$	7.5	hydride	138
$[CpRu(H_2)(dppe)]^+$	7.0	24.9	138
$[CpRu(H_2)(dfepe)]^+$	-5	29.1	139
$[OsCl(H_2)(dppe)_2]^+$	7.4	13.9	140
$[Os(CH_3CN)(H_2)(dppe)_2]^{2+}$	-2	21.4	26
$[Os(CO)(H_2)(dppp)_2]^{2+}$	-5.7	32.0	141

Depe = 1,2-bis(diethylphosphino)ethane; dppe = 1,2-bis(diphenylphosphino)ethane;
dfepe = $(C_2F_5)_2PC_2H_4P(C_2F_5)_2$; dtfpe = 1,2-bis[di-(*p*-trifluoromethylphenyl)-phosphino]ethane;
dppp = 1,2-bis(diphenylphosphino)propane; dmpe = 1,2-bis(dimethylphosphino)ethane.

well with J_{HD} except within specific complex types such as $[FeH(H_2)(depe)_2]^+$ versus $[FeH(H_2)(dppe)_2]^+$. Positive charge and electron withdrawing coligands such as CO or dfepe, particularly when *trans* to H_2 , greatly increase the acidity. A good example of the effect of charge is $W(CO)_3(PCy_3)_2(H_2)$, which as noted above can be deprotonated only by strong bases such as alkoxides and KH but can be electrochemically oxidized to $[W(CO)_3(PCy_3)_2(H_2)]^+$ that now is acidic enough to protonate weakly basic THF solvent (28).

Crabtree first demonstrated heterolytic cleavage of η^2-H_2 as in Scheme 2 by isotopic labeling studies to show that the H_2 in $[IrH(H_2)(bq)(PPh_3)_2]^+$ is deprotonated by LiR in preference to the hydride ligand (29). A milder base, NEt_3 , was shown by Chinn and Heinekey (30) to specifically deprotonate the η^2-H_2 tautomer in the equilibrium mixture (84:14 ratio of η^2-H_2 to dihydride form) in Eq. (5):

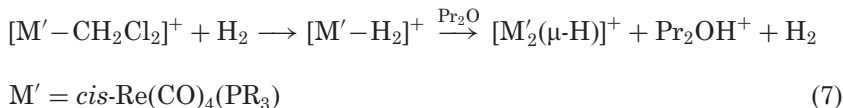
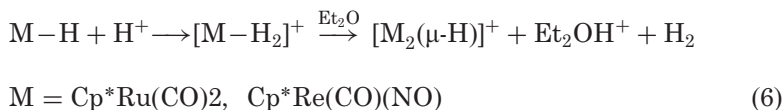


This indicated a pK_a of 17.6 in CH_3CN , and, more importantly, NMR evidence showed that the H_2 tautomer is deprotonated more rapidly than the dihydride form, which showed a *greater kinetic acidity of the*

H_2 ligand (the dihydride is actually a slightly stronger acid with a pK_a of 16.8). The main reason H_2 complexes have greater kinetic acidity than classical hydrides of similar structure is that deprotonation of an H_2 complex involves *no change in coordination number*. Also the η^2-H_2 can become polarized towards $H^{\delta-}-H^{\delta+}$, and H^+ is exceedingly mobile, especially for cationic complexes. Surprisingly the nature of the anion (e.g., BF_4^- vs. BPh_4^-) can significantly affect the kinetics of deprotonation here, probably via interaction of the anion with the H_2 ligand, as recently described for deprotonation of $[FeH(H_2)(dppe)_2]^+$ by Et_3N (31). The reason is that the size of the anion can hinder the approach of the base to the bound H_2 if the anion is associated with the H_2 . The above reactions and the ability of acidic H_2 ligands to protonate substrates such as olefins and N_2 are relevant to processes such as ionic hydrogenation (see below) and also the structure and function of metalloenzymes such as hydrogenases. Analogous increased acidity of C–H bonds in metal–alkane interactions is expected to be important in alkane activation such as methane conversion to methanol.

B. INTERMOLECULAR HETEROLYTIC CLEAVAGE OF COORDINATED H_2

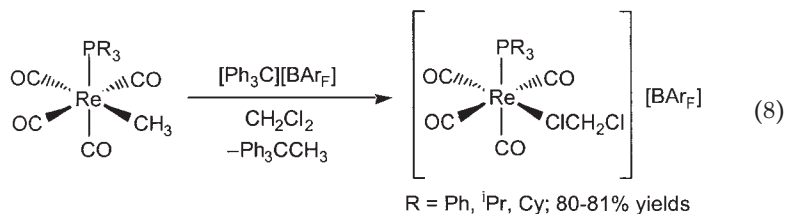
One of the best examples of intermolecular heterolytic cleavage of η^2-H_2 is the protonation of ethers by extremely electrophilic cationic H_2 complexes containing electron-withdrawing ligands such as CO [Eqs. (6)–(7)] (32).



In all cases, a hydride-bridged complex is the product even though the mononuclear hydride $M-H$ is known in Eq. (6) and is used to generate the thermally unstable H_2 complex by protonation with HBf_4 . A mononuclear hydride complex is not observed by NMR in Eq. (7), indicating strong thermodynamic preference for the $\mu-H$ dimer. Interestingly, the hydrogenase enzymes that heterolytically activate H_2 (see below) have dinuclear active sites that are capable of forming bridging hydrides by reversible protonation of $M-M$ bonds. The pK_a of bound H_2 in Eqs. (6)–(7) can be estimated to be near -2 (the pK_a of

Et_2OH^+ is -2.4 in sulfuric acid (33)), although the irreversible formation of the $\mu\text{-H}$ product provides a driving force for deprotonation that could raise the effective $\text{p}K_{\text{a}}$ of the H_2 complex a few units. A notable difference between Eqs. (6) and (7) is that $[\text{Re}(\text{H}_2)(\text{CO})_4(\text{PR}_3)]^+$ is *synthesized directly from reaction of H_2 with an isolable precursor (32b)*, while the Cp complexes are formed by protonation of a hydride with a strong acid (32a). Only a few other examples of highly acidic $\eta^2\text{-H}_2$ directly generated from H_2 are known (34–38). Although we are not aware of specific examples, it would seem likely that contacting H_2 gas with electrophilic metal centers in the solid phase (e.g., supported complexes) could effectively generate a solid acid potentially useful in heterogeneous systems.

A crucial initial step in heterolysis of σ bonds is generation of a complex with either a coordinatively unsaturated site or more commonly a site occupied by a weak, easily displaceable ligand such as a solvent molecule. Dichloromethane is very convenient here because it is an excellent solvent for cationic complexes and forms isolable complexes despite the high lability of the CH_2Cl_2 ligand. A good synthetic route to CH_2Cl_2 complexes is abstraction of a methyl ligand using a trityl salt with a low coordinating anion such as BAR_{f} ($\text{B}[3,5\text{-C}_6\text{H}_3(\text{CF}_3)_2]_4^-$). For example, treatment of $[\text{cis-Re}(\text{Me})(\text{CO})_4(\text{PR}_3)]$ ($\text{R} = \text{Ph}, \text{Cy}$) with $[\text{Ph}_3\text{C}][\text{BAR}_{\text{f}}]$ in CH_2Cl_2 solution produced $[\text{cis-Re}(\text{CO})_4(\text{PR}_3)(\text{CH}_2\text{Cl}_2)][\text{BAR}_{\text{f}}]$ [Eq. (8)] (32b).



The complexes are moderately air stable in solid and solution, although the coordinated CH_2Cl_2 is quickly replaced by adventitious water. They are stable for weeks under inert atmosphere at -30°C , but CH_2Cl_2 solutions decompose at room temperature within days to form chloride-bridged dimers $\{[\text{cis-Re}(\text{CO})_4(\text{PR}_3)]_2(\mu\text{-Cl})\}[\text{BAR}_{\text{f}}]$. The fact that CH_2Cl_2 (as well as Et_2O) complexes are isolable is attributed to the strong electrophilicity of the $16e [\text{Re}(\text{CO})_4(\text{PR}_3)]^+$ fragment. This is in direct contrast to Heinekey's analogous bis-phosphine complexes, $[\text{mer-Re}(\text{CO})_3(\text{PR}_3)_2][\text{BAR}_{\text{f}}]$, which are isolated as *agostic* complexes (intramolecular phosphine C–H binding) from $[\text{mer}-(\text{PR}_3)_2\text{Re}(\text{CO})_3\text{Me}]$ and $[\text{H}(\text{OEt}_2)_2][\text{BAR}_{\text{f}}]$ in CH_2Cl_2 (39). Furthermore, the importance

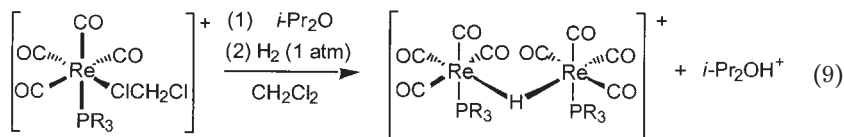
of a non-interacting counterion for weak ligand binding in this and other highly electrophilic systems is reflected by the isolation of anion-coordinated derivatives *cis*-Re(CO)₄(PPh₃)(F⁻BF₃) and *cis*-Re(CO)₄(PPh₃)(OTeF₅) (40–42).

Although dichloromethane has been traditionally thought of as a non-coordinating solvent, the isolation of stable CH₂Cl₂ complexes has been a recurring theme in recent literature (43–48), particularly for extremely electron deficient cationic metal centers with low-interacting anions such as BAr_f⁻. From crystallographic evidence, CH₂Cl₂ coordinates either monodentate, as in [Cp*Ir(PMe₃)(CH₃)(CH₂Cl₂)] [BAr_f] (45) and [*trans*-PtH(P^{*i*}Pr₃)₂(CH₂Cl₂)] [BAr_f] (46) or bidentate, as in [RuH(CO)(P^{*t*}Bu₂Me)₂(CH₂Cl₂)] [BAr_f] (48). The X-ray structure of [Re(CO)₄(PPh₃)(CH₂Cl₂)] [BAr_f] verified that the coordination mode about Re is octahedral and the CH₂Cl₂ is monodentate (as in Fig. 5). In these highly electrophilic complexes, the CH₂Cl₂ is actually tightly bound in the solid complexes and cannot be removed in vacuo, but is quite labile in solution.

Despite the lability of CH₂Cl₂ in [Re(CO)₄(PR₃)(CH₂Cl₂)]⁺ in CD₂Cl₂ solution at room temperature, no peaks attributable to the expected η²-H₂ complexes were observed in ¹H NMR spectra taken at –80 to 20°C under H₂ atmosphere. However, when solutions in non-coordinating C₆D₅F were placed under 3 atm of H₂, broad resonances for η²-H₂ were observed at –4.69 ppm for [*cis*-Re(CO)₄(PPh₃)(H₂)] [BAr_f], and –5.12 ppm for the PCy₃ analogue. The resonance for free H₂ was broad at room temperature for both complexes, indicating exchange with coordinated H₂. The addition of H₂ was completely reversible, and when solvent was removed in vacuo and the residue redissolved in CD₂Cl₂, NMR spectra showed signals due only to the CD₂Cl₂ complex. The H₂ complexes could not be isolated due to loss of H₂ and decomposition in C₆H₅F solutions. To verify that these resonances were due to H₂ rather than dihydride ligands, the HD complexes were prepared, and the *J*_{HD} coupling constants were measured to be 33.9 and 33.8 Hz for the PPh₃ and PCy₃ complexes, respectively. The high *J*_{HD} observed for these complexes is consistent with those observed in other electrophilic cationic M(H₂) systems and suggests a short H–H distance of ~0.87 Å and a bonding picture in which the metal–H₂ σ interaction is greatly enhanced relative to the back bonding interaction (8).

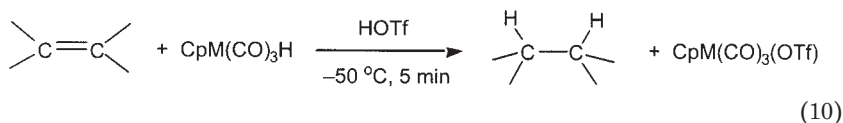
Although the ¹H NMR signals for coordinated H₂ were not observed in CD₂Cl₂ solutions of [Re(CO)₄(PR₃)(H₂)]⁺, heterolytic activation of H₂ was evident in CH₂Cl₂ by protonation of free diisopropyl ether. When ^{*i*}Pr₂O (4–10 equiv) was added to CD₂Cl₂ solutions of the CH₂Cl₂ complexes followed by placement under H₂ atmosphere, complete

conversion to the hydride-bridged dimers $\{[cis-Re(CO)_4(PR_3)]_2(\mu-H)\} \{BAr_f\}$ was observed [Eq. (9)].

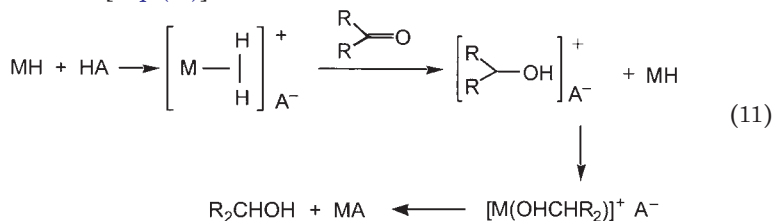


This suggests that CH_2Cl_2 and H_2 complexes are in equilibrium in CH_2Cl_2 solutions, but the exchange is too fast on the NMR time-scale to observe the intermediate $\text{Re}(\text{H}_2)$ complex. Heinekey has observed similar deprotonation of $[\text{Cp}^*\text{Re}(\text{CO})(\text{NO})(\text{H}_2)][\text{BF}_4]$ with Et_2O to provide a hydride bridged dimer (32a). The $\text{p}K_a$ of $[\text{Re}(\text{CO})_4(\text{PR}_3)(\text{H}_2)]^+$ can be estimated to be approximately -2 , although it is likely to be higher because the coproduct is a hydride-bridged dimer. Irreversible formation of the dimer provides a driving force so that even if the H_2 complex has a $\text{p}K_a$ of 1 or possibly higher, it would still be deprotonated by a base that has a conjugate acid form with $\text{p}K_a -2$. Thus a more conservative estimate of the $\text{p}K_a$ would be 1 to -2 .

The heterolytic activation of H_2 in the above system is particularly interesting in that it may be applicable to reactions in which ionic hydrogenation of hindered substrates from a metal catalyst and H_2 is desired. In 1989, Bullock reported the first examples of ionic hydrogenation wherein a mixture of an organometallic hydride such as $\text{CpMoH}(\text{CO})_3$ and a strong acid like HO_3SCF_3 reduces sterically hindered olefins to alkanes via protonation to carbocations followed by hydride transfer from the metal hydride [Eq. (10)] (49).



Several other examples have since been reported, including hydrogenation of alkynes and ketones (50). It is likely that an acidic H_2 (or dihydride) complex is involved in the proton transfer step of some of these reactions [Eq. (11)].



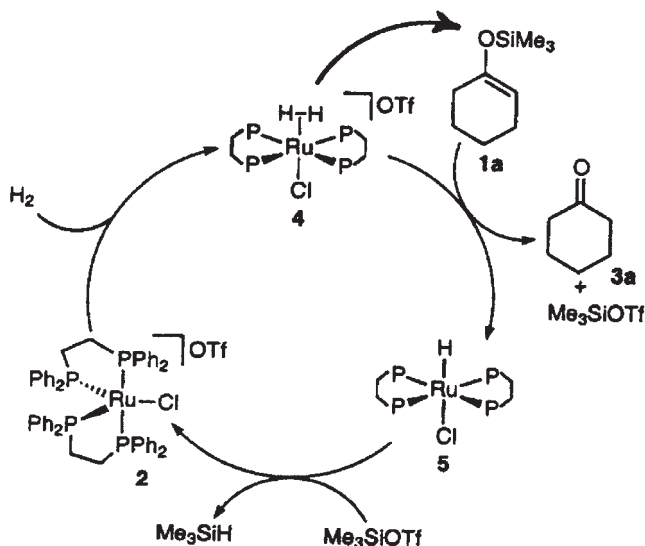


FIG. 3. Mechanism for catalytic hydrogenation involving heterolytic cleavage of $\eta^2\text{-H}_2$.

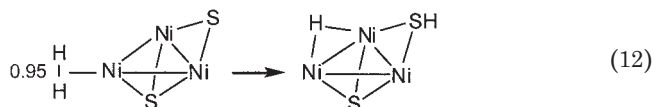
A good example of a catalytic hydrogenation process proposed to involve heterolysis of H_2 on an acidic cationic H_2 complex is shown in Fig. 3 (51). Treatment of the silyl enol ether **1a** with H_2 in the presence of a catalytic amount of **2** in benzene at 50°C for 3 h gives the cyclohexanone **3a** and Me_3SiH in nearly quantitative yield. Based on studies using D_2 , the initial step is thought to involve proton transfer from $\eta^2\text{-H}_2$ in **4** in Fig. 3 to the oxygen atom of **1a** to give **3a**, the neutral hydride **5**, and Me_3SiOTf from the triflate anion. The latter can accept a hydride to form known **2**, which then converts back to **4** under H_2 . A delicate balance between the acidity of $\eta^2\text{-H}_2$ in **4** and the nucleophilicity of the hydride **5** might be critical here.

C. INTRAMOLECULAR HETEROLYTIC CLEAVAGE OF H_2

1. Proton Transfer to Ancillary Ligands; Dihydrogen Bonding

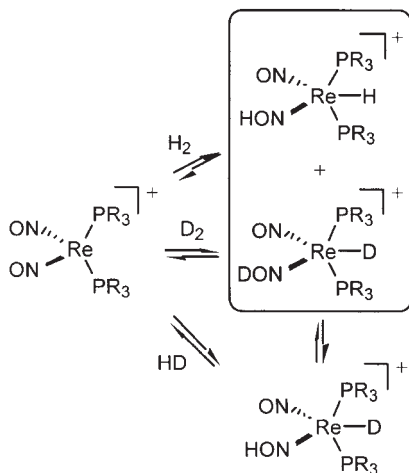
Intramolecular heterolytic cleavage of H_2 is one of the oldest reactions of H_2 and is among the first homogeneous catalytic conversions. $\eta^2\text{-H}_2$ can protonate a counteranion or a basic ancillary ligand, either at the M–L bond or at a ligand lone pair. Intramolecular heterolysis of H–H is most likely an essential step in many diverse systems ranging from industrial processes to the function of metallo enzymes such as

hydrogenase. These include heterogeneous catalysis such as in the world's largest man-made chemical reaction, hydrodesulfurization of crude oil on metal sulfides, typically MoS_2 and RuS_2 . Heterolysis of H_2 on these and other sulfides to form M-H and M-SH groups is well known (52) and has been modeled calculatively on NiS and a Ni_3S_2 cluster (52b,c). A transient Ni-H_2 species is calculated to be stable by ~ 16 kcal/mol and energetically capable of transferring one H to S [Eq. (12)] (52b).



Such cleavage can also occur to transform terminal *oxo* ligands to OH ligands, as recently shown in reaction of H_2 with a sulfido-bridged complex $\text{Cp}^*\text{W}(\text{O})(\mu\text{-S})_2\text{RuX}(\text{PPh}_3)_2$ in the presence of NaBAR_f to give $[\text{Cp}^*\text{W}(\text{OH})(\mu\text{-S})_2\text{RuH}(\text{PPh}_3)_2][\text{BAR}_f]$ (53). The imido (NPh) analogue gave a similar reaction, and a mechanism involving formation of a transient Ru-H_2 ligand followed by heterolysis involving initial proton migration to a sulfido ligand to give a $\mu\text{-SH}$ intermediate was not ruled out. The acidic SH group could then readily deliver the proton to the more basic oxo group.

Catalytic H/D scrambling of mixtures of H_2 and D_2 often takes place via intramolecular heterolysis of H_2 , as will be discussed further below. A recent example was proposed to involve cleavage of H_2/D_2 and proton transfer to NO ligands (Scheme 3) (54).



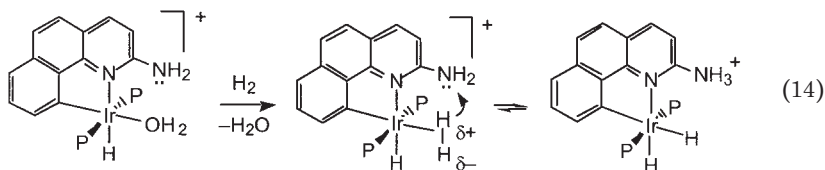
SCHEME 3.

Although the protonated NO ligands were not observed, analogous heterolysis of a silane did give a complex with a silylated nitrosyl ligand, Et_3SiON , as will be shown in [Section IIIB](#).

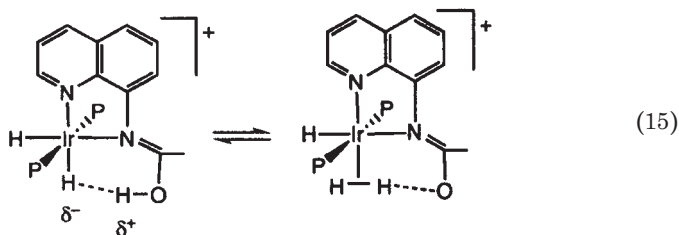
Intramolecular heterolysis of H_2 with elimination of HX is commonly observed under homogeneous reaction conditions as shown in [Eq. \(13\)](#) (55–57).



This scheme is useful for preparative and catalytic chemistry, e.g., a metal halide (including bridging X) can be converted to a metal hydride in the presence of base or under phase-transfer or high pressure conditions. Another important type of heterolytic cleavage of H_2 is shown in [Eq. \(14\)](#) (58,59).



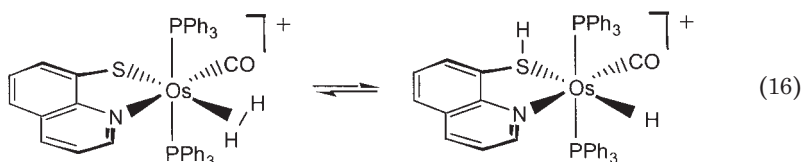
The conversion is completely reversible by removing the H_2 gas from solution and is remarkably sensitive to phosphine size and ion-pairing effects. [Equation \(14\)](#) is facilitated by hydrogen bonding interactions, e.g., [Eq. \(15\)](#) where the OH and IrH hydrogens scramble via rotation of the H_2 ligand.



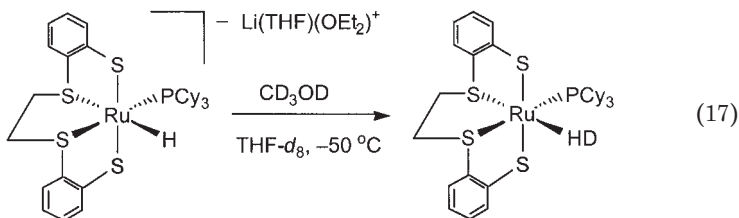
The $\text{H} \cdots \text{H}$ interactions (1.75–1.9 Å) here and related systems are referred to as “proton-hydride bonding” by Morris (60–62) and “dihydrogen bonding” by Crabtree (63–65), who along with others (66–68) have studied or reviewed such *unconventional hydrogen bonds* that include $\text{M}-\text{H} \cdots \text{H}-\text{M}'$, $\text{M}-\text{H} \cdots \text{H}-\text{X}$, and $\text{X}-\text{H} \cdots \sigma$ interactions in general ($\text{X}=\text{C}$, N , P , O , etc). These complexes represent intermediates in the heterolytic splitting of H_2 and illustrate both the basicity of the $\text{M}-\text{H}$

bond and the acidity of $\eta^2\text{-H}_2$. The interactions can be comparable in strength to classical $\text{X-H}\cdots(\text{lone pair})$ hydrogen bonds (3–7 kcal/mol). The discovery of the dihydrogen bond and new findings in this area have given significant rebirth of interest in hydrogen bonding in transition metal chemistry (69).

The first direct observation of equilibrium between an acidic H_2 complex and a corresponding hydride complex with a protonated ancillary ligand is shown in Eq. (16) (70).

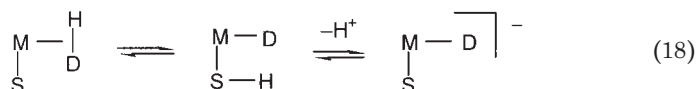


Several other cases of $\eta^2\text{-H}_2$ ligands reacting intramolecularly with thiolate and sulfide ligands are known or believed to be intermediate steps in for example SH ligand formation from reaction of sulfides with H_2 (71–82) and are relevant to biological systems such as hydrogenase enzymes (see below). In order for proton transfer from $\eta^2\text{-H}_2$ to a coordinated base to occur, the $\text{p}K_a$ of the H_2 ligand and the protonated base must be similar. Morris has estimated that coordinated alkanethiol ligands have $\text{p}K_a$ values between 5 and 10, which matches well with the acidity of many H_2 ligands (80). Protonation of an anionic Ru hydride using CD_3OD gives an unstable HD complex [Eq. (17)] (77).



This reaction can be reversed by displacing the H_2 by DMSO to give $\text{Ru}(\text{DMSO})(\text{PCy}_3)(\text{S}_4)$, which yields $\text{Na}^+[\text{RuH}(\text{PCy}_3)(\text{S}_4)]^-$ and MeOH when treated with H_2 in the presence of NaOMe. This demonstrates that H_2 can be heterolytically cleaved at M–S sites, and a mechanism had been elucidated for an analogous neutral Rh-hydride system (75,76). In this case the electrophilic metal and the basic thiolate donors attack the $\eta^2\text{-H}_2$ in concerted fashion to give an identifiable thiol hydride species, $[\text{RhH}(\text{PCy}_3)(^{\text{bu}}\text{S}_4\text{-H})]^+$. The similarity between the Ru

and Rh systems suggest that the HD (or a D₂) ligand in Eq. (17) can be intramolecularly cleaved [Eq. (18)], which is essential to rationalize the D₂/H⁺ exchange between D₂ and EtOH that these complexes catalyze.

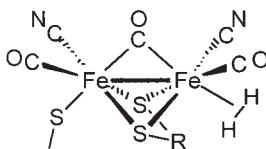


For the Ru system the thiol hydride could not be detected, while for the Rh system and also [IrH₂(HS(CH₂)₃SH)(PCy₃)₂]⁺ (which similarly catalyzes D₂/H⁺ exchange (79)), the H₂ complex could not be seen but is a transient. A related system, Ni(NHPⁿPr₃)(S₃) clearly shows that heterolysis of D₂ can also occur at nickel sites, which may be relevant to H₂ activation in [FeNi] hydrogenases (78).

The above intramolecular proton transfer from bound H₂ to sulfur or other Lewis-basic ancillary ligands is of great interest in modeling the function of redox active sites in biological systems, particularly metallo enzymes such as hydrogenases (H-ases) and nitrogenases. Biological activation as well as production of “inert” σ-bonded compounds such as H₂ and CH₄ have been known for many decades, but the mechanisms had remained a mystery. H-ases are redox enzymes that catalyze reversible interconversion of H₂ and protons to either utilize H₂ as an energy source or dispose excess electrons as H₂ [Eq. (19)].



Both CO and cyanide ligands have been identified in the dinuclear active sites of iron-only H-ases that are remarkably organometallic-like and could bind and heterolytically split H₂, most likely at an octahedral site trans to the bridging CO (83).



As originally noted by Crabtree (84), several properties of the η²-H₂ ligand such as its acidity and ability to compete with N₂ ligands clearly must be considered in relation to the structure and function of these enzymes. For example, from isotopic exchange evidence such as

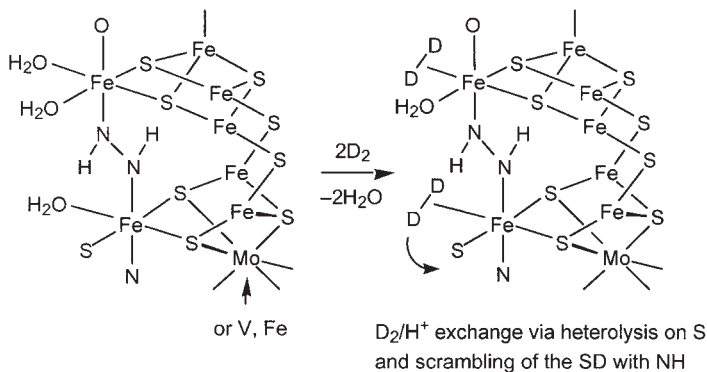
the pH-dependent reaction shown in Eq. (20), it is inferred that the H_2 molecule is split heterolytically.



An organometallic biological active site with a mix of donor and acceptor ligands such as CO is advantageous for such activation of H_2 . The CO ligands both increase the electrophilicity of the metal centers and impose a strong trans influence that has been asserted to favor both reversible η^2-H_2 binding and facile heterolytic cleavage via proton transfer to proximal basic sites such as sulfido and cysteinyl groups (85). This is much as in carbonyl-rich organometallic complexes such as $[Re(CO)_4(PR_3)(\eta^2-H_2)]^+$ discussed above [e.g., Eq. (9)]. Heterolytic activation of H_2 on hydrogenases and a variety of complexes that model them is discussed in an article by Darensbourg also published in this volume (86).

Regarding the structure and function of nitrogenases in producing ammonia from N_2 , Sellmann has studied several model systems wherein heterolytic activation of H_2 occurs on sulfur ligands (87). A core geometry based on a hybrid of the FeMoco active site structure with a dinuclear diazene complex, $[Fe("N_HS_4")]_2(\mu-N_2H_2)$, is a proposed model (Scheme 4).

In nitrogenase, H_2 reduction is proven by the formation of HD from D_2 gas and protons derived from H_2O , which occurs only in the presence of N_2 [Eq. (21)].

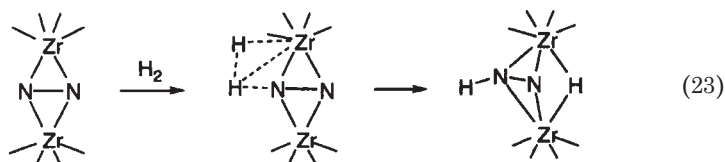


SCHEME 4.

Sellmann's model is claimed to be consistent with the severe constraints imposed on this "N₂-dependent HD formation" from D₂ and protons. Other modeling studies have shown that protons can be transferred from acidic H₂ ligands in cationic Ru–H₂ complexes to N₂ ligands in W(N₂)₂(P)₄ complexes (P = phosphine donor), in some cases even forming ammonia [Eq. (22)] (88,89).



Detailed studies with several Ru(H₂) complexes showed that the yield of NH₃ critically depended upon the pK_a value of the Ru(H₂) complexes (89). When the W–N₂ complex was treated with 10 equiv of [RuCl(H₂)(dppe)₂]⁺ (dppe = 1,2-bis(diphenylphosphino)ethane) with pK_a = 6.0 under 1 atm of H₂, NH₃ was formed in up to 79% total yield (free NH₃ plus NH₃ released on base distillation). If the pK_a of the Ru(H₂) complex was increased to ~10, the yield of ammonia decreased remarkably. Heterolytic cleavage of H₂ was proposed to occur at the Ru center via nucleophilic attack of the coordinated N₂ on the coordinated H₂ where the coordinated N₂ is protonated and a hydride remains at the Ru atom. Only a very limited number of reactions of bound N₂ with H₂ are known, e.g., Eq. (23) which slowly occurs in toluene over 1–2 weeks for a dinuclear Zr complex capped by macrocyclic ligands with N and P donor atoms (90).



However, here the reaction stopped at the stage of N₂H and no NH₃ was formed.

The discovery by the recent Nobel-laureate, Ryoji Noyori, of asymmetric hydrogenation of simple ketones to alcohols catalyzed by *trans*-RuCl₂[(S)-binap][(S,S)-dppe] (binap = [1,1'-binaphthalene-2,2'-diyl-bis(diphenylphosphane)]; dppe = diphenylethylenediamine) is remarkable in several respects (91). The reaction is quantitative within hours, gives enantiomeric excesses (ee) up to 99%, shows high chemoselectivity for carbonyl over olefin reduction, and the substrate-to-catalyst ratio is >100,000. Moreover, the non-classical metal–ligand bifunctional catalytic cycle is mechanistically novel and involves heterolytic

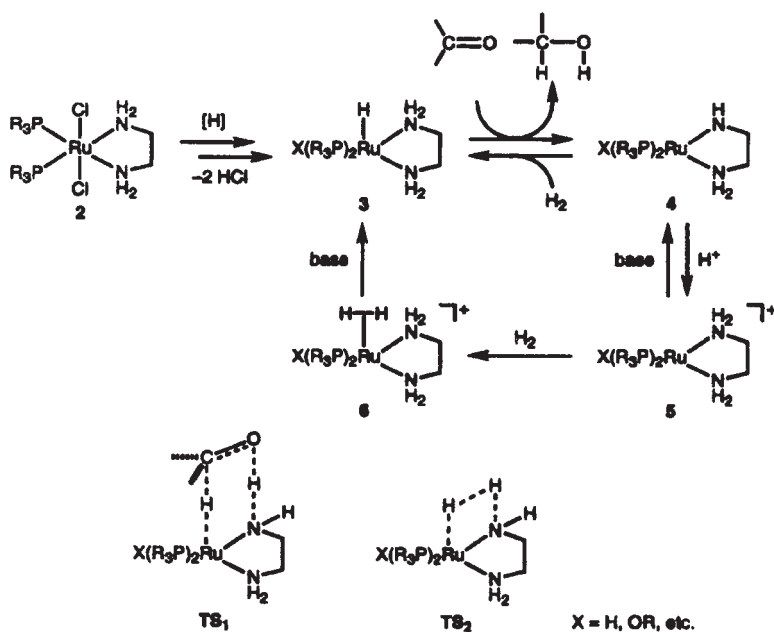


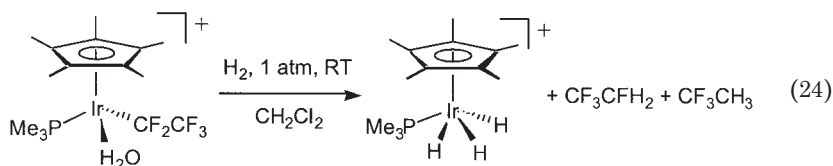
FIG. 4. Mechanism for catalytic hydrogenation in Noyori's system.

cleavage of hydrogen to form the active ruthenium hydride as a key step (Fig. 4) which differentiates this new class of Ru(II) catalysts from the structurally similar classical hydrogenation catalysts. The presence of the NH_2 functionality in the diamine ligand is crucial for the catalytic activity. First, the mixed-ligand RuCl_2 complex **2** is converted to the RuHX complex **3** ($\text{X} = \text{H}$ or OR) with the aid of 2 equiv of alkaline base and a hydride source, H_2 , and the isopropanol solvent. The catalytic cycle involves two ground-state components, **3** and its didehydro complex **4**, that are linked by transition states TS_1 and TS_2 . The NH_2 proton in **3** is key in delivering hydrogen to the ketone, while the amide nitrogen in **4** cleaves H_2 . In both steps, the Ru centers and the ligands directly cooperate in the bond-breaking and bond-forming processes. The 18-electron Ru hydride **3** reacts with the ketone via a six-membered, pericyclic transition state TS_1 , giving the 16-electron complex **4** and the alcohol product. The hydrogenating ability of coordinatively saturated **3** originates from the charge alternating $\text{H}^{\delta-}-\text{Ru}^{\delta+}-\text{N}^{\delta-}-\text{H}^{\delta+}$ arrangement which meshes well with the $\text{C}^{\delta+}=\text{O}^{\delta-}$ dipole. Thus, the hydride on Ru possesses sufficient nucleophilicity, while the NH moiety exhibits a hydrogen-bonding ability to activate the carbonyl

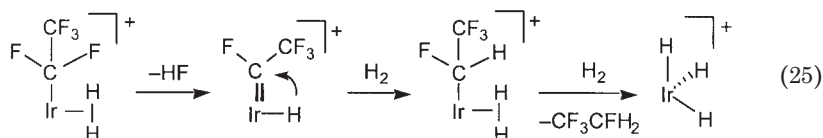
function. Because of the unique $\text{Ru}^{\delta+}-\text{N}^{\delta-}$ dipolar bond, **4** splits H_2 in a heterolytic fashion via **TS**₂ to restore the Ru hydride **3**. Alternatively, **3** may be regenerated from **4** and H_2 by way of **5** and the dihydrogen complex **6** by action of protic medium and base.

The above mechanism is novel in that it does not require the interaction of a carbonyl moiety with the metal center. Neither a ketone/Ru complex nor a Ru alkoxide is involved in the mechanism, and the alcohol forms directly from the ketone. This non-classical mechanism also explains the high functional selectivity for the C=O group. When the chiral “molecular surface” of the Ru hydride recognizes the difference of ketone enantiofaces, asymmetric hydrogenation is achieved. This is different from the earlier BINAP–Ru chemistry where the enantioface differentiation is made within the chiral “metal template” with the assistance of heteroatom/metal coordination. Similar heterolyses of H_2 ligands have been shown by Morris and others (92) to be the critical step in the mechanism of reaction processes related to the Noyori systems.

Another recent development is hydrogenolyses of C–F bonds triggered by heterolytic activation of H_2 on cationic Ir complexes with either piano stool (93) or octahedral (94) geometries.



In Eq. (24), Hughes proposed that H_2 displaces H_2O and transfers a proton to form HF and a carbene ligand that is then hydrogenated to give a fluorohydrocarbon product [Eq. (25)] (93).

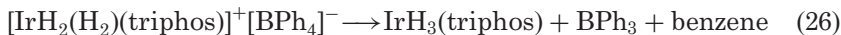


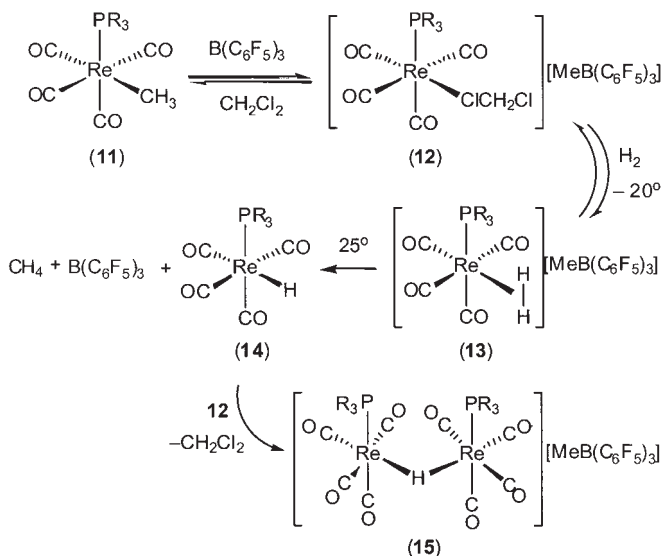
The water displaced by H_2 was proposed to be involved in the proton transfer, e.g., H_3O^+ may be formed from H_2 heterolysis and protonate the α -C–F bond. A similar proton-promoted CF activation in dicationic *cis*-[Ir(CF₃)(CO)(dppe)(DIB)]²⁺ (DIB = *o*-diiodobenzene) has also been thought to occur via heterolytic activation of H_2 , but hydrolysis to a CO ligand by adventitious moisture to eventually form [IrH₂(CO)₂(dppe)]⁺ is the outcome (94). An unobserved intermediate with CF₃

trans to an H₂ ligand that has displaced one of the iodo arms of DIB is proposed in this complicated transformation, which would seem to require proton transfer from $\eta^2\text{-H}_2$ to the distal C–F bond via a mobile proton transfer agent such as H₃O⁺. In regard to involvement of H₂O, an aqueous HNO₃ solution of [Cp*Ir(H₂O)₃]²⁺ in a pH range of about 1–4 reacts with 3 equiv of H₂ to yield a solution of [(Cp*Ir)₂($\mu\text{-H}$)₃]⁺ as a result of heterolytic H₂ activation (95). It was proposed that the H₂O ligands could act as a base to release H₃O⁺ (H₂ + H₂O → H⁺ + H₃O⁺) and accelerate the heterolytic H₂-activation to form the hydride-bridged dimer under these conditions since it has been known that polar solvents accelerate the heterolysis of H₂ (20). Theoretical studies of the assistance of heterolytic cleavage of H₂ by an external base on a model [Rh(H₂)(PH₃)₂(HCO₂)] ··· NH₃ system show how an amine can facilitate proton transfer (12). Thus, mechanisms invoking external or internal base catalysis may be used to rationalize protonations of ancillary ligands with *no* lone pairs, such as CF₃ as well as hydride, alkyl, and silyl groups.

2. Proton Transfer to Anions

Strong acids such as HCl can be eliminated by proton transfer from $\eta^2\text{-H}_2$ ligands to the counteranions of highly electrophilic [L_nM]⁺ complexes. One of the strongest acids known, *triflic acid*, CF₃SO₃H, can even be eliminated from a dicationic H₂ complex formed from H₂ gas, [Ru(H₂)(CNH)(L)₂][OTf]₂ (L = diphosphine), which contained triflate anions and a protonated cyanide ligand (35). An interesting case involves protonation of borane anions. We have found that the d⁶ rhenium(I) complex, **11**, is in nearly 1:1 equilibrium with **12**, formed by methyl abstraction by B(C₆F₅)₃ to give the MeB(C₆F₅)₃[−] counterion (Scheme 5) (38). This indicates that the electrophilicity of the [Re(CO)₄(PR₃)₃]⁺ fragment is similar to that of B(C₆F₅)₃. Complex **12** reacts under H₂ atmosphere below room temperature to form equilibrium amounts (~5%) of the H₂ complex, **13**. On warming the solution, methane, B(C₆F₅)₃, and *cis*-Re(CO)₄(PR₃)H, **14**, form apparently by protonation of the anion MeB(C₆F₅)₃[−] by the acidic H₂ in **13**. Complex **14** is not observed by NMR, but presumably quickly reacts with unreacted **12** (or **13**) to form the hydride-bridged dimer **15**, which is a “thermodynamic sink” in these systems [see Eq. (9)]. Such protonation of a borane anion has precedence as reported by Bianchini [Eq. (26)] where the H₂ complex is also unstable and is generated from H₂ gas (96).





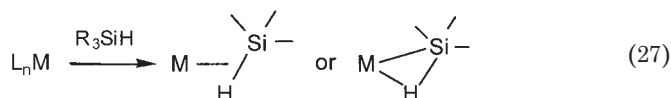
SCHEME 5.

A mononuclear hydride results here as the final organometallic product (unlike unobserved 14 in Scheme 5). Another possible scenario in Scheme 5 is *intermolecular* heterolysis of H_2 , e.g., protonation of the Me group in equilibrium quantities of 11 by the acidic H_2 in 13 to give CH_4 , 12, and 14.

III. Heterolytic Cleavage of Si-H Bonds

A. BACKGROUND

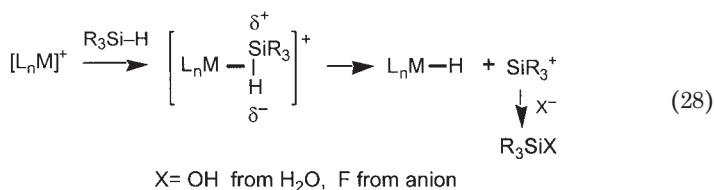
On analogy to H_2 , silanes do not have non-bonding electron pairs or π -electrons to ligate to metal centers, but hydrosilanes ($\text{R}_3\text{Si-H}$) can bind to M to form stable σ complexes through Si-H bonds to give 3c-2e $\text{M}(\eta^2\text{-Si-H})$ bonding [Eq. (27)].



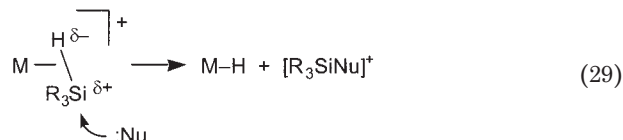
A major difference in comparison to M-H_2 complexes is that M-H-Si and M-H-X linkages are asymmetric, i.e., look like hydride-bridged

systems with M–H–Si near 90°. The bonding and activation of hydrosilanes has been the subject of several reviews (7,97–100) and book chapters (8,101). Theoretical calculations support a similar bonding picture for silane complexes as to that for H₂ complexes. However, the Si–H bond is more basic (better σ donor) than H–H (and C–H) bonds and also a better π acceptor. Nonetheless, there is a close overall relationship between Si–H, H–H, and other X–H complexes, and as for H₂ complexes a near continuum of degrees of “arrested” bond activation can exist. The effects of variation in M/L sets can be similar to that for H₂ complexes, e.g., CpMn(CO)₂(HX) are σ complexes for both X = H and SiR₃ while CpRe(CO)₂(H)(X) are classical (or have very long *d*_{XH}) because of the better back donating Re center. However, the presence of substituents R on Si leads to variations in electronics/sterics that can affect the activation of the Si–H bond regarding both homolytic and heterolytic splitting. Electron withdrawing R groups on HSiR₃ such as Cl promote Si–H homolysis (oxidative addition to MH(SiR₃)) presumably because they lower the SiH σ* orbital energy, which favors increased back donation. On the other hand, electron-donating substituents such as alkyls decrease the Si–H interaction with the metal, fostering σ coordination over oxidative addition. Lastly, there are exceptions to the above: for interaction of silanes with strongly *electrophilic* fragments with electron-withdrawing ligands on the metal such as Cr(CO)₅, the M-silane binding energy *decreases* with more electron-withdrawing substituents on Si (102). This reversal may reflect the increased importance of SiH → M σ donation relative to the back donation component of the bonding for electrophilic M, as seen for M–H₂ complexes. Clearly the M–silane interaction and activation can be finely tuned in several ways, leading at times to seemingly counter-intuitive behavior (100b).

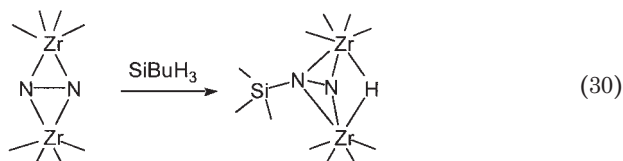
Fewer examples of heterolysis of silane Si–H bonds are known as compared to splitting of H–H bonds. However, the Si is highly activated toward nucleophilic attack by trace water, hydroxylic or halocarbon solvents, and even fluoride from anions when silanes are coordinated to electrophilic cationic centers (103).



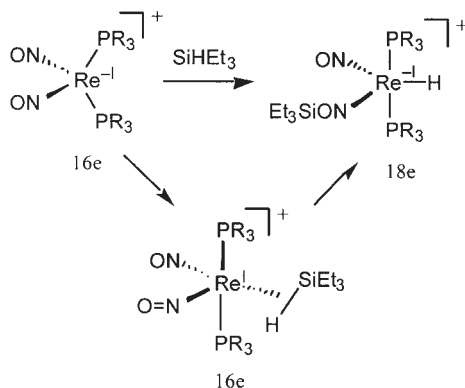
This occurs because the Si–H bond in free silanes is already polarized in the sense $\text{Si}^{\delta+}\text{--H}^{\delta-}$ and coordination to an electrophilic M increases the positive charge on Si. This favors its effective elimination as a silylium cation, R_3Si^+ , a powerful electrophile that can abstract OH^- from trace water to give R_3SiOH and also extract fluoride from counteranions such as SbF_6^- [Eq. (28)] and even the BAr_f^- anion (104). As initially proposed by Crabtree (103) and supported by calculations discussed below, the cleavage in most cases is likely to be a concerted process, i.e., the nucleophile attacks the bound Si [Eq. (29)].



Silanes and H_2 parallel each other in reactivity with organometallic compounds (105), and silanes react with coordinated N_2 and sulfide ligands much like H_2 . As in the H_2 heterolysis shown in Eq. (23) above, the macrocyclic zirconium system of Fryzuk *et al.* (90) heterolyzes Si–H bonds [Eq. (30)].



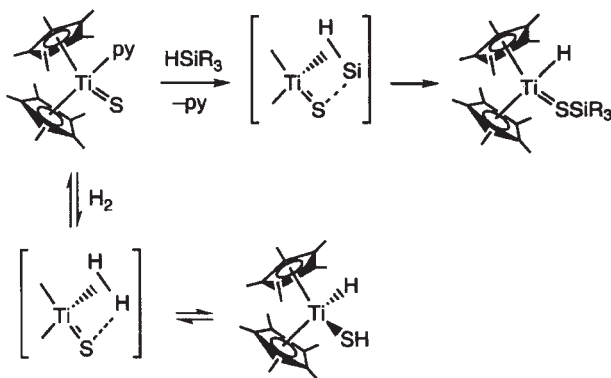
The crystal structure of the product shows Si attached to nitrogen ($\text{Si--N}=1.735(4)$) and $d_{\text{NN}}=1.530(4)$, elongated from 1.43(1) in the reactant, and DFT calculations show that Eq. (30) is exothermic by 19.7 kcal/mol for SiH_4 reaction. Thus a rare novel example of heterolytic cleavage of the Si–H bond occurs where the proton takes up a bridging hydride position. Another notable example of parallel heterolysis of H–H and Si–H bonds involves the 16e $[\text{Re}(\text{NO})_2(\text{PR}_3)_2][\text{BAr}_f^-]$ complex which heterolytically cleaves H_2 (Scheme 3) and SiH_3Et (Scheme 6) (54). The crystal structure of the silylated nitrosyl complex with $\text{R} = i\text{-Pr}$ has been determined and shows a very significant lengthening of the N–O bond (1.321(5) Å in the NOSiEt_3 ligand vs. 1.194(5) Å in the NO ligand). This system represents a rare case of silane heterolysis on a seemingly very electron-rich species (formally contains a $d^8 \text{Re}^{-1}$ center). This paradoxical result (oxidative addition would have been expected) may be ascribed to the versatility of this Re cation in adjusting to different electronic and steric conditions. Subsequent to



SCHEME 6.

coordination of the silane and because of steric repulsions, it is conceivable that bending of one NO ligand is induced by the proximity of the ethyl groups. This would change the formal oxidation state of the Re from -1 to $+1$, give a geometry closer to a tetragonal pyramid, and create a new vacancy for silane binding approximately trans to the linear NO. The strong π -acceptor nature of the NO then increases the acidity of the σ complex, in accord with the principles discussed above that favor heterolysis.

Reaction of silanes with a $\text{Ti}=\text{S}$ complex to form an $\text{S}-\text{Si}$ bond is reversible and analogous to that for H_2 addition (Scheme 7) (106). A small $k_{\text{H}}/k_{\text{D}}$ of 1.3 for addition of $(\text{H}/\text{D})\text{SiMe}_3$ is consistent with hydride transfer from the silane via a four-center transition state.

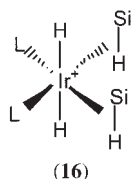


SCHEME 7.

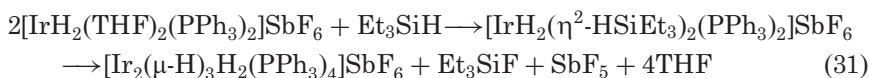
B. HETEROLYTIC CLEAVAGE OF SILANES ON ELECTROPHILIC CATIONIC CENTERS

1. Cationic Iridium and Rhenium Complexes

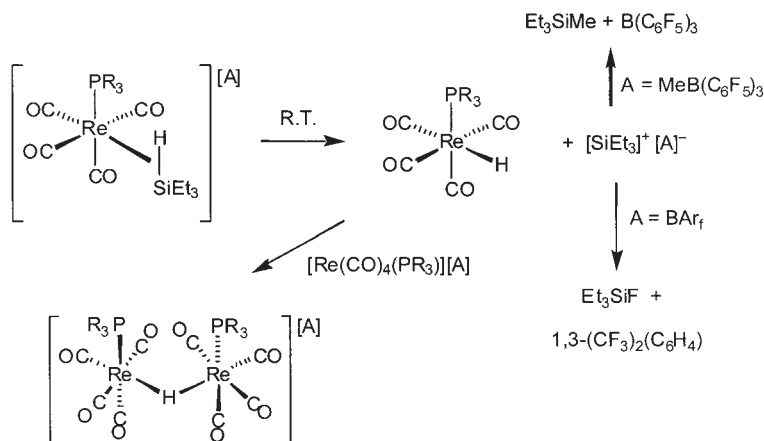
Cationic silane complexes are normally stable only in solution at low temperature and are rarely isolable (103). Thermally unstable bis(silane) adducts such as $[\text{IrH}_2(\eta^2\text{-HSiEt}_3)_2(\text{PPh}_3)_2]\text{SbF}_6$ (**16**) were reported by Crabtree to be detectable by NMR at low temperature and show intriguing reactivity, structures, and dynamics (103).



At room temperature heterolytic cleavage of the Si–H bonds in **16** occurs in CH_2Cl_2 [Eq. (31)].



If this reaction is carried out in the presence of alcohols, homogeneous catalysis of silane alcoholysis occurs, as will be discussed below. Heterolysis of Et_3SiH in the highly electrophilic complex *cis*- $\text{Re}(\text{CO})_4(\text{PR}_3)(\eta^2\text{-HSiEt}_3)[\text{A}]$ ($\text{R} = \text{Ph}$, Cy) occurs (Scheme 8) (85) much



SCHEME 8.

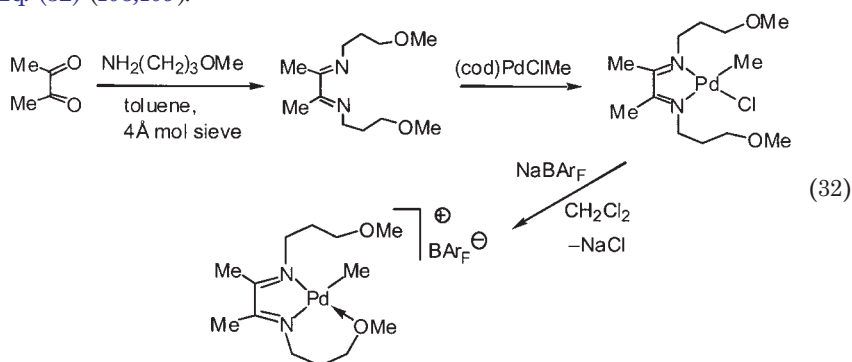
like that in the above system and is analogous to H_2 heterolysis (Eq. (9) and Scheme 5) in that a hydride-bridged dimer forms. The silane complex $[Re(CO)_4(PPh_3)(HSiEt_3)][MeB(C_6F_5)_3]$ was prepared in an NMR tube at $-40^\circ C$ by injection of one equivalent of Et_3SiH into a solution of $[Re(CO)_4(PPh_3)(CD_2Cl_2)][MeB(C_6F_5)_3]$ in CD_2Cl_2 formed from $[Re(CO)_4(PPh_3)(CH_3)]$ and $B(C_6F_5)_3$. The assignment of this product as an η^2 - $HSiEt_3$ σ complex was made on the basis of an upfield doublet at -8.89 ppm ($J_{HP}=10.5$ Hz), which had ^{29}Si satellites ($J_{HSi}=60.9$ Hz). This J_{HSi} fall in the range of values (20–70 Hz) typically found for known σ -bound silane complexes (8,98). As the NMR sample was warmed to $0^\circ C$, the intensity of the σ -complex decreased and new resonances corresponding to the hydride complex and the hydride bridged dimer in Scheme 8 began to grow in. At room temperature the ^{31}P and 1H NMR spectra corresponded to complete conversion to dimer, and resonances in the 1H NMR spectrum corresponded to the formation of the silane Et_3SiMe . There was no evidence for the formation of either methane or a Et_3Si -bridged dimer. The reaction was also carried out using the BAR_F^- derivative to see if the σ -complex would be stable at room temperature, and if not, what sort of Si containing products would be formed. When one equivalent of Et_3SiH was injected into a cooled ($-40^\circ C$) CD_2Cl_2 solution of $[cis-Re(CO)_4(PPh_3)(CD_2Cl_2)][BAR_F]$ formation of the σ -complex $[cis-Re(CO)_4(PPh_3)(\eta^2-HSiEt_3)][BAR_F]$ was observed. However, warming of the sample to room temperature for 5 min still resulted in the complete conversion to the hydride-bridge dimer. GC/MS analysis of the volatiles from this reaction revealed the presence of the disiloxane $Et_3SiOSiEt_3$, Et_3SiF , and $1,3-(CF_3)_2(C_6H_4)$. This suggests that the $Re(\eta^2-HSiEt_3)$ complex is unstable at room temperature even with the non-interacting anion BAR_F^- , and that elimination of Et_3Si^+ probably proceeds with attack on the BAR_F^- anion (or equivalently, nucleophilic attack of the anion at Si as depicted in Eq. (29)).

It is important to note that the σ silane complexes were formed in complete conversion at low temperature in the NMR spectra in CD_2Cl_2 solution, whereas the H_2 complexes (13 in Scheme 5) were only observed in low concentrations ($<5\%$) due to fast exchange with free methylene chloride in CD_2Cl_2 solution. This indicates that a tertiary Si–H bond coordinates more strongly to highly electrophilic fragments such as $[cis-Re(CO)_4(PR_3)]^+$ than an H–H bond (and CH_2Cl_2). This is in agreement with the notion that the greater basicity of the Si–H bond compared to the H–H bond makes Si–H a better σ donor, assuming that σ donation is the much greater bonding component in the Re system. Thus silanes appear to be electronically both better σ -donors and

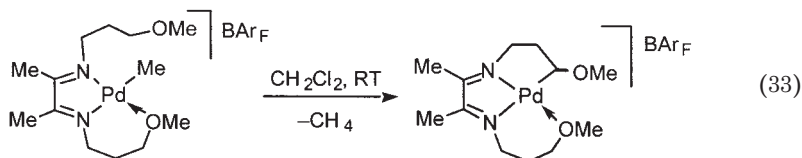
π -acceptors in comparison to H_2 . Steric effects are however much greater for silanes and more congested first-row fragments such as $(CO)_3(PCy_3)_2$ and $[Mn(CO)(diphosphine)_2]^+$ do not coordinate silanes (107) but do bind H_2 .

2. Cationic Diimine Palladium and Platinum Complexes

There are much fewer examples in the literature of the heterolytic cleavage of Si–H bonds compared to H–H and even fewer other examples in which a σ -silane complex was observed as an intermediate in the activation. We have synthesized alkyl-substituted diimine ligands with sidearms containing labile functional groups that “reserve” a vacant site for binding and activation of sigma bonds as shown in Eq. (32) (108,109).

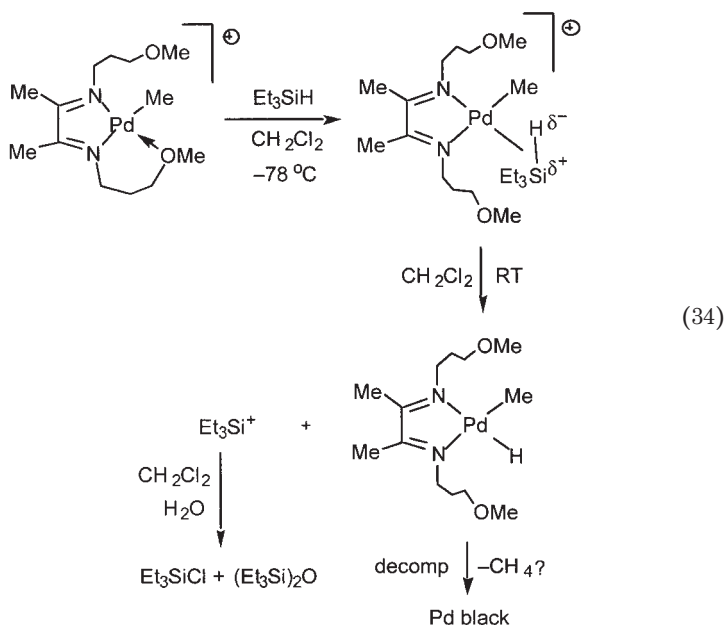


Solutions of the cationic diimine complex are stable to air/moisture and are more thermally stable than well-studied aryl diimine complexes $[(NN)Pd^{II}(Me)(OEt_2)]^+$ ($NN = ArNCMeCMeNAr$) that have a solvento ligand rather than pendant coordinating groups (110). The 1H NMR spectrum of the methoxy-substituted diimine complex in $CDCl_3$ exhibits no noticeable change at RT over 30 min, or a week if stored at $-30^\circ C$. This increased stability is likely due to the intramolecular coordination of OMe. However, prolonged standing of a solution at RT leads to the formation of a tricyclic complex which is presumably formed by addition of a C–H of the CH_2 group proximal to the coordinated OMe, followed by CH_4 elimination [Eq. (33)].



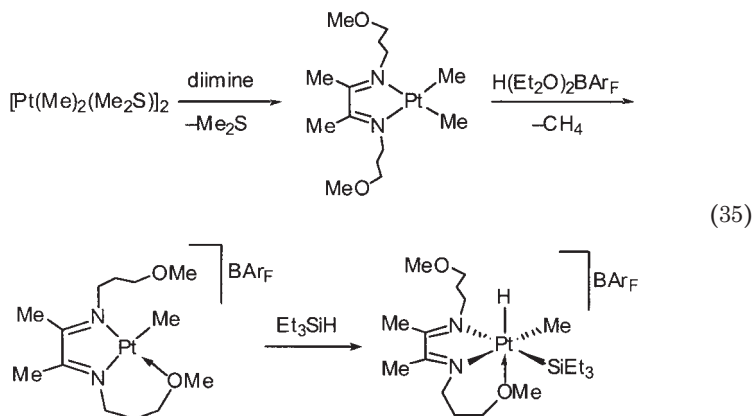
X-ray analysis shows distorted square planar coordination around Pd. This is the first example of alkyl C–H bond activation with a cationic diimine Pd(II) complex under such mild conditions.

Reaction of the above Pd methyl complex in CD_2Cl_2 with HSiEt_3 at -78°C cleanly gives a product consistent with σ -silane coordination, $[(\text{NN})\text{Pd}^{\text{II}}(\text{Me})(\eta^2\text{-H-SiEt}_3)]^+$ (108). The ^1H NMR spectrum contains a high field signal at $\delta -9.87$ corresponding to the Si–H proton, and one single peak at $\delta 3.22$ consistent with equivalent, non-coordinating OCH_3 groups. Apparently the $\eta^2\text{-H-SiEt}_3$ displaces the bound OMe, as shown in Eq. (34).



However, the complex is thermally unstable, and rapidly decomposes as its solution is warmed to RT. As measured by GC-MS, the volatile products of the reaction contain Et_3SiCl and $(\text{Et}_3\text{Si})_2\text{O}$ as two major components, characteristic of heterolytic cleavage of the $\eta^2\text{-Si-H}$ bond. The $(\text{Et}_3\text{Si})_2\text{O}$ was presumably formed by the reaction of SiEt_3^+ with adventitious H_2O , and Et_3SiCl was formed by attack of SiEt_3^+ on CD_2Cl_2 solvent. Pd black also forms, possibly due to methane elimination from an unobserved Pd methyl hydride complex and instability of the resulting Pd(0) species.

The analogous cationic Pt(II)–diimine complex is prepared by protonation of the dimethyl complex [Eq. (35)] (108).



The bound OMe has a ^1H NMR signal at δ 3.76 vs. the signal at δ 3.29 of unbound OMe. The structure is confirmed by X-ray analysis (Fig. 5) and shows a distorted square planar geometry around Pt. Unlike the Pd analogue, solutions are stable and the NMR spectra in CDCl_3 do not change for weeks at RT in air. This high stability is in drastic contrast to the analogous aryl diimine analogue $[(\text{NN})\text{Pt}^{\text{II}}(\text{Me})(\text{OEt}_2)]^+$, where $\text{NN} = \text{ArNCMeCMeNAr}$ ($\text{Ar} = p\text{-MeC}_6\text{H}_4$), which is not even observable by NMR spectroscopy because of its extremely high instability (111). It is clear that coordination of the intramolecular OMe confers stability, and, accordingly, the complex does not activate the C–H bonds of alkanes, benzene, toluene, or those in the ligand arm. However, the bound OMe is readily displaced when the complex is treated with HSiEt_3 at -30°C , eventually affording a colorless octahedral Pt(IV) hydride methyl silyl complex [Eq. (35)]. However, solutions are unstable at RT and decompose to an unidentifiable mixture within ~ 20 min. While oxidative addition of Si–H bonds to cationic diphosphine Pt(II) complexes to form Pt(IV) silyl hydrides is known (112), this is the first case of addition to a cationic diimine Pt(II) complex. Previously diimine Pt(IV) silyl hydrides were suggested to be too unstable to be observable (113), so it is likely that a pendant OMe stabilizes the complex by coordinating to the vacant sixth site (114).

3. Manganese and Rhenium Complexes with Tied-Back Phosphites

Complexes featuring the tied-back phosphite ligand, $\text{P}(\text{OCH}_2)_3\text{CMe}$, have been of considerable interest to us for the binding and activation

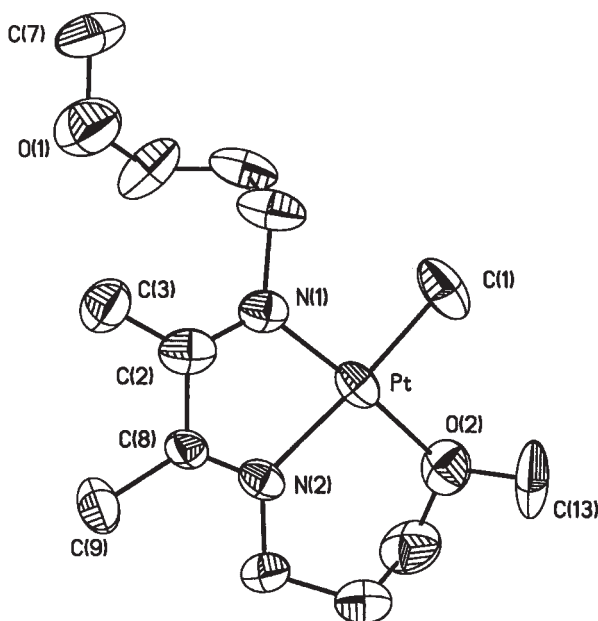
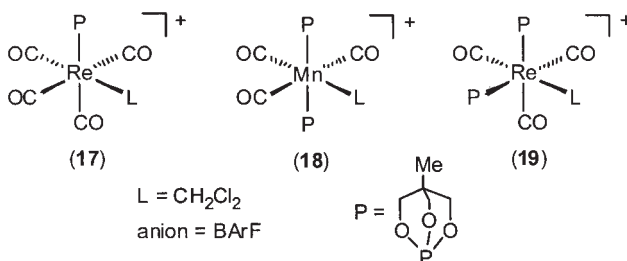


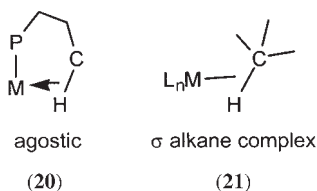
FIG. 5. X-ray structure of Pt-diimine complex showing thermal ellipsoids at 50% level. Selected bond distances (Å) and angles (deg): Pt(1)–N(1), 1.956(1); Pt(1)–N(2), 2.056(9); Pt(1)–C(1), 2.03(1); Pt(1)–O(2), 2.070(1), N(1)–C(2), 1.31(1). N(2)–Pt(1)–O(2), 96.6(4); N(2)–Pt(1)–N(1), 78.7(4); O(2)–Pt(1)–C(1), 86.1(6).

of sigma bonds, and several CO-rich cationic Mn and Re complexes **17–19** were readily synthesized (115).



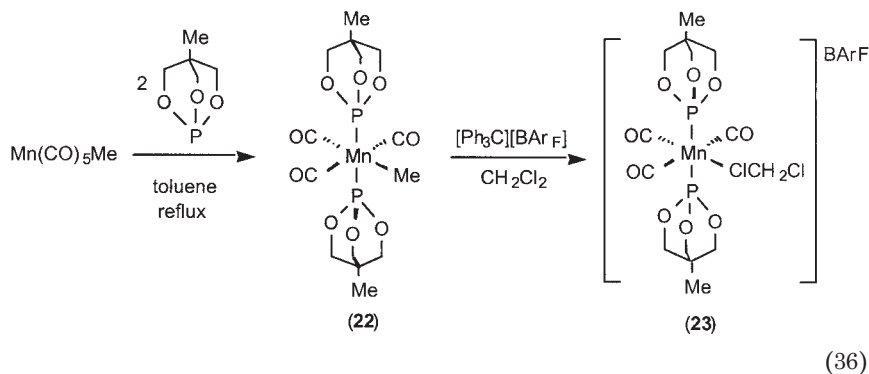
The caged phosphite is both a weaker σ -donor and a stronger π -acceptor than analogous phosphines, and should increase the electrophilicity of the metal center, which is already high because of the electron-withdrawing CO ligands and lack of strong σ -donor ligands. Most importantly, the phosphite lacks accessible C–H bonds to form agostic

interactions (**20**) that would compete with binding of very weak external ligands, e.g., alkanes.



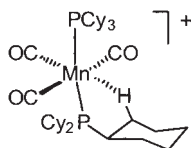
Observation of σ complexes such as **21** (which often are improperly referred to as agostic complexes) is being sought for studies of C–H activation, but ΔH of binding is only 10–15 kcal/mol (**19a**), which is hardly enough to overcome the entropic advantage for internal agostic C–H coordination. The tied-back phosphite is also sterically more compact than phosphines and may accommodate alkanes, silanes, olefins, and other more sterically demanding ligands in first-row metals. The complexes are stable crystalline solids and are valuable synthons because the dichloromethane ligand cannot be removed in vacuo in the solid but is readily displaced in solution by H_2 , ethers, amines, olefins, and silanes. As will be shown, silanes undergo facile heterolytic cleavage. As discussed above, heterolytic cleavage of both H_2 and silanes were observed on related phosphine systems, e.g., $[Re(CO)_4(PR_3)(CH_2Cl_2)]^+$.

The Mn complex, *trans*- $[Mn(CO)_3(P)_2(CH_2Cl_2)]^+$, **23**, is prepared in high yield as outlined in Eq. (36) (**115a**).



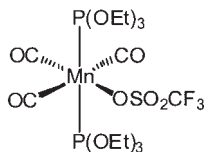
Treatment of $Mn(CO)_5Me$ with two equivalents of phosphite (**116**) in refluxing toluene yields the tricarbonyl methyl complex **22** which reacts with $[Ph_3C][BAr_F]$ in CH_2Cl_2 to give **23**. The ν_{CO} values for **23**, 2096w, 2025s, and 2004s, are much higher than those (2048w, 1962s, and 1942s)

of the analogue **24** with strongly donating PCy_3 ligands instead of phosphites (*107*), indicating that the phosphite complex is significantly more electrophilic.



(24)

The less electrophilic **24** does not bind CH_2Cl_2 but rather forms an agostic C–H interaction instead, demonstrating the usefulness of tied-back phosphites in avoiding such interactions (yet retaining a ^{31}P NMR diagnostic). Furthermore, an analogue with non tied-back phosphites, **25**, is found to coordinate the CF_3SO_3^- anion instead of CH_2Cl_2 solvent (*117*).



(25)

This demonstrates the importance of using the low-coordinating BAR_F anion. The bound CH_2Cl_2 in **23** freely exchanges with CD_2Cl_2 solvent but cannot be removed from the solid by exposure to high vacuum for hours. Dinitrogen does not displace the CH_2Cl_2 presumably because N_2 is a very poor σ donor, weaker even than CH_2Cl_2 (*107*).

X-ray structural analysis of **23** (Fig. 6) shows octahedral configuration with the CH_2Cl_2 molecule bound to Mn through one chlorine atom Cl(1) and a Mn–Cl(1) distance of 2.4109(13) Å. A weak interligand hydrogen bonding interaction appears to occur between an acidic hydrogen on CH_2Cl_2 and an oxygen atom on the phosphite ligand. The distance between O(9) and an idealized hydrogen position H(4B) is calculated to be 2.418 Å, well within the general range for C–H \cdots O hydrogen bond (*118*). Hydrogen bonding involving haloalkanes is common, and the hydrogens on the CH_2Cl_2 ligand might be expected to be more acidic than in free dichloromethane because the electrophilic metal is withdrawing electrons.

Exposure of **23** to ca. 3 atm of H_2 in CD_2Cl_2 gave only about 2–3% H_2 complex, but this is a consequence of the much greater concentration

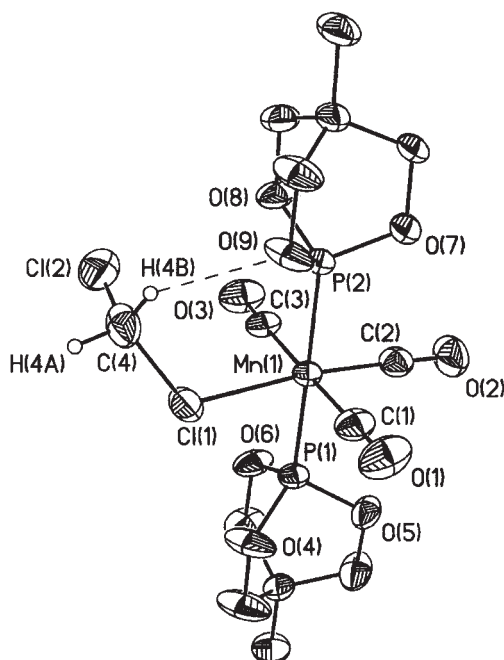
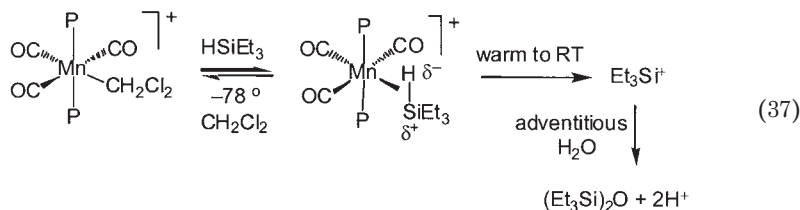


FIG. 6. X-ray structure of the cation of $[\text{Mn}(\text{CO})_3\{\text{P}(\text{OCH}_2)_3\text{CMe}\}_2(\text{CH}_2\text{Cl}_2)]$ $[\text{BARF}]$, **23**. Selected bond distance (\AA) and bond angles (deg): $\text{Mn}-\text{Cl}(1) = 2.4109(13)$, $\text{Cl}(1)-\text{C}(4) = 1.804(5)$, $\text{Cl}(2)-\text{C}(4) = 1.720(7)$, $\text{C}(4)-\text{O}(9) = 3.185(6)$, $\text{H}(4\text{B})-\text{O}(9) = 2.418$ (idealized H), $\text{Cl}(1)-\text{C}(4)-\text{Cl}(2) = 112.1(3)$, $\text{Mn}-\text{Cl}(1)-\text{C}(4) = 118.2(2)$.

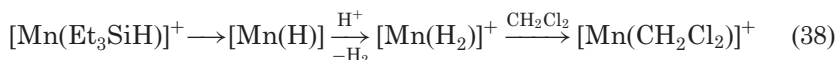
of CD_2Cl_2 over H_2 rather than relative ligand binding strengths. Replacement of H_2 with HD gas afforded the η^2 -HD complex, $[\text{mer-Mn}(\text{CO})_3\{\text{P}(\text{OCH}_2)_3\text{CMe}\}_2(\text{HD})][\text{BARF}]$, which showed a J_{HD} coupling of 34.5 Hz. This is one of the highest values ever reported and is consistent with η^2 - H_2 binding to a highly electrophilic metal center with a relatively short H-H distance (calculated to be 0.84–0.86 \AA from J_{HD}). The H_2 ligand does not appear to be as prone towards heterolytic cleavage as that in $[\text{Re}(\text{CO})_4(\text{PR}_3)(\text{H}_2)]^+$ [Eq. (9)], which can readily protonate ethers. Thus exposure of **23** to H_2 in CD_2Cl_2 at liquid nitrogen temperature followed by warming to -78° and treatment with three equivalents of $^i\text{Pr}_2\text{O}$ showed only the presence of $^i\text{Pr}_2\text{O}$ complex and free H_2 by NMR spectra taken at -80 to 25° . A similar result was obtained on reaction of the H_2 complex with $^i\text{Pr}_2\text{O}$ followed by addition of H_2 . Although the stronger binding of the ether than H_2 may interfere with a potential H_2 heterolytic cleavage process, the

acidity of the bound H_2 may be lower than that in $[Re(CO)_4(PR_3)(H_2)]^+$ which has four CO ligands.

Reaction of a CD_2Cl_2 solution of $[Mn(CO)_3\{P(OCH_2)_3CMe\}_2(CH_2Cl_2)]^+$ with a slight excess of Et_3SiH or $PhSiH_3$ at -78° produced a solution of an η^2 -bound silane complex similar to structurally characterized $Mo(CO)(\eta^2-H-SiR_3)(diphosphine)_2$ (119) and the above $[Re(CO)_4(PR_3)(\eta^2-H-SiEt_3)]^+$ (Scheme 8). J_{SiH} could not be measured due to the Mn quadrupolar broadening. When the solutions were raised to room temperature, 1H NMR spectra indicated the formation of a mixture of several unidentified products that were likely formed by heterolytic cleavage of the η^2 -Si-H bond as for the Re complex. No clear evidence was present for formation of a Mn hydride complex, either as an intermediate or a final product. GC-MS analysis of the volatiles released showed $(Et_3Si)_2O$ to be the major component, which is presumably generated from reaction of the silyl cation with adventitious moisture [Eq. (37)].



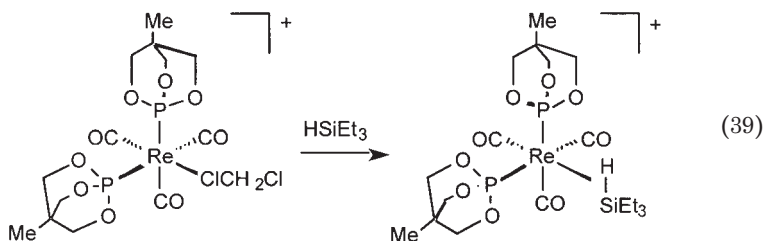
The fate of the Mn fragment is not clear, but it is conceivable that if an unobserved Mn-H species forms it could be immediately protonated to the H_2 complex by the protons released from silane hydrolysis. The labile H_2 could then in turn be displaced by CH_2Cl_2 solvent to regenerate $[Mn(CO)_3\{P(OCH_2)_3CMe\}_2(CH_2Cl_2)]^+$ [Eq. (38)].



Such formation of $[CpFe(CO)(PPh_3)(H_2)]^+$ from hydrolysis of $[CpFe(CO)(PPh_3)(HSiR_3)]^+$ has previously been observed and employed for catalytic silane alcoholysis discussed below.

The Re analogue, $[Re(CO)_3\{P(OCH_2)_3CMe\}_2(CH_2Cl_2)]^+$ was synthesized similarly, but here the phosphites adopt a cis orientation to each other as evidenced by the CO IR stretching pattern (115b). Three strong signals for ν_{CO} occur at 2088, 2025, and 1991 cm^{-1} , which is a typical pattern for this type of configuration. The cis orientation was confirmed in an X-ray structure analysis of an analogue with Et_2O instead

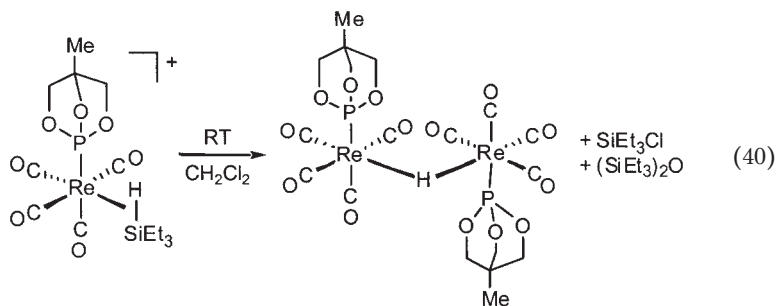
of CH_2Cl_2 . This cis orientation is likely determined by a favorable electronic influence since significant steric factors are not present. For the Mn(I) complex, **23**, a cis orientation would cause repulsive interaction between the two phosphites because of the smaller size of Mn(I) in relation to Re(I). The Re complex is the least electrophilic in this study, but the bound CH_2Cl_2 still cannot be removed under high vacuum. It can be readily displaced by Et_2O , olefins, and Et_3SiH as exemplified in Eq. (39).



In contrast to the heterolytic Si–H bond cleavage in the Mn analogue, the σ coordinated silane is stable both in the solid state and in solution, which is somewhat surprising since isolable cationic silane complexes are very rare. One of the few other examples is $[\text{CpRu}(\text{PMe}_3)_2(\text{HSiCl}_3)][\text{BAR}_\text{F}]$, for which an X-ray structure showed an Si–H distance of 1.77(5) Å (cf. 1.48 Å in free hydrosilanes), indicating the Si–H bond is close to oxidative addition (electron-withdrawing groups on Si increase $\text{M} \rightarrow (\text{Si}-\text{H}) \sigma^*$ back donation) (120) and therefore less likely to cleave heterolytically. The solution ^1H NMR spectrum of the Re–silane complex in Eq. (39) suggests that the silane is relatively strongly bound since $J_{\text{SiH}} = 66$ Hz, much smaller than the 177 Hz value found in free Et_3SiH . In comparison, the J_{SiH} coupling for $[\text{Re}(\text{CO})_4(\text{PPh}_3)(\eta^2\text{-HSiEt}_3)]^+$ is 60.9 Hz. These values indicate that the Si–H bond is elongated in both of these complexes, although not as much as in neutral M–silane complexes where most of the reported J_{SiH} couplings range from 20 to 60 Hz, i.e., closer to oxidative addition (8, 98).

More electrophilic congeners with only one phosphite and four CO ligands were also studied (115b). $[\text{Mn}(\text{CO})_4\{\text{P}(\text{OCH}_2)_3\text{CMe}\}(\text{CH}_2\text{Cl}_2)][\text{BAR}_\text{F}]$ was unstable at room temperature, although derivatives such as Et_2O and olefin complexes could be isolated. The analogous tetracarbonyl Re– CH_2Cl_2 complex, **17**, could be isolated and was more electrophilic than the tricarbonyl Mn complex with two phosphites, as evidenced by higher ν_{CO} . The bound CH_2Cl_2 was again readily displaceable by ether, olefins, and silanes. The silane complex is thermally

unstable and decomposes at RT within 10 min to give a hydride-bridged dimer [Eq. (40)].



Heterolytic cleavage of the Si–H bond presumably occurs as for the phosphine system (Scheme 8). X-ray analysis of the hydride complex showed the hydrogen atom on the two-fold rotation axis of the two Re(I) fragments, where each fragment is octahedral about Re. The average Re–H distance of 1.76(2) Å appears to be considerably shorter than the 1.92(10) Å found in the triphenylphosphine analogue (85), although the standard deviations are large here. The shorter Re–H distance demonstrates stronger Re–H bonding, consistent with a more electron deficient Re center due to the weaker electron donating ability of phosphite in relation to PPh_3 . Also, the Re–H–Re angle of 156.5° is significantly larger than the 124.4° found in the phosphine complex, consistent with a 2-electron, 3-atom bonding mode around Re–H–Re.

In summary, the highly electrophilic cationic Mn(I) and Re(I) fragments with tied-back phosphite ligands, $[\text{M}(\text{CO})_3(\text{P})_2]^+$ and $[\text{Re}(\text{CO})_4(\text{P})]^+$ ($\text{P} = \text{P}(\text{OCH}_2)_3\text{CMe}$) are more electrophilic and sterically less congested than analogous phosphine complexes, which favors strong binding of weak solvent ligands, e.g., CH_2Cl_2 . Reaction of Et_3SiH with the CH_2Cl_2 complexes leads to three different outcomes: (a) the fragment $[\text{Mn}(\text{CO})_3(\text{P})_2]^+$ gives heterolytic cleavage of the silane but a Mn–H species is not observed; (b) $[\text{Re}(\text{CO})_3(\text{P})_2]^+$ affords a rare stable cationic σ -coordinated silane complex; (c) the more electrophilic $[\text{Re}(\text{CO})_4(\text{P})]^+$ again gives heterolytic cleavage of the silane, but with formation of a hydride-bridged dimer. These highly electrophilic 16e fragments would appear to be ideally suited for observing binding of extremely weak ligands such as alkanes by e.g., solution NMR studies at low temperatures. However the insolubility of $[\text{Mn}(\text{CO})_3(\text{P})_2(\text{CH}_2\text{Cl}_2)] [\text{BAR}_\text{F}]$ and related cationic salts in hydrocarbons precluded such observation. A ligand system (or anion) must be designed such that the resulting complexes are soluble in hydrocarbons rather than

coordinating polar solvents. One possibility is attaching long alkyl or fluoroalkyl groups to the tied-back phosphite in place of the methyl group. Bidentate tied-back diphosphonite ligands, which we have recently synthesized and studied their ligation to Fe and Ru centers (121), may also be useful for designing hydrocarbon-soluble cationic 16e complexes.

C. SILANE ALCOHOLYSIS

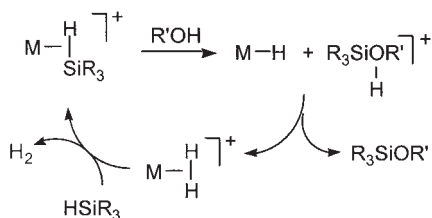
1. Iridium and Iron Complexes

The alcoholysis of hydrosilanes (Eq. 41) has important applications in the synthesis of silyl ethers and in protection of reactive OH groups in organic synthesis (103).



Luo and Crabtree had found that when the reaction in Eq. (31) was carried out in the presence of alcohols, homogeneous catalysis of silane alcoholysis occurs with high efficiency and selectivity according to Eq. (41). Vigorous evolution of hydrogen occurred immediately and cooling was necessary to control the reaction. The activity of the catalyst strongly depended on the counterion used, e.g., for SbF_6^- deactivation of the catalyst occurred much more slowly than with BF_4^- or PF_6^- . Importantly, Crabtree showed that direct nucleophilic attack by ROH on a $\eta^2\text{-Si-H}$ bond as in Eq. (29) occurred rather than initial OA. The high activity of the actual catalyst, $[\text{IrH}_2(\text{THF})_2(\text{PPh}_3)_2]^+$, has been ascribed to the possibility that, after dissociation of the labile THF ligands, both reactants (silane and alcohol) could bind to Ir at the same time, facilitating heterolysis. As will be shown below, subsequent kinetic, mechanistic, and computational studies on two different catalytic iron and manganese systems indicate that two binding sites are not needed and that nucleophilic attack by ROH on a $\eta^2\text{-Si-H}$ ligand is the key step.

Brookhart and co-workers found that the cationic σ -silane complex $[\text{CpFe}(\text{CO})(\text{PR}_3)(\text{HSiEt}_3)]^+$ was observable by NMR at RT but only in the presence of excess silane (sacrificial removal of trace H_2O as Et_3SiOH) and could not be isolated as a solid (122). The $[\text{CpFe}(\text{CO})(\text{PR}_3)]$ fragment catalyzed silane alcoholysis in the presence of the BAR_f^- counterion (123). Although rapid deactivation of the catalyst occurred with ethanol as substrate, phenol reacted continuously with turnover numbers up to 80 min^{-1} . It was proposed (Scheme 9)



SCHEME 9.

that attack of the alcohol on bound silicon would give a protonated silyl ether that could rapidly protonate $\text{M}-\text{H}$ to form a dihydrogen complex $[\text{M}-\text{H}_2]^+$ (the known complex $[\text{CpFe}(\text{CO})(\text{PR}_3)(\text{H}_2)]^+$).

The silane substrate would then displace H_2 to give back the starting silane complex for further alcoholysis, and this was determined to be the rate-limiting step. These are all known reactions, and this mechanism and rate-determining step were recently supported by theoretical calculations that showed the heterolysis to be a highly concerted process, i.e., transformation of the σ -silane complex to the H_2 complex could even take place in a single step, thus circumventing the transient hydride complex (124). It is noteworthy that the mechanism of this reaction involves two different σ complexes: $\text{M}(\eta^2\text{-Si-H})$ and $\text{M}(\eta^2\text{-H}_2)$.

Electrophilic cationic complexes are not required for catalysis of silane alcoholysis since neutral transition metal complexes as well as heterogeneous systems containing $\text{Pd}(0)$ also function well, and polar solvents such as *N,N*-dimethylacetamide can even be used (125). A transition-metal center is not even needed to heterolyze the $\text{Si}-\text{H}$ bond: a highly electrophilic borane center $\text{B}(\text{C}_6\text{F}_5)_3$ is able to fulfill this role (126). The polarization induced in the $\text{Si}-\text{H}$ bond upon electrophilic activation renders the silicon center susceptible to nucleophilic attack by the alcohol, giving essentially an alcohol adduct of a trialkyl-substituted silylium cation. Subsequent proton transfer from this acid to the “ $\text{M}-\text{H}$ ” species (in this case, $[\text{HB}(\text{C}_6\text{F}_5)_3]^-$) completes the cycle, releasing dihydrogen and regenerating the catalyst.

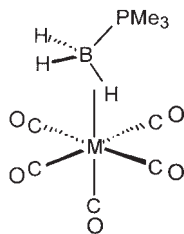
2. Manganese Complexes with Tied-Back Phosphites

The $[\text{Mn}(\text{CO})_3(\text{P})_2(\text{CH}_2\text{Cl}_2)][\text{BAr}_\text{F}]$ complex, **23**, also catalyzes reaction of phenol with triethylsilane, presumably by a mechanism similar to that proposed for the Fe system (Scheme 9). The ratio of silane to the catalyst was about 24:1, and a slight deficiency of phenol was added at -78°C in an NMR tube reaction. ^1H NMR spectra recorded from

-80°C to 25°C all showed a broad signal at -9.23 ppm presumably due to the H_2 complex formed as an intermediate in [Scheme 9](#). Upon exposure of the solution in the NMR tube to a He atmosphere after reaction was complete, the ^1H NMR spectrum showed a triplet at -16.75 ppm corresponding to the silane σ complex. The latter would be expected according to [Scheme 9](#) since unreacted silane was present (stoichiometric excess over phenol reactant) and is a stronger ligand than either H_2 or CH_2Cl_2 . The expected product of silane alcoholysis, PhOSiEt_3 , was isolated in ca. 50% yield, demonstrating that the reaction is catalytic. Manganese carbonyl species such as $\text{Mn}(\text{CO})_5(\text{CH}_3)$ and $[\text{Mn}(\text{CO})_4\text{Br}]_2$ are also effective pre-catalysts for alcoholysis of silanes ([127](#)) and may operate via a similar pathway, i.e., the true catalyst is an electrophilic unsaturated Mn fragment that heterolytically cleaves an intermediate silane σ complex.

IV. Heterolytic Cleavage of B–H and C–H Bonds

B–H σ complexes containing neutral borane ligands have recently been established. Boranes such as BH_3 are Lewis acids but their base adducts such as $\text{BH}_3 \cdot \text{PR}_3$ are potential σ ligands analogous to silanes. The X-ray structures of group 6 pentacarbonyl analogues such as $\text{W}(\text{CO})_5(\text{BH}_3 \cdot \text{PMe}_3)$ clearly show monodentate $\eta^2\text{-B-H}$ coordination ([128](#)).



M = Cr, W

(26)

Complex **26** is among the first examples of intermolecular coordination of a single B–H bond in a neutral borane to a transition metal, and these species can be regarded as models for alkane coordination. The crystal structures of borane complexes such as **26** are of interest to compare with those for other octahedral σ complexes, particularly

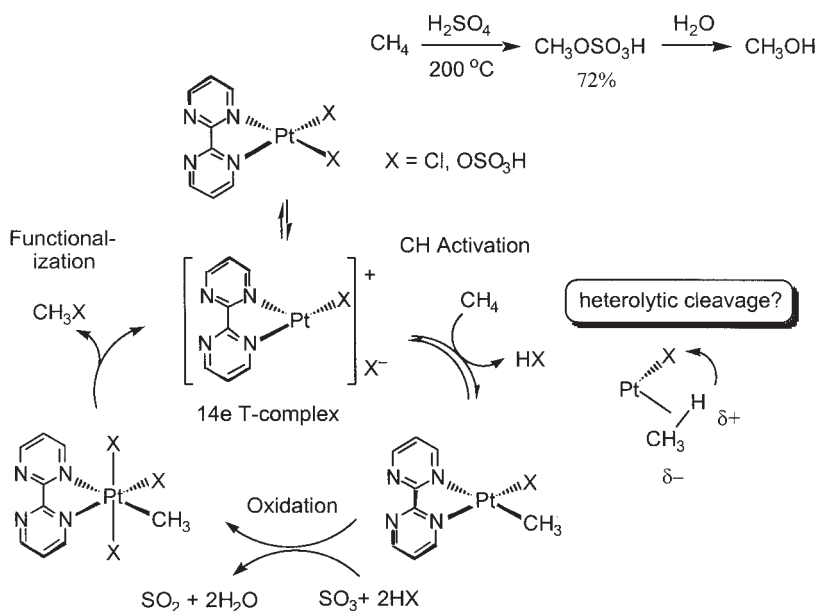
silane complexes. The d_{BH} (1.1–1.3 Å) are not well determined (large standard deviations) and are not very meaningful. The M–H–B angles in $\text{M}(\text{CO})_5(\text{BH}_3 \cdot \text{PMe}_3)$ are near 130° (again with large esd's) and can be as high as 167° in related systems. These are much larger than the angles observed in M–H–Si σ complexes and the $\text{Cp}_2\text{Ti}(\text{HBcat})_2$ and related M–H–B σ complexes characterized by Hartwig that appear to the best examples of genuine $\eta^2\text{-BH}$ σ complexes (129). Thus the bonding for these neutral borane ligands, while still bent, is closer to end-on than side-on as in borohydride complexes where M–H–B can be as high as 162° . Because phosphine borane ligands contain 4-coordinate boron when free, they are more like BH_4^- complexes even though they are neutral. There is certainly more hydridic character than in Hartwig's base-free catecholborane complexes.

Very recently cationic Mn complexes analogous to **26** have been prepared and studied by Shimoi with respect to heterolytic cleavage of the B–H bond (16). The σ complex $[\text{Mn}(\text{CO})_4(\text{PR}_3)(\text{BH}_3 \cdot \text{PMe}_3)]^+$ (**27**; $\text{PR}_3 = \text{PMe}_2\text{Ph}$ or PEt_3) was prepared either by the novel protonation of the neutral boryl complex $\text{Mn}(\text{CO})_4(\text{PR}_3)(\text{BH}_2 \cdot \text{PMe}_3)$ with $[\text{H}(\text{Et}_2\text{O})_2][\text{BAR}_\text{F}]$ or by reaction of $[\text{Mn}(\text{CO})_4(\text{PR}_3)(\text{Et}_2\text{O})]^+$ with $\text{BH}_3 \cdot \text{PMe}_3$ analogous to Eq. (39). However, deprotonation of **27** did not occur even when it was treated with strong bases such as NaH or diazabicycloundecene. Remarkably, a solution of **27** decomposed in a few days at room temperature to give a mixture containing $\text{MnH}(\text{CO})_4(\text{PR}_3)$ and $[\text{BH}_2 \cdot 2\text{PMe}_3]^+$, although the decomposition process was not very clean. This suggests that the coordinated B–H bond cleaves heterolytically into H^- and “ $[\text{BH}_2 \cdot \text{PMe}_3]^+$ ” much as for silanes on a similar electrophilic cationic Mn complex [Eq. (37)]. Natural bond order analysis based on DFT calculations on a model complex shows that the hydrogen of the borane ligand becomes more hydridic on coordination to the Mn center, facilitating heterolysis of the B–H bond.

Among the greatest challenges in chemistry is the quest for a stable alkane complex and attendant conversion of light alkanes such as CH_4 in large reserves of natural gas to liquid fuels, e.g., methanol (17–19). The $\text{CH}_3\text{--H}$ and H--H bond energies are similar and strong (ca. 104 kcal/mol), and the C–H and H–H bonds are not too dissimilar in polarity. Both molecules have σ and σ^* orbitals of reasonably similar shape, energy, and extent, although the differences in overlap with metal d-orbitals (and steric considerations) can be critical. Thus the H_2 molecule (as well as silanes and germanes) can be coordinated to a metal center in stable fashion at ambient temperature because of substantial backbonding whereas alkanes cannot (14,130). However, alkane σ complexes have been observed spectroscopically at low

temperatures (19a) and strong evidence exists that they are intermediates in C–H bond activation processes (19d). Significantly, a rhenium–cyclopentane complex has been characterized by NMR spectroscopy at low temperature (19f), giving hope for future direct observation of alkane complexes.

Despite a small M–CH₄ binding energy of only ~10 kcal/mol, alkane σ complexes are indeed believed to be intermediates in C–H bond activation, including Pt^{II}-catalyzed *methane conversions in reaction media as harsh as fuming sulfuric acid at 200°C* (Scheme 10) reported by Periana (21a).



SCHEME 10.

A major question is whether heterolytic cleavage of the H₃C–H bond occurs as depicted in Scheme 10 (maintaining the Pt^{II} state) or whether oxidative addition to a Pt^{IV} methyl hydride complex takes place. In such systems transfer of protons would be expected to be very facile because of the extremely high mobility of H⁺, and even a short-lived, very weak σ complex could be a key intermediate. The C–H bond is likely to be polarized towards C ^{δ^-} ...H ^{δ^+} on such highly electrophilic cationic metal complexes, where H⁺ can very rapidly split off and transfer to either a cis ligand or the anion as soon as the

alkane contacts the metal. The metal center may be considered to be a superelectrophile isolobal with H^+ , mimicking superacid-induced carbocation chemistry, i.e., a σ complex such as M^+-CH_4 can be considered to be related electronically to CH_5^+ . Although there is no direct experimental evidence for the C–H bond heterolysis shown in Scheme 10, electrophilic C–H activation involving H/D exchange between acidic protons in η^2 -C,H *agostic* structures and bases such as water and methanol is known (131). Also theoretical calculations support a heterolytic type of mechanism in Scheme 10 over one based on oxidative addition of the C–H bond (132). However, other calculations favor oxidative addition pathways in methane activation on model complexes such as $M(CH_3)(HN=CHCH=NH)$ ($M = Pd^+, Pt^+, Rh^+, Ir^+, Rh, Ir$), the exceptions being Pd^+ and Rh^+ (133). Thus for third-row metal centers, even if they are electrophilic, the two pathways are close in energy (and may even occur concurrently (131)), depending on factors such as ancillary ligand properties and reaction conditions. A clear example of reversible intramolecular heterolytic C–H cleavage at diazabutadiene ligands on iridium(III) has recently been reported (134). Heterolytic processes have been recognized to be of crucial importance in many aspects of metal-mediated C–H activation and functionalization chemistry (19c).

V. Concluding Remarks

A unifying principle in the research discussed above is that *any* type of electron pair (Lewis base) can be attracted to a metal binding site (Lewis acid) to form a Lewis acid–base complex (σ complex). Highly Lewis acidic (electrophilic) metal centers (e.g., electronically unsaturated cationic fragments with electron-withdrawing ligands) favor heterolytic splitting of the coordinated X–H bond. Clearly the atoms in X–Y σ bond activation do not have to be hydrogen, although the high mobility of protons is advantageous for heterolysis of X–H bonds, i.e., $[M(X-H)]^+ \rightarrow M-X + H^+$. For $X=H$, coordination of H_2 to an electrophilic center greatly increases the acidity of H_2 , effectively creating a strong acid with an acid strength as high as triflic acid. A proton from the bound H_2 can then readily transfer to cis ligands, external bases, or the anion of cationic complexes, giving either intramolecular or intermolecular splitting with concomitant formation of a hydride or hydride-bridged complex. Such processes are the key step in both industrial and biological processes, notably including the mechanism

of hydrogenases that possess organometallic-like iron active sites. Activation of hydrosilanes ($X = Si$ above) is quite different on the other hand: the Si–H bond in a free silane is already polarized in the sense $Si(\delta^+) - H(\delta^-)$ and coordination to an electrophilic M increases the positive charge on Si. This favors its effective elimination as a silylium cation, R_3Si^+ , a powerful electrophile that can react with many nucleophiles such as alcohols, an essential step in catalysis of silane alcoholysis. The Si–H cleavage in most cases is likely to be a concerted process, i.e., nucleophile attack on the bound Si in a silane σ complex. Regarding alkane activation, Chatt made the remarkable prediction 27 years ago that methane would become one of the most popular ligands in chemistry in 25 years (*135*), which it indeed now has become despite the instability of its binding! One of the critical questions is whether deprotonation of metal-bound methane (heterolytic splitting) or oxidative addition to a methyl hydride complex occurs in for example highly electrophilic platinum(II) complexes. A future goal is to obtain direct evidence for heterolysis of a C–H bond by e.g., low temperature NMR studies demonstrating transfer of a proton from a bound alkane σ ligand to a cis ligand or external base. However, a significant barrier that needs to be overcome is the low solubility in hydrocarbon solvents of the electrophilic cationic complexes designed by us and others for this purpose. Hopefully the new ligands discussed above such as tied-back diphosponites and diimines with pendant hemilabile groups can be suitably modified and play an important role in alkane C–H and other sigma-bond activation processes.

NOTE ADDED IN PROOF

Although the primary focus of this article is on heterolysis of established dihydrogen and σ bond complexes, considerable research has been carried out on heterolytic activation of hydrogen involving classical hydride systems or unidentified transient species. Important data on the thermodynamics of H_2 splitting and the hydride donor abilities of $[MH(PP)_2]^+$ ($M = Ni, Pd, Pt$; $PP =$ diphosphine) have recently been reported by DuBois and Curtis (*142*). The dicationic complexes $[M(PP)_2]^{2+}$ heterolytically cleave H_2 in equilibrium fashion in the presence of bases such as amines to give protonated amine and $[MH(PP)_2]^+$. The involvement of a dihydrogen (and/or dihydride) complex could not be identified, illustrating the frequent problem encountered in activation of σ bonds, namely does the reaction mechanism involve a σ complex, i.e., $M(\eta^2-H_2)$ (or generically $M(\eta^2-X-H)$), or oxidative addition to $M(X)(H)$?

ACKNOWLEDGMENT

The research work described above that was carried out by us was supported by the Department of Energy, Office of Science, Office of Basic Energy Sciences, Chemical Sciences Division.

REFERENCES

1. Kubas, G. J.; Ryan, R. R.; Swanson, B. I.; Vergamini, P. J.; Wasserman, H. J. *J. Am. Chem. Soc.* **1984**, *106*, 451.
2. Kubas, G. J. *Acc. Chem. Res.* **1988**, *21*, 120.
3. Crabtree, R. H. *Acc. Chem. Res.* **1990**, *23*, 95.
4. Jessop, P. G.; Morris, R. H. *Coord. Chem. Rev.* **1992**, *121*, 155.
5. *Recent Advances in Hydride Chemistry*; Eds. Peruzzini, M.; Poli, R.; Elsevier Science B.V.: Amsterdam, **2001**.
6. (a) Heinekey, D. M.; Oldham, W. J. Jr. *Chem. Rev.* **1993**, *93*, 913; (b) Heinekey, D. M.; Lledos, A.; Lluch, J. M. *Chem. Soc. Rev.* **2004**, *33*, 175.
7. Crabtree, R. H. *Angew. Chem. Int. Ed. Engl.* **1993**, *32*, 789.
8. *Metal Dihydrogen and σ -Bond Complexes*; Kubas, G. J.; Kluwer Academic/Plenum Publishers: New York, NY, **2001**.
9. Maseras, F.; Lledós, A.; Clot, E.; Eisenstein, O. *Chem. Rev.* **2000**, *100*, 601.
10. Niu, S.; Hall, M. B. *Chem. Rev.* **2000**, *100*, 353.
11. Xu, Z.; Bytheway, I.; Jia, G.; Lin, Z. *Organometallics* **1999**, *18*, 1761.
12. Hutschka, F.; Dedieu, A. *J. Chem. Soc., Dalton Trans.* **1997**, 1899.
13. Olah, G. A. *Angew. Chem. Int. Ed. Engl.* **1993**, *32*, 767.
14. Kubas, G. J. *J. Organomet. Chem.* **2001**, *635*, 37.
15. Dewar, M. J. S. *Bull. Soc. Chim. Fr.* **1951**, *18*, C79; Chatt, J.; Duncanson, L. A. *J. Chem. Soc.* **1953**, 2929.
16. Yasue, T.; Kawano, Y.; Shimoi, M. *Angew. Chem. Int. Ed.* **2003**, *42*, 1727.
17. Arndtsen, B. A.; Bergman, R. G.; Mobley, T. A.; Peterson, T. H. *Acc. Chem. Res.* **1995**, *28*, 154.
18. Crabtree, R. H. *Chem. Rev.* **1995**, *95*, 987.
19. (a) Hall, C.; Perutz, R. N. *Chem. Rev.* **1996**, *96*, 3125; (b) Shilov, A. E.; Shul'pin, G. B. *Chem. Rev.* **1997**, *97*, 2879; (c) Shilov, A. E.; Shul'pin, G. B. *Activation and Catalytic Reactions of Saturated Hydrocarbons in the Presence of Metal Complexes*; Kluwer Academic Publishers: Dordrecht, **2000**; (d) Labinger, J. A.; Bercaw, J. E. *Nature* **2002**, *417*, 507; (e) Periana, R. A.; Taube, D. J.; Gamble, S.; Taube, H.; Satoh, T.; Fujii, H. *Science* **1998**, *280*, 560; (f) Geftakis, S.; Ball, G. E. *J. Am. Chem. Soc.* **1998**, *120*, 9953.
20. Brothers, P. J. *Prog. Inorg. Chem.* **1981**, *28*, 1.
21. For a retrospective account of homogenous catalytic hydrogenation, see: Halpern, J. *J. Organomet. Chem.* **1980**, *200*, 133.
22. Calvin, M. *Trans. Faraday Soc.* **1938**, *34*, 1181; Calvin, M. *J. Am. Chem. Soc.* **1939**, *61*, 2230.
23. Buncel, E.; Menon, B. *J. Am. Chem. Soc.* **1977**, *99*, 4457.
24. Van Der Sluys, L. S.; Miller, M. M.; Kubas, G. J.; Caulton, K. G. *J. Am. Chem. Soc.* **1991**, *113*, 2513.
25. Jia, G.; Lau, C.-P. *Coord. Chem. Rev.* **1999**, *190–192*, 83.
26. Morris, R. H. *Can. J. Chem.* **1996**, *74*, 1907.
27. Abdur-Rashid, K.; Fong, T. P.; Greaves, B.; Gusev, D. G.; Hinman, J. G.; Landau, S. E.; Lough, A. J.; Morris, R. H. *J. Am. Chem. Soc.* **2000**, *122*, 9155, and references therein.
28. Bruns, W.; Kaim, W.; Waldhor, E.; Krejciak, M. *Inorg. Chem.* **1995**, *34*, 663.
29. Crabtree, R. H.; Lavin, M. *J. Chem. Soc., Chem. Commun.* **1985**, 794.
30. Chinn, M. S.; Heinekey, D. M. *J. Am. Chem. Soc.* **1987**, *109*, 5865.
31. Basallote, M. G.; Besora, M.; Duran, J.; Fernandez-Trujillo, M. J.; Lledos, A.; Manez, M. A.; Maseras, F. *J. Am. Chem. Soc.* **2004**, *126*, 2320.

32. (a) Chinn, M. S.; Heinekey, D. M.; Payne, N. G.; Sofield, C. D. *Organometallics* **1989**, *8*, 1824; (b) Huhmann-Vincent, J.; Scott, B. L.; Kubas, G. J. *J. Am. Chem. Soc.* **1998**, *120*, 6808; *Inorg. Chem.* **1999**, *38*, 115.
33. Perdoncin, G.; Scorrano, G. *J. Am. Chem. Soc.* **1977**, *99*, 6983.
34. Bianchini, C.; Moneti, S.; Peruzzini, M.; Vizza, F. *Inorg. Chem.* **1997**, *36*, 5818.
35. Fong, T. P.; Lough, A. J.; Morris, R. H.; Mezzetti, A.; Rocchini, E.; Rigo, P. *J. Chem. Soc., Dalton* **1998**, 2111.
36. Fong, T. P.; Forde, C. E.; Lough, A. J.; Morris, R. H.; Rigo, P.; Rocchini, E.; Stephan, T. *J. Chem. Soc., Dalton Trans.* **1999**, 4475.
37. Ontko, A. C.; Houllis, J. F.; Schnabel, R. C.; Roddick, D. M.; Fong, T. P.; Lough, A. J.; Morris, R. H. *Organometallics* **1998**, *17*, 5467.
38. Huhmann-Vincent, J.; Scott, B. L.; Kubas, G. J. *Inorg. Chim. Acta.* **1999**, *294*, 240.
39. Heinekey, D. M.; Radzewich, C. E.; Voges, M. H.; Schomber, B. M. *J. Am. Chem. Soc.* **1997**, *119*, 4172.
40. Cheng, T. Y.; Bullock, R. M. *Organometallics* **1995**, *14*, 4031.
41. Beck, W.; Schweiger, M. Z. *Anorg. Allg. Chem.* **1991**, *595*, 203.
42. Brewer, S. T.; Bugg, L. A.; Holloway, J. H.; Hope, E. G. *J. Chem. Soc. Dalton Trans.* **1995**, 2941.
43. Fernandez, J. M.; Gladysz, J. A. *Organometallics* **1989**, *8*, 207.
44. Colman, M. R.; Newbound, T. D.; Marshall, L. J.; Noirot, M. D.; Miller, M. M.; Wulfborg, G. P.; Frye, J. S.; Anderson, O. P.; Strauss, S. H. *J. Am. Chem. Soc.* **1990**, *112*, 2349.
45. (a) Arndtsen, B. A.; Bergman, R. G. *Science* **1995**, *270*, 1970; (b) Tellers, D. M.; Bergman, R. G. *J. Am. Chem. Soc.* **2001**, *123*, 11508.
46. Butts, M. D.; Scott, B. L.; Kubas, G. J. *J. Am. Chem. Soc.* **1996**, *118*, 11831.
47. Fornies, J.; Martinez, F.; Navarro, R.; Urriolabeitia, E. P. *Organometallics* **1996**, *15*, 1813.
48. Huang, D.; Huffman, J. C.; Bollinger, J. C.; Eisenstein, O.; Caulton, K. G. *J. Am. Chem. Soc.* **1997**, *119*, 7398.
49. (a) Bullock, R. M.; Rappoli, B. J. *J. Chem. Soc., Chem. Commun.* **1989**, *15*, 1447; (b) Bullock, R. M.; Song, J.-S.; Szalda, D. J. *Organometallics* **1996**, 2504.
50. (a) Bullock, R. M.; Voges, M. H. *J. Am. Chem. Soc.* **2000**, *122*, 12594; (b) Voges, M. H.; Bullock, R. M. *J. Chem. Soc., Dalton Trans* **2002**, *424*, 759; (c) Dioumaev, V. K.; Bullock, R. M. *Nature* **2000**, 530.
51. (a) Nishibayashi, Y.; Takei, I.; Hidai, M. *Angew. Chem. Int. Ed. Engl.* **1999**, *38*, 3047; (b) Takei, I.; Nishibayashi, Y.; Ishii, Y.; Mizobe, Y.; Uemura, S.; Hidai, M. *J. Organomet. Chem.* **2003**, *679*, 32.
52. (a) Breyse, M.; Furimsky, E.; Kasztelan, S.; Lacroix, M.; Perot, G. *Catal. Rev.* **2002**, *44*, 651; (b) Neurock, M.; van Santen, R. A. *J. Am. Chem. Soc.* **1994**, *116*, 4427; (c) Hwang, D.-Y.; Mebel, A. M. *J. Phys. Chem. A* **2002**, *106*, 520.
53. Ohki, Y.; Matsura, N.; Manumoto, T.; Kawaguchi, H.; Tatsumi, K. *J. Am. Chem. Soc.* **2003**, *125*, 7978.
54. Llamazares, A.; Schmalle, H. W.; Berke, H. *Organometallics* **2001**, *20*, 5277.
55. Grushin, V. V. *Acc. Chem. Res.* **1993**, *26*, 279; Kuhlman, R. *Coord. Chem. Rev.* **1997**, *167*, 205.
56. Chin, B.; Lough, A. J.; Morris, R. H.; Schweitzer, C.; D'Agostino, C. *Inorg. Chem.* **1994**, *33*, 6278.
57. Bianchini, C.; Barbaro, P.; Scapacci, G.; Zanolini, F. *Organometallics* **2000**, *19*, 2450.
58. Lee, D.-H.; Patel, B. P.; Clot, E.; Eisenstein, O.; Crabtree, R. H. *Chem. Comm.* **1999**, 297.

59. Gruet, K.; Clot, E.; Eisenstein, O.; Lee, D. H.; Patel, B. P.; Macchioni, A.; Crabtree, R. H. *New J. Chem.* **2003**, 27, 80.
60. Lough, A. J.; Park, S.; Ramachandran, R.; Morris, R. H. *J. Am. Chem. Soc.* **1994**, 116, 8356.
61. Park, S.; Lough, A. J.; Morris, R. H. *Inorg. Chem.* **1996**, 35, 3001.
62. Abdur-Rashid, K.; Gusev, D. G.; Landau, S. E.; Lough, A. J.; Morris, R. H. *Organometallics* **2000**, 19, 1652.
63. Lee, J. C. Jr.; Peris, E.; Rheingold, A. L.; Crabtree, R. H. *J. Am. Chem. Soc.* **1994**, 116, 11014.
64. Crabtree, R. H.; Siegbahn, P. E. M.; Eisenstein, O.; Rheingold, A. L.; Koetzle, T. F. *Acc. Chem. Res.* **1996**, 29, 348.
65. Crabtree, R. H. *Science* **1998**, 282, 2000.
66. Custelcean, R.; Jackson, J. E. *Chem. Rev.* **2001**, 101, 1963.
67. Epstein, L. M.; Shubina, E. S. *Coord. Chem. Rev.* **2002**, 231, 165.
68. Liu, Q.; Hoffmann, R. *J. Am. Chem. Soc.* **1995**, 117, 10108.
69. Braga, D.; Grepioni, F. *Coord. Chem. Rev.* **1999**, 183, 19; Braga, D.; Grepioni, F.; Desiraju, G. R. *Chem. Rev.* **1998**, 98, 1375.
70. Schlaf, M.; Lough, A. J.; Morris, R. H. *Organometallics* **1996**, 15, 4423.
71. (a) Rakowski DuBois, M.; Jagirdar, B.; Noll, B.; Dietz, S., "Transition Metal Sulfur Chemistry", ACS Symposium Series No. 653; Eds. Stiefel, E. I.; Matsumoto, K.; American Chemical Society: Washington D.C., **1996**, pp. 269–281; (b) Bianchini, C.; Mealli, C.; Meli, A.; Sabat, M. *Inorg. Chem.* **1986**, 25, 4618; (c) Kato, H.; Seino, H.; Mizobe, Y.; Hidai, M. *J. Chem. Soc., Dalton Trans* **2002**, 1494.
72. Sweeney, Z. K.; Polse, J. L.; Andersen, R. A.; Bergman, R. G. *Organometallics* **1999**, 18, 5502.
73. Linck, R. C.; Pafford, R. J.; Rauchfuss, T. B. *J. Am. Chem. Soc.* **2001**, 123, 8856.
74. Kuwata, S.; Hidai, M. *Coord. Chem. Rev.* **2001**, 213, 211.
75. Sellmann, D.; Kappler, J.; Moll, M. *J. Am. Chem. Soc.* **1993**, 115, 1830.
76. Sellmann, D.; Rackelmann, G. H.; Heinemann, F. W. *Chem. Eur. J.* **1997**, 3, 2071.
77. Sellmann, D.; Gottschalk-Gaudig, T.; Heinemann, F. W. *Inorg. Chem.* **1998**, 37, 3982.
78. Sellmann, D.; Geipel, F.; Moll, M. *Angew. Chem. Int. Ed.* **2000**, 39, 561.
79. Jessop, P. G.; Morris, R. H. *Inorg. Chem.* **1993**, 32, 2236.
80. Morris, R. H. *NATO ASI Ser., Ser. 3* **1998**, 60 (Transition Metal Sulfides), 57.
81. "Transition Metal Sulfur Chemistry", ACS Symposium Series No. 653; Eds. Stiefel, E. I.; Matsumoto, K.; American Chemical Society: Washington D.C., **1996**.
82. Bayon, J. C.; Claver, C.; Masdeu-Bulto, A. M. *Coord. Chem. Rev.* **1999**, 193–195, 73.
83. (a) Peters, J. W.; Lanzilotta, W. N.; Lemon, B. J.; Seefeldt, L. C. *Science* **1998**, 282, 1853; (b) Nicolet, Y.; Piras, C.; Legrand, P.; Hatchikian, C. E.; Fontecilla-Camps, J. C. *Structure* **1999**, 7, 13; (c) Darensbourg, M. Y.; Lyon, E. J.; Smees, J. J. *Coord. Chem. Rev.* **2000**, 206–207, 533; (e) Darensbourg, M. Y.; Lyon, E. J.; Zhao, X.; Georgakaki, I. P. *PNAS* **2003**, 100, 3683.
84. Crabtree, R. H. *Inorg. Chim. Acta* **1986**, 125, L7.
85. Huhmann-Vincent, J.; Scott, B. L.; Kubas, G. J. *Inorg. Chim. Acta* **1999**, 294, 240.
86. Tye, J. W.; Hall, M. B.; Georgakaki, I. P.; Darensbourg, M. Y. *Adv. Inorg. Chem.*, this volume, 1–26.
87. Sellmann, D.; Fursattel, A.; Sutter, J. *Coord. Chem. Rev.* **2000**, 200–202, 545, and references therein.
88. Jia, G.; Morris, R. H.; Schweitzer, C. T. *Inorg. Chem.* **1991**, 30, 594.
89. Nishibayashi, Y.; Takemoto, S.; Iwai, S.; Hidai, M. *Inorg. Chem.* **2000**, 39, 5946.

90. Fryzuk, M. D.; Love, J. B.; Rettig, S. J.; Young, V. G. *Science* **1997**, *275*, 1445; Basch, H.; Muev, D. G.; Morokuma, K.; Fryzuk, M. D.; Love, J. B.; Seidel, W. W.; Albinati, A.; Koetzle, T. F.; Klooster, W. T.; Mason, S. A.; Eckert, J. *J. Am. Chem. Soc.* **1999**, *121*, 523; see also Pool, J. A.; Lofkovsky, E.; Chirik, P. J. *Nature* **2004**, *427*, 527.
91. (a) Noyori, R.; Koizumi, M.; Ishii, D.; Ohkuma, T. *Pure Appl. Chem.* **2001**, *73*, 227; (b) Ohkuma, T.; Noyori, R. *J. Am. Chem. Soc.* **2003**, *125*, 13490, and references therein; (c) Nobel Lecture 2001: Noyori, R. *Angew. Chem., Int. Ed.* **2002**, *41*, 2008.
92. (a) Hartmann, R.; Chen, P. *Angew. Chem., Int. Ed.* **2001**, *40*, 3581; (b) Abdur-Rashid, K.; Clapham, S. E.; Hadzovic, A.; Harvey, J. N.; Lough, A. J.; Morris, R. H. *J. Am. Chem. Soc.* **2002**, *124*, 15104; (c) Dahlenburg, L.; Gotz, R. *Inorg. Chem. Commun.* **2003**, *6*, 443.
93. Hughes, R. P.; Smith, J. M. *J. Am. Chem. Soc.* **1999**, *121*, 6084; Hughes, R. P.; Willemssen, S.; Williamson, S.; Zhang, D. *Organometallics* **2002**, *21*, 3085.
94. Albietz, P. J.; Houllis, J. F.; Eisenberg, R. *Inorg. Chem.* **2002**, *41*, 2001.
95. Ogo, S.; Nakai, H.; Watanabe, Y. *J. Am. Chem. Soc.* **2002**, *124*, 597.
96. Bianchini, C.; Moneti, S.; Peruzzini, M.; Vizza, F. *Inorg. Chem.* **1997**, *36*, 5818.
97. Schubert, U. *Adv. Organomet. Chem.* **1990**, *30*, 151.
98. Corey, J. Y.; Braddock-Wilking, J. *Chem. Rev.* **1999**, *99*, 175.
99. Schneider, J. J. *Angew. Chem. Int. Ed. Engl.* **1996**, *35*, 1068.
- 100a. Lin, Z. *Chem. Soc. Rev.* **2002**, *31*, 239.
- 100b. Nikonov, G. I. *Organometallics* **2003**, *22*, 1597.
101. Schubert, U. "Advances in Organosilicon Chemistry"; Eds. Marciniak, B.; Chojnowski, J.; Gordon and Breach: Yverdon-les-Bains, Switzerland, **1994**.
102. Zhang, S.; Dobson, G. R.; Brown, T. L. *J. Am. Chem. Soc.* **1991**, *113*, 6908.
103. Luo, X.-L.; Crabtree, R. H. *J. Am. Chem. Soc.* **1989**, *111*, 2527.
104. Reed, C. A. *Acc. Chem. Res.* **1998**, *31*, 325.
105. Tilley, T. D. "The Chemistry of Organic Silicon Compounds"; Eds. Patai, S.; Rappoport, Z.; John Wiley & Sons: New York, **1989**.
106. Sweeney, Z. K.; Polse, J. L.; Andersen, R. A.; Bergman, R. G.; Kubinec, M. G. *J. Am. Chem. Soc.* **1997**, *119*, 4543.
107. Toupadakis, A.; Kubas, G. J.; King, W. A.; Scott, B. L.; Huhmann-Vincent, J. *Organometallics* **1998**, *17*, 5315; King, W. A.; Scott, B. L.; Eckert, J.; Kubas, G. J. *Inorg. Chem.* **1999**, *38*, 1069.
108. Fang, X.; Scott, B. L.; Watkin, J. G.; Kubas, G. J. *Organometallics* **2000**, *19*, 4193.
109. Fang, X.; Scott, B. L.; Watkin, J. G.; Kubas, G. J. *Organometallics* **2001**, *20*, 3351.
110. Ittel, S. D.; Johnson, L. K.; Brookhart, M. *Chem. Rev.* **2000**, *100*, 1169.
111. Johansson, L.; Ryan, O. B.; Tilset, M. *J. Am. Chem. Soc.* **1999**, *121*, 1974.
112. For example, see: Pfeiffer, J.; Kickelbick, G.; Schubert, U. *Organometallics* **2000**, *19*, 62, and references therein.
113. Hill, G. S.; Rendina, L. M.; Puddephatt, R. J. *J. Chem. Soc., Dalton Trans.* **1996**, 1809.
114. For similar nitrogen stabilized Pt(IV) alkyl hydrides see: (a) O'Reilly, S. A.; White, P. S.; Templeton, J. L. *J. Am. Chem. Soc.* **1996**, *118*, 5684; (b) Wick, D. D.; Goldberg, K. *J. Am. Chem. Soc.* **1997**, *119*, 10235; (c) Canty, A. J.; Dedieu, A.; Jin, H.; Milet, A.; Richmond, M. K. *Organometallics* **1996**, *15*, 2845; (d) Prokopchuk, E. M.; Jenkins, H. A.; Puddephatt, R. J. *Organometallics* **1999**, *18*, 2861; (e) Haskel, A.; Keinan, E. *Organometallics* **1999**, *18*, 4677.

115. (a) Fang, X.; Huhmann-Vincent, J.; Scott, B. L.; Kubas, G. J. *J. Organometal. Chem.* **2000**, 609, 95; (b) Fang, X.; Scott, B. L.; John, K. D.; Kubas, G. J. *Organometallics* **2000**, 19, 4141.
116. Verkade, J. G.; Huttemann, T. J.; Fung, M. K. *Inorg. Chem.* **1965**, 4, 228.
117. Albertin, G.; Antoniutti, S.; Bettiol, M.; Bordignon, E.; Busatto, F. *Organometallics* **1997**, 16, 4959.
118. Desiraju, G. R. *Acc. Chem. Res.* **1991**, 24, 290.
119. (a) Luo, X.-L.; Kubas, G. J.; Bryan, J. C.; Burns, C. J.; Unkefer, C. J. *J. Am. Chem. Soc.* **1994**, 116, 10312; (b) Huhmann-Vincent, J.; Scott, B. L.; Butcher, R.; Luo, S.; Unkefer, C. J.; Kubas, G. J.; Lledos, A.; Maseras, F.; Tomas, J. *Organometallics* **2003**, 22, 5307.
120. Freeman, S. T. N.; Lemke, F. R.; Brammer, L. *Organometallics* **2002**, 21, 2030.
121. Fang, X.; Scott, B. L.; Watkin, J. G.; Kubas, G. J. *Organometallics* **2001**, 20, 2413.
122. Scharer, E.; Chang, S.; Brookhart, M. *Organometallics* **1995**, 14, 5686.
123. Chang, S.; Scharer, E.; Brookhart, M. *J. Mol. Catal. A: Chem.* **1998**, 130, 107.
124. Buhl, M.; Mauschick, F. T. *Organometallics* **2003**, 22, 1422.
125. Chung, M.-K.; Ferguson, G.; Robertson, V.; Schlaf, M. *Can. J. Chem.* **2001**, 79, 949.
126. Blackwell, J. M.; Foster, K. L.; Beck, V. H.; Piers, W. E. *J. Org. Chem.* **1999**, 64, 4887.
127. Gregg, B. T.; Cutler, A. R. *Organometallics* **1994**, 13, 1039.
128. Shimoi, M.; Nagai, S.; Ichikawa, M.; Kawano, Y.; Katoh, K.; Uruichi, M.; Ogino, H. *J. Am. Chem. Soc.* **1999**, 121, 11704, and references therein.
129. (a) Muhoro, C. N.; He, X.; Hartwig, J. F. *J. Am. Chem. Soc.* **1999**, 121, 5033; (b) Schlecht, S.; Hartwig, J. F. *J. Am. Chem. Soc.* **2000**, 122, 9435.
130. Saillard, J.-Y.; Hoffmann, R. *J. Am. Chem. Soc.* **1984**, 106, 2006.
131. Rybtchinski, B.; Cohen, R.; Ben-David, Y.; Martin, J. M. L.; Milstein, D. *J. Am. Chem. Soc.* **2003**, 125, 11041, and references therein.
132. (a) Kua, J.; Xu, X.; Periana, R. A.; Goddard, W. A. III. *Organometallics* **2002**, 21, 511; (b) Gilbert, T. M.; Hristov, I.; Ziegler, T. *Organometallics* **2001**, 20, 1183.
133. Heiberg, H.; Gropen, O.; Swang, O. *Int. J. Quantum Chem.* **2003**, 92, 391.
134. Wik, B. J.; Romming, C.; Tilset, M. *J. Mol. Catal. A* **2002**, 189, 23.
135. See Chapter 2 in Shilov, A. E. "Metal Complexes in Biomimetic Chemical Reactions"; CRC Press: Boca Raton, FL, **1997**.
136. Cappellani, E. P.; Drouin, S. D.; Jia, G.; Maltby, P. A.; Morris, R. H.; Schweitzer, C. T. *J. Am. Chem. Soc.* **1994**, 116, 3375.
137. Morris, R. H. *Inorg. Chem.* **1992**, 31, 1471.
138. Jia, G.; Morris, R. H. *J. Am. Chem. Soc.* **1991**, 113, 875.
139. Ontko, A. C.; Houliis, J. F.; Schnabel, R. C.; Roddick, D. M.; Fong, T. P.; Lough, A. J.; Morris, R. H. *Organometallics* **1998**, 17, 5467.
140. Maltby, P. A.; Schlaf, M.; Steinbeck, M.; Lough, A. J.; Morris, R. H.; Klooster, W. T.; Koetzle, T. F.; Srivastava, R. C. *J. Am. Chem. Soc.* **1996**, 118, 5396.
141. Rocchini, E.; Mezzetti, A.; Ruegger, H.; Burckhardt, U.; Gramlich, V.; Del Zotto, A.; Martinuzzi, P.; Rigo, P. *Inorg. Chem.* **1997**, 36, 711.
142. (a) Curtis, C. J.; Miedaner, A.; Raebiger, J. W.; DuBois, D. L. *Organometallics* **2004**, 23, 511; (b) Curtis, C. J.; Miedaner, A.; Ciancanelli, R.; Ellis, W. W.; Noll, B. C.; Rakowski DuBois, M.; DuBois, D. L. *Inorg. Chem.* **2003**, 42, 216; (c) Curtis, C. J.; Miedaner, A.; Ellis, W. W.; DuBois, D. L. *J. Am. Chem.* **2002**, 124, 1918.

TETRAPODAL PENTADENTATE NITROGEN LIGANDS: ASPECTS OF COMPLEX STRUCTURE AND REACTIVITY

ANDREAS GROHMANN

Institut für Chemie, Technische Universität Berlin, Straße des 17. Juni 135,
10623 Berlin, Germany

- I. Introduction
- II. Overview
- III. Tetrapodal Pentadentate Coordination Modules
 - A. Zinc
 - B. Copper
 - C. Nickel
 - D. Cobalt
 - E. Iron
- IV. Conclusion
- References

I. Introduction

Tetrapodal pentadentate ligands have the ability to stabilize transition metal centers possessing a single labile coordination site, thereby providing attractive platforms for reactivity studies in complexes of overall octahedral geometry. Reports of the first such ligand date from the early 1980s ([1,2](#)) when, in the context of dioxygen activation studies, *Tagaki* and coworkers in Japan made a pyridine ligand carrying four identical imidazolyl subunits, {6-[Hydroxy-bis-(1-methyl-1*H*-imidazol-2-yl)-methyl]-pyridin-2-yl}-bis-(1-methyl-1*H*-imidazol-2-yl)-methanol (ligand **5**, below), and investigated its cobalt(II) complex. Other N₅ ligands with a square-pyramidal topology were subsequently made, in which the nitrogen atoms are embedded in aromatic ring systems. These imine-type donors have π^* orbitals available for back-donation of electron density from the metal, thereby contributing to the overall stability of the complexes. It was in this context that we introduced a highly symmetrical *aliphatic* NN₄ ligand, which consists of a “central” pyridine unit and four equivalent primary amino groups (“pyN₄”, **1**).

This polyamine has predominantly σ donor character, is expected to render the coordinated metal ion electron-rich, imposes virtually no steric constraints, and may thus be construed as a "chelating analogue" of the pentaammine donor set $(\text{NH}_3)_5$. This contribution reviews the progress we have made in the study of "pyN₄" complexes, highlighting similarities and differences in the coordination chemistry of other square-pyramidal chelators along the way.

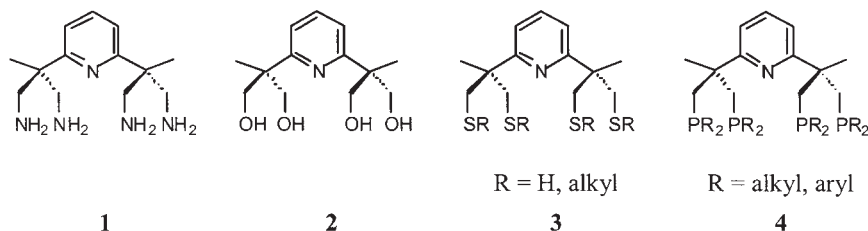
II. Overview

This overview presents chelators with a tetrapodal pentadentate topology, that have recently been introduced as ligands in coordination chemistry. The overview is followed by a review of the more prominent ligands, their complexes and selected aspects of their reactivity.

Work in our group has been concerned with C_{2v} -symmetrical ligands in which a "central" heterocycle carries four aliphatic sidearms (type I ligands) (3). In other cases, the donor set AE_4 (A: apical donor, E: equatorial donor) has the same overall symmetry, but consists entirely of heteroaromatics (type II ligands). Thirdly, two ligands have so far been described which have overall C_s symmetry, in which the "central", apical donor atom is part of an aliphatic backbone (type III ligands).

Type I ligands have a pyridine ring as the central unit, which carries two branched aliphatic sidearms, resulting in a 2,6-disubstitution pattern. The sidearms are C_3 units whose central carbon atom – i.e., C-2' – is connected to the pyridine ring. The donor atoms are appended in the 1' and 3' positions, respectively. Suitable donors are N, O, S, or P (1–4).

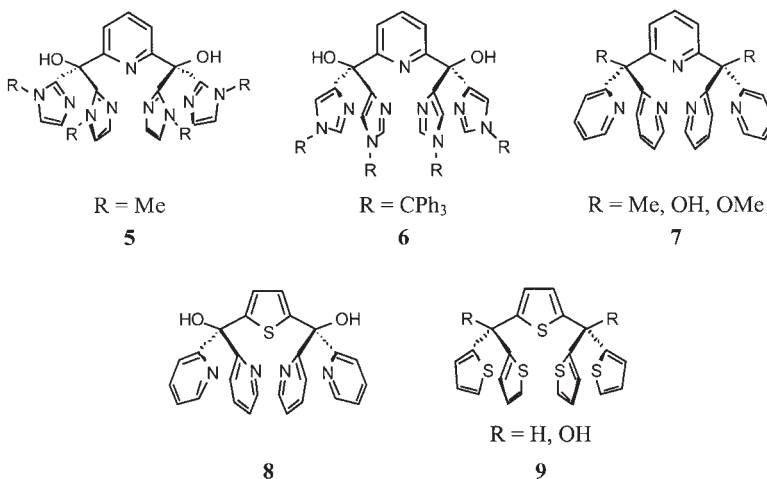
Type I ligands



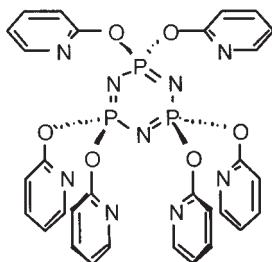
The first report of a type II ligand dates back to 1981 (1,2). In view of the biochemical relevance of imidazol ligands, Tagaki and co-workers synthesized a pyridine carrying four imidazolyl substituents (5) and

investigated the coordination behavior of this ligand towards cobalt(II), in the context of studies aimed at dioxygen activation. The analytical data suggested square-pyramidal coordination of the ligand, but the postulated mononuclear superoxo complex $[(5)\text{Co}(\text{O}_2)]^{2+}$ could not be structurally characterized. A closely related tetrakis(imidazolyl) derivative (**6**) was described by Collman in 1999 (4). By contrast, the pentadentate donor set of the ligand **7** ($\text{R} = \text{Me}$) introduced by *Canty* in 1986 consists entirely of pyridine nitrogen atoms (5). The potential of this ligand ($\text{R} = \text{OH}$, OMe) to act as a pentadentate coordination cap was not explored until 1997, when complexes of metals of the first transition series were first presented (6–10). The motivation of this work was, for one part, the search for multidentate ligands whose low-valent iron or manganese complexes will stabilize intermediates of biochemical oxygenations and, for another, the search for functional lipoxygenase models. In a similar vein, the iron(II) complex of a type II ligand derived from thiophene (**8**) was studied by *Kläui* and co-workers as a structural and functional model of cytochrome P450 (11). Investigated substrates include cyclooctene and norbornene, and the complex does show moderate catalytic activity. A potential SS_4 donor set is provided by two further derivatives of thiophene (**9**), synthesized by *Nakayama* and *Hanack* in the course of work on electrically conducting polymers, with no coordination chemical perspective (12,13). Whether or not these molecules have ligand qualities is as yet unclear, but is doubtful in view of the poor donor qualities of the thiophene sulfur atom (14).

Type II ligands

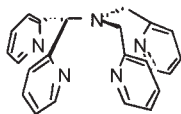


Similarly high symmetry is shown by a ligand with a central cyclo-triphosphazene unit (**10**), whose chlorocopper(II) complex was recently reported in the context of studies of polymeric phosphazene metal adducts (*Ainscough, Brodie*) (**15**). Unlike ligands **1–9**, the bridge-head atoms in **10** (λ^5 -P) are part of the central unit. They each carry two 2-pyridyloxy substituents, whose nitrogen atoms are coordinated to the CuCl fragment in the equatorial positions, whereas a nitrogen atom of the phosphazene ring takes the apical position.

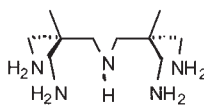


One of the tetrapodal pentadentate ligands of lesser symmetry (C_s , type III), which also forms mononuclear complexes, is formally derived from trimethylamine; one of the carbon atoms acts as a bridgehead carrying two 2-pyridyl substituents, while the other two carbon atoms each carry one such substituent (**11**). The iron complex of this ligand was studied as a model for non-heme iron centers in oxygen activation (**16,17**), and discussed as a functional model of the active site in the metalloglycopeptide iron bleomycin (*Que, Feringa*) (**18–21**). The ligand “ditame” **12**, which may be construed as the “aliphatic analogue” of the pyridine derivative **1**, is C_2 symmetrical and has a central secondary and four terminal primary amino functionalities. The protonation and metal complex formation of this ligand with a series of late transition metals have been studied (*Sargeson, Hegetschweiler*) (**22,23**).

Type III ligands



11



12

III. Tetrapodal Pentadentate Coordination Modules

Whereas the classification of the previous section was by ligand type and donor set, the present section presents the material grouped by the identity of the central metal, in order to facilitate comparisons of reactivity. The discussion will concentrate on the metal ions Zn, Cu, Ni, Co, and Fe, and on ligands with a predominance of nitrogen donor atoms. More elaborate ligand structures derived from **1** by templated condensation reactions are not covered by this review (24–28). The same applies to ligands with NO₄ (29), NS₄, and NP₄ donor sets (30), for which the reader is referred to the literature.

A. ZINC

Zinc has been shown to act as a “protective group” in selective derivatization reactions of certain tetraazamacrocycles, since only three out of the four nitrogen atoms of the ligand bind to the zinc(II) cation. The nitrogen atom which remains uncoordinated can then react with a suitable partner to afford, after demetallation, the desired mono-derivative (31). On a similar note, polyamine complexes of zinc undergo partial dissociation and partial ligand protonation as a function of pH, as has been reported for the complex [Zn(**12**)]²⁺ (23). These observations were the initial stimulus for an exploration of the zinc coordination chemistry of the pyridine derivative **1**, which produced the aqua complex [Zn(**1**)(H₂O)]Br₂, **13** (32). Complex **13** appears to be the first structurally characterized *octahedral* zinc aqua complex of a polyamine ligand. The bond length Zn–O involving the aqua ligand (2.179(4) Å) is significantly longer than in pentacoordinate [Zn(tren)(H₂O)](ClO₄)₂ (2.121(4) Å) (33), or in tetracoordinate complexes of aromatic amine ligands (2.011(3) Å) (34). The Zn–N bond lengths involving the primary amino groups of **1** and tren, respectively, follow a similar pattern.

The study of zinc-aqua complexes as synthetic carbonic anhydrase models has shown a low coordination number and a hydrophobic environment to be prerequisites for a low pK_a value of the aqua ligand, which is essential for efficient enzyme function. The pK_a value in the case of **13** is expected to be greater than 10.7, which is the value determined for pentacoordinate [Zn(tren)(H₂O)](ClO₄)₂, in which the water ligand is more strongly bound and thus expected to be more acidic (cf. the discussion of bond lengths, above). Thus, **13** is not expected to show carbonic anhydrase-like reactivity. However, in related tetraazamacrocyclic systems it has been shown that upon

replacement of coordinated water by ROH, the alcohol is activated, and that the system can take up CO₂ to yield bridged carbonate complexes. Indeed, in methanolic solution, **13** does react with gaseous CO₂, and a white precipitate is immediately formed. If the gas stream is interrupted and the suspension allowed to stand for a few minutes, the solid redissolves, but may be regenerated if more CO₂ is passed through the solution. Spectroscopic data are fully consistent with the dinuclear complex [(1)₂Zn₂(μ₂-(η¹-O,η¹-O)O₂COCH₃)](Br)₃ (**14**), and a mechanism for its formation has been proposed (**32**).

B. COPPER

Copper(II) polyamine complexes are substitutionally labile, in a manner similar to the corresponding nickel(II) complexes. This means that individual donor atoms may at times decoordinate and thus be available for derivatization reactions, e.g., with suitable carbonyl compounds. More complex ligands may thus be constructed, including macrocycles (**35**), polymacrocycles (**36–38**), and concave chelators (**35**). The copper(II) complex of **1** was synthesized as a starting material for reactions aiming at the derivatization of the pentaamine ligand (**24–28**).

A solution of the pentaamine **1** (HBr adduct) in methanol, when heated to reflux with one equivalent of CuCl₂ · 2 H₂O, deposits the complex [(1)Cu]Br₂ · 2 MeOH (**15**) as a purple microcrystalline solid (**28**). The salts [(1)Cu](SCN)₂ · H₂O and [(1)Cu](Br)(PF₆) are accessible by recrystallizing **15** from methanol/water in the presence of NH₄SCN and NH₄PF₆, respectively. The perchlorate [(1)Cu](ClO₄)₂, obtained directly from the reaction of [Cu(DMF)₆](ClO₄)₂ with the pentaamine in methanol, is the only one out of this series that is readily soluble in organic solvents, such as methanol or acetone. The magnetic moment determined for **15** (μ_{eff} = 1.7 BM) corresponds to one unpaired electron, as expected for Cu^{II} and its d⁹ configuration. In the cyclic voltammogram, the Cu^{II}/Cu^I couple has a quasi-reversible redox wave at E_{1/2} = -0.62 V (in DMSO, vs. NHE). This value is within the range commonly found for pentacoordinate polyamine copper(II) complexes (**39**). Crystallographic analysis confirmed the presence of square-pyramidal coordinated copper(II) ions in all salts. The pyridine nitrogen atom of the pentaamine ligand is in the axial, the primary amino functions are in the basal positions. In all structures, the axial bond Cu–N_{py} is significantly longer than the basal Cu–N bonds; average values for d(Cu–N_{py}) and d(Cu–N_{bas}) are 2.16 Å and 2.03 Å, respectively. Pentacoordinate copper(II) complexes having square-pyramidal or

trigonal-bipyramidal coordination are relatively common; while their orbital symmetry cannot give rise to classical Jahn-Teller distortions, the observed metal to ligand bond lengths vary over a wide range, when compared to other metal ions. This variability in the structural chemistry of copper(II) has been termed a “plasticity effect” (40,41). There is no obvious correlation with the nature of the ligands present (unidentate, or chelate ligand), as is evident from the comparison of the structures of $[(1)\text{Cu}](\text{SCN})_2 \cdot \text{H}_2\text{O}$ (**16**) and $\text{K}[\text{Cu}(\text{NH}_3)_5](\text{PF}_6)_3$ (42).

The structure of the cation in **16** is shown in Fig. 1 (crystallographic C_1 symmetry). The bonds from the central ion to the primary amino nitrogen atoms at the base of the pyramid are of similar length (average 2.039(3) Å), whereas the distance to the pyridine nitrogen atom is much longer at 2.207(2) Å. For comparison, the corresponding values in the pentaammine copper(II) cation in $\text{K}[\text{Cu}(\text{NH}_3)_5](\text{PF}_6)_3$, which is likewise square pyramidal, are 2.03(2) Å and 2.19(2) Å, respectively (42). All angles of the type $\text{N}_{\text{ax}}\text{--Cu--N}_{\text{bas}}$ in **16** are approximately 90° . The pyridine ring is tilted by $27.3(1)^\circ$ from the perpendicular, and the non-bonded distances between the methylene carbon atoms C16/C21 and C17/C20 are therefore 5.301(5) Å and 4.516(5) Å, respectively. In the crystal lattice of **16**, one of the thiocyanate ions is parallel to the CuN_4 basis of the cation, and the sulfur atom is at a distance of 2.991(1) Å to the copper ion. This value is smaller than the sum of the van-der-Waals radii of Cu^{II} and S [3.20 Å (43)]. Apparently, this contact is responsible for the blue color of **16** in the solid state. The other copper complexes of the type $[(1)\text{Cu}]\text{X}_2$ are all purple solids, and there are no cation–anion interactions.

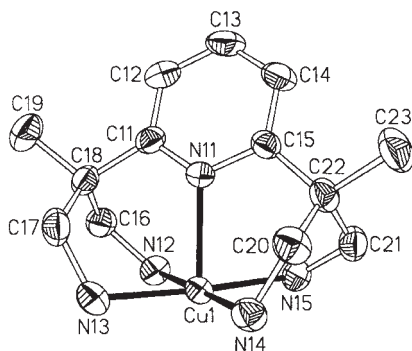


FIG. 1. Molecular structure of the cation in the copper(II) complex $[(1)\text{Cu}](\text{SCN})_2 \cdot \text{H}_2\text{O}$ (**16**).

In the case of the *purely* aliphatic ligand 2,2,6,6-tetrakis(amino-methyl)-4-azaheptane (**12**), complex formation with copper appears to proceed in two steps, as elucidated by titration experiments with the fully protonated ligand (**12**·5 HCl). Three and two protons from $(\text{H}_5\text{12})^{2+}$ are sequentially abstracted, and the predominant species after full deprotonation appears to be a dinuclear complex in which two copper(II) ions are coordinated, each in square planar fashion, by the 1,3-diaminoprop-2-yl units of two molecules of pentaamine ligand, thus forming a macrocyclic complex of composition $[\text{Cu}_2(\text{12})_2]^{4+}$ (**23**). The UV/vis spectral data show an interesting solvent dependence, suggesting an equilibrium between $[\text{Cu}_2(\text{12})_2]^{4+}$ and two equivalents of mononuclear complex $[\text{Cu}(\text{12})]^{2+}$ under suitable conditions. ESR spectroscopic data are also compatible with the formulation of a dinuclear species. Further addition of base to an aqueous solution of $[\text{Cu}_2(\text{12})_2]^{4+}$ gives the mononuclear hydroxo complex $[(\text{12})\text{Cu}(\text{OH})]^+$, as inferred from the UV/vis spectroscopic data.

C. NICKEL

The formation of nickel(II) complexes of the pyridine-derived pentaamine ligand **1** is also straightforward (**44**). Addition of $\text{NiCl}_2 \cdot 6 \text{H}_2\text{O}$ to a solution of **1** in dilute aqueous ammonia produces an immediate color change from green to purple, indicating spontaneous complex formation. Adsorption of the solution onto Sephadex and gradient elution with sodium chloride solution gives a single purple-colored fraction, which contains the aqua complex $[(\text{1})\text{Ni}(\text{OH}_2)]\text{Cl}_2$ (**17**). The complex crystallizes upon reducing the volume of the solution, and may be recrystallized from aqueous methanol. The aqua ligand is – as expected for a complex of high-spin nickel(II) – bound only weakly, and is easily exchanged upon crystallization in the presence of other neutral or ionic species. This has provided access to a series of nickel(II) complexes, all of which are high-spin (a selection is shown in Table I): the perchlorato complex **18** has a representative ^1H -NMR spectrum, with paramagnetically broadened and shifted signals between 0 and +140 ppm, which may be assigned on the basis of their integrated intensities and demonstrate the C_{2v} symmetry of the square-pyramidal coordination module in solution (solvent: $[\text{D}_6]\text{DMSO}$; the species present in solution presumably is the DMSO complex). As expected, the protons nearest the nickel atom ($-\text{NH}_2$, $-\text{CH}_2-$) experience the strongest paramagnetic shifts (128 ppm and 100 ppm, respectively) and the greatest line widths. The protons $\text{H}^3(\text{meta})$, $\text{H}^4(\text{para})$ and those of the CH_3 group follow, with line widths and paramagnetic

TABLE I

NICKEL (II) COMPLEXES OF THE PENTAAMINE LIGAND **1** OBTAINED BY RECRYSTALLIZATION OF $[(1)\text{Ni}(\text{OH}_2)]\text{Cl}_2$ (**17**) IN THE PRESENCE OF THE REAGENTS LISTED; IN SOME CASES, ADDED NH_4PF_6 PRODUCES THE HIGHLY CRYSTALLINE HEXAFLUOROPHOSPHATE SALTS

Reagent	Complex formed
NaClO_4	$[(1)\text{Ni}(\text{OClO}_3)]\text{ClO}_4$ (18)
NH_4PF_6	$[(1)\text{Ni}(\mu\text{-Cl})\text{Ni}(1)](\text{PF}_6)_3$ (19)
NaN_3	$[(1)\text{Ni}(\text{N}_3)]\text{PF}_6$ (21)
$\text{Na}[\text{Ag}(\text{CN})_2]$	$[(1)\text{Ni}(\text{NC-Ag-CN})]\text{PF}_6$ (22) or $[(1)\text{Ni}(\text{NC-Ag-CN})]\text{PF}_6 \cdot \text{H}_2\text{O}$ (23)

shifts (43 ppm, 20 ppm, 1 ppm) decreasing in this order, in concert with their increasing distance from the nickel center. The recrystallization of **17** in the presence of NH_4PF_6 gives a μ -chloro-bridged dinuclear complex, **19**. Variable-temperature data for the effective magnetic moment of this complex indicate strong antiferromagnetic coupling between the nickel atoms *via* the Cl bridge (diamagnetic ground state with total spin $S_T = 0$). When **17** is recrystallized in the presence of NaI, no iodo complex is formed; instead, the uncoordinated chloride ions are exchanged, and $[(1)\text{Ni}(\text{OH}_2)]\text{I}_2$ (**20**) is produced. Apparently, iodide is too large a ligand to coordinate to the $[(1)\text{Ni}]^{2+}$ complex fragment without repulsive van-der-Waals interactions between it and the basal amino groups (45).

In the solid state structures of the nickel(II) perchlorato complex **18** and its relatives, the pentaamine ligand acts as a square-pyramidal coordination cap, in the same way as in its zinc(II) and copper(II) complexes. Six six-membered chelate rings are thus formed, all of which have a boat conformation. Unlike copper, a sixth ligand completes the coordination octahedron in the case of zinc and nickel. The latter type of complex in particular has bonding parameters within the donor cap which indicate largely strain-free coordination: the Ni–N bond lengths (2.01...2.16 Å) are within the range of values determined for other nickel(II) polyamine complexes (46,47), and the bond angles deviate from the expected mean of 90° by $\pm 7^\circ$. A structural *trans* influence of the sixth ligand (in the sense of a systematic variation of the bond length $d(\text{Ni-N}_{\text{py}})$) is not observed, which is further support for the notion that the sixth ligand is only weakly bound (high-spin Ni^{II}). Independent of the arrangement of the N_5 donor set, however – which is square-pyramidal to a first approximation – some crystal structures do show a distortion in the carbon backbone of the chelate ligand.

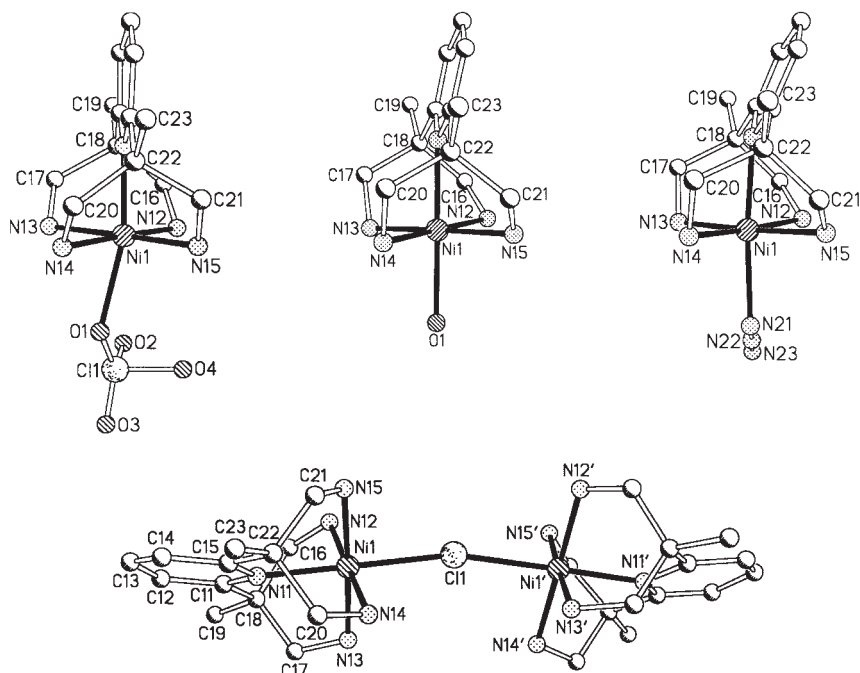


FIG. 2. Molecular structures of the cations in the complexes [(1)Ni(OCIO₃)ClO₄] (18, left), [(1)Ni(OH₂)I₂] (20, middle), [(1)Ni(N₃)PF₆] (21, right) und [(1)Ni(μ-Cl)Ni(1)](PF₆)₃ (19, below). The side views illustrate the varying distortion of the ligand cap.

It consists in a more or less pronounced departure of the pyridine ring from the plane defined by the quaternary carbon atoms in the side-arms and the exocyclic methyl carbon atoms, which is reflected by an expansion or contraction of the non-bonded distances between pairs of methylene groups in both halves of the molecule, as defined by the pyridine ring plain (Fig. 2). The distortion is minor in the case of the perchlorato complex (perchlorate salt, 18), more pronounced in the case of the μ-Cl-bridged dinuclear complex (hexafluorophosphate salt, 19) and the aqua complex (iodide salt, 20), and strongest in the case of the azido complex (hexafluorophosphate salt, 21). The distortion is mainly a consequence of crystal packing in the solid, as may be seen from the comparison of structures of two independently isolated forms of a dicyanoargentate complex (hexafluorophosphate salts in both cases, 22 and 23; see Table I): While the degree of distortion is very different in the two structures, the crystalline forms differ only

in that one contains one molecule of solvent water per formula unit, whereas the other does not. Theoretical work on the related iron complexes of **1** (see below) has shown that the normal IR mode describing the tilting of the pyridine ring is the lowest in all complexes (at ca. 55 cm^{-1}). Hence, such a distortion is expected to be facile if a small force is exerted on the complex by the crystal environment.

The molecular structure of a “ditame” complex of nickel(II), [(12)Ni(EtOH)]Br₂, shows the coordination behavior of this ligand and **1** towards Ni^{II} to be identical, with similar structural parameters (23). The bond from the metal center to the secondary amine donor in the apical position is shorter at 2.050(5) Å than the equatorial Ni–N bonds, whose average is 2.112(7) Å, in the same way as in the complexes of the pyN₄ ligand (44). The secondary nature of the apical donor atom in [(12)Ni(EtOH)]Br₂ gives rise to crystallographic disorder, which has been resolved.

D. COBALT

We have studied cobalt(III) complexes of the pentaamine ligand **1** in the context of dioxygen activation (48), as well as elementary cobalamin modelling (49), as outlined below. Dioxygen-bridged cobalt complexes of the “ditame” ligand **12** have subsequently been reported (22,23). Further, as **1** was the only polyamine at the time to enforce coordination of a pyridine ring *trans* to the exchangeable ligand, we were interested in elucidating the mechanism of base hydrolysis of the mononuclear chloro complex [(1)CoCl]²⁺ (50–52). This work was carried out in collaboration with the groups of *van Eldik* in Erlangen and *Elias* in Darmstadt (50).

Reaction of the hydrogen chloride adduct of the pentaamine, **1**·4 HCl, under a dinitrogen atmosphere, in water or a water/methanol mixture, with freshly prepared sodium tris(carbonato)cobaltate, Na₃[Co(CO₃)₃]·3 H₂O, gives, once the carbon dioxide evolution has ceased, a red solution from which the mononuclear complex [(1)CoCl](Cl)(ClO₄)·H₂O (**24**) is deposited as a crystalline burgundy-colored solid upon addition of NaClO₄ (3). The complex is diamagnetic, and its ¹H NMR spectrum (DMSO-*d*₆) has, in addition to the signals expected for the pyridine and methyl protons, two pairs of broadened multiplets (at $\delta = 5.85/5.29$ and $2.74/2.25$ ppm, intensity ratio 1:1:1:1), which may be assigned to the diastereotopic protons of the methylene and primary amine groups. The number of signals and their splitting pattern indicate the high symmetry of the complex and the desired

TABLE II

COMPARISON OF BOND LENGTHS [\AA] AT COBALT IN THE COMPLEXES
 $[(1)\text{CoCl}](\text{Cl})(\text{ClO}_4) \cdot \text{H}_2\text{O}$ (**24**), $[(1)\text{Co}(\text{SO}_3)]\text{Br}$ (**27**), $[(1)\text{Co}(\mu\text{-O}_2)\text{Co}(1)](\text{S}_2\text{O}_6)\text{Cl}_2 \cdot 6$
 H_2O (**28**), $[(1)\text{Co}(\mu\text{-O}_2)\text{Co}(1)](\text{S}_2\text{O}_6)_2\text{Cl} \cdot 10 \text{H}_2\text{O}$ (**29**), $[(1)\text{Co}(\text{OH})](\text{ClO}_4)_2$ (**30**)
 AND $[(1)\text{Co}(\text{CH}_3)]\text{S}_2\text{O}_6$ (**31a**); PARAMETERS FOR THE "DITAME" COMPLEXES
 $[(12)\text{CoCl}](\text{ZnCl}_4)_2$ (**A**), $[(12)\text{Co}(\mu\text{-O}_2)\text{Co}(12)]\text{Cl}_4 \cdot 4 \text{H}_2\text{O}$ (**B**),
 $[(12)\text{Co}(\mu\text{-O}_2)\text{Co}(12)]\text{Cl}_5 \cdot 2 \text{H}_2\text{O}$ (**C**) ARE LARGELY SIMILAR (22,23)
 (STANDARD DEVIATIONS IN PARENTHESES)

Distance	24	27	28	29	30	31a
Co–N _{py}	1.928(3)	1.997(3)	1.928(4)	1.928(2)	1.934(2)	2.018(2)
Co–N _{eq}	1.951(4)...	1.968(4)...	1.945(3)...	1.946(2)...	1.958(2)...	1.947(2)...
(Min...Max)	1.957(4)	1.978(4)	1.956(3)	1.958(2)	1.963(2)	1.967(2)
Co–X ^a	2.265(2)	2.226(1)	1.883(3)	1.915(2)	1.897(2)	1.975(4)

^a**24**: X = Cl; **27**: X = S; **28**: X = O (peroxo); **29**: X = O (superoxo); **30**: X = O (hydroxo); **31a**: X = C.

Distance	A	B	C
Co–N _{sec}	1.936(11)	1.920(7)	1.949(6)
Co–N _{eq}	1.956(10)...	1.950(8)...	1.956(6)...
(Min...Max)	1.968(10)	1.987(8)	1.966(6)
Co–X ^a	2.305(4)	1.951(7)	1.917(5)

^a**A**: X = Cl; **B**: X = O (peroxo); **C**: X = O (superoxo).

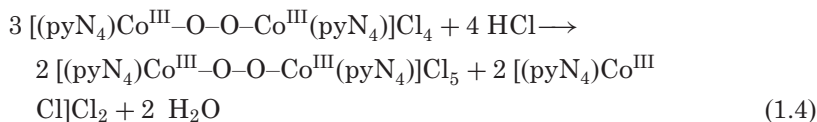
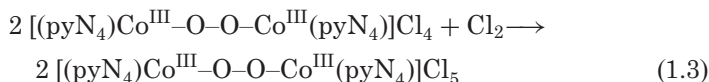
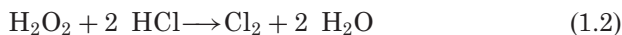
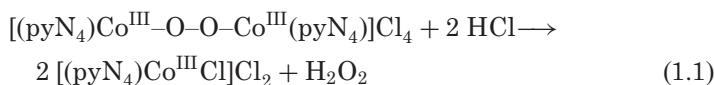
coordination of the ligand as a square-pyramidal coordination cap. Both conclusions are borne out by X-ray crystallography. The structure of the cation resembles that of the nickel(II) complexes, with Co–N bond lengths around 1.95 \AA and thus typical of cobalt(III) (Table II).

Dinuclear $\mu_2\text{-}\eta^1\text{:}\eta^1$ peroxocobalt(III) complexes of N donor ligands are usually prepared by aerobic oxidation of the corresponding cobalt(II) precursor. This method also works well for the pentaamines **1** and **12**, and dicobalt(III) complexes having an O_2^{2-} bridge are thus obtained (23,48). The procedure for **1** is as follows: When air is passed through an ice-cooled aqueous solution containing stoichiometric amounts of $\text{Co}(\text{NO}_3)_2 \cdot 6 \text{H}_2\text{O}$ and 1.4 HCl as well as a slight excess of KOH (4 eq + 0.1 mmol), the dinuclear peroxo complex $[(1)\text{Co}\text{-O}_2\text{-Co}(1)]\text{Cl}_4$ (**25**) begins to precipitate as a brown microcrystalline solid after a few minutes. It may be recrystallized from water without decomposition, and its solubility in other polar protic solvents such as MeOH (non-absolute) or DMSO is also high. In contrast to other such complexes, **25** does not liberate O_2 when heated in a vacuum (145°C,

12 h); rather, the peroxo complex is re-isolated unchanged. An alternative synthesis of this complex combines 1.4 HCl with $\text{Na}_3[\text{Co}(\text{CO}_3)_3] \cdot 3 \text{H}_2\text{O}$ in water/methanol *in air*. Once the precipitated product has been removed, treatment of the mother liquor with hydrochloric acid and subsequent work-up on an ion-exchange column allow the sequential isolation of the superoxo complex $[(1)\text{Co}-\text{O}_2-\text{Co}(1)]\text{Cl}_5$ (**26**) and the mononuclear chloro complex $[(1)\text{CoCl}]\text{Cl}_2$. A quantitative study of the formation of **25** under these conditions (Co^{III} precursor, oxygen from air) helped prove that part of the pentaamine serves as a reducing agent in this case (48), thereby lending support to a similar observation in the literature where a dicobalt(III) peroxo complex is obtained from a cobalt(III) precursor in air in the presence of an amino acid ester (53). In the Raman spectrum, the peroxo complex **25** has an intense absorption at 800 cm^{-1} , which is assigned to the O–O stretching vibration. (The value determined for the analogous complex of **12**, $[(12)\text{Co}(\mu\text{-O}_2)\text{Co}(12)]\text{Cl}_4 \cdot 4 \text{H}_2\text{O}$ (**B**), is 810 cm^{-1}). The complex is diamagnetic, and its ^1H NMR spectrum resembles that of the mononuclear chloro complex **24**. In particular, the methylene and primary amine groups again give rise to two pairs of signals, allowing one to conclude equivalence of the groups as well as the diastereotopicity of their geminal protons. As the Co–O–O–Co unit is expected to be bent rather than linear, the symmetry of the system in solution as deduced from the NMR spectra suggests rotation of the $[(1)\text{Co}]$ fragments around the Co–O bonds which is fast on the NMR time scale. The UV/vis spectrum of **25** has an intense band at 295 nm which, in analogy to other dicobalt(III) peroxo complexes ($[(12)\text{Co}(\mu\text{-O}_2)\text{Co}(12)]\text{Cl}_4 \cdot 4 \text{H}_2\text{O}$, **B**: 296 nm), is assigned to the LMCT transition $\pi_{\text{O}}^*(\text{O}_2^{2-}) \rightarrow d_{z^2}(\text{Co})$ (54). The cyclic voltammogram shows a quasi-reversible redox wave for the peroxo/superoxo system at $E_{1/2} = +0.40 \text{ V}$ (relative to NHE); two irreversible one-electron processes at $E_{1/2} = -1.11 \text{ V}$ and $E_{1/2} = -1.67 \text{ V}$ may be attributed to the sequential reduction of the cobalt(III) centers to cobalt(II). Overall similar behavior has been reported for the corresponding “ditame” complex, $[(12)\text{Co}(\mu\text{-O}_2)\text{Co}(12)]\text{Cl}_4 \cdot 4 \text{H}_2\text{O}$ (**B**) (22,23).

After isolation of the microcrystalline precipitate which is the peroxo complex **25**, there remains a reddish brown filtrate which contains further peroxo complex. Acidification of the latter with hydrochloric acid produces, after a few hours, the superoxo complex $[(1)\text{Co}-\text{O}_2-\text{Co}(1)](\text{Cl})_5$ (**26**) in the form of green microcrystals. As has already been mentioned, mononuclear chloro complex may finally be isolated from the red mother liquor of this preparation. If **25** is treated with a measured quantity of aqueous hydrochloric acid, the superoxo

complex and the chloro complex will form in equal amounts. If one uses sulfuric acid instead of hydrochloric acid, the superoxo complex will form only if the *chloride* salt of the peroxo complex has been used. If the perchlorate salt is used, hydrochloric acid has to be employed for acidification in order to form **26**; sulfuric acid will cause a color change of the solution to orange, indicating the formation of the mononuclear aqua complex $[(1)\text{Co}(\text{OH}_2)]^{3+}$. An aqueous solution of hydrogen peroxide reacts neither with the chloride nor with the perchlorate salt. On the other hand, a mixture of hydrogen peroxide and hydrochloric acid will convert the chloride salt of the peroxo complex much faster into the superoxo complex than hydrochloric acid alone. All these observations suggest the following scenario for the transformation of the peroxo complex **25** into the superoxo complex **26**: Initially, a certain amount of **25** is decomposed by hydrochloric acid with concomitant formation of hydrogen peroxide. Mixtures of H_2O_2 and HCl are known to liberate chlorine above a critical HCl concentration, and Cl_2 will convert the remaining peroxo complex into the superoxo complex. These processes are summarized in Eqs. (1.1)–(1.4). There is precedent in the literature both for the decomposition of peroxo complexes to generate hydrogen peroxide, and for the formation of dicobalt(III) superoxo complexes from the reaction of the corresponding peroxo complexes with halogens (55,56).

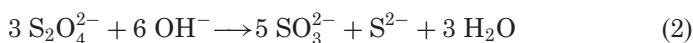


The ESR spectrum of **26** (DMSO, 120 K) is in accord with the formulation as a singly bridged dicobalt(III) superoxo complex ($g = 2.0629$). No hyperfine splitting from coupling with the ^{59}Co nucleus is observed (56,57). In the Raman spectrum, **26** shows an intense absorption at

1075 cm⁻¹, a value typical of the O–O stretching vibration in $\mu_2\text{-}\eta^1\text{:}\eta^1$ superoxocobalt(III) complexes (58). The UV/vis spectrum has bands of varying intensity at 208, 307, 464, and 698 nm, and is thus in good qualitative agreement with spectra of the ammine complex $[(\text{NH}_3)_5\text{Co-O-O-Co}(\text{NH}_3)_5]\text{Cl}_5 \cdot 4 \text{H}_2\text{O}$ (59). As expected, the cyclic voltammogram of **26** is identical to that of the peroxo complex **25** (see above).

The pH-dependent reactivity of **25** and **26** resembles that of related complexes with other polyamine ligands (55) and may be summarized as follows: The peroxo complexes may be transformed into the dinuclear superoxo complexes plus a mononuclear halo species by addition of a suitable acid. In aqueous alkaline solution (pH ≥ 12), the peroxo complexes are stable over several hours, whereas the superoxo complexes will react immediately even with dilute aqueous ammonia to reform the peroxo complexes.

An unexpected result was obtained upon reaction of the pentaamine ligand **1** with $\text{Na}_3[\text{Co}(\text{CO}_3)_3] \cdot 3 \text{H}_2\text{O}$ in water in the presence of sodium dithionite and sodium hydrogencarbonate. The experiment aimed to answer the question whether, in the presence of an external reducing agent such as $\text{Na}_2\text{S}_2\text{O}_4$, the starting materials and aerobic oxygen would produce a higher yield of dicobalt(III) peroxo complex. The upshot of this was that a reaction without aerobic oxidation produced the mononuclear *S*-sulfito cobalt(III) complex $[(1)\text{Co}(\text{SO}_3)]\text{Br}$ (**27**) and Co_2S_3 (48). The formation of both products requires the disproportionation of the dithionite anion which, in basic medium and in the presence of metal ions able to form insoluble sulfides, proceeds according to Eq. (2).



As there is a paucity of structural data for dicobalt(III) superoxo complexes and, in particular, of structural comparisons between pairs of the type $[(\text{L})\text{Co-O}_2\text{-Co}(\text{L})]^{4+/5+}$ with identical ligands L (23,56,60,61), a brief discussion detailing crystallographic features appears appropriate. Structures were determined for the dithionate/chloride salts $[(1)\text{Co-O-O-Co}(1)](\text{S}_2\text{O}_6)\text{Cl}_2 \cdot 6 \text{H}_2\text{O}$ (**28**) and $[(1)\text{Co-O-O-Co}(1)](\text{S}_2\text{O}_6)_2\text{Cl} \cdot 10 \text{H}_2\text{O}$ (**29**) (48). The parameters within the square-pyramidal coordinated $\{(1)\text{Co}\}$ fragments resemble those of the chloro complex $[(1)\text{CoCl}](\text{Cl})(\text{ClO}_4) \cdot \text{H}_2\text{O}$ (Table II), but there is a distinct difference in the conformations of the Co–O–O–Co units (cf. Fig. 3). In the peroxo complex, this unit is virtually coplanar with the pyridine rings, whereas it is at right angles with the pyridine rings in the superoxo complex. The charge on the cation in the peroxo complex (4+)

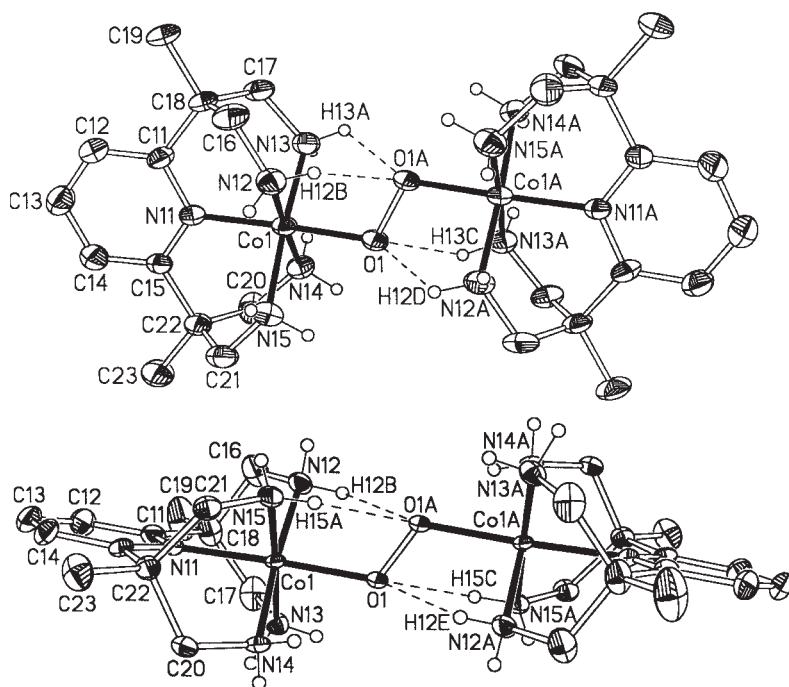


FIG. 3. Molecular structures of the cations in the peroxo complex $[(1)\text{Co}(\mu\text{-O}_2)\text{Co}(1)](\text{S}_2\text{O}_6)\text{Cl}_2 \cdot 6 \text{H}_2\text{O}$ (**28**) (left) and superoxo complex $[(1)\text{Co}(\mu\text{-O}_2)\text{Co}(1)](\text{S}_2\text{O}_6)_2\text{Cl} \cdot 10 \text{H}_2\text{O}$ (**29**) (right); broken lines indicate intramolecular hydrogen bonds.

indicates the presence of a peroxo bridge, and the bond lengths Co–O [1.883(3) Å] and O–O [1.467(5) Å] as well as the angle Co–O–O [110.7(3)°] are within the range of values observed for other $\text{Co}(\text{N}_5)$ peroxo complexes, including the recently reported “ditame” complex $[(12)\text{Co}(\mu\text{-O}_2)\text{Co}(12)]\text{Cl}_4 \cdot 4 \text{H}_2\text{O}$ (**B**) (**23,62**). The Co–N bond *trans* to the O_2^{2-} group [1.928(4) Å] is significantly shorter than the equatorial Co–N bonds [average: 1.950(3) Å]. In the solid state, the Co–O–O–Co central unit of the peroxo complex maintains four intramolecular hydrogen bonds with primary amine protons, as indicated by the dashed lines in Fig. 3. Similar three-point interactions have previously been found in the complexes $[(\text{en})(\text{dien})\text{Co}-\text{O}-\text{O}-\text{Co}(\text{dien})(\text{en})](\text{ClO}_4)_4$ (**63**), $[(\text{tren})(\text{NH}_3)\text{Co}-\text{O}-\text{O}-\text{Co}(\text{NH}_3)(\text{tren})](\text{SCN})_4 \cdot 2 \text{H}_2\text{O}$ (**64**) and $[(\text{papd})\text{Co}-\text{O}-\text{O}-\text{Co}(\text{papd})](\text{S}_2\text{O}_6)(\text{NO}_3)_2 \cdot 4 \text{H}_2\text{O}$ (**65**) (papd = 1,5,8,11,15-pentaazapentadecane).

In the superoxo complex (Fig. 3), the O_2^- nature of the bridge may be inferred from the charge ($5+$) determined for the cation, and from the O–O bond length [$1.325(3)$ Å] which is much shorter than in the peroxo complex. This value and the Co–O distance [$1.915(2)$ Å] as well as the angle Co–O–O [$116.5(2)^\circ$] resemble the values determined for other $\text{Co}(\text{N}_5)$ superoxo complexes (23,56,60,66,67). The equatorial Co–N bond lengths in the superoxo cation [average $1.952(2)$] are virtually identical to those in the peroxo cation; given the expected difference in *trans* influences of an O_2^- versus an O_2^{2-} group, a particularly striking observation is the fact that the Co–N bond *trans* to the superoxo bridge in **29** has the same length within experimental error as the bond *trans* to the peroxo group in **28**. There are intramolecular three-center hydrogen bonds also in the superoxo complex (Fig. 3), but in this case involving only *one* primary amine group of each diaminopropyl sidearm of the pentaamine ligand. Two factors appear to be responsible for the conformational change upon going from the peroxo to the superoxo complex: changes in the geometry of Co–O–O–Co scaffold, and changes in the electrostatics of the crystal lattice caused by a different set of counterions and increased amount of lattice solvent. For more structural details concerning this and the more recently investigated peroxo/superoxo complex pairs, the reader is referred to the original publications (23,48).

The pentaamine ligand **1** also provided new impetus for kinetic studies of the base-assisted hydrolysis of Werner-type complexes of the type $[(\text{N donor})_5\text{Co}(\text{Cl})]^{2+}$, as it contains a pyridine ligand *trans* to the leaving group as a structural feature that had previously been lacking in the chemistry of such complexes, despite a number of attempted syntheses (68,69). In cases where a pyridine ligand is coordinated *cis* to the leaving group, rate enhancements for the base-assisted hydrolysis of such complexes had been observed and a number of studies had, sometimes controversially, suggested that this is due to the operation of a pseudo-base mechanism (50). A detailed kinetic study of the complex $[(\mathbf{1})\text{CoCl}](\text{Cl})(\text{ClO}_4) \cdot \text{H}_2\text{O}$ (**24**), which also determined the pressure dependence of the rate constant, led to second-order kinetics and supported the operation of the conjugate base mechanism, D_{cb} (or better: I_{ACB} (51)) with intermediate deprotonation occurring *cis* to the leaving chloride ion (50). The special structural features of the pentadentate ligand cause the reaction to be slowed considerably. The product is a rare example of a mononuclear cobalt(III) complex with a terminal hydroxo ligand, $[(\mathbf{1})\text{Co}(\text{OH})](\text{ClO}_4)_2$ (**30**), which we were able to characterize completely, both spectroscopically and by means of an X-ray structure analysis. The study

finally provided clear evidence that in the case of $[(\text{N donor})_5\text{Co}(\text{Cl})]^{2+}$ complexes, a *trans*-coordinated pyridine ligand does *not* have any significant labilizing effect on the leaving group, thereby reinforcing the previously recognized analogy between the pentaamine ligand **1** and the classical pentaammine donor set. By contrast, the base hydrolysis rate constant for the “ditame” complex $[(\mathbf{12})\text{CoCl}]^{2+}$ is 250-fold greater than that for the analogous $[\text{Co}(\text{NH}_3)_5\text{Cl}]^{2+}$ ion. This difference is attributed to an enhanced *trans* influence and a bond-coupled cooperative mechanism that facilitate the Cl^- dissociation in the conjugate base of $[(\mathbf{12})\text{CoCl}]^{2+}$ (**22**).

In coenzyme B_{12} (adenosylcobalamin) the cobalt(III) center is octahedrally surrounded by five nitrogen donors and one carbon atom. The ligand *trans* to the alkyl group is a benzimidazol residue which is covalently linked to the corrin macrocycle whose four nitrogen donors occupy the equatorial positions. The strong *trans*-influence of the alkyl group facilitates dissociation of the benzimidazol ligand from the metal center, which is the key step in the binding of coenzyme B_{12} to enzymes such as methionine synthetase (**70**). The study of model compounds for coenzyme B_{12} has revealed the decisive influence of the ligand *trans* to the alkyl group on the properties of the cobalt(III)–carbon bond (**71**). The *trans* ligand is labile in most cases, which motivated us to obtain a simple cobalt(III) alkyl complex of the pentaamine ligand **1**, where the axial N ligand is non-dissociable. The synthesis of the methylcobalt(III) complex $[(\mathbf{1})\text{Co}(\text{CH}_3)](\text{NO}_3)_2$ (**31**) uses the precursor pentaammine complex $[(\text{NH}_3)_5\text{Co}(\text{CH}_3)](\text{NO}_3)_2$, first prepared by *Kofod* from the reaction of cobalt(II) nitrate with methylhydrazine in aqueous ammonia in the presence of oxygen from air (dinitrogen and hydrogen peroxide being the other products) (**72,73**). When reacting equivalent amounts of this complex and **1** in concentrated aqueous ammonia, complex **31** is formed by straightforward ligand exchange (**49**). Its spectral features resemble those of the chloro complex **24**, with the exception of prominent signals in the ^1H and ^{13}C NMR spectra ($\text{DMSO}-d_6$) at $\delta = 2.04$ ppm and $\delta = 4.1$ ppm for the $\text{Co}-\text{CH}_3$ methyl protons and carbon atom, respectively. The structure of the complex cation (Fig. 4) (determined for the anion-exchanged dithionate $[(\mathbf{1})\text{Co}(\text{CH}_3)]\text{S}_2\text{O}_6$ **31a**) is remarkable for the very long $\text{Co}-\text{N}_{\text{py}}$ bond [2.018(2) Å], which reflects the strong structural *trans* influence of the CH_3 ligand (the average value for this bond length in other cobalt(III) complexes of **1** is 1.928(4) Å (Table II).

A large number of methylcobalt(III) complexes with unsaturated ligands has been structurally characterized (**74**). In compounds where

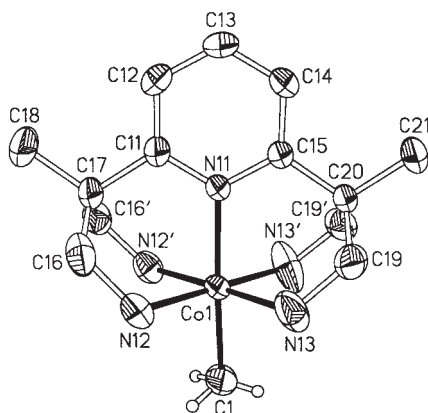


FIG. 4. Molecular structure of the cation in $[(1)\text{Co}(\text{CH}_3)]\text{S}_2\text{O}_6$ (**31a**).

a pyridine donor is *trans* to the methyl group, the Co–N_{py} bond lengths range from 2.068(9) Å for $[\text{Co}(\text{Hdmg})_2(\text{CH}_3)(\text{py})]$ (**75**) to 2.214(9) Å for $[\text{Co}(\text{OEP})(\text{CH}_3)(\text{py})]$ (**76**) (Hdmg = dimethylglyoximate; OEP = octaethylporphyrin dianion). The Co–N_{py} bond length in $[\text{Co}((\text{DO})(\text{DOH})\text{Me}_2\text{pn})(\text{CH}_3)(\text{py})]^+$ is 2.105(3) Å (**77**), and it is not significantly shorter in a related compound having a pyridyl ligand which is covalently linked to the equatorial donor set (2.07(1) Å; $(\text{DO})(\text{DOH})\text{Me}_2\text{pn} = \text{N}^2, \text{N}^{2'}\text{-2,2-dimethylpropanediyl-bis(2,3-butanedione-2-imine-3-oxime)}$) (**78**). A number of reasons is discussed to rationalize the observed variation of Co–N_{py} bond lengths. In some cases, the bond length may depend on the orientation of the pyridine ring relative to the equatorial ligands (steric factor), and in other cases the macrocyclic ligand may exert an electronic *cis* influence. Still, comparison shows that the Co–N_{py} bond in **31** at 2.018(2) Å is the shortest of all such complexes. Apparently, the podand nature of the pentadentate amine ligand prevents the bond between the metal center and the apical nitrogen donor atom to be elongated beyond a certain limit.

E. IRON

Iron complexes of the new tetrapodal pentadentate ligands highlighted in this contribution are probably the most diverse and depart most strongly from previously established patterns of reactivity (**8,21,79**).

Only a handful of reports on iron(II) and iron(III) complexes of *open-chain* aliphatic polyamine ligands had previously existed in

the literature, apparently due to the lack of stability of such systems with respect to hydrolysis and – in the case of iron(II) – oxidation, which induce decomposition leading to iron oxide/hydroxide species and $\text{Fe}(\text{OH})_3$, respectively. By contrast, iron complexes of *macrocyclic* aliphatic amines (80–83) are considerably more stable as a consequence of the macrocyclic effect (84). Furthermore, ligands with *imine*-type nitrogen donors (polypyridines, Schiff bases) provide stabilization by being able to accept electron density from the metal through π back-bonding (85). The following is a brief list of the previously known and fully characterized mononuclear iron(II) and iron(III) complexes of non-macrocyclic aliphatic amines whose nitrogen donor atoms are to a large part or exclusively primary (including NH_3).

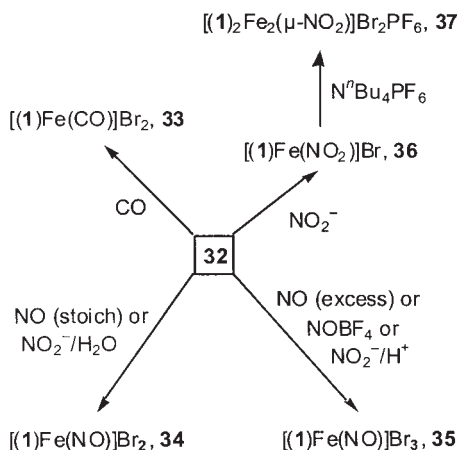
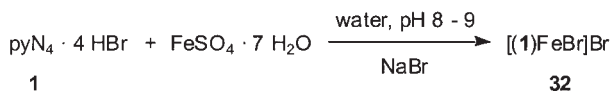
- $[\text{Fe}(\text{NH}_3)_6]\text{Br}_2$: When an excess of gaseous ammonia is passed through a freshly prepared solution of elemental iron in hydrobromic acid (40%), the bromide salt of the hexaammine iron(II) complex is deposited (86). The cation is also found in certain carbonyl ferrates, such as $[\text{Fe}(\text{NH}_3)_6][\text{Fe}_3(\text{CO})_{11}]$, which are obtained from the reaction of triiron dodecacarbonyl with ammonia in an autoclave (87).
- $[\text{Fe}(\text{en})_3]\text{Cl}_2$ (en = ethylenediamine): The complex forms when, under anhydrous and anaerobic conditions, an excess of ethylenediamine is added to a solution of iron(II) chloride in ethanol. The product may be condensed with acetone, producing a tetraazacyclotetradecadiene macrocycle by way of a metal template reaction (88). $[\text{Fe}(\text{en})_3]\text{Cl}_3$ is produced in a similar manner by reacting anhydrous iron(III) chloride with ethylenediamine (89).
- $[(\text{tetraen})\text{Fe}(\text{CO})]\text{I}_2$ (tetraen = tetraethylenpentaamine): With air excluded, an aqueous solution of tetraen is reacted with hydroiodic acid and iron(II) sulfate, and the pH subsequently raised to pH 8.5 by addition of NaOH. A stream of CO is passed through the solution to produce the carbonyl complex which must be swiftly isolated to avoid decomposition; it is insoluble in all common solvents except water. In water, however, when no CO is added and even though air may have been rigorously excluded, the complex is reported to decompose spontaneously to form rust-like products (90–92).
- Complexes of the ligand 1,3,5-triamino-1,3,5-trideoxy-*cis*-inositol and its derivatives. These ligands act as N_3 donors towards both iron(II) and high-spin iron(III), although ring inversion could make a facially coordinating O_3 donor set available (93,94).

The complexes are obtained in an air-free aqueous solution by addition of the ligands to a suitable iron salt.

Complexes of iron(II) with nitrogen donor ligands that are *not* derived from porphyrins have recently come under intense scrutiny, both in a search for robust oxidation catalysts (activation of H_2O_2 and O_2) and as model compounds for non-heme iron centers in metalloproteins (95). The foremost aim is to stabilize intermediates such as hydroperoxo, superoxo, or oxo species (HOO^- , O_2^- , O^{2-}) at such iron centers in order to control their further reactions (96). In this context, mononuclear iron(II) complexes with a single labile coordination site may serve as models for naturally occurring oxygenases and peroxidases whose active sites share these structural features (95,97). The pentaamine ligand **1** may serve as a building block for more complex ligand architectures, by suitable derivatization of the primary amino functions, e.g., through imine formation. Iron(II) complexes of **1** have turned out to be surprisingly stable towards hydrolysis and oxidation, and preliminary results indicate that the corresponding iron(III) complexes, such as $[(\mathbf{1})\text{Fe}(\text{N}_3)]\text{X}_2$ or $[(\mathbf{1})_2\text{Fe}_2(\mu\text{-O})]\text{X}_4$, are also accessible.

The iron complexes of the pentaamine **1** that have been isolated so far have the bromo complex $[(\mathbf{1})\text{FeBr}]\text{Br}$ (**32**) as their common precursor. Reactivity patterns are shown in Scheme 1. The carbonyl and nitro derivatives $[(\mathbf{1})\text{Fe}(\text{CO})]\text{Br}_2$ (**33**) and $[(\mathbf{1})\text{Fe}(\text{NO}_2)]\text{Br}$ (**34**) may be obtained from **32** simply by ligand exchange. Complex **32** is readily formed as a yellow microcrystalline solid in an air-free aqueous solution containing iron(II) sulfate, an excess of sodium bromide, and the pentaamine ligand, once the pH has been raised to pH 8...9 by addition of sodium hydroxide. The determined magnetic moment ($\mu_{\text{eff}} = 5.23$) indicates four unpaired electrons and thus a high-spin Fe d^6 center, in full agreement with the Mössbauer spectral data. The high-spin character of the metal center is also evident from the Fe–N bond lengths determined by single-crystal X-ray diffraction. The average is 2.169(6) Å and thus close to the value of 2.21(1) Å reported for the prototypical high-spin Fe^{II} complex $[\text{Fe}(\text{en})_3]\text{X}_2$ (en = ethylenediamine) (98,99).

The carbonyl complex **33** is obtained in a clean displacement reaction when carbon monoxide is passed through a solution of **32** in methanol. Due to the increased charge on the cation, the product precipitates in the process. The rather low frequency of the C–O stretching vibration in the IR spectrum of the solid (KBr disc) at 1960 cm^{-1} points to a strong Fe–CO interaction (100), as expected for the highly basic NN_4 ligand environment. Similarly low values ($1940\text{--}1960\text{ cm}^{-1}$) were reported for the pentaamine iron(II) complexes



SCHEME 1.

$[(\text{tetraen})\text{Fe}(\text{CO})]\text{X}_2$ (tetraen = tetraethylenepentaamine; $\text{X} = \text{Cl}, \text{I}, \text{ClO}_4$) which have already been mentioned (90–92). In the case of compounds **32** and **33**, replacement of bromide by the strong-field ligand CO causes the product to be low-spin, and hence diamagnetic. Its ^1H and $\{^1\text{H}\}^{13}\text{C}$ NMR spectra are well resolved, with patterns supporting a C_{2v} symmetrical structure of the cation in solution, and overall similar to those observed for the series of cobalt(III) complexes of the pentaamine ligand discussed above (48). The ^{13}C resonance of the carbonyl ligand occurs at 220.71 ppm (D_2O). This is an extreme value for an $\text{Fe}^{\text{II}}\text{--CO}$ complex when compared to the range of chemical shifts found for the CO adducts of hemoproteins and porphyrin-based model complexes (208–202 ppm) (101). Compound **33** is unusual in that it appears to be the first octahedral $\text{Fe}^{\text{II}}\text{--CO}$ complex with a non-porphyrin N donor environment to have been structurally characterized. The most striking structural feature of **3** (Fig. 5), when compared to **2**, is the sharp contraction of the $\text{Fe}\text{--N}$ bonds, in accord with a low-spin Fe^{II} formulation. The mean length of 2.02(1) Å is in the range of values determined for low-spin Fe^{II} complexes of macrocyclic aliphatic amines (102) and podand polyamines with predominantly

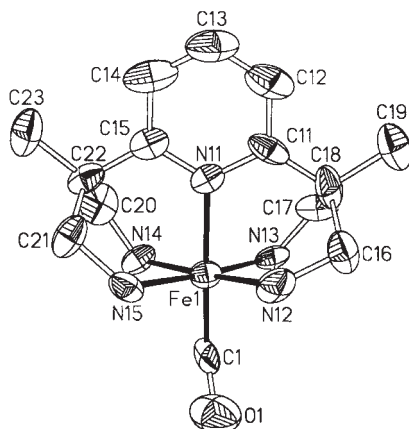


FIG. 5. Molecular structure of the cation in the carbonyl complex [(1)Fe(CO)]Br₂ (**33**).

imine donor sets (6,99,103). The coordination of the carbonyl ligand is essentially linear ((Fe1–C1–O1)=166(2)°), and the Fe–C bond length (1.73(2) Å) is similar to values determined for porphyrinato Fe^{II}–CO complexes with aromatic imines in the *trans* position (e.g., 1.744(5) Å (104)).

The carbonyl complex **33** in particular had thus served to demonstrate the novel qualities of the pentaamine ligand **1** as a chelating, “superpodal” analogue of the pentaammine, (NH₃)₅ donor set, and we extended our ligand exchange experiments to include the NO_x species NO, NO⁺, and NO₂[−]. The reaction of the bromo complex **32** with a stoichiometric amount of nitrogen oxide, in methanolic solution, produces the 19 valence electron iron nitrosyl complex [(1)Fe(NO)]Br₂ (**34**), classified as {Fe(NO)}⁷ according to the Enemark-Feltham notation (Scheme 1) (105). Its low ν_{NO} stretching frequency (1620 cm^{−1}; KBr disc) points to an electron-rich metal center, due to the almost exclusive σ -character of the NN₄ donor set, which enhances M → N–O back donation. The complex is paramagnetic, with an S = 1/2 ground state. In the ESR spectrum, the observed *g* tensor is rhombic (*g*₁ = 2.051, *g*₂ = 2.005, *g*₃ = 1.966), with ¹⁴N hyperfine coupling due to the nitrosyl ligand resolved for *g*₂; the coupling constant is A(¹⁴NO) = 22.9 G. The occurrence of ¹⁴N-induced hyperfine splitting suggests the HOMO of the {Fe(NO)}⁷ unit to retain a substantial amount of NO-based orbital character (106,107), with the pyN₄ ligand imposing an overall spacing of molecular orbitals as predicted for the strong-field limit (106).

The spectrum resembles that of the tetraphenylporphyrinato nitrosyl iron complex with piperidine as an axial base ($g_1=2.080$, $g_2=2.040$, $g_3=2.003$; $A(^{14}\text{NO})=21.7\text{ G}$) (108), and a similar set of parameters was also determined for the nitrosyl derivative of myoglobin (MbNO) (109). The cyclic voltammogram of **34** shows two redox waves; a quasi-reversible one-electron oxidation ($E_{1/2}=+0.18\text{ V}$) yields the 18 valence electron complex **5** ($\{\text{Fe}(\text{NO})\}^6$, below), whereas an irreversible reduction at -1.06 V is assigned to the formation of a 20 valence electron species, $\{\text{Fe}(\text{NO})\}^8$, for which there is precedent in the literature (107,110). When comparing the solid state structural parameters of the $\{(1)\text{Fe}\}$ fragments in **34** (Fig. 6) and in the carbonyl complex **33**, the only striking difference involves the pyridine–iron bond lengths *trans* to the CO and NO ligands, respectively; these are $d(\text{Fe}-\text{N})=2.02(1)\text{ \AA}$ in **33**, and $d(\text{Fe}-\text{N})=2.095(5)\text{ \AA}$ in **34**. This suggests the singly occupied molecular orbital in **34** to be antibonding with respect to $\text{Fe}-\text{N}_{\text{py}}$ and bonding with respect to the $\text{Fe}-\text{N}_{\text{eq}}$ interactions, a conclusion borne out by comprehensive theoretical calculations based on DFT (79). The NO ligand in **34** is coordinated to the iron center at an angle of $139.4(5)$. This angle is 10° to 20° smaller than for other six-coordinate $\{\text{Fe}(\text{NO})\}^7$ complexes (107,111), possibly due to an intramolecular hydrogen bond between the nitrosyl ligand and one of the amine protons. The bond lengths $\text{Fe}-\text{N}_{\text{NO}}$ and $\text{N}-\text{O}$ in the case of **34**

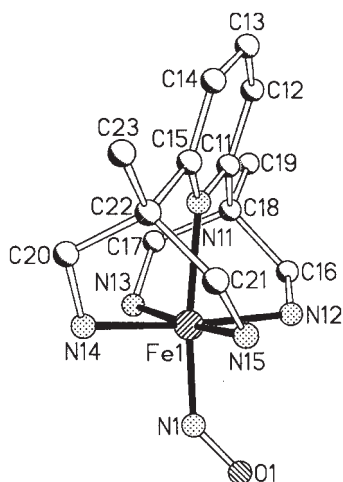


FIG. 6. Molecular structure of the cation in the 19 valence electron nitrosyl complex $[(1)\text{Fe}(\text{NO})]\text{Br}_2$ (**34**).

(1.737(6) Å and 1.175(8) Å, respectively) agree with previously reported structural data (107,111).

The 18 valence electron nitrosyl complex [(1)Fe(NO)]Br₃ (**35**), which is isoelectronic with the carbonyl complex **33**, is directly accessible from the bromo complex **32** by reaction with an NO⁺ source such as NOBF₄. There is a strong absorption in the IR spectrum (KBr disc) at 1926 cm⁻¹ (ν_{NO} str). We interpret the extreme shift of the NO stretching vibration upon going from {Fe(NO)}⁷ to {Fe(NO)}⁶ as an indication of the oxidation being largely centered on the NO ligand, in agreement with the Mössbauer data and DFT calculations (79). Compound **35** is diamagnetic, and its ¹H and ¹³C NMR spectra show no unusual deviations from those of the carbonyl complex **33**. The cyclic voltammogram shows the same redox behavior as the 19 valence electron complex **34**, as expected. Preliminary X-ray structural data have established the connectivity and overall geometry of the cation, in which the Fe–N–O unit is linear. Approximate lengths of the Fe–N bonds between the iron ion and the pentadentate ligand are between 1.97 and 2.02 Å, and the values for d(Fe–NO) and d(N–O) are 1.67 Å and 1.12 Å, respectively. The parameters within Fe–N–O are comparable to those of an 18 valence electron iron nitrosyl complex with an NS₄ ligand, which has no podand character (107).

Formation of the NO₂⁻ complex **36** (Scheme 1) upon addition of NaNO₂ to [(1)FeBr]Br in methanol is immediate. The product has been fully characterized by IR, NMR, UV/Vis spectroscopies and other methods. Attempts to obtain single crystals of **36**, however, revealed a remarkable transformation into the nitrosyl complex {Fe(NO)}⁷ by slow hydrolysis. Complex **36** is diamagnetic with well-resolved NMR spectra which, similar to the spectra of the carbonyl and {Fe(NO)}⁶ complexes, indicate a C_{2v} symmetrical cation in solution. The cyclic voltammogram (DMSO solution) has one quasi-reversible one-electron redox wave at -0.07 V as the only feature, which we assign to the Fe^{II}/Fe^{III} couple of the mononuclear complex. Addition of water to methanol solutions of **36** (in sub-stoichiometric or stoichiometric amounts) under anaerobic conditions leads to the formation of the 19 valence electron complex [(1)Fe(NO)]Br₂ ({Fe(NO)}⁷, **34**) as the major product. This hydrolysis reaction, in which the nitro ligand is reduced to coordinated nitric oxide, is remarkable in that it parallels the reactivity of certain heme *cd*₁-dependent nitrite reductases at physiological pH (112). It is important to note that the hydrolysis of **36** to give **34** proceeds under neutral conditions (79). The reduction equivalents necessary for the NO₂⁻ → NO conversion may either be supplied by the pentaamine ligand (48), or by part of the Fe^{II} ions, which should

lead to the formation of **34** (which contains formal Fe^{II}) and an Fe^{III} species in a 1:1 ratio. We have no indications for either process. The most likely explanation for the observed reactivity is to invoke methanol as a reducing agent. When adding H^+ to a methanolic solution of **36**, formation of $\{\text{Fe}(\text{NO})\}^6$ by loss of water from coordinated NO_2^- is rapid, and the product is protected against reduction by its low solubility. When adding H_2O to a methanolic solution of **36**, the formation of $\{\text{Fe}(\text{NO})\}^6$ proceeds much more slowly, so that whatever product is formed can immediately be reduced to $\{\text{Fe}(\text{NO})\}^7$, with no precipitation of $\{\text{Fe}(\text{NO})\}^6$. Methanol would thus play the same role in this functional model as do non-physiological reducing agents (such as ascorbate) coupled with heme *c* in the case of heme *cd*₁-dependent nitrite reductase, where such agents have been shown to sustain the function of the enzyme *in vitro* (112–114).

Finally, attempts to obtain single crystals of the mononuclear nitro complex **36** under strictly anhydrous conditions gave a *dinuclear* iron(II) complex instead, containing an *N,O*-coordinated nitrite bridge (**37**, Fig. 7). The $\mu_2-(\eta^1\text{-N}:\eta^1\text{-O})\text{-NO}_2$ bridge, which is unsupported by other ligands, is an unprecedented feature in the coordination chemistry of iron(II), and the only other instance where this bonding mode has been found in a non-polymeric compound appears to be a dinuclear copper(I) complex of macrocyclic ligands derived from triaza-cyclononane, synthesized as models for the active sites of copper-dependent nitrite reductases (115,116). While the bond angles in the $\{\text{(I)Fe}\}$ fragment of **37** are similar to those of the other structures, the Fe–N bonds in **37** are significantly longer than in the other low-spin

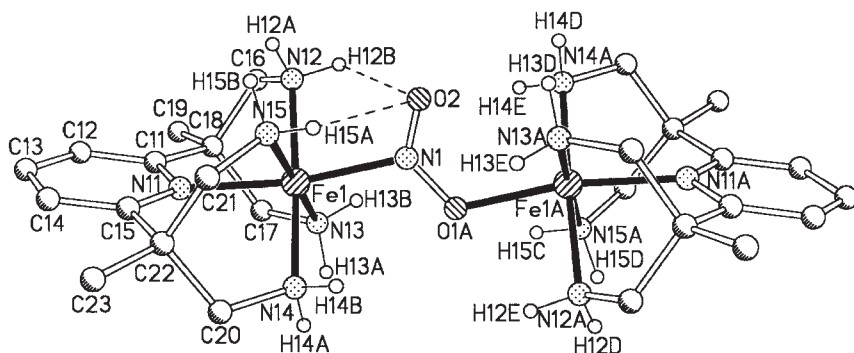


FIG. 7. Molecular structure of the cation in the bridged iron(II) nitro/nitrito complex $[(\text{I})_2\text{Fe}_2\{\eta^1\text{-N}:\eta^1\text{-O})\text{-NO}_2\}]\text{Br}_2\text{PF}_6$ (**37**); intramolecular hydrogen bonds are shown as broken lines.

complexes of the series that have been structurally characterized, **33** and **34**. There is, however, no indication of an incipient crossover to the high-spin configuration in **37**. The bond angles at the nitrogen atom of the NO₂ ligand deviate from the expected value of 120°, and the angle N_{py}–Fe–N_{NO2} is contracted to 169.6(1)° from the expected value of 180°. These distortions are, to a large part, due to intramolecular hydrogen bonds between the uncoordinated NO₂ oxygen atom and protons on the primary amino groups of the pentadentate ligand.

The pentapyridyl ligand 2,6-(bis-(bis-2-pyridyl)methoxymethane)pyridine **7** (R = OMe) was used to prepare a series of iron(II) complexes, a number of which have been structurally characterized (**6,9**). In much the same manner as **1**, the ligand binds ferrous iron in a square-pyramidal geometry, leaving a single coordination site accessible for complexation of monodentate exogenous ligands, such as MeCN, MeOH, H₂O, pyridine, N₃[−], or MeO[−]. Depending on the nature of the monodentate ligand, high-spin or low-spin electronic ground states are observed. From a comparison (in methanol solution) of binding affinities of the monodentate ligands, the charge on the latter appears to be the major factor in controlling complex formation, and a preference of anionic ligands over neutral ligands has been observed for the {(**7**)Fe} fragment (R = OMe). Amongst possible monodentate ligands, if charges are equal, strongfield ligands are bound in preference to weak-field ligands. In methanol solution, strongly basic ligands preferentially deprotonate coordinated methanol to yield [(**7**)Fe(OMe)]²⁺, rather than ligate to the ferrous center. Interestingly, and in contrast to the iron complexes of **1**, the formation of iron(III) complexes of **7** is disfavored; attempted preparations with iron(III) salts resulted in spontaneous reduction in most cases, presumably through oxidation of the solvent. One of the accessible ferric complexes of **7** is [(**7**)Fe(OMe)](OTf)₂ (R = OMe), prepared from the corresponding iron(II) methanol complex by oxidation with hydrogen peroxide or iodosobenzene, and this complex has been used in modelling studies for the nonheme iron enzyme lipoyxygenase (**7,8**). Substrates with a weak C–H bond, such as cyclohexadiene, are reported to reduce the ferric complex. The iron(II) methanol complex as well as a radical species are formed in the process, in a manner similar to the C–H bond activation step in the proposed mechanism of lipoyxygenase.

In the context of model studies of iron enzymes involved in oxygen transfer, the pentapyridine ligand **7** (R = OMe), the tetrapyridine ligand **11**, and a number of other, less symmetrical N₅ ligands have been used to prepare iron(II) complexes that react with hydrogen peroxide to generate transient low-spin Fe^{III}–OOH intermediates (**17,18,21,117**), with

hydroperoxo-to-iron(III) charge-transfer bands between 500 and 600 nm. Their resonance Raman frequencies for the O–O stretching vibration lie near 800 cm^{-1} and are thus significantly lower than those observed for related high-spin complexes. The hydroperoxo-to-iron(III) charge-transfer transition shifts to higher wavenumbers and the O–O stretching frequency of the Fe–OOH unit decreases as the N_5 ligand becomes more electron donating, which indicates progressive weakening of the O–O bond with increasing electron density at the low-spin iron(III) center. The metal center thus appears to prime the O–O bond for homolysis prior to substrate attack. This reactivity has been documented for the complex $[(\mathbf{11})\text{Fe}^{\text{III}}(\eta^1\text{-OOH})]^{2+}$, in the oxidation of cyclohexane. The hydroperoxo complex may be converted to its conjugate base, and the obtained data (ESR, Mössbauer, EXAFS) suggest this to be a high-spin iron(III) complex with a peroxo ligand in side-on coordination, $[(\mathbf{11})\text{Fe}^{\text{III}}(\eta^2\text{-O}_2)]^+$. A number of structural parameters (such as Fe–O and O–O bond lengths) have been extracted from the EXAFS data, but crystal structures of the complexes have so far not been obtained.

IV. Conclusion

As is evident from the results obtained so far by our group and others, there is an emerging rich coordination chemistry of tetrapodal pentadentate N_5 donor ligands, particularly towards iron. “Superpodal” ligands with primary amino groups, such as **1**, have the potential for further derivatization. In contrast to previous reports of iron complexes with open-chain aliphatic amine ligands, iron complexes of **1** show remarkable stability, both with respect to oxidative degradation of the ligand and to unspecific hydrolysis. The ligand, which may be construed as a chelating analogue of the pentaammine donor set, has predominant σ -donor character, thereby providing an electron-rich coordination environment for the metal center. This gives rise to unusual reactivity, such as the observed reduction of coordinated nitrite to NO.

REFERENCES

1. Takano, S.; Yano, Y.; Tagaki, W. *Chem. Lett.* **1981**, 1177–1180.
2. Tamagaki, S.; Kanamaru, Y.; Ueno, M.; Tagaki, W. *Bull. Chem. Soc. Jpn.* **1991**, *64*, 165–174.
3. Grohmann, A.; Knoch, F. *Inorg. Chem.* **1996**, *35*, 7932–7934.

4. Collman, J. P.; Min Zhong; Zhong Wang. *Org. Lett.* **1999**, *1*, 949–951.
5. Canty, A. J.; Minchin, N. J.; Skelton, B. W.; White, A. H. *J. Chem. Soc. Dalton Trans.* **1986**, 2205–2210.
6. de Vries, M. E.; La Crois, R. M.; Roelfes, G.; Kooijman, H.; Spek, A. L.; Hage, R.; Feringa, B. L. *J. Chem. Soc. Chem. Comm.* **1997**, 1549–1550.
7. Jonas, R. T.; Stack, T. D. P. *J. Am. Chem. Soc.* **1997**, *119*, 8566–8567.
8. Goldsmith, C. R.; Jonas, R. T.; Stack, T. D. P. *J. Am. Chem. Soc.* **2002**, *124*, 83–96.
9. Goldsmith, C. R.; Jonas, R. T.; Cole, A. P.; Stack, T. D. P. *Inorg. Chem.* **2002**, *41*, 4642–4652.
10. Klein Gebbink, R. J. M.; Jonas, R. T.; Goldsmith, C. R.; Stack, T. D. P. *Inorg. Chem.* **2002**, *41*, 4633–4641.
11. Fazio, O.; Gnida, M.; Meyer-Klaucke, W.; Frank, W.; Kläui, W. *Eur. J. Inorg. Chem.* **2002**, 2891–2896.
12. Ishii, A.; Horikawa, Y.; Takaki, I.; Shibata, J.; Nakayama, J.; Hoshino, M. *Tetrahedron Lett.* **1991**, *32*, 4313–4316.
13. Hieber, G.; Hanack, M.; Wurst, K.; Strähle, J. *Chem. Ber.* **1991**, *124*, 1597–1605.
14. Angelici, R. J. *Coord. Chem. Rev.* **1990**, *105*, 61–76.
15. Ainscough, E. W.; Brodie, A. M.; Depree, C. V. *J. Chem. Soc. Dalton Trans.* **1999**, 4123–4124.
16. Lubben, M.; Meetsma, A.; Wilkinson, E. C.; Feringa, B.; Que, L. Jr. *Angew. Chem. Int. Ed.* **1995**, *34*, 1512–1514.
17. Roelfes, G.; Lubben, M.; Chen, K.; Ho, R. Y. N.; Meetsma, A.; Genseberger, S.; Hermant, R. M.; Hage, R.; Mandal, S. K.; Young, V. G. Jr.; Zang, Y.; Kooijman, H.; Spek, A. L.; Que, L. Jr.; Feringa, B. L. *Inorg. Chem.* **1999**, *38*, 1929–1936.
18. Roelfes, G.; Lubben, M.; Leppard, S. W.; Schudde, E. P.; Hermant, R. M.; Hage, R.; Wilkinson, E. C.; Que, L. Jr.; Feringa, B. L. *J. Mol. Catal. A.* **1997**, *117*, 223–227.
19. Ho, R. Y. N.; Roelfes, G.; Feringa, B. L.; Que, L. Jr. *J. Am. Chem. Soc.* **1999**, *121*, 264–265.
20. Ho, R. Y. N.; Roelfes, G.; Hermant, R.; Hage, R.; Feringa, B. L.; Que, L. *J. Chem. Soc. Chem. Comm.* **1999**, 2161–2162.
21. Roelfes, G.; Vrajasu, V.; Chen, K.; Ho, R. Y. N.; Rohde, J.-U.; Zondervan, C.; la Crois, R. M.; Schudde, E. P.; Lutz, M.; Spek, A. L.; Hage, R.; Feringa, B. L.; Muenck, E.; Que, L. Jr. *Inorg. Chem.* **2003**, *42*, 2639–2653.
22. Fabius, B.; Geue, R. J.; Hazell, R. G.; Jackson, W. G.; Krebs Larsen, F.; Qin, C. J.; Sargeson, A. M. *J. Chem. Soc. Dalton Trans.* **1999**, 3961–3972.
23. Hegetschweiler, K.; Maas, O.; Zimmer, A.; Geue, R. J.; Sargeson, A. M.; Harmer, J.; Schweiger, A.; Buder, I.; Schwitzgebel, G.; Reiland, V.; Frank, W. *Eur. J. Inorg. Chem.* **2003**, 1340–1354.
24. Dietz, C.; Heinemann, F. W.; Grohmann, A. *Eur. J. Inorg. Chem.* **1999**, 2147–2156.
25. Schmidt, S.; Bauer, W.; Heinemann, F. W.; Lanig, H.; Grohmann, A. *Angew. Chem. Int. Ed.* **2000**, *39*, 913–916.
26. Grohmann, A.; Lanig, H.; Bauer, W.; Schmidt, S.; Heinemann, F. W. *J. Mol. Model.* **2000**, *6*, 119–125.
27. Dietz, C.; Heinemann, F. W.; Grohmann, A. *Z. Naturforsch. B* **2000**, *55b*, 1037–1044.
28. Zimmermann, C.; Heinemann, F. W.; Grohmann, A. *Eur. J. Inorg. Chem.* **2001**, 547–555.
29. Schmidt, S.; Omnès, L.; Heinemann, F. W.; Kuhnigk, J.; Krüger, C.; Grohmann, A. *Z. Naturforsch. B* **1998**, *53b*, 946–954.
30. Zimmermann, C.; Bauer, W.; Heinemann, F. W.; Grohmann, A. *Z. Naturforsch.* **2002**, *57*, 1256–1264.

31. Isabel Burguete, M.; Luis, S. V.; Miravet, J. F.; Paya, L.; Querol, M.; Garcia-Espana, E.; Soriano, C. *J. Chem. Soc. Chem. Comm.* **1998**, 1823–1824.
32. Pitarch López, J.; Heinemann, F. W.; Grohmann, A. *Z. Anorg. Allg. Chem.* **2003**, 629, 2449–2457.
33. Ibrahim, M. M.; Shimoura, N.; Ichikawa, K.; Shiro, M. *Inorg. Chim. Acta.* **2001**, 313, 125–136.
34. Brandsch, T.; Schell, F.; Weiss, K.; Ruf, M.; Müller, B.; Vahrenkamp, H. *Chem. Ber./Recueil* **1997**, 130, 283–289.
35. Gerbeleu, N. V.; Arion, V. B.; Burgess, J. “*Template Synthesis of Macrocyclic Compounds*”, Chapters 3, 4; Wiley-VCH: Weinheim, **1999**.
36. Suh, M. P.; Lee, J.; Han, M. Y.; Yoon, T. S. *Inorg. Chem.* **1997**, 36, 5651–5654.
37. Kang, S.-G.; Ryu, K.; Suh, M. P.; Jeong, J. H. *Inorg. Chem.* **1997**, 36, 2478–2481.
38. Suh, M. P.; Han, M. Y.; Lee, J. H.; Min, K. S.; Hyeon, C. *J. Am. Chem. Soc.* **1998**, 120, 3819–3820.
39. Goodwin, J. A.; Stanbury, D. M.; Wilson, L. J.; Eigenbrot, C. W.; Scheidt, W. R. *J. Am. Chem. Soc.* **1987**, 109, 2979–2991.
40. Reinen, D. *Comments Inorg. Chem.* **1983**, 2, 227–246.
41. Hathaway, B. J. *Struct. Bonding* **1984**, 57, 55–118.
42. Duggan, M.; Ray, N.; Hathaway, B.; Tomlinson, G.; Brint, P.; Pelin, K. *J. Chem. Soc. Dalton Trans.* **1980**, 1342–1348.
43. Bondi, A. *J. Phys. Chem.* **1964**, 68, 441–451.
44. Dietz, C.; Heinemann, F. W.; Kuhnigk, J.; Krüger, C.; Gerdan, M.; Trautwein, A. X.; Grohmann, A. *Eur. J. Inorg. Chem.* **1998**, 1041–1049.
45. Martell, A. E.; Hancock, R. D., “*Metal Complexes in Aqueous Solution*”; Plenum Press: New York, **1996**, p. 55.
46. McAuley, A.; Beveridge, K.; Subramanian, S.; Whitcombe, T. W. *Can. J. Chem.* **1989**, 67, 1657–1665.
47. McAuley, A.; Subramanian, S. *Inorg. Chem.* **1991**, 30, 371–378.
48. Schmidt, S.; Heinemann, F. W.; Grohmann, A. *Eur. J. Inorg. Chem.* **2000**, 1657–1667.
49. Grohmann, A.; Heinemann, F. W.; Kofod, P. *Inorg. Chim. Acta* **1999**, 286, 98–102.
50. Poth, T.; Paulus, H.; Elias, H.; van Eldik, R.; Grohmann, A. *Eur. J. Inorg. Chem.* **1999**, 643–650.
51. Jackson, W. G. *Inorg. React. Mech.* **2002**, 4, 1–30.
52. Jackson, W. G.; McKeon, J.; Marty, W. *Inorg. React. Mech.* **2002**, 4, 125–132.
53. Gainsford, G. J.; Jackson, W. G.; Sargeson, A. M. *Aust. J. Chem.* **1986**, 39, 1331–1336.
54. Solomon, E. I.; Tuzcek, F.; Root, D. E.; Brown, C. A. *Chem. Rev.* **1994**, 94, 827–856.
55. Fallab, S.; Mitchell, P. R. “*Advances in Inorganic and Bioinorganic Mechanisms*”, Vol. 3; Academic Press: London, **1984**, pp. 311–377.
56. Dexter, D. D.; Sutherby, C. N.; Grieb, M. W.; Beaumont, R. C. *Inorg. Chim. Acta* **1984**, 86, 19–31.
57. Duffy, D. L.; House, D. A.; Weil, J. A. *J. Inorg. Nucl. Chem.* **1969**, 31, 2053–2058.
58. Ramprasad, D.; Gilicinski, A. G.; Markley, T. J.; Pez, G. P. *Inorg. Chem.* **1994**, 33, 2841–2847.
59. Miskowski, V. M.; Robbins, J. L.; Treitel, I. M.; Gray, H. B. *Inorg. Chem.* **1975**, 14, 2318–2321.
60. Schaefer, W. P.; Marsh, R. E. *Acta Cryst.* **1966**, 21, 735–743.
61. Schaefer, W. P. *Inorg. Chem.* **1968**, 7, 725–731.
62. Gatehouse, B. M.; McLachlan, G.; Martin, L. L.; Martin, R. L.; Spiccia, L. *Aust. J. Chem.* **1991**, 44, 351–359.
63. Fritch, J. R.; Christoph, G. G.; Schaefer, W. P. *Inorg. Chem.* **1973**, 12, 2170–2175.

64. Thewalt, U.; Zehnder, M.; Fallab, S. *Helv. Chim. Acta* **1977**, *60*, 867–873.
65. Zehnder, M.; Thewalt, U. *Z. Anorg. Allg. Chem.* **1980**, *461*, 53–60.
66. Bernhardt, P. V.; Lawrance, G. A.; Hambley, T. W. *J. Chem. Soc. Dalton Trans.* **1990**, 235–241.
67. Miskowski, V. M.; Santarsiero, B. D.; Schaefer, W. P.; Ansok, G. E.; Gray, H. B. *Inorg. Chem.* **1984**, *23*, 172–176.
68. Cameron, B. R.; House, D. A.; McAuley, A. *J. Chem. Soc. Dalton Trans.* **1993**, 1019–1022.
69. Ahmed, E.; Chatterjee, C.; Cooksey, C. J.; Tobe, M. L.; Williams, G.; Humanes, M. *J. Chem. Soc. Dalton Trans.* **1989**, 645–654.
70. Drennan, C. L.; Huang, S.; Drummond, J. T.; Matthews, R. G.; Ludwig, M. L. *Science* **1994**, *266*, 1669–1674.
71. Wolowiec, S.; Balt, S.; de Bolster, M. W. G. *Inorg. Chim. Acta* **1991**, *181*, 131–136.
72. Kofod, P. *Inorg. Chem.* **1995**, *34*, 2768–2770.
73. Kofod, P.; Harris, P.; Larsen, S. *Inorg. Chem.* **1997**, *36*, 2258–2266.
74. Randaccio, L.; Bresciani-Pahor, N.; Zangrando, E.; Marzilli, L. G. *Chem. Soc. Rev.* **1989**, *18*, 225–250.
75. Bigotto, A.; Zangrando, E.; Randaccio, L. *J. Chem. Soc. Dalton Trans.* **1976**, 96–104.
76. Summers, J. S.; Petersen, J. L.; Stolzenberg, A. M. *J. Am. Chem. Soc.* **1994**, *116*, 7189–7195.
77. Yohannes, P. G.; Bresciani-Pahor, N.; Randaccio, L.; Zangrando, E.; Marzilli, L. G. *Inorg. Chem.* **1988**, *27*, 4738–4744.
78. Gerli, A.; Sabat, M.; Marzilli, L. G. *J. Am. Chem. Soc.* **1992**, *114*, 6711–6718.
79. Pitarch López, J.; Heinemann, F. W.; Prakash, R.; Hess, B. A.; Horner, O.; Jeandey, C.; Oddou, J.-L.; Latour, J.-M.; Grohmann, A. *Chem. Eur. J.* **2002**, *8*, 5709–5722.
80. Pohl, K.; Wieghardt, K.; Kaim, W.; Steenken, S. *Inorg. Chem.* **1988**, *27*, 440–447.
81. Bernhardt, P. V.; Comba, P.; Hambley, T. W.; Lawrance, G. A. *Inorg. Chem.* **1991**, *30*, 942–946.
82. Börzel, H.; Comba, P.; Pritzkow, H.; Sickmüller, A. F. *Inorg. Chem.* **1998**, *37*, 3853–3857.
83. Meyer, K.; Bill, E.; Mienert, B.; Weyhermüller, T.; Wieghardt, K. *J. Am. Chem. Soc.* **1999**, *121*, 4859–4876.
84. Hancock, R. D.; Martell, A. E. *Comments Inorg. Chem.* **1988**, *6*, 237–284.
85. Bernhardt, P. V.; Comba, P.; Mahu-Rickenbach, A.; Stebler, S.; Steiner, S.; Várnagy, K.; Zehnder, M. *Inorg. Chem.* **1992**, *31*, 4194–4200.
86. Watt, G. W.; Jenkins, W. A. *Inorg. Synth.* **1953**, *4*, 161–163.
87. Behrens, H. *Adv. Organomet. Chem.* **1980**, *18*, 1–53.
88. Sadasivan, N.; Endicott, J. F. *J. Am. Chem. Soc.* **1966**, *88*, 5468–5472.
89. Renovitch, G. A.; Baker, W. A. Jr. *J. Am. Chem. Soc.* **1968**, *90*, 3585–3587.
90. Melby, L. R. *Inorg. Chem.* **1970**, *9*, 2186–2188.
91. Coda, A.; Kamenar, B.; Prout, K.; Carruthers, J. R.; Rollett, J. S. *Acta Crystallogr., Sect. B* **1975**, *B31*, 1438–1442.
92. Hanson, M. V.; Marsh, W. E.; Carlisle, G. O. *Inorg. Nucl. Chem. Letters* **1977**, *13*, 277–282.
93. Hegetschweiler, K.; Ghisletta, M.; Hausherr-Primo, L.; Kradolfer, T.; Schmalle, H. W.; Gramlich, V. *Inorg. Chem.* **1995**, *34*, 1950–1953.
94. Ghisletta, M.; Hausherr-Primo, L.; Gajda-Schranz, K.; Machula, G.; Nagy, L.; Schmalle, H. W.; Rihs, G.; Endres, F.; Hegetschweiler, K. *Inorg. Chem.* **1998**, *37*, 997–1008.
95. Que, L.; Ho, R. Y. N. *Chem. Rev.* **1996**, *96*, 2607–2624.

96. MacBeth, C. E.; Golombek, A. P.; Young, V. G. Jr.; Cheng Yang; Kuczera, K.; Hendrich, M. P.; Borovik, A. S. *Science* **2000**, *289*, 938–941.
97. Bernal, I.; Jensen, I. M.; Jensen, K. B.; McKenzie, C. J.; Toftlund, H.; Tuchagues, J.-P. *J. Chem. Soc. Dalton Trans.* **1995**, 3667–3675.
98. Li, J.; Chen, Z.; Emge, T. J.; Proserpio, D. M. *Inorg. Chem.* **1997**, *36*, 1437–1442.
99. Diebold, A.; Hagen, K. S. *Inorg. Chem.* **1998**, *37*, 215–223.
100. Goedken, V. L. “*Coordination Chemistry of Macrocyclic Compounds*”, Chapter 10; Ed. Melson, G. A.; Plenum Press: New York, London, **1979**.
101. Matsu-ura, M.; Tani, F.; Naruta, Y. *J. Am. Chem. Soc.* **2002**, *124*, 1941–1950.
102. Boeyens, J. C. A.; Forbes, A. G. S.; Hancock, R. D.; Wieghardt, K. *Inorg. Chem.* **1985**, *24*, 2926–2931.
103. Al-Obaidi, A. H. R.; Jensen, K. B.; McGarvey, J. J.; Toftlund, H.; Jensen, B.; Bell, S. E. J.; Carroll, J. G. *Inorg. Chem.* **1996**, *35*, 5055–5060.
104. Salzmann, R.; McMahon, M. T.; Godbout, N.; Sanders, L. K.; Wojdelski, M.; Oldfield, E. *J. Am. Chem. Soc.* **1999**, *121*, 3818–3828.
105. Richter-Addo, G. B.; Legzdins, P. “*Metal Nitrosyls*”, Chapter 1; Oxford University Press: New York, Oxford, **1992**.
106. Shepherd, R. E.; Sweetland, M. A.; Junker, D. E. *J. Inorg. Biochem.* **1997**, *65*, 1–14.
107. Sellmann, D.; Blum, N.; Heinemann, F. W.; Hess, B. A. *Chem. Eur. J.* **2001**, *7*, 1874–1880.
108. Wayland, B. B.; Olson, L. W. *J. Am. Chem. Soc.* **1974**, *96*, 6037–6041.
109. Dickinson, L. C.; Chien, J. C. W. *J. Am. Chem. Soc.* **1971**, *93*, 5036–5040.
110. Hauser, C.; Glaser, T.; Bill, E.; Weyhermüller, T.; Wieghardt, K. *J. Am. Chem. Soc.* **2000**, *122*, 4352–4365.
111. Enemark, J. H.; Feltham, R. D.; Huie, B. T.; Johnson, P. L.; Bizot Swedo, K. *J. Am. Chem. Soc.* **1977**, *99*, 3285–3292.
112. Averill, B. A. *Chem. Rev.* **1996**, *96*, 2951–2964.
113. Kanti Das, T.; Wilson, E. K.; Cutruzzolà, F.; Brunori, M.; Rousseau, D. L. *Biochemistry* **2001**, *40*, 10774–10781.
114. Cutruzzolà, F.; Brown, K.; Wilson, E. K.; Bellelli, A.; Arese, M.; Tegoni, M.; Cambillau, C.; Brunori, M. *Proc. Natl. Acad. Sci. U. S. A.* **2001**, *98*, 2232–2237.
115. Halfen, J. A.; Mahapatra, S.; Olmstead, M. M.; Tolman, W. B. *J. Am. Chem. Soc.* **1994**, *116*, 2173–2174.
116. Halfen, J. A.; Tolman, W. B. *J. Am. Chem. Soc.* **1994**, *116*, 5475–5476.
117. Roelfes, G.; Lubben, M.; Hage, R.; Que, L.; Feringa, B. L. *Chem. Eur. J.* **2000**, *6*, 2152–2159.

EFFICIENT, ECOLOGICALLY BENIGN, AEROBIC OXIDATION OF ALCOHOLS

ISTVÁN E. MARKÓ¹, PAUL R. GILES¹, MASAO TSUKAZAKI¹,
ISABELLE CHELLÉ-REGNAUT¹, ARNAUD GAUTIER¹,
RAPHAEL DUMEUNIER¹, FREDDI PHILIPPART¹, KANAE DODA¹,
JEAN-LUC MUTIONKOLE¹, STEPHEN M. BROWN² and
CHRISTOPHER J. URCH³

¹Université Catholique de Louvain, Département de Chimie, Laboratoire
de Chimie Organique, Bâtiment Lavoisier, Place Louis Pasteur 1,
B-1348 Louvain-la-Neuve, Belgium

²Zeneca Process Technology Department, Huddersfield Works, P.O. Box A38,
Leeds Road, Huddersfield HD2 1FF, UK

³Zeneca Agrochemicals, Jealott's Hill Research Station, Bracknell,
Berkshire RG42 6ET, UK

- I. Introduction
- II. First Generation Copper-Catalyzed Aerobic Oxidation Protocol
 - A. Testing the Rivière and Jallabert System
 - B. The First Breakthrough
- III. Second Generation Copper-Catalyzed Aerobic Oxidation Protocol
 - A. Unusual Reactivity of Hydrazines. The Second Breakthrough
 - B. A Mechanistic Hypothesis
 - C. Supporting Experiments
 - D. Tuning the Hydrazine Structure
- IV. Third Generation Copper-Catalyzed Aerobic Oxidation Protocol
 - A. Variation in the Structure of the Base
 - B. A Unique Solvent Effect
- V. Towards a Truly Efficient, Aerobic, Catalytic Oxidation Protocol
 - A. ^tBuOK: A Unique Base
 - B. The Problem of Aliphatic Primary Alcohols
 - C. Remarkable Effect of Heterocyclic Amines
 - D. A Fully Integrated Mechanism
- References

I. Introduction

The transformation of alcohols into aldehydes and ketones is of paramount importance in organic chemistry, both for laboratory-scale experiments and in the manufacturing processes (1). Unfortunately, the vast majority of the common oxidants have to be used at least in stoichiometric amount. Moreover, they are usually hazardous or toxic and generate large quantities of noxious by-products (2). Whilst many ecologically benign processes have been developed for the reduction of carbonyl derivatives (3), similar procedures have been far less investigated for the oxidation of alcohols (4).

Despite their obvious economical and ecological importance, few catalytic systems are available for the transformation of alcohols into aldehydes and ketones, using molecular oxygen or air as the ultimate, stoichiometric oxidant (5). Moreover, most of the currently available catalytic oxidation processes suffer from severe limitations, being usually only effective with reactive alcohols, such as benzylic and allylic ones, or requiring high pressures, temperatures, and catalyst loading.

In this chapter, we wish to summarize our work on the discovery and optimization studies of a novel and ecologically friendly, catalytic aerobic protocol for the efficient oxidation of alcohols **1** into carbonyl derivatives **2** (Fig. 1) (6).

During the establishment of the scope and limitations of this useful catalytic process, some mechanistic studies have been performed that allowed us to propose a plausible catalytic cycle rationalizing our observations.

II. First Generation Copper-Catalyzed Aerobic Oxidation Protocol

A. TESTING THE RIVIÈRE AND JALLABERT SYSTEM

Our own work in the area of aerobic oxidations was inspired by the exquisite research performed on the structure and reactivity of the binuclear copper proteins (7), hemocyanin and tyrosinase, and by the seminal contribution of Rivière and Jallabert (8). These two authors have shown that the simple copper complex $\text{CuCl} \cdot \text{Phen}$ ($\text{Phen} = 1,10\text{-phenanthroline}$) promoted the aerobic oxidation of benzylic alcohols to the corresponding aromatic aldehydes and ketones (Fig. 2).

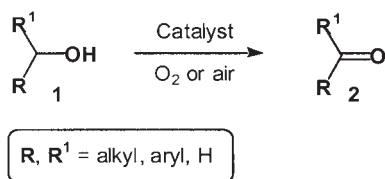


FIG. 1.

Unfortunately, two equivalents of the copper complex have to be used to achieve good conversions and the system is severely limited to benzylic substrates. Aliphatic alcohols proved to be either unreactive or underwent competing C–C bond cleavage (9).

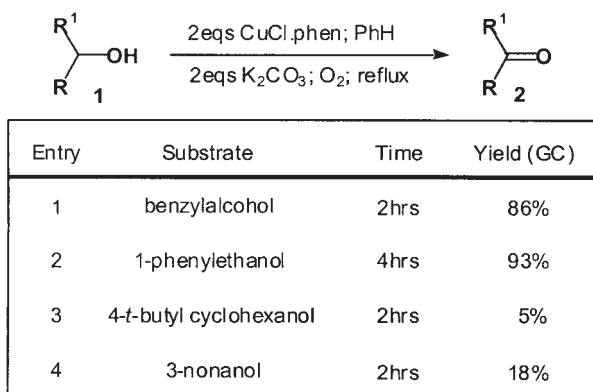


FIG. 2.

Our fascination for the Rivière and Jallabert procedure prompted us to reinvestigate this system and to modify various parameters with the hope of achieving catalyst turnover and establishing a useful and efficient aerobic protocol for the oxidation of all classes of alcohols into carbonyl derivatives.

Our initial experiments were performed on *p*-chlorobenzyl alcohol and employed two equivalents of CuCl·Phen. It was rather disappointing to find that, beside NaOAc, all the other bases tested were far less efficient than K₂CO₃ (10). However, during the course of these optimization studies, a dramatic influence of the solvent on the reaction rate was uncovered. For example, a 3–4-fold acceleration was obtained when toluene was substituted for benzene. In contrast, replacing benzene by *m*- or *p*-xylene resulted in a decrease in the rate

of the reaction. Although it is difficult to offer a rational explanation for the profound effect displayed by minute changes in the structure of the solvent, it is quite reasonable to assume that the coordinating properties of these aromatic solvents may alter significantly the stability and reactivity of the copper complexes (11). Finally, it was also discovered that molecular oxygen could be replaced by air, a more readily available and inexpensive stoichiometric oxidant (12).

B. The FIRST BREAKTHROUGH

The real breakthrough was achieved when it was decided to lower the amount of the catalyst (Fig. 3). Under the original Rivière and Jallabert conditions (2 equiv CuCl·Phen; **benzene**) any attempt to decrease the concentration of the catalyst resulted in a disastrous curtailment in the reaction conversion. However, **in toluene**, reducing the quantity of the copper chloride·Phen complex did not impair the oxidation of the benzylic alcohol. Although the reaction took longer to reach completion, **quantitative formation of *p*-chlorobenzaldehyde could be accomplished using as little as 0.05 equiv of the catalyst.**

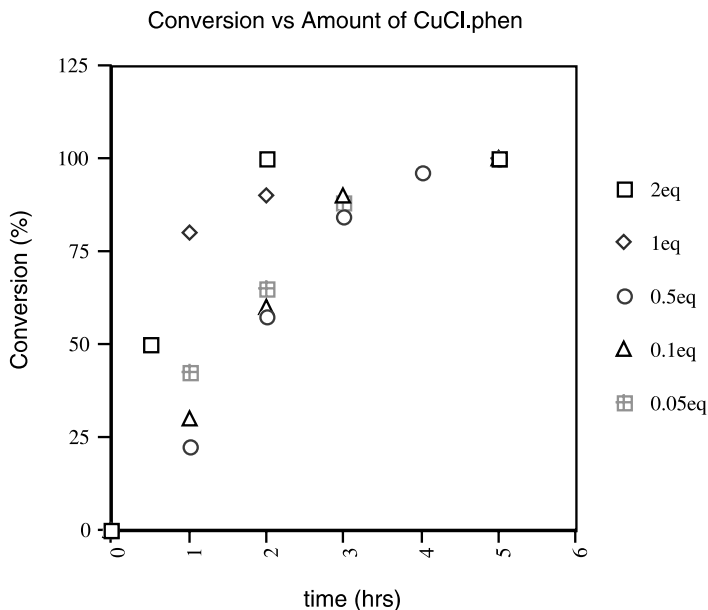


FIG. 3.

Unfortunately, this initial catalytic system proved among other things, to be severely restricted to benzylic alcohols. Based upon previous work in the biochemistry of hemocyanins and tyrosinases (7), a reasonable mechanism for this aerobic oxidation could be envisioned, in which the μ^2 -peroxide **6** occupies a cardinal position (Fig 4). This intermediate **6** can be formed by two different pathways: (1) either by the displacement of the chloride ion in complex **3** by the alcohol nucleophile (13), followed by dimerization in the presence of O_2 or (2) by the initial formation of a chloro *bis*-copper peroxide **4** followed by the exchange of the chloride substituent for the alcohol ligand. The loaded μ^2 -peroxide **6** can then undergo homolytic cleavage of the labile O–O bond and generate the reactive species **7**. Intramolecular hydrogen abstraction leads to the copper-bound carbonyl derivative **8** with concomitant reduction of Cu^{II} (or Cu^{III}) to Cu^I . Finally, ligand

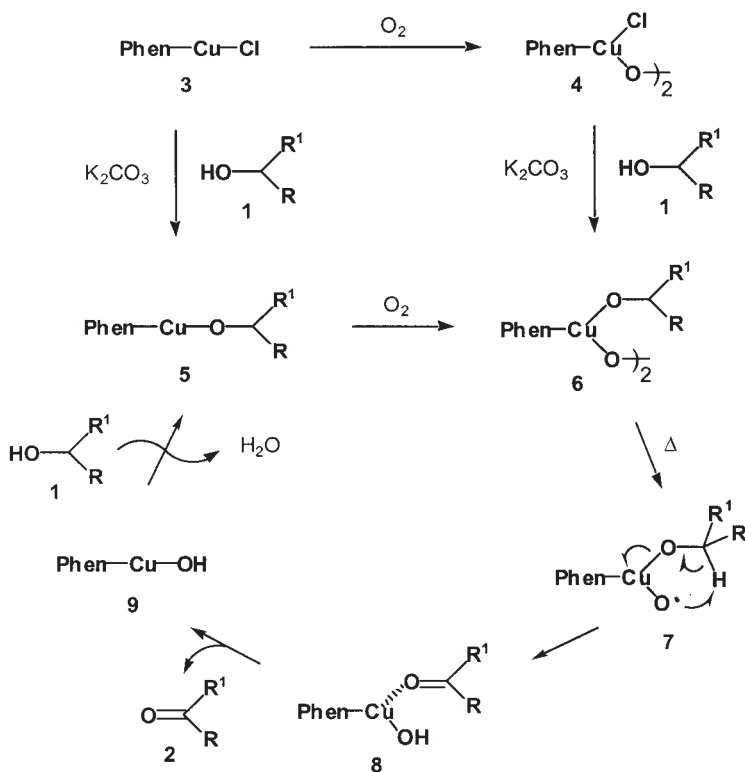


FIG. 4.

exchange with the starting alcohol and release of H₂O completes the catalytic cycle (Fig. 4).

Such a simple mechanistic proposal accommodated the observation that highly activated, benzylic alcohols were good substrates due to the enhanced lability of their α -hydrogen atoms. In contrast, aliphatic alcohols are far less reactive towards H-radical abstraction and, accordingly, poor conversions should ensue. However, it was rather disturbing to note that allylic alcohols, such as geraniol and nerol, displayed poor reactivity in this system. Furthermore, it was observed that the aerobic oxidation of aliphatic alcohols invariably resulted in the rapid formation of a green copper(II) salt, with concomitant deactivation of the catalyst.

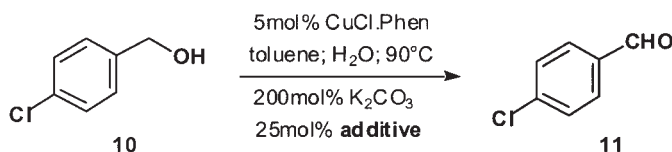
III. Second Generation Copper-Catalyzed Aerobic Oxidation Protocol

A. UNUSUAL REACTIVITY OF HYDRAZINES. THE SECOND BREAKTHROUGH

The previous observation strongly suggested that the regeneration of the active copper(I) species was a serious predicament in the oxidation of aliphatic alcohols. It was therefore decided to test the effect of various reductants in this aerobic oxidation reaction. Naturally, we turned to the hydrazine family of reducing agents (Table I) (14).

Remarkably, addition of hydrazine or *N,N*-dimethylhydrazine (20 mol%) to the reaction mixture resulted in a significant enhancement in the rate of the oxidation reaction. The presence of electron-withdrawing groups on the hydrazine led to an even more dramatic improvement both in yield and reaction rate; the oxidation of **10** being virtually complete within 15 min using DEAD–H₂ (Entry 3). Although the efficiency of the hydrazine additive depended to a small extent on steric hindrance, it was largely affected by electronic factors. For example, whilst a small methyl ester substituent proved less efficient than the bulkier ethyl group, a more sterically demanding isopropyl ester only reduced slightly the rate of the reaction; complete conversion being observed in 30 min (Table I, Entries 2, 3, and 4). More importantly, if the ester substituent is replaced by an acyl function, such as acetyl or benzoyl, virtually no oxidation took place, regardless of the *s-cis* or *s-trans* conformation of the acyl group (Table I, Entries 5–7). Having found that

TABLE I
EFFECT OF THE HYDRAZINE ADDITIVES



Entry	Additive	Conversion (%) ^a	
		15 min	30 min
1	Me ₂ NNH ₂	10	39
2	(MeO ₂ CNH-) ₂	31	56
3	(EtO₂CNH-)₂ (DEAD-H₂)	98	> 99
4	(ⁱ PrO ₂ CNH-) ₂ (DIAD-H ₂)	70	99
5	(MeCONH-) ₂	5	5
6	(PhCONH-) ₂	< 1	< 1
7	phthalhydrazide	< 1	< 1

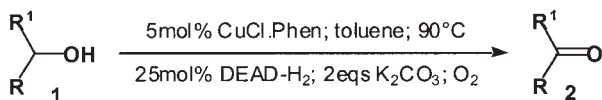
^aThe conversions were determined by ¹H NMR spectroscopy and/or capillary GC analysis.

optimum conversions could be achieved using as little as 25 mol% of DEAD-H₂, we then applied these conditions to the oxidation of a range of representative alcohols. Some pertinent results are collected in Table II.

As can be seen from the Table, both benzylic and allylic alcohols underwent smooth and quantitative transformation into the corresponding aldehyde or ketone within 1 to 4 h. It is noteworthy that the catalyst tolerates sulfur heterocycles (15). The stereochemical integrity of the C–C double bond of the starting allylic alcohols is also retained in the final products, with geraniol giving solely geranial (Table II, Entry 5). Remarkably, trifluoromethyl alcohols and α-ketols are excellent substrates, affording the corresponding trifluoromethyl ketone and 2α-diketone respectively, in high yield (Table II, Entries 3 and 6).

Interestingly, the corresponding azo dicarboxylate (DEAD) could be substituted to the hydrazide derivative (DEAD-H₂) with equal efficiency. Unfortunately, both primary and secondary aliphatic alcohols proved to be poor substrates and only modest conversions could be achieved under these conditions, even when a larger amount of the CuCl·Phen catalyst was employed (Table II, Entries 7 and 8).

TABLE II

COPPER-CATALYSED AEROBIC OXIDATION OF ALCOHOLS USING DEAD-H₂

Entry	Substrate	Product	Conversion ^a
1			100%
2			100%
3			100%
4			100%
5			80% ^b
6			100%
7			40% ^c
8			44% ^d

^aThe conversions were determined by ¹H NMR spectroscopy and/or capillary GC analysis.^bNeral was not detected in this reaction.^c20 mol% CuCl · Phen was employed in this reaction.^d30 mol% CuCl · Phen was employed in this reaction.

B. A MECHANISTIC HYPOTHESIS

A plausible mechanism, involving both the azo and hydrazide derivatives can be formulated as shown in Fig. 5.

In the presence of DEAD-H₂ **12** and base (K₂CO₃), displacement of the chloride ligand by the hydrazide nucleophile takes place, affording the hydrazino copper(I) complex **13** (**16**). A rapid reaction with oxygen then ensues, leading to the μ^2 -peroxo-*bis*-copper(II) derivative **14**. It is believed that upon heating, this complex undergoes homolytic cleavage of the labile O-O peroxidic bond resulting in the generation of the copper-alkoxy radical **15**. Intramolecular hydrogen atom abstraction ensues, affording the capto-datively stabilized nitrogen-centered radical **16**, which is nothing other than the azo-substituted copper(I) hydroxyl species **17**. This particular sequence is thus responsible for the reduction of the copper (II) species to the catalytically active copper(I) complex. Ligand exchange with the alcohol and concomitant release of H₂O then results in the formation of the ternary loaded catalyst **18**. In this complex, both the alcohol and azo-substituents are held together in close proximity

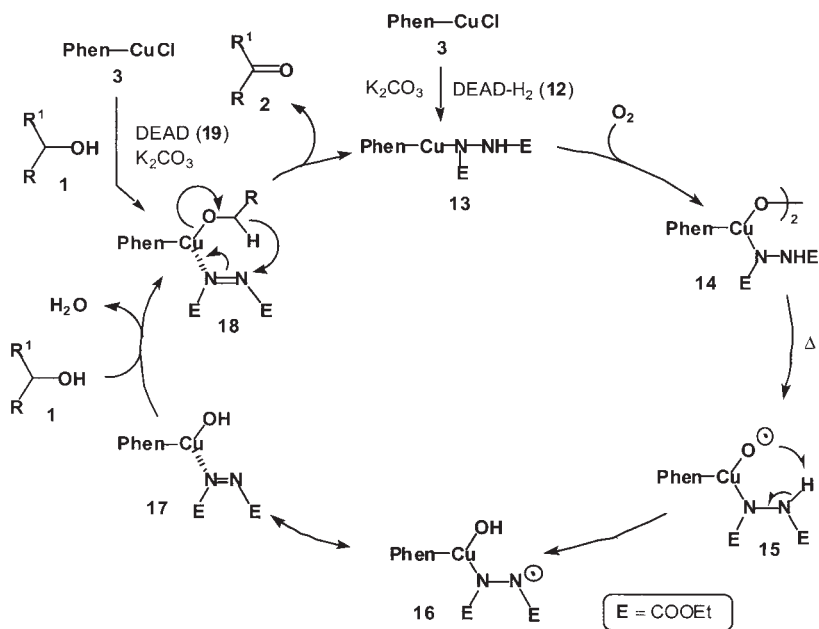


FIG. 5.

by coordination to the copper center. An intramolecular hydrogen shift, akin to the Meerwein–Pondorff–Verley–Oppenauer reaction (18), then takes place affording transiently a carbonyl-bound hydrazido-copper derivative (19).

The aldehyde or ketone can now desorb, leading to the initial copper(I) hydrazide complex **13** which re-enters the catalytic cycle. The replacement of DEAD–H₂ **12** by DEAD **19** can be easily understood when considering this catalytic cycle. Indeed, several entries to the main catalytic cycle are possible, either *via* the hydrazino copper species **13** or *via* the direct formation of the ternary loaded complex **18** from the azo-derivative **19**, Phen·CuCl **3** and the alcohol **1**. The key-role played by the hydrazine or azo compounds can also be readily appreciated when considering the proposed mechanistic rationale. The hydrazide, not only helps in reducing the copper(II) salt to the copper(I) state but, by virtue of its easy passage into the azo derivative, it also acts as a hydrogen acceptor, allowing the efficient oxidation of the alcohol into the carbonyl compound.

Moreover, we believe that the azo form helps in stabilizing several of the reactive copper complexes involved in this catalytic cycle such as the hydroxy copper complex **17**. Thus, we surmise that this novel catalytic, aerobic oxidation procedure for alcohols into carbonyl derivatives proceeds *via* a dehydrogenation mechanism and relies on the effective role of hydrazine or azo compounds as hydrogen shuttles and stabilizing ligands for the various copper complexes (20).

C. SUPPORTING EXPERIMENTS

Further evidence for the occurrence of this dehydrogenation mechanism can be gathered from the following experiments. The hydrazido-copper complex **13** can be independently prepared by reacting Phen·CuCl **3** with the sodium salt of DEAD–H₂. Addition of an alcohol in the absence of O₂ results in no oxidation to the corresponding carbonyl compound. However, when oxygen is admitted into the reaction medium, rapid and quantitative conversion into the desired product is achieved. Moreover, combining an alcohol with Phen·CuCl and DEAD under anaerobic condition led to the rapid oxidation of the starting material and the simultaneous generation of equimolar amounts of DEAD–H₂. The proportion of aldehyde/ketone and hydrazine formed is equivalent to the quantity of starting azo derivative. Independent reaction of the alcohol with DEAD and K₂CO₃ in the absence of air and copper salts results in the quantitative

recovery of the starting alcohol (21). Although we have not yet been able to obtain direct evidence for some of the intermediates postulated in this catalytic scheme, we believe that the above-mentioned experiments lend credit to the involvement of complex 13, 14, and 18 and strongly support our proposed mechanism.

D. TUNING THE HYDRAZINE STRUCTURE

At this stage, two major observations still need to be accounted for: the lack of reactivity of aliphatic substrates and the need for a five-fold excess of DEAD or DEAD-H₂ over CuCl·Phen to achieve quantitative oxidations of benzylic and allylic alcohols.

An interesting clue to these questions was provided when monitoring the fate of the reagents and products involved in the aerobic catalytic oxidation of undecanol to undecanal (Fig. 6) (22).

Whereas the decay of the alcohol follows the expected kinetic course, the formation of the aldehyde shows an abnormal behavior. In the early part of the reaction, the aldehyde formation matches almost perfectly the disappearance of the alcohol. However, after c.a. 50% conversion, it reaches a maximum and then slowly begins to

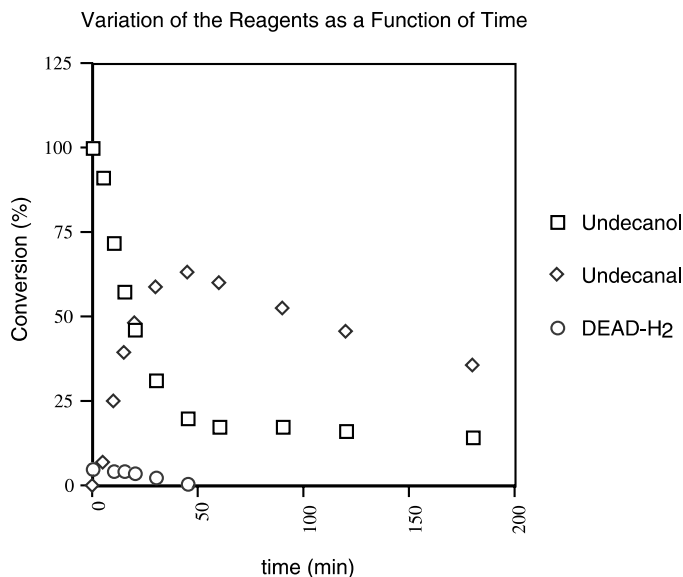


FIG. 6.

decrease. Clearly, a side reaction is consuming the alcohol substrate as soon as the aldehyde concentration attains a critical value. The fate of the DEAD-H₂ additive is even more interesting. In strong contrast to our expectation, the concentration of DEAD-H₂ does not remain constant throughout the course of the reaction but gradually decreases over time. The disappearance of DEAD-H₂ corresponds exactly to the point of maximum aldehyde formation. Thus, the destiny of the aldehyde and the DEAD-H₂ additive are intimately linked and, as the hydrazide is removed from the reaction mixture, the formation of the aldehyde simultaneously stops and its concentration decreases after the hydrazide has been totally consumed. A similar pattern is observed for the related DEAD compound. In this case, however, an initial and extremely rapid transformation of DEAD into DEAD-H₂ takes place. Only the hydrazide can be observed later in the reaction medium. Closer examination of the reaction by-products using stoichiometric DEAD under anaerobic conditions led to the isolation of unexpectedly large quantity of the mixed carbonate **20** (Fig. 7).

Thus, the hydrazide or its azo analogue not only plays a key-role in the catalytic cycle as a hydrogen acceptor and a reductant for the copper catalyst, but it also acts as an acyl transfer reagent generating competitively the undesired mixed carbonate **20**. This by-product presumably originates from the inter- or intra-molecular nucleophilic attack of the alcohol on either the copper-hydrazide or azo complexes **13** or **18** respectively, resulting ultimately in the deactivation of the catalyst. To minimize this undesired *trans*-acylation reaction, sterically demanding azo-derivatives were tested (Fig. 7). Whilst di-isopropyl

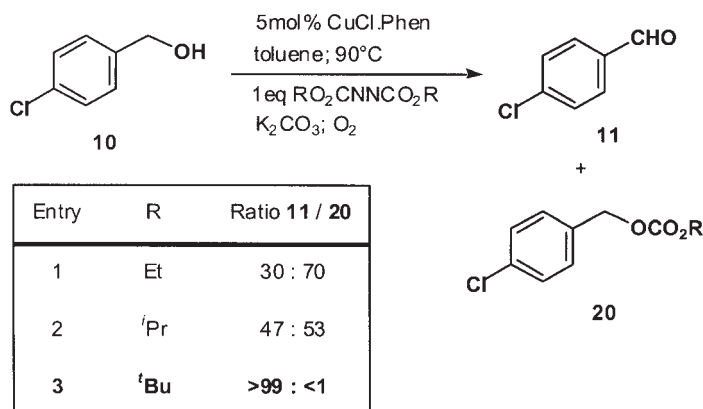


FIG. 7.

azodicarboxylate (DIAD) produced a more favorable aldehyde/carbonate ratio (Fig. 7, Entry 2), we were gratified to find that the corresponding di-tertbutyl azo-dicarboxylate (DBAD) led solely to the formation of the desired oxidation product with no trace of the mixed carbonate contaminant (Fig. 7, Entry 3).

Under these optimized conditions, the aerobic oxidation of alcohols can be efficiently achieved using as little as 5 mol% of the DBAD or DBAD-H₂ additives (Table III).

Using this improved protocol, a variety of allylic, benzylic, and secondary alcohols are now smoothly oxidized to the corresponding carbonyl derivatives in high yield. Unfortunately, primary aliphatic alcohols still appear to be poor substrates and a conversion of only 65% can be achieved before catalyst deactivation (Table III, Entry 9).

Careful analysis of the reaction products revealed the absence of a mixed carbonate akin to **20** even though gradual decomposition of DBAD was again observed (23). This observation suggested that the rather basic reaction conditions might be responsible for the degradation of the azo derivative and that a decrease in the amount of K₂CO₃ is mandatory if better conversions and longer catalyst lifetime are to be attained.

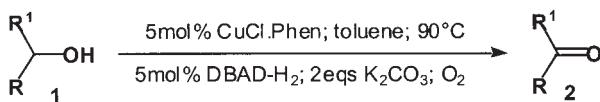
IV. Third Generation Copper-Catalyzed Aerobic Oxidation Protocol

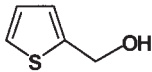
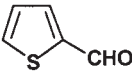
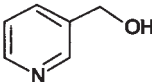
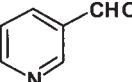
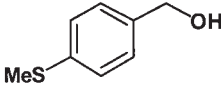
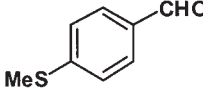

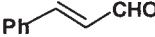
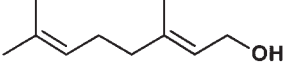
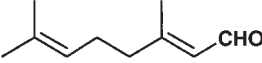
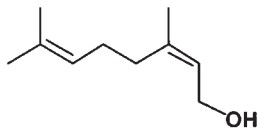
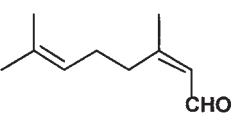
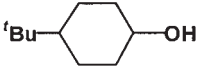
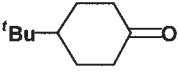
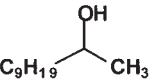
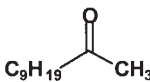
The stringent requirement for 2 equivalents of K₂CO₃ in toluene was puzzling and we initiated some studies in order to understand the role(s) of this heterogeneous base. In particular, we wondered if suitable reaction conditions might be found in which smaller quantities of base could be employed in order to transform our original system into a more ecologically friendly protocol.

A. VARIATION IN THE STRUCTURE OF THE BASE

A variety of other bases (Na₂CO₃, Li₂CO₃, Na₂HPO₄, NaH₂PO₄, Al₂O₃, NaOAc, KOAc, KOH, and CuCO₃) were tested in this aerobic oxidation system. Surprisingly, none proved to be as efficient as K₂CO₃ (24). Examination of the postulated mechanism of this transformation (Fig. 5) suggested a number of possible roles for K₂CO₃ (25). First, K₂CO₃ should act as a base and react with the HCl formed during the initial replacement of the chloride ligand of **3** by the alcohol

TABLE III

COPPER-CATALYZED AEROBIC OXIDATION OF ALCOHOLS USING DBAD-H₂

Entry	Substrate	Product	Yield ^a
1			85%
2			81%
3			92%
4			89%
5			71% ^b
6			73% ^c
7			84% ^d
8			88% ^e
9	$\text{C}_9\text{H}_{19}-\text{CH}_2\text{OH}$	$\text{C}_9\text{H}_{19}-\text{CHO}$	65%

^a All yields refer to pure, isolated compounds.^b Neral was not detected in this reaction.^c Geranial was not detected in this experiment.^d 10 mol% CuCl·Phen and 10 mol% DBAD were used in this reaction.^e 5 mol% DBAD was employed instead of DBAD-H₂.

1 or the hydrazine **12**. However, if this was the sole purpose of K_2CO_3 , then only 5 mol% should actually be necessary in the reaction to fulfill the requirement of catalyst formation.

Second, examination of the oxidation in toluene revealed its heterogeneous nature. Filtration of the dark-brown suspension gave a filtrate devoid of oxidizing activity and a solid material which, once re-suspended in toluene, smoothly oxidized alcohols to the corresponding ketones and aldehydes. It thus appears that K_2CO_3 may also serve as a solid support on which the copper catalyst can be adsorbed. Finally, since water is released during the oxidation process, K_2CO_3 might also be acting as a water scavenger.

The importance of the dehydrating properties of K_2CO_3 was clearly revealed by performing the oxidation reaction using only 10 mol% K_2CO_3 in the presence of an excess of 4 Å MS. Although 4 Å MS proved to be less efficient than K_2CO_3 in trapping the released water (larger loading and longer reaction time are required), the oxidation went smoothly to completion.

B. A UNIQUE SOLVENT EFFECT

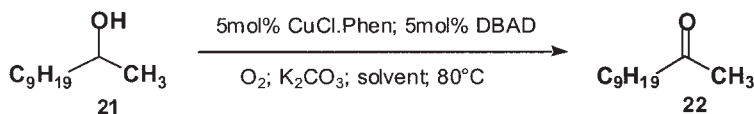
A major breakthrough was accomplished while studying the influence of the solvent on the amount of K_2CO_3 required for the aerobic oxidation of 2-undecanol into 2-undecanone (Table IV) (26).

Whereas in toluene, 2 equivalents of K_2CO_3 are necessary to achieve complete conversion of alcohol **21** into ketone **22** (Table IV, Entries 1–3), we were quite surprised to find that only a mediocre yield of the desired ketone was obtained in fluorobenzene (Table I, Entry 4) under comparable conditions (27). Unexpectedly, **lowering the amount of K_2CO_3 dramatically increased the conversion of 21 into 22, reaching a 100% conversion even when only 25 mol% of the base was employed** (Table IV, Entry 7). Under these conditions, 2-undecanone **22** could be isolated in up to 99% yield. These optimized conditions were then applied to the aerobic oxidation of a variety of structurally representative alcohols. The results are summarized in Table V.

It is quite remarkable that essentially every type of alcohol is smoothly oxidized into the corresponding carbonyl derivative in high yield and with good to complete conversion. Under these conditions, primary aliphatic, allylic, and benzylic alcohols afford the expected aldehydes and secondary alcohols are smoothly transformed into ketones. Geraniol produces geranial and nerol gives neral with no detectable loss of the geometric integrity of the C–C double bond

TABLE IV

SOLVENT AND BASE EFFECTS IN THE AEROBIC OXIDATION OF 2-NONANOL



Entry	Solvent	K ₂ CO ₃	Conversion ^a	Yields ^b
1	CH ₃ C ₆ H ₅	2 equiv	90%	88%
2	CH ₃ C ₆ H ₅	1 equiv	70%	61% ^c
3	CH ₃ C ₆ H ₅	0.5 equiv	< 20%	11%
4	FC ₆ H ₅	2 equiv	50%	44% ^d
5	FC ₆ H ₅	1 equiv	100%	94%
6	FC ₆ H ₅	0.5 equiv	100%	> 99%
7	FC ₆ H ₅	0.25 equiv	100%	> 99%
8	FC ₆ H ₅	0.1 equiv	60%	58% ^e

^aThe % conversion was measured by ¹H NMR spectroscopy and by capillary GC analysis.^bAll yields are for pure, isolated compounds.^cThe reaction was stopped after 5 h.^dThe reaction was stopped after 3 h.^eThe reaction was stopped after 8 h.

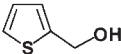
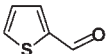
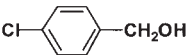
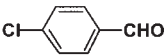
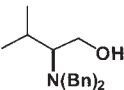
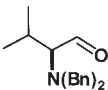
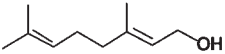
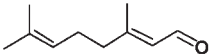
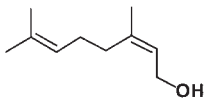
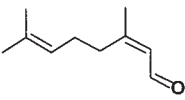
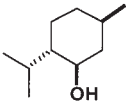
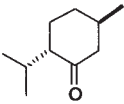
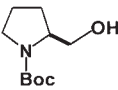
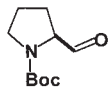
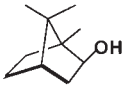
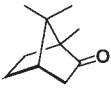
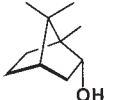
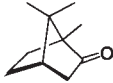
(Table V, Entries 5 and 6). The catalyst tolerates both sulfur and nitrogen substituents (Table V, Entries 2, 4, and 8). Protected β-amino-alcohols are smoothly converted into the corresponding aldehydes without detectable racemisation (Table V, Entries 4 and 8) (28). It is also noteworthy that the reaction conditions are sufficiently mild as to be compatible with the Boc protecting group (Table V, Entry 8).

Interestingly, both *endo*- and *exo*-borneol are oxidized to camphor at the same rate, despite the enormous difference in the steric environment of these two alcohols (Table V, Entries 9 and 10).

Using our new protocol, only 25 mol% of K₂CO₃ is required for optimum activity. This unexpected breakthrough thus provides us with a novel system which is completely catalytic in all its ingredients. Such a low loading of the heterogeneous base appears to be highly specific to fluorobenzene as the solvent (compare Table IV, Entries 1–3 with Entries 4–8). The property of fluorobenzene which is responsible for its unequalled behavior is not yet known (29,30) although we believe that it is a combination rather than a single factor that gives fluorobenzene its uniqueness.

When less than 25 mol% of K₂CO₃ was employed in this protocol (Table IV, entry 8), the reaction became rather sluggish and proved

TABLE V
AEROBIC, CATALYTIC OXIDATION OF ALCOHOLS IN FLUOROBENZENE

Entry	Substrate	Product	Yield ^a
1	$\text{C}_9\text{H}_{19}\text{CH}_2\text{OH}$	$\text{C}_9\text{H}_{19}\text{CHO}$	65% ^b
2			85%
3			87%
4			85% ^c
5			86% ^d
6			80% ^d
7			75% ^d
8			80% ^e
9			93%
10			90%

^a All yields are for pure, isolated compounds. Complete conversions were achieved unless specified.

^b In this case, the reaction was stopped after 70% conversion. The recovered alcohol amounted to ~30%.

^c No racemisation was observed in this oxidation reaction. The aldehyde was reduced to the alcohol (LiAlH_4 in THF) and the ee of the resulting amino alcohol was measured by HPLC analysis: Daicel chiralpak column; 2% i -PrOH in hexane; 1 mL/min; $T = 20^\circ\text{C}$; $\lambda = 254\text{ nm}$; (*R*)- $\text{Bn}_2\text{Valinol}$: 11.16 min; (*S*)- $\text{Bn}_2\text{Valinol}$: 12.70 min; ee > 99%.

^d No double bond isomerisation took place under these conditions.

^e No racemisation was observed in this oxidation reaction. The ee was measured by chiral GC (CP-Chiral-Dex CB, 25m; $\phi = 0.25\text{ mm}$, $\text{DF} = 0.25\mu\text{L}$, 130°C for 12 min then 1°C per min) of the derived bis-Boc-prolinol obtained by LiAlH_4 reduction of Boc-prolinal followed by derivatisation with Boc_2O ($R_t(R)$ -enantiomer: 43.1 min, $R_t(S)$ -enantiomer: 43.6 min).

to be difficult to transpose to other alcohols. The search for an alternative to K_2CO_3 then became one of our prime objectives.

V. Towards a Truly Efficient, Aerobic, Catalytic Oxidation Protocol

A. t BuOK: A UNIQUE BASE

After screening unsuccessfully a number of different additives, we were gratified to find that t BuOK uniquely satisfied our requirements. Interestingly, we also noticed that the mode of addition of the various reaction partners played a crucial role in the success of this new procedure (Fig. 8).

Thus, it appeared that addition of the base to the pre-formed $CuCl \cdot Phen/DBAD$ complex resulted in rapid deactivation of the system, as demonstrated by the poor conversion of 2-undecanol **21** into the corresponding ketone **22** (Fig. 8, Entry 1) (31). On the other hand, adding t BuOK to $CuCl \cdot Phen$, **in the presence of 2-undecanol**, followed by the addition of DBAD and heating under a gentle stream of oxygen led to complete conversion of **21** into **22** (Fig. 8, Entry 2). This efficient, catalytic, procedure was then applied to a range of representative alcohols. Some selected examples are shown in Table VI.

As can be seen from Table VI, secondary aliphatic, allylic, and benzylic alcohols are all quantitatively converted into the corresponding carbonyl derivatives. It is interesting to note that no epimerization of menthone takes place under these conditions (Entry 3). Furthermore, rather hindered decaline derivatives (Entry 5) are also smoothly oxidized.

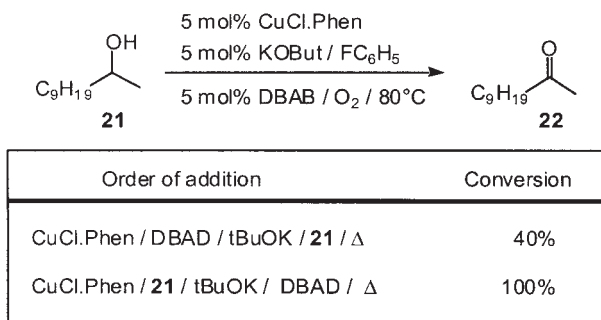
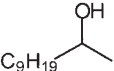
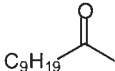
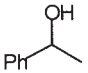
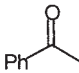
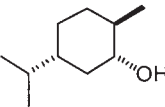
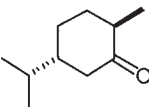
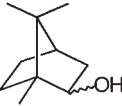

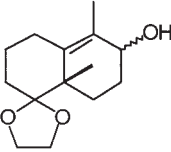
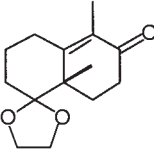
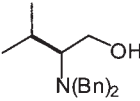
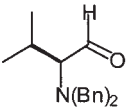
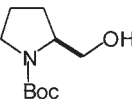
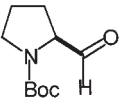


FIG. 8.

TABLE VI
AEROBIC OXIDATION OF ALCOHOLS USING t BuOK^a

Entry	Substrate	Product	Yield ^{b,c}
1			90%
2			93%
3			92%
4			93% ^d
5			84% ^{e,f}
6			84% ^{g,h}
7			97% ^h

^aThe reaction conditions are described in Ref. (32).

^b All yields refer to pure, isolated products.

^cUnless otherwise stated, all the conversions are quantitative.

^dThe oxidation was performed on a 80/20 mixture of borneol and *iso*-borneol.

^eThe oxidation was effected on a 30/70 mixture of axial and equatorial isomers.

^fThe conversion amounted to 95% in this case.

^g After silica gel column chromatography.

^h No racemisation was detected.

These observations imply that the Cu oxidant is little sensitive to the steric surroundings of the hydroxyl function. The scope of the reaction can be further extended to protected primary β -amino alcohols with equal efficiency. The oxidation of dibenzyl valinol (Entry 6), which contains a tertiary nitrogen atom, proceeds in excellent yield. Moreover, the involvement of a neutral medium is ideally demonstrated by the lack of racemization of both dibenzyl valinal and Boc-prolinal (Entries 6 and 7). Purification of this latter product, which was prepared on a gramm-scale, necessitated only a simple filtration (32).

It is important to note that this new protocol operates under completely neutral conditions. Indeed, addition of t BuOK to the copper chloride·Phen/alcohol mixture generates the corresponding copper alkoxide. From that point onward, the oxidation proceeds under neutral conditions since all the base has been consumed. It is noteworthy that sensitive substrates do not undergo epimerization or racemization.

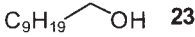
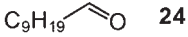
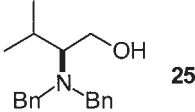
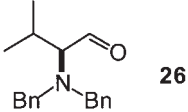
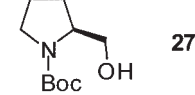
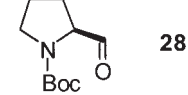
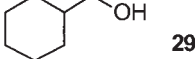
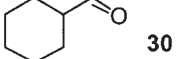
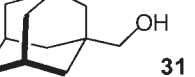
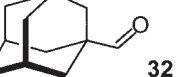
B. The PROBLEM OF ALIPHATIC PRIMARY ALCOHOLS

Unfortunately, even using this optimized procedure, we were not able to improve the conversion of primary alcohols into the corresponding aldehydes. However, close examination of the oxidation behavior of several primary aliphatic alcohols revealed intriguing features (Table VII). Whilst poor conversion of 1-decanol **23** to decanal **24** was achieved (Table VII, Entry 1), dibenzyl leucinol **25** and Boc-prolinol **27** were quantitatively transformed into the corresponding aldehydes (Table VII, Entries 2 and 3). The enhanced reactivity of **25** and **27** could be due either to an increased steric effect at the α -carbon center, to an electronic influence of the α -nitrogen substituent or to a combination of both. To test the importance of steric hindrance, the aerobic oxidation of cyclohexane methanol **29** and adamantane methanol **31** was carried out. Much to our surprise, oxidation of **29** afforded **30** in 70% conversion (Table VII, Entry 4) and transformation of **31** to **32** proceeded with 80% conversion (Table VII, Entry 5). Clearly increased substitution at the α -position favors the oxidation of primary aliphatic alcohols, although the conversions are still not optimum.

C. REMARKABLE EFFECT OF HETEROCYCLIC AMINES

In order to improve this transformation, a variety of selected additives were tested in the aerobic oxidation of 1-decanol **23**. The high

TABLE VII
COPPER-CATALYSED AEROBIC OXIDATION OF SELECTED PRIMARY ALCOHOLS

Entry	Substrate	Product	Yield ^{a,b}
1	 23	 24	(60%) 51%
2	 25	 26	(100%) 84%
3	 27	 28	(100%) 97%
4	 29	 30	(70%) 64%
5	 31	 32	(80%) 77%

^aValues in parentheses refer to the percentage conversion of the starting material.

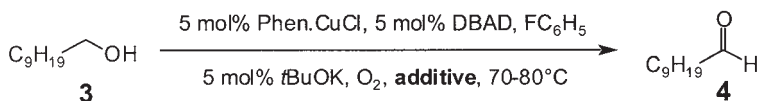
affinity of heterocyclic amines for copper salts, coupled with their ubiquitous presence as ligands in biologically-active copper-containing proteins (33), prompted us to investigate them initially. Some selected results are collected in Table VIII.

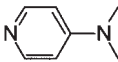
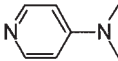
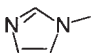
As can be seen from Table VIII, the conversion of 1-decanol **23** to the desired aldehyde **24** proceeded poorly in the absence of additive (Table VIII, Entry 1). In the presence of 5 mol% of 4-DMAP (4-dimethylaminopyridine), a significant increase in the transformation of **23** to **24** was observed (Table VIII, Entry 2) and complete conversion was eventually reached using 10 mol% of 4-DMAP (Table VIII, Entry 3). Interestingly, only 7 mol% of NMI (*N*-Methyl imidazole) was required to transform **23** completely into **24** (Table VIII, Entry 4).

These conditions were next applied to the aerobic oxidation of a variety of primary alcohols. A selection of pertinent examples is displayed in Table IX.

As can be seen from Table IX, all the primary alcohols employed were quantitatively converted into the corresponding aldehydes

TABLE VIII
INFLUENCE OF ADDITIVES ON THE AEROBIC OXIDATION OF 1-DECANOL



Entry	Additive	Amount	Conversion ^a
1	none	none	60%
2		5 mol%	80%
3		10 mol%	100%
4		7 mol%	100%

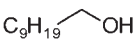
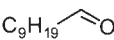
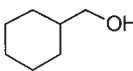
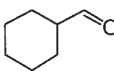

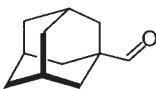

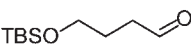
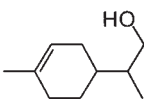
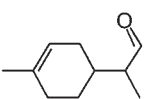
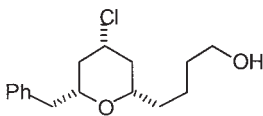
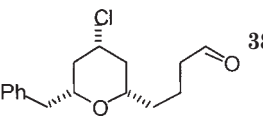
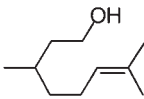
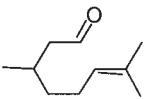

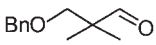
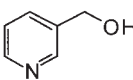
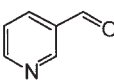
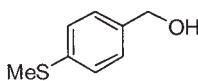
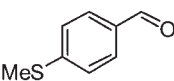
^aThe conversions were measured by capillary gas chromatography using the internal standard method.

with 100% selectivity. It is noteworthy that no trace of carboxylic acid was observed under these aerobic conditions. The reaction tolerates both simple aliphatic primary alcohols (Table IX, Entry 1) and more hindered derivatives (Table IX, Entries 2 and 3) as well as various protecting groups (Table IX, Entries 4 and 8). Simple alkenes are unaffected (Table IX, Entry 5) and base-sensitive substrates are smoothly oxidized (Table IX, Entry 6). It is interesting to note that under these neutral conditions, highly acid sensitive substrates are also quantitatively converted into the corresponding aldehydes (Table IX, Entry 7). Finally, a significant impediment pertaining to all the other reported aerobic oxidation protocols is their inability to oxidize alcohols possessing a chelating function, a nitrogen atom or a sulfur substituent. Such is not the case for the copper catalyst which transforms the strongly coordinating substrate **41** quantitatively into the aldehyde **42** (Table IX, Entry 8) and tolerates both heteroatoms (Table IX, Entries 9 and 10).

The remarkable effect of 4-DMAP and NMI on the ability of the copper catalyst to oxidize efficiently a wide range of primary alcohols is surprising and the origin of this effect was investigated, initially using the mechanistically simpler anaerobic system. In the absence of

TABLE IX

EFFICIENT, AEROBIC, CATALYTIC OXIDATION OF PRIMARY ALCOHOLS

Entry	Substrate	N°	Product	N°	Yield ^a
1		23		24	95%
2		29		30	93%
3		31		32	95%
4		33		34	94%
5		35		36	94%
6		37		38	83%
7		39		40	82%
8		41		42	97%
9		43		44	93%
10		45		46	95%

^a All yields are for pure, isolated products.

oxygen and NMI, 1-decanol was smoothly and quantitatively oxidized to decanal. Addition of 7 mol% NMI did not improve the conversion, nor the rate of the reaction; rather, NMI had a slightly retarding effect (34).

D. A FULLY INTEGRATED MECHANISM

In order to reconcile these observations with the previously established catalytic cycle for the aerobic oxidation of alcohols using the $\text{CuCl} \cdot \text{Phen}/\text{DBAD}$ system, a new catalytic manifold has to be operative in the presence of NMI (Fig. 9).

The productive catalytic cycle begins with the ternary loaded complex **A**. Intramolecular hydrogen transfer from the alkoxy substituent to the azo ligand generates copper(I) hydrazide **B**. Subsequent release of the aldehyde produces complex **C**, which is rapidly captured by oxygen, affording Cu(II) hydrazide derivative **D**. Reorganisation of **D** under the thermal conditions of the reaction leads to the hydroxy copper(I) species **E**. Finally, ligand exchange and elimination of water regenerates the active, loaded complex **A** and a new catalytic cycle ensues. Amongst the various active species involved in this system, complex **C**, bearing an empty coordination site, appears to be the most likely candidate to suffer a competitive deactivation by the primary alcohols (35).

Indeed, whilst **C** usually reacts rapidly with oxygen, it can occasionally undergo competitive coordination to an alcohol, producing the copper derivative **F** that might undergo hydrogen transfer and loss of the hydrazine substituent, resulting in the inactive complex **G** (36,37).

In the case of secondary alcohols, competitive coordination of the OH function and oxygen to **C** largely favors the latter and the

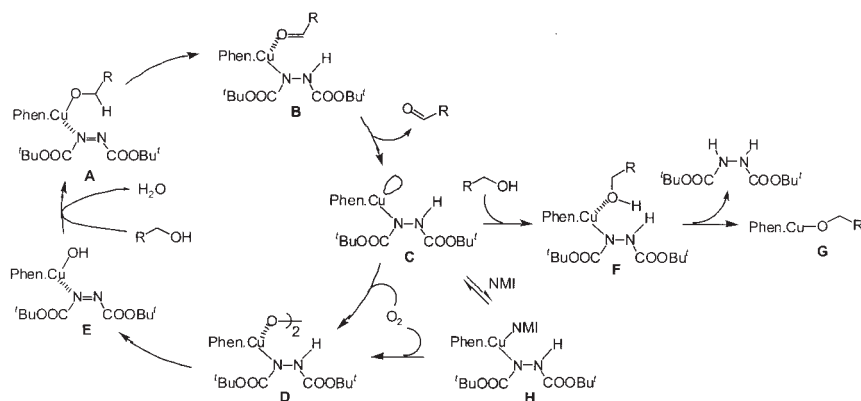


FIG. 9.

bis-copper peroxide **D** is formed. However, when primary aliphatic alcohols are employed, coordination of the less hindered OH group now becomes competitive. The formation of inactive complex **G** gradually depletes the catalytic cycle in the active oxidizing species and the reaction comes to a halt. This mechanistic proposal also explains the observed increased conversions when employing more hindered aliphatic primary alcohols.

The role of NMI and 4-DMAP would thus be to bind rapidly to copper complex **C**, generating intermediate **H** which is probably in equilibrium with **C**. Such coordination would preclude the competitive addition of the alcohol and suppress the undesired formation of the inert derivative **G** (38).

In summary, we have discovered a simple and environmentally friendly, catalytic aerobic protocol for the efficient oxidation of a wide variety of alcohols into aldehydes and ketones. This novel catalytic system uses oxygen or air as the stoichiometric oxidant and releases water as the sole by-product. We have also shown that the use of the simple and inexpensive additive NMI, strongly modified the course of the copper-catalyzed aerobic oxidation of primary aliphatic alcohols. Under these novel conditions, a wide range of primary substrates could be transformed efficiently into the corresponding aldehydes with no trace of over-oxidized carboxylic acids being detected. Moreover, the neutral conditions employed are compatible with base and acid sensitive substrates. Furthermore, these results have shed some light on an unsuspected decomposition pathway, the inhibition of which held the key to a highly successful aerobic oxidation procedure for primary alcohols. To the best of our knowledge, the copper-catalyzed aerobic system is thus far the only catalytic procedure that is able to oxidize, with equal efficiency, substrates belonging to all the different classes of alcohols.

Although much remains to be done, we believe that a genuine leap has been realized in the establishment of mild and functionally tolerant, ecologically benign, catalytic systems for the oxidation of alcohols into carbonyl derivatives.

ACKNOWLEDGMENTS

This contribution is dedicated in memory of Professor Dieter Sellman who left us far too soon. Financial support was provided by Zeneca Limited, through the Zeneca Strategic Research Fund. IEM is grateful to Zeneca for receiving the *Zeneca Fellowship* (1994–1997) and the 2003 Astra-Zeneca European Lectureship.

REFERENCES

1. For general reviews on oxidation reactions see: (a) Larock, R. C. "*Comprehensive Organic Transformations*"; VCH Publishers Inc.: New York, **1989**, p. 604; (b) Procter, G. "*Comprehensive Organic Synthesis*"; Vol. 7; Ed. Ley, S. V.; Pergamon: Oxford, **1991**, p. 305; (c) Ley, S. V.; Madin, A. "*Comprehensive Organic Synthesis*"; Vol. 7; Eds. Trost, B. M.; Fleming, I.; Pergamon: Oxford, **1991**, p. 251; (d) Lee, T. V. "*Comprehensive Organic Synthesis*"; Vol. 7; Eds. Trost, B. M.; Fleming, I.; Pergamon: Oxford, **1991**, p. 291.
2. Trahanovsky, W. S. "*Oxidation in Organic Chemistry*"; Eds. Blomquist, A. T.; Wasserman, H. Part A–D, Acad. Press.
3. Noyori, R.; Hashigushi, S. *Acc. Chem. Res.* **1997**, *30*, 97, and references cited therein.
4. (a) Sheldon, R. A.; Kochi, J. K. "*Metal-Catalyzed Oxidations of Organic Compounds*", Academic Press: New York, **1981**; (b) Ley, S. V.; Norman, J.; Griffith, W. P.; Marsden, S. P. *Synthesis* **1994**, 639; (c) Murahashi, S.-I.; Naota, T.; Oda, Y.; Hirai, N. *Synlett* **1995**, 733; (d) Krohn, K.; Vinke, I.; Adam, H. *J. Org. Chem.* **1996**, *61*, 1467; (e) Strukul, G. "*Catalytic Oxidations with Hydrogen Peroxide as Oxidant*", Kluwer Academic Publishers: London, **1992**; (f) Sato, K.; Takagi, J.; Aoki, M.; Noyori, R. *Tetrahedron Lett.* **39**, 1998, 7549; (g) Sato, K.; Aoki, M.; Noyori, R. *Science* **1998**, *281*, 1646; (h) Berkessel, A.; Sklorz, C. A. *Tetrahedron Lett.* **1999**, *40*, 7965.
5. (a) Sheldon, R. A. "*Dioxygen Activation and Homogeneous Catalytic Oxidation*"; Ed. Simandi, L. L.; Elsevier: Amsterdam, **1991**, p. 573; (b) James, B. R. "*Dioxygen Activation and Homogeneous Catalytic Oxidation*"; Ed. Simandi, L. L.; Elsevier: Amsterdam, **1991**, p. 195; (c) Bäckvall, J.-E.; Chowdhury, R. L.; Karlsson, U. *J. Chem. Soc., Chem. Commun.* **1991**, 473; (d) Iwahama, T.; Sakaguchi, S.; Nishiyama, Y.; Ishii, Y. *Tetrahedron Lett.* **1995**, *36*, 6923; (e) Mandal, A. K.; Iqbal, J. *Tetrahedron* **1997**, *53*, 7641; (f) Masutani, K.; Uchida, T.; Irie, R.; Katsuki, T. *Tetrahedron Lett.* **2000**, *41*, 5119; (g) Lee, M.; Chang, S. *Tetrahedron Lett.* **2000**, *41*, 7507; (h) Sheldon, R. A.; Arends, I. W. C. E.; Dijkman, A. *Catal Today* **2000**, *57*, 157; (i) Matsumoto, M.; Ito, S. *J. Chem. Soc., Chem. Commun.* **1981**, 907; (j) Hinzen, B.; Lenz, R.; Ley, S. V. *Synthesis* **1998**, 977; (k) Bleloch, A.; Johnson, B. F. G.; Ley, S. V.; Price, A. J.; Shephard, D. S.; Thomas, A. W. *Chem. Commun.* **1999**, 1907; (l) Iwahama, T.; Sukaguchi, S.; Nishiyama, Y.; Ishii, Y. *Tetrahedron Lett.* **1998**, *36*, 6923; (m) Iwahama, T.; Yoshino, Y.; Keitoku, T.; Sakaguchi, S.; Ishii, Y. *J. Org. Chem.* **2000**, *65*, 6502; (n) Blackburn, T. F.; Schwartz, J. *J. Chem. Soc., Chem. Commun.* **1997**, 157; (o) Kaneda, K.; Fujie, Y.; Ebitani, K. *Tetrahedron Lett.* **1997**, *38*, 9023; (p) ten Brink, G.-J.; Arends, I. W. C. E.; Sheldon, R. A. *Science* **2000**, *287*, 1636; (q) Hallman, K.; Moberg, C. *Adv. Synth. Catal.* **2001**, *343*, 260; (r) Kakiuchi, N.; Maeda, Y.; Nishimura, T.; Uemura, S. *J. Org. Chem.* **2001**, *66*, 6620; (s) Schultz, M. J.; Park, C. C.; Sigman, M. S. *Chem. Commun.* **2002**, 3034.
6. (a) Markó, I. E.; Giles, P. R.; Tsukazaki, M.; Brown, S. M.; Urch, C. J. *Science* **1996**, *274*, 2044; (b) Markó, I. E.; Giles, P. R.; Tsukazaki, M.; Chellé-Regnaut, I.; Urch, C. J.; Brown, S. M. *J. Am. Chem. Soc.* **1997**, *119*, 12661; (c) Markó, I. E.; Tsukazaki, M.; Giles, P. R.; Brown, S. M.; Urch, C. J. *Angew. Chem. Int. Ed., Engl.* **1997**, *36*, 2208; (d) Markó, I. E.; Giles, P. R.; Tsukazaki, M.; Brown, S. M.; Urch, C. J. "*Transition Metals for Organic Synthesis*"; chapter 2.12, Vol. 2; Eds. Beller, M.; Bolm, C.; **1998**, p. 350; (e) Markó, I. E.; Gautier, A.; Chellé-Regnaut, I.; Giles, P. R.; Tsukazaki, M.; Urch, C. J.; Brown, S. M. *J. Org. Chem.* **1998**, *63*, 7576; (f) Markó, I. E.; Gautier, A.; Muttonkole, J.-L.; Dumeunier, R.; Ates, A.; Urch, C. J.; Brown, S. M. *J. Organomet.*

- Chem.* **2001**, *624*, 344; For an independent report of the aerobic TPAP catalysed oxidation of alcohols see: Lenz, R.; Ley, S. V. *J. Chem. Soc., Perkin I* **1997**, 3291.
7. For excellent reviews on the formation isolation and reactions of dinuclear copper (II) peroxides see: (a) Karlin, K. D.; Gultneh, Y. *Progress in Inorganic Chemistry* **1987**, *35*, 219–327; (b) Zuberbühler, A. D. “*Copper Coordination Chemistry: Biochemical and Inorganic Perspectives*”; Eds. Karlin, K. D.; Zubieta, J.; Adenine: Guilderland, New York, **1983**; (c) Sakharov, A. M.; Skibida, I. P. *Kinetics and Catalysis* **1988**, *29*, 96–102; (d) Tyleklar, Z.; Jacobson, R. R.; Wei, N.; Murthy, N. N.; Zubieta, J.; Karlin, K. D. *J. Am. Chem. Soc.* **1993**, *115*, 2677–2689; (e) Kitajima, N.; Fujisawa, K.; Fujimoto, C.; Moro-oka, Y.; Hashimoto, S.; Kitagawa, T.; Toriumi, K.; Tatsumi, K.; Nakamura, A. *ibid* **1992**, *114*, 1277–1291; (f) Fox, S.; Nanthakumar, A.; Wikstrom, M.; Karlin, K. D.; Blackburn, N. J. *ibid.* **1996**, *118*, 24–34; (g) Solomon, E. I.; Sundaram, U. M.; Machonkin, T. E. *Chem. Rev.* **1996**, *96*, 2563–2605.
 8. (a) Jallabert, C.; Rivière, H. *Tetrahedron Lett.* **1977**, 1215; (b) Jallabert, C.; Lapinte, C.; Rivière, H. *J. Mol. Catal* **1980**, *7*, 127; (c) Jallabert, C.; Rivière, H. *Tetrahedron* **1980**, *36*, 1191; (d) Jallabert, C.; Lapinte, C.; Rivière, H. *J. Mol. Catal.* **1982**, *14*, 75; For other pertinent studies on aerobic oxidation of alcohols using copper complexes see for example: (a) Capdevielle, P.; Sparfel, D.; Baranne-Lafont, J.; Cuong, N. K.; Maumy, M. *J. Chem. Research, (S)* **1993**, 10 and references cited therein; (b) Munakata, M.; Nishibayashi, S.; Sakamoto, H. *J. Chem. Soc., Chem. Commun.* **1980**, 219; (c) Bhaduri, S.; Sapre, N. Y. *J. Chem. Soc., Dalton Trans.* **1981**, 2585; (d) Semmelhack, M. F.; Schmid, C. R.; Cortes, D. A.; Chon, C. S. *J. Am. Chem. Soc* **1984**, *106*, 3374.
 9. See for example Ref. (8a).
 10. Other bases tested include e.g. Na_2CO_3 , Li_2CO_3 , Na_2HPO_4 , NaH_2PO_4 , Al_2O_3 , NaOAc , KOAc , KOH , and CuCO_3 . Only KOBu^t appears to act as an efficient base in the catalytic oxidation process. Its use is however limited at present to the oxidation of secondary alcohols (Markó, I. E.; Gautier, A.; Chellé-Régnaud, I.; Muttonkole K. Unpublished results).
 11. Solomon, R. G.; Kochi, J. K. *J. Am. Chem. Soc* **1973**, *95*, 3300.
 12. The use of air instead of oxygen results in a slower reaction rate. The oxidation can be increased by passing the air through a porous glass frit which creates microbubbles. Under these conditions, the speed of the catalytic oxidation of alcohols using air matches the one employing oxygen.
 13. The preparation of Copper(I) alkoxydes and their reactivity towards O_2 have been reported in the literature. See for example: Capdevielle, P.; Audebert, P.; Maumy, M. *Tetrahedron Lett.* **1984**, *25*, 4397–4400.
 14. Stoichiometric amounts of substituted azo-compounds have been used to oxidize magnesium alkoxides to the corresponding carbonyl compounds: Narasaka, K.; Morikawa, A.; Saigo, K.; Mukaiyama, T. *Bull. Chem. Soc. Jpn.* **1977**, *50*, 2773; The decomposition mechanism of hydrazines in the presence of copper-complexes has been reported: (a) Erlenmeyer, H.; Flierl, C.; Sigel, H. *J. Am. Chem. Soc.* **1969**, *91*, 1065; (b) Zhong, Y.; Lim, P. K. *J. Am. Chem. Soc* **1989**, *111*, 8398.
 15. Alcohols containing nitrogen heterocycles are also smoothly oxidized to the corresponding carbonyl compounds. These heterocycles include pyridine, imidazole and triazole derivatives.
 16. The intermediacy of complex **13** in the aerobic oxidations was supported by the following observations: (1) independently generated complex **13**($\text{CuCl} \cdot \text{Phen}/\text{DBADH}_2/\text{NaH}$) proved to be unreactive under anaerobic conditions; (2) passing O_2 through

the reaction mixture containing **13** and alcohol **1** restored the catalytic activity and good yields of aldehyde **2** were again obtained.

17. (a) Sustmann, R.; Müller, W.; Mignani, S.; Merényi, R.; Janousek, Z.; Viehe, H. G. *New. J. Chem.* **1989**, *13*, 557; (b) De Boeck, B.; Janousek, Z.; Viehe, H. G. *Tetrahedron* **1995**, *51*, 13239–13246.
18. For general reviews on Oppenauer-type oxidations see: (a) de Graauw, C. F.; Peters, J. A.; Vandekum, H.; Huskens, J. *Synthesis* **1994**, 1007–1017; (b) Djerassi, C. *Org. React. (N.Y.)* **1951**, *6*, 207–212; (c) Krohn, K.; Knauer, B.; Kupke, J.; Seebach, D.; Beck, A. K.; Hayakawa, M. *Synthesis* **1996**, 1341–1344.
19. The use of stoichiometric amounts of dipiperidyl azodicarboxamide to oxidize magnesium alkoxides to the corresponding carbonyl compounds has been described: Narasaka, K.; Morikawa, A.; Saigo, K.; Mukaiyama, T. *Bull. Chem. Soc. Jpn* **1977**, *50*, 2773. No reaction is observed under our catalytic anaerobic conditions if DBAD is replaced by the azodicarboxamide derivative..
20. Another argument against the oxo-transfer mechanism in our catalytic aerobic oxidation protocol is the lack of formation of sulfoxides from sulfides, N-oxydes from amines and phosphine oxydes from phosphines. Alkenes also proved to be inert towards oxidation; no epoxide formation could be detected under our reaction conditions.
21. The oxidation of alcohols using azodicarboxylates has been previously reported (Yoneda, F.; Suzuki, K.; Nitta, Y. *J. Org. Chem* **1967**, *32*, 727–729). Control experiments were therefore performed to establish the need for copper salts in our oxidation procedure. Thus under our reaction conditions no aldehyde or ketone could be detected **in the absence** of the CuCl · Phen catalyst even if phenanthroline was added as an activating base. Moreover, certain reactive alcohols were oxidized partially by CuCl · Phen **in the absence** of the azo-derivative **19**, though only in moderate yields. These control experiments thus clearly establish the key-role of the copper ion in these oxidations.
22. The oxidation reactions were monitored by GC (PermaBond SE-52-DF-0.25; 25 m × 0.25 mm ID) using tetradecane as the internal standard.
23. The decomposition appears to result from the activation of the azo derivative by the copper complex in conjunction with the deprotonation of the 'Butyl substituent by the base resulting in the loss of CO₂ and isobutene.
24. One rare exception appears to be KOBu^t. For example, the aerobic oxidation of 2-undecanol (5 mol% CuCl · Phen, 5 mol% KOBu^t, toluene, 80–90°C) afforded 2-undecanone in almost quantitative yields. However, this system appears, so far, to be limited to secondary alcohol oxidations.
25. For a discussion of the possible mechanism of this reaction, see: Markó, I. E.; Tsukazaki, M.; Giles, P. R.; Brown, S. M.; Urch, C. J. *Angew. Chem. Int. Ed., Engl.* **1997**, *36*, 2208.
26. It is interesting to note that other solvents gave repeatedly poorer conversions (benzene, xylenes) or destroyed the catalyst activity (CH₂Cl₂, CHCl₃, ClCH₂CH₂Cl, DMF, and MeCN).
27. It is interesting to note that fluorobenzene was also used successfully by Mukaiyama and co-workers as a solvent in their Mn(salen) catalysed epoxidation of alkenes using the O₂/aldehyde protocol: Yamada, T.; Imagawa, K.; Nagata, T.; Mukaiyama, T. *Chem. Lett.* **1992**, *11*, 2231.
28. A small amount of racemisation was observed during the oxidation of Boc-prolinol.
29. Fluorobenzene possesses some remarkable properties. For example the solubility of O₂ in FC₆H₅ is greater than for other alkylbenzene or monohalobenzene derivatives.

The relative solubility of O₂ in toluene is 8.77 as compared to 15.08 for FC₆H₅ (Naumenko, N. V.; Mukhin, N. N.; Aleskovikii, V. B. *Zh. Prikl. Khim (Leningrad)* **1969**, *42*, 2522). Furthermore fluorobenzene possesses unusual solvent property parameters and is more polar than toluene.

Parameters ^a	Toluene	Fluorobenzene
Gutmann donor number	0.1	3.00
Dipole moment	1.0	4.90
Dielectric constant	2.38	5.42
E _T (30)	33.9	37
Solvatochromic π*	0.54	0.62

^a These data were measured at Zeneca Ltd.

Like most aromatic solvents fluorobenzene is highly flammable (Fp = −12°C). It is irritant to the skin and can cause serious damage to the eyes. It is only weakly toxic by inhalation (rat; LC50 = 27 mg/l) and even less by ingestion (rat; LC50 = 4000 mg/l). On large-scale experiments it can be easily recycled by drying and distillation

30. It is possible that the greater polarity of fluorobenzene, which can lead to a higher concentration of soluble base, might be responsible in part for the improved yields and rate of reaction observed in this medium. Moreover, the amount of oxygen dissolved in boiling fluorobenzene might be greater than in toluene, leading to a more efficient reoxidation of the active copper species. In this regard, it is noteworthy that finely divided oxygen or air bubbles (obtained by passing the gas through a glass frit) results in enhanced reaction rate.
31. The deactivation of the catalyst could arise from base-catalysed decomposition of copper-coordinated DBAD by ^tBuOK in the absence of added alcohol.
32. **Aerobic Oxidation of Boc-prolinol.** 1,10-Phenanthroline (45 mg, 0.25 mmol, 5 mol%) was added to 45 mL of dry FC₆H₅ followed by solid CuCl (25 mg, 0.25 mmol, 5 mol%). After stirring for 5 min at room temperature, (L)-Boc-prolinol (1.0 g, 4.97 mmol) was added followed by solid KOBu^t (28 mg, 0.25 mmol, 5 mol%). The resulting yellowish solution was stirred at room temperature for 10 min before DBAD (57.5 mg, 0.25 mmol, 5 mol%) was added. The reaction mixture was refluxed under a gentle stream of O₂ during 4.5 h. After cooling to 20°C, celigel (1 g, 80/20 w/w mixture of celite and silica gel) was added and stirring was continued for 2 min. Filtration, washing off of the solid residue with 100 mL of ether and evaporation of the solvents *in vacuo* afforded pure (L)-Boc-prolinol as a colorless oil (960 mg, 97%). ¹H NMR (CDCl₃, 200 MHz). δ = 9.55 (brs, 1 H, rotamer 1), 9.45 (brd, *J* = 3 Hz, 1H, rotamer 2), 4.3 (m, 1H, rotamer 1), 4.0 (m, 1H, rotamer 2), 3.6–3.3 (m, 2H), 2.2–1.8 (m, 4H), 1.45 (brs, 9H, rotamer 1), 1.40 (brs, 9H, rotamer 2). ¹³C NMR (CDCl₃, 75 MHz). δ = 199.5, 199.3, 79.5, 64.4, 46.2, 28.1, 27.6, 24.4, 23.8. The ee was measured by chiral GC (CP-Chiral-Dex CB, 25 m; *F* = 0.25 mm, 130°C for 12 min then 1°C per min) of the derived *bis*-Boc-prolinol obtained by LiAlH₄ reduction of Boc-prolinol followed by derivatisation with Boc₂O (*t*_R (*R*)-enantiomer, 43.1 min; *t*_R (*S*)-enantiomer, 43.6 min).
33. (a) Karlin, K. D.; Gultneh, Y. *Progr. Inorg. Chem* **1987**, *35*, 219; (b) Sakharov, A. M.; Skibida, I. P. *Kinet. Catal* **1988**, *29*, 96; (c) Kitajima, N.; Fujisawa, K.; Fujimoto, C.; Moro-oka, Y.; Hashimoto, S.; Kitagawa, T.; Toriumi, K.; Tatsumi, K.; Nakamura, A. *J. Am. Chem. Soc.* **1992**, *114*, 1277; (d) Solomon, E. I.; Sundaram, U. M.; Machonkin, T. E. *Chem. Rev.* **1996**, *96*, 2563.

34. Whereas quantitative conversion of **23** into **24** occurred in the absence and presence of 7 mol% of NMI, the oxidation of **23** proceeded more slowly in the presence of this additive. The coordination of NMI to copper results in a slower exchange with the excess DBAD and hence, in a longer reaction time.
35. Studies performed on the anaerobic version of this catalytic system revealed that aliphatic primary alcohols were oxidized with the same efficiency as all the other classes of alcohols, thus ruling out complexes **A**, **B**, and **E** as the culprit for the decomposition pathway. Whilst we could not experimentally discard complex **D**, coordination of an alcohol to **D** should involve the participation of a pentacoordinated copper species. Whilst these are not uncommon, their formation requires a higher activation energy than the coordination to **C**.
36. This hydrogen transfer is essentially an intramolecular acid-base reaction. The hydrogen of the coordinated alcohol function is acidified by coordination to the copper center whilst the hydrazine ligand possesses basic properties. The elimination of the hydrazine substituent is irreversible under these neutral conditions. Indeed, in the absence of excess base, DBADH₂ is unable to displace the alkoxide ligand from the copper complex **G**.
37. We have previously demonstrated that **G** was not a competent catalyst in the aerobic oxidation protocol when R = alkyl.
38. Markó, I. E.; Tsukazaki, M.; Giles, P. R.; Brown, S. M.; Urch, C. J. *Angew. Chem. Int. Ed., Engl.* **1997**, *36*, 2208.

VISIBLE LIGHT PHOTOCATALYSIS BY A TITANIA TRANSITION METAL COMPLEX

HORST KISCH, GERALD BURGETH and WOJCIECH MACYK

Institut für Anorganische Chemie, Universität Erlangen-Nürnberg, Egerlandstr. 1,
D-91058 Erlangen, Germany

- I. Introduction
- II. Preparation and Characterization of Photocatalysts
 - A. Preparation
 - B. Characterization
- III. Photocatalytic Degradation with Artificial Visible Light ($\lambda \geq 455$ nm)
- IV. Photodegradation with Natural Indoor Daylight
- V. Photodegradation with Sunlight
- VI. Mechanism
- VII. Summary
- References

I. Introduction

Supporting a soluble metal complex catalyst onto an inorganic carrier is a well known method in thermal catalysis. As a consequence thereof, the catalyst becomes easily separable from the reaction products while retaining in most cases its over-all catalytic activity. In the following an opposite case observed in the field of photocatalysis is reported. Here an inactive homogeneous transition metal complex becomes active when supported onto an inorganic carrier. A further difference is that, depending on the reaction conditions, the carrier itself may also exhibit photocatalytic activity. Hexachloroplatinic acid in solution only induces a stoichiometric visible light photooxidation of the ubiquitous water pollutant 4-chlorophenol (4-CP) whereas the reaction becomes photocatalytic when the complex is supported onto titania. It was found that the most active catalyst was obtained when the complex was covalently attached to titania. Thus, the titania support can be considered as an unconventional semiconductor ligand in a heterogeneous transition metal complex.

Both in fundamental and applied aspects of semiconductor photocatalysis, titania is the most commonly employed material (1). However, a serious problem in technical applications is the fact that it absorbs only 3% of solar light. Accordingly, extensive efforts have been made to sensitize titania for visible light induced photocatalytic reactions. In general, doping by transition metal ions is not connected with a shift of the photocatalytic activity into the visible but rather with promotion of photocorrosion and charge recombination. Exceptions are Cr^{3+} (2), Fe^{3+} (3,4), and V^{4+} (5) volume-doped materials prepared by rather sophisticated methods like ion implantation or chemical vapor deposition. The vanadium doped titania was present as a monolayer and enabled the photooxidation of gaseous ethanol with light of $\lambda = 396\text{--}450\text{ nm}$ as indicated by solid-state NMR analysis (5). Although a semiconductor photocatalysis mechanism was invoked for this and the reactions in the presence of the Cr^{3+} and Fe^{3+} doped titania, no photoelectrochemical experiments were performed to experimentally support this hypothesis. We have shown that simple inorganic compounds like $\text{Na}_2[\text{PtCl}_6]$, AuCl_3 , and RhCl_3 introduced into the bulk of amorphous microporous titania (6–8) by sol–gel methods induce the photomineralization of 4-chlorophenol (4-CP) with visible light. In the platinum modified material, isolated PtCl_4 units are present without any bonding interactions with the titania matrix. However, when these are introduced through the application of an alternative synthetic method, a photocatalyst of the type $\{[\text{TiO}_2]\text{--O--PtCl}_4\text{L}\}^{n-}$, $\text{L} = \text{H}_2\text{O}$, OH^- , $n = 1, 2$, is obtained having a much higher activity (9–11). In this heterogeneous transition metal complex titania plays the role of an unconventional ligand. Herein we briefly summarize how the photoredox properties of titania are changed by the covalent attachment to chloroplatinate and how the primary photoprocesses of charge separation and interfacial electron transfer can be described. Detailed information is available from recent original publications.

II. Preparation and Characterization of Photocatalysts

A. PREPARATION

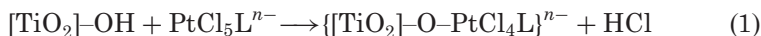
Upon stirring a suspension of titania powders in an aqueous solution of $\text{H}_2[\text{PtCl}_6]$ in the dark, different maximum amounts were adsorbed. Whereas 4.0 and 1.1% were taken up by the anatase and

anatase/rutile samples TH and P25, respectively, only traces were adsorbed onto the rutile material Ald. The almost four times larger amount of hexachloroplatinic acid adsorbed by TH corresponds with the about four times larger surface area of TH as compared to P25 (vide infra). Surface modification may be performed also by simple grinding with PtCl_4 , as in the case of $[\text{PtCl}_4]/\text{P25}$, but the resulting photocatalysts are of lower photocatalytic activity and lower stability (9,11).

B. CHARACTERIZATION

Transmission electron microscopy and X-ray powder diffraction of 4.0% $\text{H}_2[\text{PtCl}_6]/\text{TH}$ revealed the presence of about 200 nm large aggregates consisting of 2–4 nm sized anatase crystallites (12). Specific surface areas of unmodified P25 (50 m^2/g) and Ald (3 m^2/g) were not changed upon modification whereas the area of TH decreased from 334 m^2/g to 260 m^2/g .

Dark desorption experiments were conducted with potassium fluoride in various concentrations since it is known that fluoride irreversibly adsorbs onto titania through displacement of surface hydroxide (13–17). When 4.0% $\text{H}_2[\text{PtCl}_6]/\text{TH}$ was suspended in water, a pH value of 3.4 was generated. No desorption of $[\text{PtCl}_6]^{2-}$ was observable upon stirring this suspension for four days in the presence of 0.01 M KF. Only at a ten-fold higher fluoride concentration considerable desorption up to 21% took place. When the suspension was neutralized before, the amount of desorption decreased to 2% although the fluoride concentration employed was as high as 0.5 M. This suggests that chemisorption has occurred according to Eq. (1) ($\text{L} = \text{Cl}, \text{OH}$) and that desorption is an acid catalyzed process



which may occur also in the absence of fluoride ions. Accordingly, prolonged stirring of a suspension in the dark, brought to pH 1 by addition of hydrochloric acid, induced complete desorption of $[\text{PtCl}_6]^{2-}$ as indicated by UV spectroscopy. The remaining TH sample upon irradiation with visible light exhibited negligible photocatalytic activity. From this and the amount of chloride released into solution after stirring 4.0% $\text{H}_2[\text{PtCl}_6]/\text{TH}$ in NaOH in the dark, it is estimated that the surface complex has the composition $\{[\text{Ti}]\text{-O-PtCl}_4\text{L}\}^{n-}$, $\text{L} = \text{H}_2\text{O}, \text{OH}^-$, $n = 1, 2$ (18). Since only 1% was desorbed in nitric acid

and 0% in sodium chloride solution, it follows that both the presence of protons and chloride ions favor an efficient photodesorption process. It is known that chloride dark adsorption onto titania is favored at low pH values (15,16).

In the corresponding photodesorption experiments ($\lambda \geq 455$ nm) with 4.0% $\text{H}_2[\text{PtCl}_6]/\text{TH}$ suspended in water no desorption occurred within 24 h of irradiation time, whereas in the presence of 0.1 M HCl desorption of $[\text{PtCl}_6]^{2-}$ was almost complete.

The diffuse reflectance spectra (19–21) of P25, TH, 1% $[\text{PtCl}_4]/\text{P25}$ and 4.0% $\text{H}_2[\text{PtCl}_6]/\text{TH}$ are compared in Fig. 1a. The pronounced absorption of the modified material in the visible region was

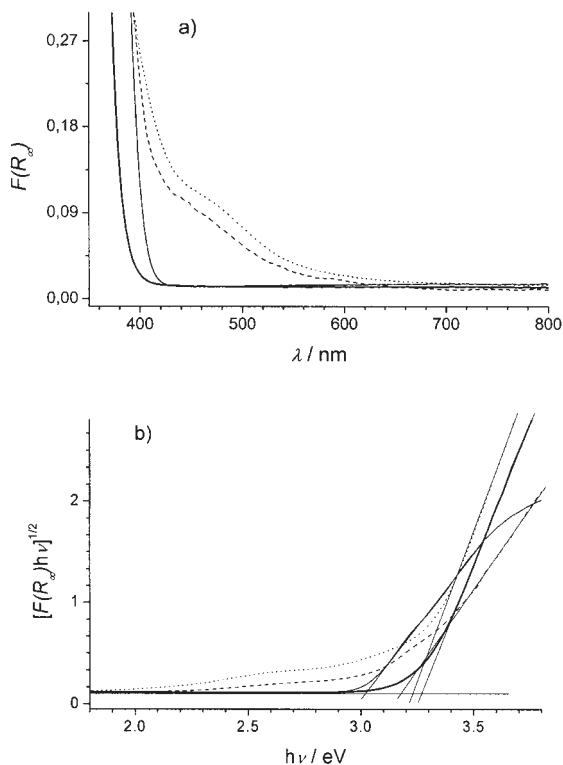


FIG. 1. (a) Diffuse reflectance spectra of P25 (thin line), TH (thick line), 3% $[\text{PtCl}_4]/\text{P25}$ (dashed line) and 4.0% $\text{H}_2[\text{PtCl}_6]/\text{TH}$ (dotted line). The Kubelka-Munk function, $F(R_\infty)$, is used as the equivalent of absorbance. (b) Transformed diffuse reflectance spectra of P25 (thin line), TH (thick line), 3% $[\text{PtCl}_4]/\text{P25}$ (dashed line) and 4.0% $\text{H}_2[\text{PtCl}_6]/\text{TH}$ (dotted line). The bandgap energy was obtained by extrapolation of the linear part.

tentatively assigned to a ligand-field transition of the platinum(IV) chloride, by analogy with the solution spectrum of $\text{Na}_2[\text{PtCl}_6]$ (9,22,23). Below 400 nm a sharp increase in the absorption of the modified sample indicates bandgap absorption of TiO_2 , as inferred from the absorption features of unmodified TiO_2 . For an indirect crystalline semiconductor the bandgap energy is obtained by extrapolation of the linear part of the plot of $(F(R_\infty)h\nu)^{1/2}$ vs. $h\nu$ (24). All given values are the arithmetic means of three independent measurements (Fig. 1b, Table I), the bandgap absorption of the titania matrix in platinum(IV) modified TH is slightly red-shifted whereas it is blue-shifted in modified P25. In addition, these materials show significant absorbance within the visible region down to 620–650 nm corresponding to 2.0 and 1.9 eV for 3% $[\text{PtCl}_4]/\text{P25}$ and 4.0% $\text{H}_2[\text{PtCl}_6]/\text{TH}$, respectively.

Different from a single crystal electrode, it is more difficult to measure the flatband potential of a semiconductor powder, which is necessary to estimate the absolute positions of the valence and conduction band edges. However, the “suspension method” developed by Bard and co-workers (25,26) and modified by Roy *et al.* (27), allows to obtain this important potential. The method is based on the pH-dependence of the flatband potential of TiO_2 [Eq. (2)].

$$E_{\text{fb}}(\text{pH}) = E_{\text{fb}}(\text{pH} = 0) - k \text{ pH} \quad (2)$$

where $E_{\text{fb}}(\text{pH})$ is the flatband potential at a given pH and k is usually equal to 59 mV (28). Bard *et al.* measured the photocurrent generated in the presence of methyl viologen (MV^{2+}) and a reducing agent, whereas Roy recorded the photovoltage in the absence of a reducing

TABLE I

BANDGAP ENERGIES OF SOME TITANIA-BASED CATALYSTS CALCULATED FROM TRANSFORMED DIFFUSE REFLECTANCE SPECTRA

Material	Bandgap energy ^a /eV	Bandgap/nm
P25	3.03	409
3% $[\text{PtCl}_4]/\text{P25}$	3.17 (ca. 2.0) ^b	391 (ca. 620)
TH	3.27	379
4.0% $\text{H}_2[\text{PtCl}_6]/\text{TH}$	3.21 (ca. 1.9)	386 (ca. 650)

^a ± 0.05 eV.

^b Values in parentheses correspond to the absorption onset.

agent. In the latter case the shape of the sigmoidal voltage/pH curve depends on the potential of the reference electrode, the $[\text{MV}^{2+}]/[\text{MV}^{+\bullet}]$ ratio, the pH value, k , and on E_{fb} . At the pH value of the inflection point (pH_0) the flatband potential is equal to the potential of methyl viologen. From this the potential at any pH can be calculated according to Eq. (3) (27).

$$E_{\text{fb}}(\text{pH}) = E_{\text{MV}^{2+/\bullet}}^{\circ} + k(\text{pH}_0 - \text{pH}) \quad (3)$$

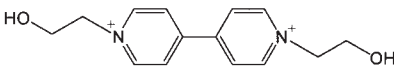
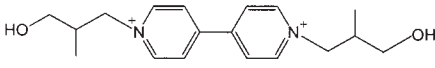
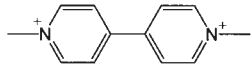
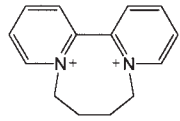
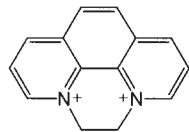
This is only possible if the factor k is known. Roy *et al.* obtained it from the slope of the voltage/pH plot above the inflection point whereas Bard *et al.* calculated it from the slope of the onset of photocurrent vs. pH (26). However, only poorly reproducible values were obtained by the former and latter method due to high voltage fluctuations and too low photocurrents, respectively. We have determined the k value by a new method through variation of the redox couple ($\text{A}_i^{2+}/\text{A}_i^{+\bullet}$). In this case a linear relation between the pH_0 value and the redox potential of the pH-independent redox couple is expected [Eq. (4)].

$$k = (E_{\text{Ai}^{2+/\bullet}}^{\circ} - E_{\text{Aj}^{2+/\bullet}}^{\circ})/(\text{pH}_{0j} - \text{pH}_{0i}) \quad (4)$$

Table II summarizes structures and potentials of the bipyridinium compounds employed as redox couples. A plot of the pH_0 values, as measured for P25 (the reference material) and 4.0% $\text{H}_2[\text{PtCl}_6]/\text{TH}$ in the presence of appropriate redox systems, versus the redox potential affords straight lines (Fig. 2). From the corresponding slope the k values of 50 and 60 mV for P25 and 4.0% $\text{H}_2[\text{PtCl}_6]/\text{TH}$ are obtained, respectively. This is in good agreement with the value of 59 mV reported for TiO_2 , SnO_2 , and SrTiO_3 electrodes (28).

The plots of photovoltage vs. pH for TH and a series of $\text{H}_2[\text{PtCl}_6]/\text{TH}$ materials are summarized in Fig. 3. Upon increasing the pH value a blue color is developed when approaching inflection points (pH_0), due to formation of the $\text{MV}^{+\bullet}$ radical cation, as indicated in the figure and summarized in Table III. Observed pH_0 values of 4.45 and 5.4 for P25 and TH, respectively, are significantly lower than that of 6.72 as reported by Bard *et al.* for commercially available MCB anatase (25). The corresponding apparent flatband potentials at $\text{pH} = 7$, as obtained via Eq. (3) assuming $k = 0.059$ V are -0.58 V (P25), -0.54 V (TH), and -0.46 V (MCB). The value for a single crystal of anatase was reported to be -0.59 V ($\text{pH} = 7$) (29).

TABLE II
 REDOX POTENTIALS OF VARIOUS ELECTRON ACCEPTORS MEASURED IN
 AQUEOUS SOLUTIONS

Compound	Structure of cation	$E_{A^{2+}/+ \cdot}$ / V vs. NHE ^a
(HEV)(PF ₆) ₂		−0.399
(HiBV)Br ₂		−0.414
(MV)Cl ₂		−0.450
(BQ)Br ₂		−0.640 ^b
(DP)Br ₂		−0.268 ^b

^a ± 0.010 V.^b Irreversible.

Relative to the value of TH (−0.54 V) the apparent flatband potential shifts anodically by 0.05, 0.09, and 0.26 V in the case of 1, 2, and 4.0% H₂[PtCl₆]/TH, respectively (Table III). Accordingly, the anodic shift becomes higher with increasing concentration of the surface platinum(IV) complex. Since the absorption onset of the TiO₂ part of the 4.0% H₂[PtCl₆]/TH spectrum remains nearly unchanged (compare Fig. 1 and Table I), the anodic shift of the conduction band edge is accompanied by an anodic shift of the valence band edge. This should improve the oxidation potential of holes generated upon UV-light irradiation. In accord with this postulate, significant differences in the photocatalytic activities of TH and 4.0% H₂[PtCl₆]/TH were observed (vide infra).

Photocurrent measurements performed for unmodified P25 point to an *n*-type semiconductor behavior. Calculated IPCE values for P25

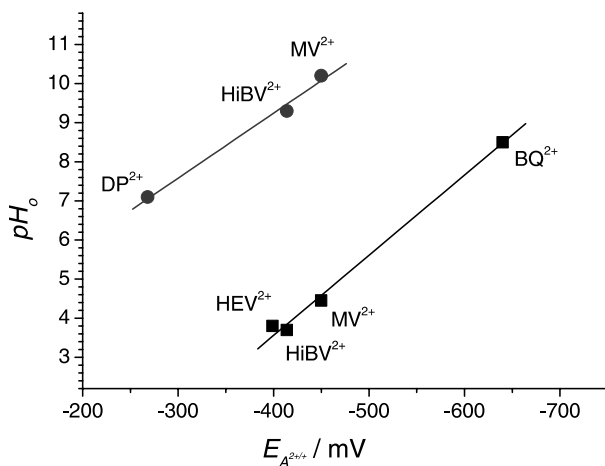


FIG. 2. $E_{A^{2+}/+}$ vs. pH_0 for P25 (squares) and 4.0% $\text{H}_2[\text{PtCl}_6]/\text{TH}$ (circles) suspensions.

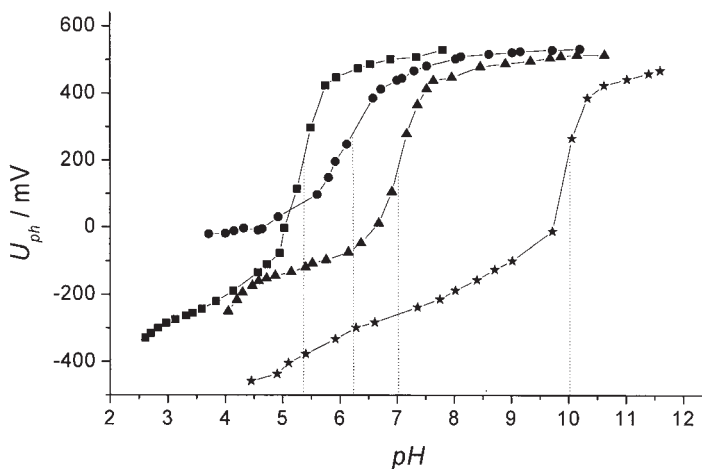


FIG. 3. Photovoltage recorded for TH (squares), 1.0% (circles), 2.0% (triangles) and 4.0% $\text{H}_2[\text{PtCl}_6]/\text{TH}$ (stars) suspensions in 0.1 M KNO_3 in the presence of MV^{2+} irradiated with full light of an XBO-lamp. The position of the inflection point pH_0 is marked with a dotted line.

are presented in Fig. 4a. The onset of photoactivity is localized at ca. 420 nm. This value, too high as compared to 409 nm obtained from the diffuse reflectance spectrum of P25 (compare Table I), is caused by relatively broad bandwidth of light at the exit slit of the

TABLE III
APPARENT FLATBAND POTENTIAL VALUES AND RELATED DATA

Material	pH ₀	<i>k</i> /mV	<i>E</i> _{fb} (pH = 0)/ V vs. NHE	<i>E</i> _{fb} (pH = 7)/ V vs. NHE
P25	4.45 ± 0.05	50 ^a	−0.23 ± 0.01	−0.58 ± 0.01
TH	5.4 ± 0.1	59 ^b	−0.13 ± 0.02	−0.54 ± 0.02
1.0% H ₂ [PtCl ₆]/TH	6.2 ± 0.1	59 ^b	−0.08 ± 0.02	−0.49 ± 0.02
2.0% H ₂ [PtCl ₆]/TH	7.0 ± 0.1	59 ^b	−0.04 ± 0.02	−0.45 ± 0.02
4.0% H ₂ [PtCl ₆]/TH	10.2 ± 0.1	60 ^a	+ 0.13 ± 0.02	−0.28 ± 0.02

^a Measured as described in the text.

^b Values taken from Ref. (28).

monochromator. The photocurrent action spectrum of 3% [PtCl₄]/P25 exhibits photoactivity even upon visible light irradiation down to 550 nm. Therefore, the corresponding photocurrent must be generated by electron injection from the chloroplatinum surface complex into the conduction band of titania. In the presence of methanol or formate the current-doubling effect leads to 6–10 times higher currents.

III. Photocatalytic Degradation with Artificial Visible Light ($\lambda \geq 455$ nm)

Curves A–C of Fig. 5 illustrate the photodegradation of 4-chlorophenol (4-CP) with visible light ($\lambda \geq 455$ nm) in the presence of the three photocatalysts. 4.0% H₂[PtCl₆]/TH induced also a fast mineralization as indicated by the TOC/TOC₀ values represented by curve D. Reaction rates increased with increasing catalyst concentration, reaching a constant value at 0.5 to 0.8 g/L.

Large differences in the visible light ($\lambda \geq 455$ nm) induced catalytic activity are observed for the three photocatalysts. Whereas the rutile based H₂[PtCl₆]/Ald was inactive (Fig. 5, curve A), in accord with the very small surface area and the trace amounts of adsorbed chloroplatinate, 1.1% H₂[PtCl₆]/P25, and 4.0% H₂[PtCl₆]/TH were active, inducing 50% degradation after 95 min and 15 min, respectively (Fig. 5, curves B, C). 4.0% H₂[PtCl₆]/TH also initiated a fast mineralization as indicated by curve D in Fig. 5.

Since the mineralization process produces CO₂, H₂O, and HCl, the initial pH value of 3.4 decreased to 3.0 at 120 min irradiation

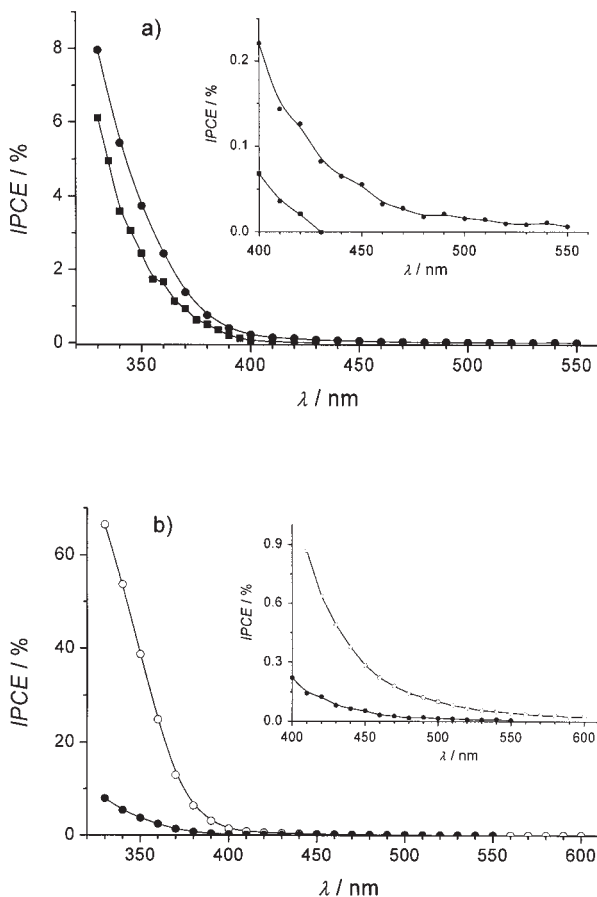


FIG. 4. Dependence of incident photon to current efficiency (IPCE) on excitation wavelength and presence of current-doubling agent. ITO electrodes were covered with P25 (squares) or 3% [PtCl₄]/P25 (circles) and biased at a constant potential of 0.7 V vs. Ag/AgCl in 0.1 M NaOH solution (a). After addition of 0.1 M HCOONa the IPCE values increased (open circles, (b)). The inserts show the zoomed visible region.

time. These conditions should favor photodesorption (*vide supra*) and therefore a long-term irradiation was conducted in the presence of NaHCO₃ to neutralize the generated acid. In this experiment the concentration of 4-CP was readjusted to its original value when the c/c_0 values approached zero (Fig. 6). Whereas in the absence of bicarbonate the activity decreased to 50% of its original value already

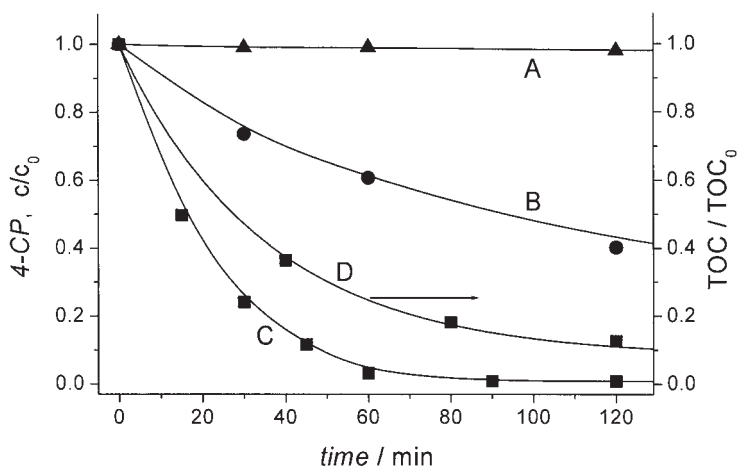


FIG. 5. 4-CP degradation upon visible light irradiation; $\lambda \geq 455$ nm. (A) $\text{H}_2[\text{PtCl}_6]/\text{Ald}$, (B) 1.1% $\text{H}_2[\text{PtCl}_6]/\text{P25}$, (C) 4.0% $\text{H}_2[\text{PtCl}_6]/\text{TH}$, (D) 4-CP mineralization as catalyzed by 4.0% $\text{H}_2[\text{PtCl}_6]/\text{TH}$ (10).

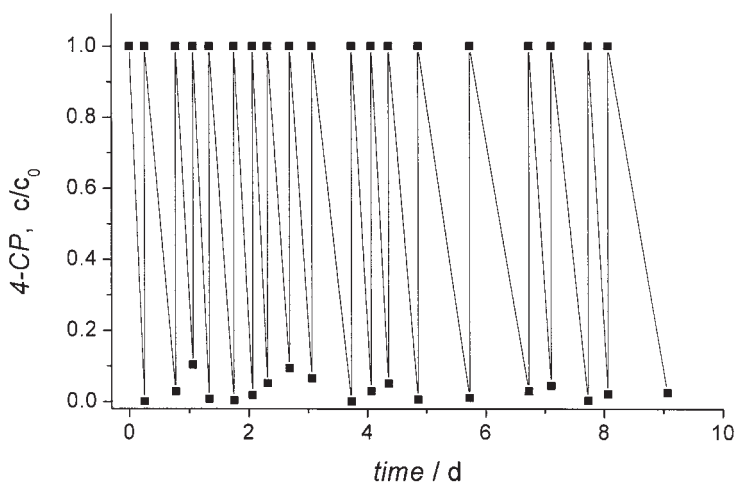


FIG. 6. Long term visible light degradation of 4-CP at 4.0% $\text{H}_2[\text{PtCl}_6]/\text{TH}$ in the presence of 0.01 M NaHCO_3 ; $\lambda \geq 400$ nm (10); for details see text.

at the third cycle, it changed only little even after 19 cycles when bicarbonate was present. Whereas in the sixth cycle an irradiation time of 7.5 h was required to obtain 98% degradation, in the 16th cycle only half an hour longer was necessary to reach a value of

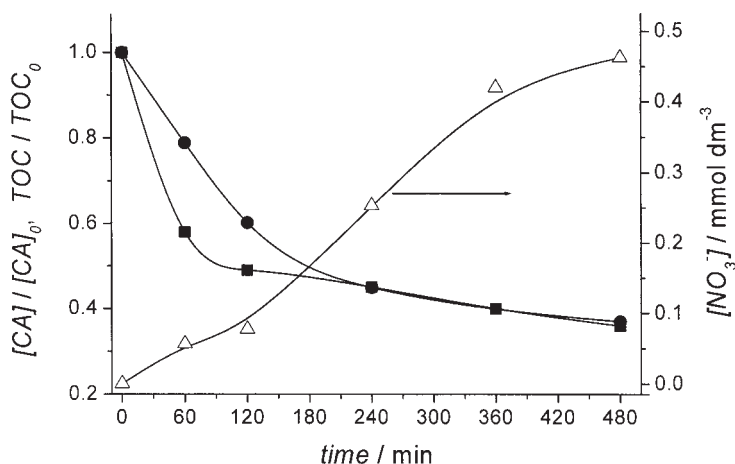


FIG. 7. Photodegradation of cyanuric acid (CA) at 4.0% $\text{H}_2[\text{PtCl}_6]/\text{TH}$ upon irradiation through the cut-off filter of 320 nm as monitored by disappearance of cyanuric acid (squares) and by the change of total organic carbon content (circles) and formation of NO_3^- (triangles). Initial parameters: pH = 9, $[\text{CA}]_0 = 0.25 \text{ mmol L}^{-1}$.

95% (Fig. 6). This clearly proves the catalytic nature of the photodegradation reaction.

Other pollutants like atrazine, dichloroacetic acid, lindane, and trichloroethylene also undergo almost complete mineralization ($\lambda \geq 455 \text{ nm}$). The degradation of atrazine in general affords cyanuric acid as the final product when the photocatalyst is an unmodified titania material (30). The same was observed for TH. However, when 4.0% $\text{H}_2[\text{PtCl}_6]/\text{TH}$ was employed, even cyanuric acid was mineralized by UV ($\lambda > 320 \text{ nm}$) and visible ($\lambda > 455 \text{ nm}$) light as indicated by TOC and nitrate determinations (Fig. 7). After 6 h about 60% of the starting material was completely mineralized.

IV. Photodegradation with Natural Indoor Daylight

The superior photocatalytic activity of 4.0% $\text{H}_2[\text{PtCl}_6]/\text{TH}$ became even more evident, when the reaction was conducted in diffuse indoor laboratory daylight. Under these conditions both unmodified P25 and TH are inactive whereas the 1.1% and 4.0% surface modified

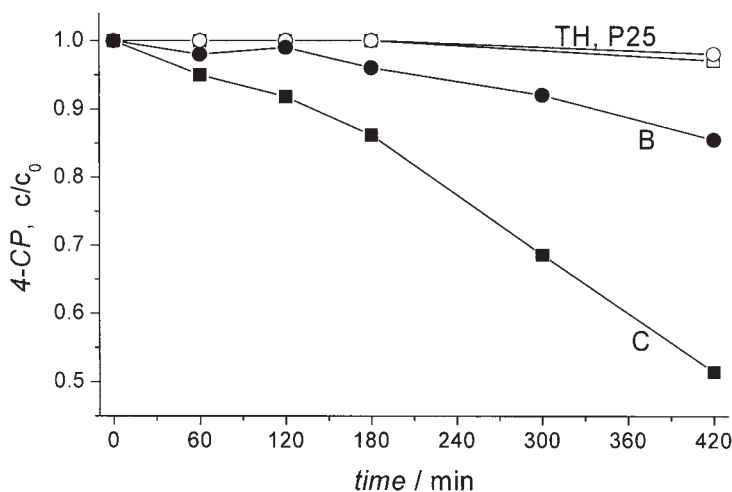


FIG. 8. Diffuse indoor daylight induced degradation of 4-CP in the presence of TH, P25, 1.1% $\text{H}_2[\text{PtCl}_6]/\text{P25}$ (B) and 4.0% $\text{H}_2[\text{PtCl}_6]/\text{TH}$ (C).

counterparts exhibited 10% degradation after 420 and 120 min, respectively (Fig. 8).

V. Photodegradation with Sunlight

In the photodegradation with sunlight a significant difference between the photocatalysts prepared by adsorption from solution and by grinding (9) becomes apparent. Contrary to the ground material 2% $[\text{PtCl}_4]/\text{P25}$ which is less active than P25, the sample 1.1% $\text{H}_2[\text{PtCl}_6]/\text{P25}$, as prepared by adsorption, induced a slightly faster reaction as illustrated in Fig. 9a (curves B and P25). The strong and positive influence of surface complexation is more significant for the TH based photocatalyst (curves C and TH, Fig. 9a).

As expected, the higher photocatalytic activity of modified TH materials as compared to P25 was even more pronounced when the solar irradiation was replaced by artificial UV light. 2.0% $\text{H}_2[\text{PtCl}_6]/\text{TH}$ induced 90% degradation already after 12 min, the time by which only 50% were degraded by P25 (curves D and P25, Fig. 9b). Under these reaction conditions the ground material 2% $[\text{PtCl}_4]/\text{P25}$ led to only 30% degradation (curve E, Fig. 9b). In the case of 4.0% $\text{H}_2[\text{PtCl}_6]/\text{TH}$ only traces of 4-CP could be detected after this period of time (curves C, Fig. 9b).

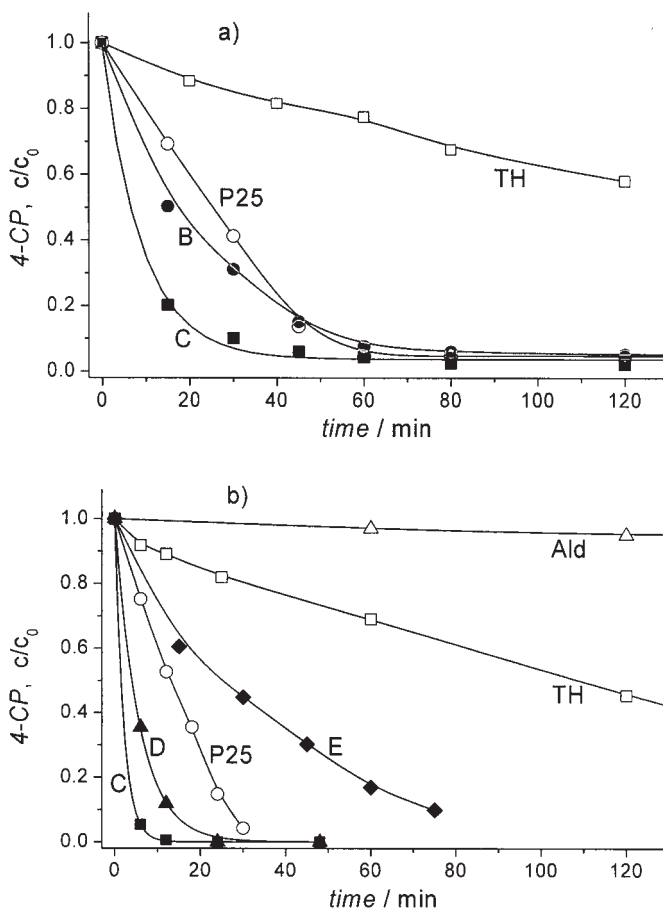
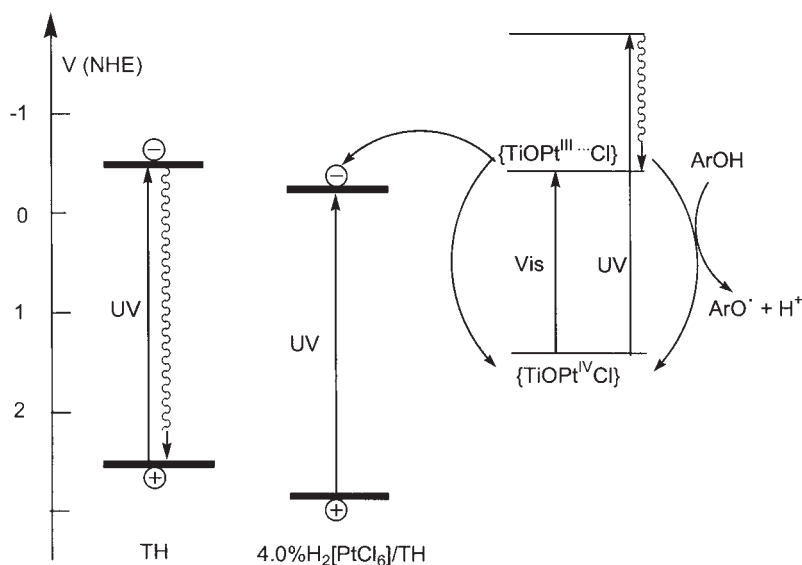


FIG. 9. (a) Sunlight induced degradation of 4-CP in the presence of TH, P25, 1.1% $\text{H}_2[\text{PtCl}_6]/\text{P25}$ (B), and 4.0% $\text{H}_2[\text{PtCl}_6]/\text{TH}$ (C). (b) 4-CP degradation upon UV irradiation; $\lambda \geq 320$ nm. 4.0% $\text{H}_2[\text{PtCl}_6]/\text{TH}$ (C), 2.0% $\text{H}_2[\text{PtCl}_6]/\text{TH}$ (D), 2% $[\text{PtCl}_4]/\text{P25}$ (E).

VI. Mechanism

As mechanistic hypothesis it was proposed (9–11) that the excited platinum complex undergoes homolytic Pt–Cl cleavage affording a Pt^{III} intermediate and an adsorbed chlorine atom (Scheme 1), by analogy with the known photochemistry of hexachloroplatinate in homogeneous solution (23,31). Electron injection from the platinum(III) complex into the titania conduction band reforms Pt^{IV} . Thus, the



SCHEME 1. Schematic representation of primary photoprocesses upon visible and UV excitation. The bold lines correspond to the potentials of conduction and valence band edges.

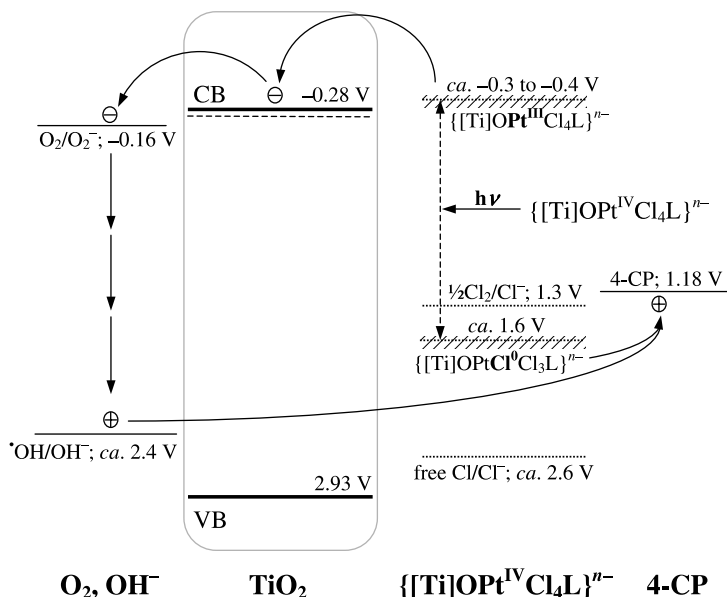
reductive and oxidative centers become spatially separated and charge recombination should be inhibited. The trapped conduction band electron reduces oxygen to superoxide and finally hydroxyl radicals as evidenced by scavenging experiments with benzoic acid and tetranitromethane (9). The adsorbed chlorine atom was assumed to oxidize 4-CP to the corresponding oxyl radical which is eventually converted to CO_2 and HCl , in analogy with the photomineralization catalyzed by unmodified titania (32,33). Intermediate chlorine atoms were evidenced by formation of chlorinated phenols when unsubstituted phenol was used as substrate (9). Adsorbed chlorine atoms were also proposed as intermediates in the photodegradation of trichloroethylene (34). It is noted, that the alternative mechanism, i.e., electron injection from the excited chloroplatinate resulting in a platinum(V) intermediate cannot be completely ruled out.

To estimate the redox potential of the intermediate surface species, the following considerations are made. As summarized above, excitation of the surface complex $\{[\text{Ti}]\text{--O--PtCl}_4\text{L}\}^{n-}$ leads to formation of two new redox centers. The oxidative one can be described as a kind of Cl/Cl^- pair coordinated weakly to a metal center. It is reasonable

to assume that this oxidant is weaker than the free Cl/Cl^- pair ($E^\circ_{\text{Cl}/\text{Cl}^-} = 2.6$ V, value for aqueous solution (35)), but stronger than $\frac{1}{2}\text{Cl}_2/\text{Cl}^-$ ($E^\circ_{\frac{1}{2}\text{Cl}_2/\text{Cl}^-} = 1.3$ V (36)). In addition, the required potential has to be higher than 1.18 V, the oxidation potential of 4-CP, and lower than 2.4 V, the estimated redox potential of $\bullet\text{OH}/\text{OH}^-$ couple, because no hydroxyl radical formation could be observed in scavenging experiment with benzoic acid (9). Thus, the potential of the oxidative center should be in the range of 1.3–2.4 V.

Unfortunately, the redox potential of the $\text{Pt}^{4+/3+}$ couple is not known in literature. Although some stable Pt^{III} compounds have been isolated and characterized (37), the oxidation state III is reached usually only in unstable intermediates of photoaquation reactions (38–40) and on titania surfaces as detected by time resolved diffuse reflectance spectroscopy (41). To estimate the potential of the reductive surface center one has to recall that the injection of an electron into the conduction band of titania (TH) occurs at $\text{pH}=7$, as confirmed by photocurrent measurements. Therefore, the redox potential of the surface $\text{Pt}^{4+/3+}$ couple should be equal or more negative than -0.28 V, i.e., the flatband potential of 4.0% $\text{H}_2[\text{PtCl}_6]/\text{TH}$ at $\text{pH}=7$. From these results a potential energy diagram can be constructed as summarized in Scheme 2 for 4.0% $\text{H}_2[\text{PtCl}_6]/\text{TH}$ at $\text{pH}=7$. It includes the experimentally obtained positions of valence and conduction band edges, estimated redox potentials of the excited state of the surface platinum complex and other relevant potentials taken from literature. An important remark which should be made here is concerned with the error of the estimated potentials. Usually they are measured in simplified systems – for instance in the absence of titania – while adsorption at the surface, presence of various redox couples and other parameters can influence their values. Therefore the presented data may be connected with a rather large error.

As described above the oxidation potential of the platinum(III) species should be equal or more negative than -0.28 V. This is supported by the pH dependence of 4-CP photodegradation in presence of 4.0% $\text{H}_2[\text{PtCl}_6]/\text{TH}$ (10). The reaction is slowed down in basic media and almost suppressed at $\text{pH}=11$ –12. Since Bahnemann *et al.* observed a contrary tendency, i.e., a slight increase in 4-CP degradation rate with increasing pH for unmodified P25 (42), our observation may be connected with a too cathodic position of the flatband potential and therefore the electron injection should be much slower in basic suspensions. This supports the estimation of the redox potential of $\text{Pt}^{4+/3+}$ couple to be at ca. -0.3 to -0.4 V, i.e., around the flatband potential of the catalyst at $\text{pH}=7$ –8. However,



SCHEME 2. Potential diagram for 4.0% $\text{H}_2[\text{PtCl}_6]/\text{TH}$ at $\text{pH} = 7$. All potentials are given versus NHE.

the pH-dependence of the reaction may also be caused by rather slow substitution of Cl^- ligands with OH^- (43,44).

The difference between the redox potentials of reductive and oxidative surface centers cannot be higher than the absorbed light energy divided by the elemental charge. In the case of irradiation near to the absorption onset (620–650 nm) this difference is ca. 2 V. $E_{\text{Pt-(Cl/Cl}^\bullet\text{)}}$ can be estimated as described above at ca. $-0.4 \text{ V} + 2.0 \text{ V} = 1.6 \text{ V}$ (Scheme 2).

Whereas the results obtained for the photodegradation with visible light ($\lambda \geq 455 \text{ nm}$, “Vis” in Scheme 1) can be rationalized within the proposed mechanism, this is not possible for the observations made during the UV experiments ($\lambda \geq 320 \text{ nm}$, “UV” in Scheme 1). As mentioned above, surface modification of P25 by grinding produced a catalyst more active in the visible but less in the UV, as compared to P25. This was rationalized by an “inner filter effect” of the metal complex, thus diminishing band-to-band excitation of the unmodified P25 surface and therefore the steady-state concentration of the reactive e^-/h^+ pairs. The same argument should hold also for the comparison of 2.0% $\text{H}_2[\text{PtCl}_6]/\text{TH}$, prepared by adsorption from

solution, with TH. However, in this case the modified material is more active also upon UV irradiation. This significant difference can be rationalized by first recalling that unmodified TH is much less active than P25 (curves TH and P25 in Fig. 9b), suggesting that electron-hole recombination is much stronger in TH. Accordingly, the inner filter effect should be much less pronounced and may be overruled by a more efficient electron transfer arising from an additional contribution of the higher excited states of the platinum component (Scheme 1).

VII. Summary

Chemisorption of $\text{H}_2[\text{PtCl}_6]$ onto high surface anatase powder leads to formation of the surface complex $\{[\text{Ti}]\text{OPtCl}_4\text{L}\}^{n-}$, $\text{L} = \text{H}_2\text{O}$, OH^- , $n = 1, 2$, in which titania acts as a ligand. Depending on the coverage, the chloroplatinate group induces an anodic shift of the band edges by up to 260 mV, thus changing the photoredox properties of the semiconductor substantially. Efficient charge separation upon visible light excitation most likely occurs through initial Pt–Cl bond homolysis followed by fast electron injection into the titania conduction band. The resulting spatial separation of the charges should disfavor recombination. This novel semiconducting surface metal complex is an excellent photocatalyst for the mineralization of various pollutants by artificial visible and even natural indoor daylight.

ACKNOWLEDGMENTS

This work was supported by the Bavarian State program *BayFORREST* and the Deutsche Forschungsgemeinschaft (SFB 583).

REFERENCES

1. Tryk, D. A.; Fujishima, A.; Honda, K. *Electrochim. Acta* **2000**, *45*, 2363–2376.
2. Yamashita, H.; Ichihashi, Y.; Takeuchi, M.; Kishiguchi, S.; Anpo, M. *J. Synchrotron Radiat.* **1999**, *6*, 451–452.
3. Yamashita, H.; Harada, M.; Misaka, J.; Takeuchi, M.; Ichihashi, Y.; Goto, F.; Ishida, M.; Sasaki, T.; Anpo, M. *J. Synchrotron Radiat.* **2001**, *8*, 569–571.
4. Yamashita, H.; Harada, M.; Misaka, J.; Takeuchi, M.; Ikeue, K.; Anpo, M. *J. Photochem. Photobiol., A* **2002**, *148*, 257–261.
5. Klosek, S.; Raftery, D. *J. Phys. Chem. B* **2001**, *105*, 2815–2819.
6. Kisch, H.; Zang, L.; Lange, C.; Maier, W. F.; Antonius, C.; Meissner, D. *Angew. Chem., Int. Ed.* **1998**, *37*, 3034–3036.

7. Zang, L.; Lange, C.; Abraham, I.; Storck, S.; Maier, W. F.; Kisch, H. *J. Phys. Chem. B* **1998**, *102*, 10765–10771.
8. Zang, L.; Macyk, W.; Lange, C.; Maier, W. F.; Antonius, C.; Meissner, D.; Kisch, H. *Chem. Eur. J.* **2000**, *6*, 379–384.
9. Macyk, W.; Kisch, H. *Chem. Eur. J.* **2001**, *7*, 1862–1867.
10. Burgeth, G.; Kisch, H. *Coord. Chem. Rev.* **2002**, *230*, 41–47.
11. Macyk, W.; Burgeth, G.; Kisch, H. *Photochem. Photobiol. Sci.* **2003**, *2*, 322–328.
12. Burgeth, G.; Fernandez, A.; Kisch, H. *Unpublished results*.
13. Boehm, H. P.; Herrmann, M. *Z. Anorg. Allg. Chem.* **1967**, *352*, 156–167.
14. Hermann, M.; Boehm, H. P. *Z. Anorg. Allg. Chem.* **1969**, *368*, 73–86.
15. Flaig-Baumann, R.; Herrmann, M.; Boehm, H. P. *Z. Anorg. Allg. Chem.* **1970**, *372*, 296–307.
16. Herrmann, M.; Kaluza, U.; Boehm, H. P. *Z. Anorg. Allg. Chem.* **1970**, *372*, 308–313.
17. Van Veen, J. A. R. *Z. Phys. Chem.* **1989**, *162*, 215–229.
18. A final structural assignment based on EXAFS measurements is in progress.
19. Kortuem, G. *Reflection Spectroscopy*; Springer: New York, **1969**.
20. Edreva-Kardjieva, R. *Bulg. Chem. Commun.* **1992**, *25*, 166–192.
21. Weckhuysen, B. M.; Schoonheydt, R. A. *Catal. Today* **1999**, *49*, 441–451.
22. Cox, L. E.; Peters, D. G. *Inorg. Chem.* **1970**, *9*, 1927–1930.
23. Cox, L. E.; Peters, D. G.; Wehry, E. L. *J. Inorg. Nucl. Chem.* **1972**, *34*, 297–305.
24. Tauc, J.; Grigorovici, R.; Vancu, A. *Phys. Stat. Sol.* **1966**, *15*, 627–637.
25. Ward, M. D.; White, J. R.; Bard, A. J. *J. Am. Chem. Soc.* **1983**, *105*, 27–31.
26. White, J. R.; Bard, A. J. *J. Phys. Chem.* **1985**, *89*, 1947–1954.
27. Roy, A. M.; De, G. C.; Sasmal, N.; Bhattacharyya, S. S. *Int. J. Hydrogen Energy* **1995**, *20*, 627–630.
28. Bolts, J. M.; Wrighton, M. S. *J. Phys. Chem.* **1976**, *80*, 2641–2645.
29. Kavan, L.; Graetzel, M.; Gilbert, S. E.; Klemen, C.; Scheel, H. J. *J. Am. Chem. Soc.* **1996**, *118*, 6716–6723.
30. Tetzlaff, T. A.; Jenks, W. S. *Org. Lett.* **1999**, *1*, 463–465.
31. Davidson, C. M.; Jameson, R. F. *Trans. Faraday Soc.* **1965**, *61*, 2462–2467.
32. Mills, A.; Davies, R. H.; Worsley, D. *Chem. Soc. Rev.* **1993**, *22*, 417–425.
33. Linsebigler, A. L.; Lu, G.; Yates, J. T. Jr. *Chem. Rev.* **1995**, *95*, 735–758.
34. Pruden, A. L.; Ollis, D. F. *J. Catal.* **1983**, *82*, 404–417.
35. Malone, S. D.; Endicott, J. F. *J. Phys. Chem.* **1972**, *76*, 2223–2229.
36. “CRC Handbook of Chemistry and Physics”, 80 edn.; CRC Press: Boca Raton, New York, London, Tokyo, **1999**: 8–22.
37. Usón, R.; Fornies, J.; Tomás, M.; Menjón, B.; Sünkel, K.; Bau, R. *J. Chem. Soc., Chem. Commun.* **1984**, 751–752.
38. Wright, R. C.; Laurence, G. S. *J. Chem. Soc. Chem. Commun.* **1972**, 132–133.
39. Rehorek, D.; Dubose, C. M.; Janzen, E. G. *Inorg. Chim. Acta* **1984**, *83*, L7–L8.
40. Waltz, W. L.; Lilie, J.; Goursot, A.; Chermette, H. *Inorg. Chem.* **1989**, *28*, 2247–2256.
41. Draper, R. B.; Fox, M. A. *Langmuir* **1990**, *6*, 1396–1402.
42. Theurich, J.; Lindner, M.; Bahnemann, D. W. *Langmuir* **1996**, *12*, 6368–6376.
43. Holleman, A. F.; Wiberg, E. “*Lehrbuch der Anorganischen Chemie*”; Ed. Auflage; Walter de Gruyter: Berlin, New York, **1985**, pp. 91–100.
44. Johnson, R. C.; Basolo, F.; Pearson, R. G. *J. Inorg. Nucl. Chem.* **1962**, *24*, 59–71.

INDEX

- Acetone
 - $\{(\mu\text{-H})(\mu\text{-pdt})[\text{Fe}(\text{CO})_2(\text{PMe}_3)_2]\}^+$
 - reaction with, 20–22
 - $\{(\mu\text{-H})(\mu\text{-pdt})[\text{Fe}(\text{CO})_2(\text{PMe}_3)_2]\}^+[\text{PF}_6]^-$
 - reactions with, 4–5
- Acetone complex, 22
- Acetonitrile complex, 20
- Acidic H_2 complex, 143
- Adenosylcobalamin, 196
- Agostic complexes, 137
- Alcohols
 - aerobic oxidation, 211–240
 - transformation into aldehydes and ketones, 212
- Aldehydes, transformation of alcohol into, 212
- Aliphatic primary alcohols, 230
- Alkyl C–H bond activation, 157
- Ammonia, dinitrogen conversion to, 27
- Anions, proton transfer to, 149–150
- Arg425, 105
- Aryl diimine complexes, 156
- Asp490, 113
- ATP formation via ATPase, 101
- ATPase, ATP formation via, 101
- B3LYP, 104–105, 108, 119, 121, 123
- Back donation, 129–130
- Bandgap energies, 245
- $\text{B}(\text{C}_6\text{F}_5)_3$, 149, 167
- Benzene, 214
- B–H bond, 131
 - heterolytic cleavage, 168–171
- BINAP–Ru chemistry, 148
- Binuclear reductive elimination, 17
- Bis(dinitrogen) complex, 51
- Bond dissociation energies, 9
- bonding, non-classical, 129
- C. vinosum*, 102
- Catalytic H/D scrambling, 141
- Catalytic hydrogenation, 140
 - mechanism for, 147
- Catalytic potential, 78–80
- Cationic diimine palladium complexes, 156–158
- Cationic diimine platinum complexes, 156–158
- Cationic iridium complexes, 154–156
- Cationic rhenium complexes, 154–156
- Cationic silane complexes, 154
- C–H bonds, heterolytic cleavage of, 168–171
- C–H cleavage, 131
- C–H vibrations, 84
- CH_2Cl_2 , 161, 164
 - lability of, 138
- Chelate ligand modification, 85–88
- Chemisorption of H_2 [PtCl₆], 258
- p*-chlorobenzaldehyde, 214
- Chlorocopper(II) complex, 182
- 4-Chlorophenol (4-CP), 241–242
- Closed-shell systems, 94
- CN–H bond, 113
- CO binding, 108
- CO ligands, 144–145
 - lability of, 7
- CO/ CH_3CN exchange, 21
- Cobalt, tetrapodal pentadentate
 - coordination modes, 189–197
- Cobalt complexes, comparison of bond lengths, 190
- $[\text{Co}(\text{CH}_3)]\text{S}_2\text{O}_6$, 197
- Compressed dihydride, 130
- Coordinated didazene, photoisomerization, 82–88
- Coordinated H_2
 - heterolytic cleavage and acidity, 132–150
 - intermolecular heterolytic cleavage, 136–140
- Coordination number, 136
- Copper, tetrapodal pentadentate
 - coordination modes, 184–186
- Copper-catalyzed aerobic oxidation protocol
 - first generation, 212–216
 - mechanistic hypothesis, 219–220
 - second generation, 216–223
 - supporting experiments, 220
 - ^tBuOK, 228–230

- Copper-catalyzed aerobic oxidation
 protocol (*cont.*)
 third generation, 223–228
 tuning the hydrazine structure, 221–223
 unique solvent effect, 225–228
 using DBAD–H₂, 224
 variation in structure of base, 223–225
 Copper(II) complex, molecular structure
 of cation, 185
 Copper(II) polyamine complexes, 184
 [CpFe(CO)(PR₃)(H₂)]⁺, 167
 [CpFe(CO)(PR₃)(HSiEt₃)]⁺, 166
 CpMoH(CO)₃, 139
 [CpRu(PMe₃)₂(HSiCl₃)] [BAR_F], 164
 CuCl·Phen/DBAD complex, 228, 234
 Cyanide ligands, 144
 Cyanuric acid, photodegradation of, 252
 Cys70, 109, 114
 Cys492, 109–110, 114–115, 122–123
 Cys495, 109, 111, 114–115, 118
 CysSe492, 106, 109

D. fructosovorans, 102
D. gigas, 102, 104
D. vulgaris, 102
 Dark desorption experiments, 243
 D–D bond, 18
 DEAD–H₂, 216–222
 1-Decanol, 232
 Dehydrogenation mechanism, 220
 Density Functional Theory (DFT), 3, 6,
 23, 29, 32, 44, 57, 59–60, 62, 93,
 104, 123
Desulfomicrobium baculatum, 103
 Dewar–Chatt–Duncanson, 129
 D₂/μ-H exchange, 20
 D₂/H⁺ exchange, 64
 D₂/H₂O mixtures, 7, 23
 H/D exchange, 4, 12
 D₂/H₂O scrambling, 17–19
 Diatomic ligands, 2
cis-diazene
 coordination process, 70
 energy difference of coordinated, 76
 stabilization effects, 69–70
trans-diazene, 67–69, 73
 coordination process, 70
 electronic coordination energy of, 77–78
 energy difference of coordinated, 76
 stabilization effects, 69–70

 Diazene complexes, 65, 74
 Lewis structures, 71
 Diazene-coordinating complex, 82
 Diazene isomers, 76
 Dichloromethane, 13
 Dielectric constant, 105
 Dielectric continuum, 105
 Diffuse reflectance spectra, 244
 Dihydride complex, 17
 Dihydrogen
 activation, 105, 108–109
 heterolytic cleavage, 101
 insertion of, 13
 water-assisted activation, 15
 water-free activation, 15
 Dihydrogen binding, 108
 Dihydrogen bonding, 140–149
 Dihydrogen cleavage, 106
 Dihydrogen complexes, 13, 17, 130
 Dihydrogen coordination, 10, 127
 Diiron complexes, 5
 Diiron(II) complexes, 3
 Di-isopropylazodicarboxylate (DIAD),
 222–223
N,N-dimethylacetamide, 167
N,N-dimethylhydrazine, 216
 Dinitrogen
 conversion to ammonia, 27
 end-on terminal reduction pathway of,
 27–53
 end-on versus side-on binding, 75–76
 reduction energetics, 79
 Dinitrogen complexes, 74
 MO scheme, 44
 QCA–NCA, 30–35
 vibrational spectroscopy, 30–35
 Dinuclear complexes, hydrogen bonding in,
 70–74
 Dinuclear N₂ complex, 88–92
 Di-tertbutylazodicarboxylate (DBAD),
 223
Dm. baculatum, 102
 4-DMAP, 232, 235

 Electron acceptors, 247
 Electron affinity, 118–119
 Electron pair, 171
 bonding, 128
 non-bonding, 128
 2-Electron–2-proton transfer, 64–74

- Electron transfers in [NiFe] hydrogenase, 101–125
- Electronic absorption spectroscopy, 43–50
- Electronic coordination energy of *trans*-diazene, 77–78
- Electronic properties, 2
- Electronic structure, 43–50
- Electrophilic cationic centers, 154–166
- Electrophilic metal centers, 127–177
- End-on terminal reduction pathway of dinitrogen, 27–53
- EPR spectroscopy, 102
- (Et₃Si)₂O, 157
- Et₃SiCl, 157
- Et₃SiON, 142
- η^2 -H₂, 143–144, 162
- Fe–CO bond, 13
- Fe–CO bond dissociation energies, 11
- FeFe nitrogenase, 62
- FeH₂(H₂)(PR₃)₂, 134
- [Fe]H₂ase active site, CO-inhibited oxidized form, 3
- [Fe]H₂ase active site models
- chemistry, 2
 - H/D exchange activity assays in, 1
- [Fe]H₂ase enzyme, redox levels, 2
- Fe^IFe^I catalyst, 4, 19
- Fe^IFe^I precursors, 6
- Fe(II) centers, 74–82
- Fe(II) complexes, hydrogen bonds in, 65–69
- Fe^{II}Fe^{II} complexes, 6–7
- functional models, 3
- FeMo-cofactor (FeMoco), 27, 56–61
- new structure, 58, 62
 - resting states, 60
 - X-ray diffraction, 58
- FeMo nitrogenase, 56, 62
- Fe–NCMe bond, 13
- [Fe(“NHS₄”)]₂(μ -N₂H₂) 145
- [FeNi] hydrogenases, 144
- Fe-only hydrogenase, 8
- Fe–S based catalytic transition metal complex, 93
- Fe–S bond, 13
- Fe–S clusters, 102, 112, 116, 119
- Fe–S complexes, 59–60, 65
- Fe(II)–S complexes, 92
- FeV nitrogenase, 62
- Flatband potential values, 249
- Fluorobenzene, 227
- Fuel cell development, 1
- Gauge-Independent Atomic Orbital (GIAO) method, 6
- GAUSSIAN, 93
- Glu23, 106, 109, 114
- ¹H NMR spectroscopy, 10, 21–22, 167–168
- ²H NMR spectroscopy, 3, 7, 10, 18–19
- H₂
- activation of, 132
 - cleavage, 2, 109
 - exchange without ligand loss, 12
 - intermolecular heterolysis of, 150
 - intramolecular heterolytic cleavage of, 140–150
- H₂ complexes, highly acidic species, 135
- Haber–Bosch process, 56
- [HB(C₆F₅)₃][–], 167
- HBF₄, protonation with, 29
- HD complex, 143
- H/D exchange
- activity assays in [Fe]H₂ase active site models, 1
 - catalysis, 8
 - general mechanism, 18
 - inhibition, 13–14
 - into μ -H position, 16–17
 - reaction, 23–24
- H/D isotopic scrambling process, 23
- H₂/D₂ mixtures, H/D exchange, 12
- H₂/D₂O mixtures, 23
- H/D exchange reactivity in, 4
- H/D scrambling, 7
- Heterocyclic amines, 230–233
- Heterolytic cleavage, 131
- B–H bonds, 168–171
 - C–H bonds, 168–171
 - Si–H bonds, 150–153
 - silanes, 154–166
- Heterolytic splitting, 127–177
- Hexachloroplatinic acid, 241
- Hexafluorophosphate salts, 187
- H–H bond, 18, 127–128
- H–H bond cleavage, 14–16, 120–123
- in [NiFe] hydrogenase, 110–111
- His72, 106

- His77, 109, 111–115, 117–121, 123
 charged, 118–121
 uncharged, 106–118
 His430, 113
 HO₃SCF₃, 139
 HOD formation, 19
 Homolytic cleavage, 131
 H₂[PtCl₆], chemisorption of, 258
 H–S bonds, 70
 H–S distances, 74
 Hydrazidium complexes, 29
 MO schemes, 45
 Hydrazines, unusual reactivity,
 216–218
 Hydride transfer, 119
 Hydrogen, binding energy, 112–113
 Hydrogen bond energy, 67, 73–74
 Hydrogen bonds
 in dinuclear complexes, 70–74
 in Fe(II) complexes, 65–69
 in *trans*-2(N₂H₂), 67
 unconventional, 142
 Hydrogenase enzymes, 1–2, 101
 Hydrogenases, main classes, 101–102

 Incident photon to current efficiency
 (IPCE), 247–248, 250
 INDO method, 59
 Infrared spectroscopy, 29
 Intermolecular heterolysis of H₂, 150
 Intermolecular heterolytic cleavage, 133
 Intramolecular heterolytic cleavage, 133
 of H₂, 140–150
cis-[Ir(CF₃)(CO)(dppe)(DIB)]²⁺, 148
 [IrH₂(CO)₂(dppe)]⁺, 148
 [IrH₂(HS(CH₂)₃SH)(PCy₃)₂]⁺, 144
 Iridium complexes, 166–167
 Iron, tetrapodal pentadentate coordination
 modules, 197–206
 Iron complexes, 166–167
 Iron–molybdenum cofactor *see* FeMo-
 cofactor (FeMoco)
 Isomerization mechanisms, 76

 Jahn-Teller axis, 113
 J_{HD} values, 134–135

 K₂CO₃, 223, 225–228
 Ketones, transformation of alcohol
 into, 212

 Kinetic acidity, 135–136
 Kohn-Sham method, 59, 94

 Lewis bases, 82
 Lewis structures, 83
 Ligand bonding energies, 77–78

 Manganese complexes with tied-back
 phosphites, 158–168
 [MCl(NNH₃)(depe)₂]Cl, experimental
 and calculated transition
 energies, 49
 [M(diphosphine)₂] systems, N₂ protonation
 in, 45
 Meerwein–Pondorf–Verley–Oppenauer
 reaction, 220
 Metal–H₂ complexes, 127
 Methylcobalt(III) complexes, 196
 [MF(¹⁵N¹⁵NH₃)(depe)₂](BF₄)₂, 41
 [MF(NNH₃)(depe)₂](BF₄)₂
 experimental and calculated transition
 energies, 49
 observed and calculated frequencies, 41
 [Mn(CO)₃{P(OCH₂)₃CMe}₂(CH₂Cl₂)]
 [BAr_F], 162–164
 [Mn(CO)₃(P)₂(CH₂Cl₂)] [BAr_F], 165
 [Mn(CO)₄{P(OCH₂)₃CMe}(CH₂Cl₂)]
 [BAr_F], 164
trans-[Mn(CO)₃(P)₂(CH₂Cl₂)]⁺, 160
 M–N force constants, 42
 [MoF(NNH₃)(depe)₂](BF₄)₂, solid-state
 UV/Vis absorption spectra, 48
 Molecular orbitals of N₂ upon conversion
 to NNH₃[−], 43
 Molybdenum complexes, 27–53
 Molybdenum triamidoamine complex, 28
 Mo–N stretch, 39
 Mo/N₂H_x complexes, 30
 Mo–NNH₃ complex, 40
 UV/Vis spectra, 47
 Mo/W–N₂ complexes, 30
 Mo/W–N₂ depe complexes, vibrational
 spectroscopic properties, 35
 {(μ-H)(μ-pdt)[Fe(CO)₂(PMe₃)₂]}⁺, reaction
 with acetone, 20–22
 {(μ-H)(μ-pdt)[Fe(CO)₂(PMe₃)₂]}⁺ [PF₆][−],
 reactions with acetone, 4–5

 N₂ protonation in [M(diphosphine)₂]
 systems, 45

- N_2 reduction, 56
 mechanism of, 27
 N_2 species, metal–ligand bonding
 properties, 43
 N_2H_x species, metal–ligand bonding
 properties, 43
 $\text{Na}^+ [\text{RuH}(\text{PCy}_3)(\text{S}_4)]^-$, 143
 $\text{Na}_2[\text{PtCl}_6]$, 245
N–H stretching modes, 84
N–H stretching vibrations, 36, 39
 ^{14}N –I infrared spectra, 33
 ^{15}N –I infrared spectra, 33
N–N force constants, 42
N–N stretch vibration, 84
Ni–A, 106
Ni–C–O bond angle, 108
Ni–CO dehydrogenase, 102
Nickel, tetrapodal pentadentate
 coordination modules, 186–189
Nickel(II) complexes, 186
Ni–Fe bond, 109, 113, 123
Ni–Fe dimer, 102, 108
NiFe complex, 109
NiFe(I,II), 114
NiFe(II,II), 108, 111, 123
NiFe(II,II) oxidation state, 105
NiFe(III,II), 106–107, 111–113
[NiFe] hydrogenase
 catalytic cycle, 117, 120–121, 123
 crystal structure, 102
 electron transfers in, 101–125
 first electron transfer in, 112
 H–H bond cleavage in, 110–111
 molecular hydrogen complex, 107
 proton transfers in, 101–125
 second electron transfer, 116
[NiFeSe] enzymes, 102, 121
Ni–H bond, 109
Ni–SCys495, 109
Nitrogen fixation
 concept of activation, 28
 quantum chemical investigations,
 55–100
Nitrogenase, 27
 Thorneley/Lowe kinetic scheme of, 28
Nitrogenase active site, 57–61
 X-ray structure, 56–57
NMI, 232–233, 235
NMR sample tubes, 5
NMR shielding tensors, 6, 22–23
NMR spectra, 138
NNH₂ complex, MO scheme, 45–46
2-Nonanol, 226
Open site capture process, 14
Open site creation, 10–12
Peroxo complex, molecular structures, 194
Photocatalysts
 characterization, 243–249
 preparation, 242–243
Photocatalytic degradation with artificial
 visible light, 249–252
Photochemical reduction mechanism,
 89–92
Photocurrent measurements, 247
Photodegradation
 of cyanuric acid, 252
 with natural indoor daylight, 252–253
 with sunlight, 253
Photodesorption experiments, 244
Photoisomerization of coordinated
 didazene, 82–88
Photovoltage vs. pH, 246
 π -complexes, 128–129
 pK_a , 134–135, 139
Platinum complex, homolytic Pt–Cl
 cleavage, 254
Platinum(III) complex, 254
Platinum(IV) chloride, 245
 PMe_3 ligands, 3, 8
Poisson–Boltzmann solver, 105
Polarization functions, 105
Polymeric phosphazene metal adducts, 182
Primary alcohols
 copper-catalysed aerobic oxidation, 231
 efficient, aerobic, catalytic oxidation, 233
Protein crystal structures, 1
Proton transfer
 in [NiFe] hydrogenase, 101–125
 to ancillary ligands, 140–149
 to anions, 149–150
Protonation
 of anionic Ru hydride, 143
 with HBF_4 , 29
Protonation reduction step, 63
Pt–Cl bond homolysis, 258
QCA-NCA, 29
 dinitrogen complexes, 30–35

- Quadratic Synchronous Transit (QST3)
method, 6
- Quantum chemical methodology, 93–96
- Quantum Chemistry Assisted Normal
Coordinate Analysis *see* QCA-NCA
- Raman scattering factors, 96
- Raman spectroscopy, 29
- Raman vibrational frequencies, 87
- $[\text{Re}(\text{CO})_3\{\text{P}(\text{OCH}_2)_3\text{Cme}\}_2(\text{CH}_2\text{Cl}_2)]^+$, 163
- $[\text{Re}(\text{CO})_4(\text{P})]^+$, 165
- $[\text{Re}(\text{Co})_4(\text{PR}_3)(\eta^2\text{-H}_2)]^+$, 145
- cis*- $\text{Re}(\text{CO})_4(\text{PR}_3)\text{H}$, 149
- $\text{Re-CH}_2\text{Cl}_2$, 164
- Redox potential, 119, 247, 255–256
- Resonance Raman methods, 82
- Rhenium complexes with tied-back
phosphites, 158–166
- $[\text{RhH}(\text{PCy}_3)(^{\text{bu}}\text{S}_4\text{-H})]^+$, 143
- Rivière and Jallabert system, 212–214
- $\text{Ru}(\text{II})$ catalysts, 147
- $\text{Ru}(\text{II})\text{-S}$ complexes, 92
- trans*- $\text{RuCl}_2[(\text{S})\text{-binap}][\text{S},\text{S})\text{-dpen}]$, 146
- $\text{Ru}(\text{DMSO})(\text{PCy}_3)(\text{S}_4)$, 143
- $\text{Ru}(\text{H}_2)$ complexes, 146
- $[\text{Ru}(\text{H}_2)(\text{CNH})(\text{L})_2][\text{OTf}]_2$, 149
- RuHX complex, 147
- $\{[\text{Ru}(\text{P}^i\text{Pr}_3)(\text{N}_2\text{Me}_2\text{S}_2)]_2\text{N}_2\}$, 88
- Ruthenium hydride, 147
- Secondary alcohols, 234–235
- Selenium substitution, 121–123
- Sellmann-type $\text{Fe}(\text{II})$ complexes, 75
- Sellmann-type metal complexes, 61–64
- Sellmann-type metal diazene complexes, 70
- Semiconductor photocatalysis, 242
- Shared-electron number (SEN) method,
66–67, 85, 95
- σ bonds, 137
- σ complexes, 128–129
- Sigmoidal voltage/pH curve, 246
- Si–H bonds, 131
- heterolytic cleavage, 150–153
- Si–H cleavage, 172
- Silanes
- alcoholysis, 166–168
- heterolytic cleavage, 154–166
- reaction of, 153
- Silylium bonds, 131
- Spin barriers, 81–82
- Steric repulsions, 153
- Sulfur substitution, 122–123
- Superelectrophilic metal centers, 132
- Superoxo complex, molecular structures,
194
- TDDFT (time-dependent DFT), 29, 47, 49
- Terminal-ligand dissociation, 11
- 2,2,6,6-Tetrakis(aminomethyl)-4-
azaheptane, 186
- Tetrapodal pentadentate coordination
modules, 183–206
- cobalt, 189–197
- copper, 184–186
- iron, 197–206
- nickel, 186–189
- zinc, 183–184
- Tetrapodal pentadentate nitrogen ligands,
179–210
- Tetrapodal pentadentate topology, 180
- Thorneley/Lowe kinetic scheme of
nitrogenase, 28
- Thr448, 106
- Tied-back phosphite ligands, 165
- Tied-back phosphites, 158–166
- manganese complexes with, 167–168
- Titania transition metal complex, 241–259
- Toluene, 214, 223
- Transmission electron microscopy, 243
- Triflic acid, 149
- Tungsten complexes, 27–53
- TURBOMOLE, 93–95
- Type I ligands, 180
- Type II ligands, 180–181
- Type III ligands, 182
- Tyr442, 113
- UV spectroscopy, 243
- UV/Vis absorption spectroscopy, 44
- UV/Vis spectra, Mo-NNH_3 complex, 47
- Vanadium doped titania, 242
- Vibrational spectroscopy, 29
- dinitrogen complexes, 30–35
- $\text{W-N}_2\text{H}_x$ complexes, 35–43
- Visible light photocatalysis, 241–259
- mechanism, 254–258
- $[\text{WCl}(\text{NNH}_2)(\text{depe})_2](\text{BF}_4)_2$, solid-state
UV/Vis absorption spectra, 48

- W(CO)₃(PCy₃)₂(H₂), 135
W(CO)₃(P^{*i*}Pr₃)₂(H₂), 127–128
W(CO)₃(PR₃)₂(H₂), 134
W(CO)₅(BH₃ · PMe₃), 168
Werner-type complexes, 128, 195
[WF(NNH₃)(depe)₂](BF₄)₂, solid-state
 UV/Vis absorption spectra, 48
[WF(NNH)(dppe)₂], observed and
 calculated frequencies, 38
W–N₂H_x complexes, vibrational
 spectroscopy, 35–43
[W(N₂)₂(dppe)₂](¹⁴N–I), IR spectra, 32
[W(N₂)₂(dppe)₂]
 force constants, 34
 observed and calculated frequencies, 34
W(N₂)₂(P)₄ complexes, 146
[W(¹⁵N₂)₂(dppe)₂](¹⁵N–I), IR spectra,
 32
W–NNH₃ complexes, 51
Xenon binding experiments, 108
X–H bonds, 131
X-ray crystallography, 8
X-ray diffraction, FeMoco structure, 58
X-ray powder diffraction, 243
Zinc, tetrapodal pentadentate coordination
 modules, 183–184
Zinc-aqua complexes, 183

CONTENTS OF PREVIOUS VOLUMES

VOLUME 42

Substitution Reactions of Solvated Metal Ions

*Stephens F. Lincoln and
André E. Merbach*

Lewis Acid–Base Behavior in Aqueous Solution: Some Implications for Metal Ions in Biology

Robert D. Hancock and Arthur E. Martell

The Synthesis and Structure of Organosilanols

Paul D. Lickiss

Studies of the Soluble Methane Monooxygenase Protein System: Structure, Component Interactions, and Hydroxylation Mechanism

Katherine E. Liu and Stephen J. Lippard

Alkyl, Hydride, and Hydroxide Derivatives in the *s*- and *p*-Block Elements Supported by Poly(pyrazolyl)borato Ligation: Models for Carbonic Anhydrase, Receptors for Anions, and the Study of Controlled Crystallographic Disorder

Gerard Parkin

INDEX

VOLUME 43

Advances in Thallium Aqueous Solution Chemistry

Julius Glaser

Catalytic Structure–Function: Relationships in Heme Peroxidases

*Ann M. English and
George Tsapralis*

Electron-, Energy-, and Atom-Transfer Reactions between Metal Complexes and DNA

H. Holden Thorp

Magnetism of Heterobimetallics: Toward Molecular-Based Magnets

Olivier Kahn

The Magnetochemistry of Homo- and Hetero-Tetranuclear First-Row *d*-Block Complexes

Keith S. Murray

Diiron–Oxygen Proteins

*K. Kristoffer Andersson and
Astrid Gräslund*

Carbon Dioxide Fixation Catalyzed by Metals Complexes

Koji Tanaka

INDEX

VOLUME 44

Organometallic Complexes of Fullerenes

*Adam H. H. Stephens and
Malcolm L. H. Green*

Group 6 Metal Chalcogenide Cluster Complexes and Their Relationships to Solid-State Cluster Compounds

Taro Saito

Macrocyclic Chemistry of Nickel

Myunghyun Paik Suh

Arsenic and Marine Organisms

*Kevin A. Francesconi and
John S. Edmonds*

The Biochemical Action of Arsonic Acids Especially as Phosphate Analogues

Henry B. F. Dixon

Intrinsic Properties of Zinc(II) Ion
Pertinent of Zinc Enzymes
Eiichi Kimura and Tohru Koike

Activation of Dioxygen by Cobalt Group
Metal Complexes
Claudio Bianchini and Robert W. Zoellner

Recent Developments in Chromium
Chemistry
Donald A. House

INDEX

VOLUME 45

Syntheses, Structures, and Reactions of
Binary and Tertiary Thiomolybdate
Complexes Containing the
(O)Mo(S_x) and (S)Mo(S_x)
Functional Groups (*x* = 1, 2, 4)
Dimitri Coucouvanis

The Transition Metal Ion Chemistry of
Linked Macrocyclic Ligands
Leonard F. Lindoy

Structure and Properties of Copper–
Zinc Superoxide Dismutases
*Ivano Bertini, Stefano Mangani, and
Maria Silvia Viezzoli*

DNA and RNA Cleavage by Metal
Complexes
*Genevieve Pratviel, Jean Bernadou, and
Bernard Meunier*

Structure–Function Correlations in
High Potential Iron Problems
J. A. Cowan and Siu Man Lui

The Methylamine Dehydrogenase
Electron Transfer Chain
*C. Dennison, G. W. Canters,
S. de Vries, E. Vijgenboom, and
R. J. van Spanning*

INDEX

VOLUME 46

The Octahedral M₆Y₆ and M₆Y₁₂ Clusters
of Group 4 and 5 Transition Metals
Nicholas Prokopuk and D. F. Shriver

Recent Advances in Noble–Gas
Chemistry
John H. Holloway and Eric G. Hope

Coming to Grips with Reactive
Intermediates
Anthony J. Downs and Timothy M. Greene

Toward the Construction of Functional
Solid-State Supramolecular Metal
Complexes Containing Copper(I)
and Silver(I)
*Megumu Munakata, Liang Ping Wu,
and Takayoshi Kuroda-Sowa*

Manganese Redox Enzymes and Model
Systems: Properties, Structures,
and Reactivity
*Neil A. Law, M. Tyler Caudle, and
Vincent L. Pecoraro*

Calcium-Binding Proteins
Bryan E. Finn and Torbjörn Drakenberg

Leghemoglobin: Properties and
Reactions
*Michael J. Davies, Christel Mathieu,
and Alain Puppo*

INDEX

VOLUME 47

Biological and Synthetic [Fe₃S₄] Clusters
*Michael K. Johnson, Randall E.
Duderstadt, and Evert C. Duin*

The Structures of Rieske and Rieske-
Type Proteins
Thomas A. Link

Structure, Function, and Biosynthesis of
the Metallosulfur Clusters in
Nitrogenases
Barry E. Smith

The Search for a “Prismane” Fe–S Protein
*Alexander F. Arendsen and
Peter F. Lindley*

NMR Spectra of Iron–Sulfur Proteins
*Ivano Bertini, Claudio Luchinat, and
Antonio Rosato*

Nickel–Iron–Sulfur Active Sites:

Hydrogenase and CO
Dehydrogenase*Juan C. Fontecilla-Camps and
Stephen W. Ragsdale*FeS Centers Involved in Photosynthetic
Light Reactions*Barbara Schoepp, Myriam Brugna,
Evelyne Lebrun, and Wolfgang Nitschke*Simple and Complex Iron–Sulfur Proteins
in Sulfate Reducing Bacteria*Isabel Moura, Alice S. Pereira,
Pedro Tavares, and José J. G. Moura*Application of EPR Spectroscopy to the
Structural and Functional Study of
Iron–Sulfur Proteins*Bruno Guigliarelli and
Patrick Bertrand*

INDEX

VOLUME 48

Cumulative Index for Volumes 1–47

VOLUME 49

Inorganic and Bioinorganic Reaction
Mechanisms: Application of High-
Pressure Techniques*Rudi van Eldik, Carlos Dücker-Benfer,
and Florian Thaler*Substitution Studies of Second- and
Third-Row Transition Metal Oxo
Complexes*Andreas Roodt, Amira Abou-Hamdan,
Hendrik P. Engelbrecht, and
Andre E. Merbach*Protonation, Oligomerization, and
Condensation Reactions of
Vanadate(V), Molybdate(VI), and
Tungstate(VI)*J. J. Cruywagen*

Medicinal Inorganic Chemistry

*Zijian Guo and Peter J. Sadler*The Cobalt(III)-Promoted Synthesis of
Small Peptides*Rebecca J. Browne,
David A. Buckingham,
Charles R. Clark, and Paul A. Sutton*Structures and Reactivities of
Platinum–Blues and the Related
Amidate-Bridged Platinum^{III}
Compounds*Kazuko Matsumoto and Ken Sakai*

INDEX

VOLUME 50

The Reactions of Stable Nucleophilic
Carbenes with Main Group Compounds*Claire J. Carmalt and Alan H. Cowley*Group 1 Complexes of P- and As-Donor
Ligands*Keith Izod*

Aqueous Solution Chemistry of Beryllium

*Lucia Alderighi, Peter Gans,
Stefano Midollini, and
Alberto Vacca*Group 2 Element Precursors for the
Chemical Vapor Deposition of
Electronic Materials*Jason S. Matthews and
William S. Rees Jr.*Molecular, Complex Ionic, and Solid-
State PON Compounds*Roger Marchand, Wolfgang Schnick, and
Norbert Stock*Molecular Clusters of Dimetalated
Primary Phosphanes and Arsanes*Matthias Driess*

Coordination Complexes of Bismuth(III)

Involving Organic Ligands with
Pnictogen or Chalcogen Donors*Glen G. Briand and Neil Burford*Phanes Bridged by Group 14 Heavy
Elements*Hideki Sakurai*

INDEX

VOLUME 51

Clinical Reactivity of the Active Site of
Myoglobin
Emma Lloyd Raven and A. Grant Mauk

Enzymology and Structure of Catalases
*Peter Nicholls, Ignacio Fita, and
Peter C. Loewen*

Horseradish Peroxidase
Nigel C. Veitch and Andrew T. Smith

Structure and Enzymology of Diheme
Enzymes: Cytochrome *cd*₁ Nitrate
and Cytochrome *c* Peroxidase
*Vilmos Fülöp, Nicholas J. Watmough,
and Stuart J. Ferguson*

Binding and Transport of Iron-
Porphyrins by Hemopexin
William T. Morgan and Ann Smith

Structures of Gas-Generating Heme
Enzymes: Nitric Oxide Synthase and
Heme Oxygenase
*Thomas L. Poulos, Huiying Li,
C. S. Raman, and David J. Schuller*

The Nitric Oxide-Releasing Heme
Proteins from the Saliva of the
Blood-Sucking Insect
Rhodnius prolixus
F. Ann Walker and William R. Montfort

Heme Oxygenase Structure and Mechanism
*Paul R. Ortiz de Montellano and
Angela Wilks*

De Novo Design and Synthesis of
Heme Proteins
Brian R. Gibney and P. Leslie Dutton

INDEX

VOLUME 52

High-Nuclearity Paramagnetic 3*d*-
Metal Complexes with Oxygen- and
Nitrogen-Donor Ligands
Richard E. P. Winpenny

Transition Metal–Noble Gas Complexes
D. C. Grills and M. W. George

The Materials Chemistry of
Alkoxystillbazoles and their Metal
Complexes
Duncan W. Bruce

Tetra- and Trinuclear Platinum(II)
Cluster Complexes
Tadashi Yamaguchi and Tasuku Ito

Complexes of Squaric Acid and
Its Monosubstituted Derivatives
Lincoln A. Hall and David J. Williams

Applications for Polyaza Macrocycles
with Nitrogen-Attached Pendant
Arms
Kevin P. Wainwright

Perfluorinated Cyclic Phosphazenes
Anil J. Elias and Jean'ne M. Shreeve
INDEX

VOLUME 53

Wheel-Shaped Polyoxo and
Polyoxothiometalates: From the
Molecular Level to Nanostructures
Anne Dolbecq and Francis Sécheresse

Redox Chemistry and Functionalities
of Conjugated Ferrocene Systems
Hiroshi Nishihara

New Aspects of Metal–Nucleobase
Chemistry
Andrew Houlton

Advances in the Chemistry of
Chlorocyclophosphazenes
*Vadapalli Chandrasekhar and
Venkatasubbaiah Krishnan*

Self-Assembly of Porphyrin Arrays
Laura Baldini and Christopher A. Hunter

INDEX

VOLUME 54

Solvent Exchange on Metal Ions
*Frank A. Dunand, Lothar Helm,
and André E. Merbach*

Ligand Substitution Reactions

John Burgess and Colin D. Hubbard

Oxygen Transfer Reactions: Catalysis by Rhenium Compounds

James H. Espenson

Reaction Mechanisms of Nitric Oxide with Biologically Relevant Metal Centers

Peter C. Ford, Leroy E. Laverman and Ivan M. Lorkovic

Homogeneous Hydrocarbon C–H Bond Activation and Functionalization with Platinum

Ulrich Fekl and Karen I. Goldberg

Density Functional Studies of Iridium Catalyzed Alkane Dehydrogenation

Michael B. Hall and Hua-Jun Fan

Recent Advances in Electron-Transfer Reactions

David M. Stanbury

Metal Ion Catalyzed Autoxidation Reactions: Kinetics and Mechanisms

István Fábián and Viktor Csordás

INDEX

VOLUME 55

Dioxygen Activation by Transition Metal Complexes. Atom Transfer

and Free Radical Chemistry in Aqueous Media

Andreja Bakac

Redox Reactivity of Coordinated Ligands in Pentacyano(L)Ferrate Complexes

José A. Olabe

Carbonato Complexes: Models for Carbonic Anhydrase

Achyuta N. Acharya, Arabinda Das and Anadi C. Dash

Transition Metal Chemistry of Glucose Oxidase, Horseradish Peroxidase, and Related Enzymes

Alexander D. Ryabov

Properties of Transition Metal Complexes with Metal–Carbon Bonds in Aqueous Solutions as Studied by Pulse Radiolysis

Alexandra Masarwa and Dan Meyerstein

Transition Metal Complexes with Bis(Hydrazone) Ligands of 2,6-Diacetylpyridine. Hepta-Coordination of 3d Metals

Ivana Ivanović-Burmazović and Katarina Andjelković

Potential Applications for the Use of Lanthanide Complexes as Luminescent Biolabels

Graham R. Motson, Jean S. Fleming and Sally Brooker

INDEX

CONTENTS

PREFACE	ix
-------------------	----

Synergy Between Theory and Experiment as Applied to H/D Exchange Activity Assays in [Fe]H₂ase Active Site Models

JESSE W. TYE, MICHAEL B. HALL, IRENE P. GEORGAKAKI AND
MARCETTA Y. DARENSBOURG

I. Introduction	1
II. Experimental Section	4
III. Results and Discussion	6
IV. Conclusions	23
References	24

Electronic Structure and Spectroscopic Properties of Molybdenum and Tungsten N₂, NNH, NNH₂, and NNH₃ Complexes With Diphosphine co-ligands: Insights into the End-On Terminal Reduction Pathway of Dinitrogen

FELIX TUCZEK

I. Introduction	27
II. Vibrational Spectroscopy and QCA-NCA	30
III. Electronic Structure and Electronic Absorption Spectroscopy	43
IV. Conclusions	50
References	52

Quantum Chemical Investigations into the Problem of Biological Nitrogen Fixation: Sellmann-Type Metal–Sulfur Model Complexes

MARKUS REIHER AND BERND A. HESS

I. Introduction	56
II. The Active Site of Nitrogenase: FeMo-Cofactor	57
III. Biomimetic Sellmann-Type Metal Complexes	61
IV. The First 2-Electron–2-Proton Transfer	64

V.	Reaction Energetics of the Reduction at Mononuclear Fe(II) Centers	74
VI.	Photoisomerization of Coordinated Diazene	82
VII.	Study of the First Dinuclear N ₂ Complex with Biologically Compatible Ligand Sphere	88
VIII.	Conclusion	92
IX.	Appendix: Quantum Chemical Methodology	93
	References	97

Proton and Electron Transfers in [NiFe] Hydrogenase

PER E.M. SIEGBAHN

I.	Introduction	101
II.	Computational Details	104
III.	Results and Discussion	105
IV.	Conclusions	123
	References	123

Heterolytic Splitting of H–H, Si–H, and Other σ Bonds on Electrophilic Metal Centers

GREGORY J. KUBAS

I.	Introduction	127
II.	Heterolytic Cleavage and Acidity of Coordinated H ₂	132
III.	Heterolytic Cleavage of Si–H Bonds	150
IV.	Heterolytic Cleavage of B–H and C–H Bonds	168
V.	Concluding Remarks	171
	References	172

Tetrapodal Pentadentate Nitrogen Ligands: Aspects of Complex Structure and Reactivity

ANDREAS GROHMANN

I.	Introduction	179
II.	Overview	180
III.	Tetrapodal Pentadentate Coordination Modules	183
IV.	Conclusion	206
	References	206

Efficient, Ecologically Benign, Aerobic Oxidation of Alcohols

ISTVÁN E. MARKÓ, PAUL R. GILES, MASAO TSUKAZAKI, ISABELLE CHELLÉ-REGNAUT,
 ARNAUD GAUTIER, RAPHAEL DUMEUNIER, FREDDI PHILIPPART, KANAE DODA,
 JEAN-LUC MUTONKOLE, STEPHEN M. BROWN AND CHRISTOPHER J. URCH

I. Introduction	212
II. First Generation Copper-Catalyzed Aerobic Oxidation Protocol	212
III. Second Generation Copper-Catalyzed Aerobic Oxidation Protocol	216
IV. Third Generation Copper-Catalyzed Aerobic Oxidation Protocol	223
V. Towards a Truly Efficient, Aerobic, Catalytic Oxidation Protocol	228
References	236

Visible Light Photocatalysis by a Titania Transition Metal Complex

HORST KISCH, GERALD BURGETH AND WOJCIECH MACYK

I. Introduction	241
II. Preparation and Characterization of Photocatalysts	242
III. Photocatalytic Degradation with Artificial Visible Light ($\lambda \geq 355$ nm)	249
IV. Photodegradation with Natural Indoor Daylight	252
V. Photodegradation with Sunlight	253
VI. Mechanism	254
VII. Summary	258
References	258
INDEX	261
CONTENTS OF PREVIOUS VOLUMES	269

PREFACE

This thematic volume focuses on ‘Redox-active Metal Complexes’ and is dedicated to the late Dieter Sellmann. The theme of this issue is taken from a collaborative research program, the so-called “Sonderforschungsbereich 583” initiated by Dieter Sellmann and funded by the Deutsche Forschungsgemeinschaft. In this program, active since July 2001, 16 research groups from different areas in Chemistry and Physics collaborate at the University of Erlangen-Nürnberg with the common goal to control reactivity of redox-active metal complexes through molecular architecture. As part of this activity an international symposium was organized in April 2003 on the theme of this volume, and speakers were invited to contribute to this thematic volume, scheduled to be co-edited by Dieter Sellmann. Unfortunately, Dieter Sellmann died unexpectedly on 6 May 2003. In order to acknowledge his important contributions in this area and his remarkable input to initiate the “Sonderforschungsbereich 583”, it was decided to dedicate this volume to the memory of Dieter Sellmann.

Dieter Sellmann studied chemistry in Tübingen and München, and did post-doctoral work at Princeton University, New Jersey. He completed his Habilitation in 1972 at the Technical University in München on dinitrogen fixation, a topic that fascinated him and his many collaborators over many years to come. He held his first teaching position in Paderborn, and in 1980 accepted a call to the University of Erlangen-Nürnberg as Professor of Inorganic and General Chemistry. He was a remarkably active researcher and published close to 250 research papers in top international journals. He had many friends all over the world and was well respected by many inorganic and bioinorganic chemists.

The present volume includes eight contributions. The first chapter by Michael Hall, Marcetta Darensbourg and co-workers presents a detailed account of the synergy between experiment and theory on the

H/D exchange activity of [Fe]H₂ase active site models. In the subsequent chapter, Felix Tuczek focuses on the end-on terminal reduction pathway of dinitrogen at Mo and W centers. Markus Reiher and Bernd Hess use quantum mechanical calculations to investigate biological nitrogen fixation in Chapter 3. In another theoretical chapter, Per Siegbahn describes proton and electron transfer in [NiFe] hydrogenase. In the following chapter, Gregory Kubas presents a detailed account of the heterolytic splitting of H–H, Si–H and other σ bonds. Subsequently, Andreas Grohmann reports on the development of tetrapodal pentadentate nitrogen donor ligands and their coordination compounds. In Chapter 7, István Markó and his co-workers report on the catalytic aerobic oxidation of alcohols, which is followed by the final chapter with a contribution from Horst Kisch and co-workers on visible light photolysis catalysed by titania transition metal complexes. I sincerely appreciate the effective collaboration with all authors in the preparation of this special issue of the series.

I thoroughly believe that these contributions cover important advances in inorganic and bioinorganic chemistry with respect to redox-active metal complexes, and trust that the inorganic chemistry community will benefit from them.

Rudi van Eldik
University of Erlangen-Nürnberg
Germany